Magnetism in Frustrated Magnets revealed by Neutron Polarimetry

or

Symmetry, Polarimetry and Frustration

Amy Poole

Supervisor: Andrew Wills

For Tom

Abstract

The work in this thesis uses neutron polarimetry and representational analysis to illuminate complex magnetic structures. The combination of these techniques is particularly suited to examining magnetic materials that have frustrated magnetic order and domain structures. The materials that are investigated in depth are $Er_2Ti_2O_7$ and $MnWO_4$.

$Er_2Ti_2O_7$ is a member of the pyrochlore family of materials and exhibits the classic signs of geometric frustration. The material has been proposed as an XY antiferromagnet that selects a specific basis vector ground state due to an order-by-disorder transition. The previous experimental work could not fully determine the precise details of the ground state and hence was not able to fully confirm the proposed theory. The structure was examined using neutron polarimetry and representational analysis to try and determine the magnetic order at low temperature.

$MnWO_4$ is an example of a magnetic material with complex order and frustration that arises due to competing exchange interactions. The material has a cycloidal magnetic structure that breaks the inversion symmetry and gives rise to different **k**-domains. The population of these different domains is intrinsically linked to the electronic polarization of the material, such that when one domain is populated $MnWO_4$ has a spontaneous electric polarization and is belongs to the multiferroic family of materials. By using representation analysis the number of parameters that is required to describe the magnetic structure is greatly reduced and the link between inversion symmetry breaking and multiferroicity may be better understood.

This thesis aims to identify the structures of both $Er_2Ti_2O_7$ and $MnWO_4$ as well as develop the interpretation of the polarimetry techniques.

Acknowledgements

I would like to thank all of those that have helped me with my homework:

First and foremost I would like to thank Jane Brown at the ILL. She has been an inspiration, an immense help and has supported the majority of the CRYOPAD experiments that I undertook during my Phd.

Amy Dee, Eddy Lelievre-Berna and Maria Theresa Fernandez helped enormously with the $Er_2Ti_2O_7$ data collection.

The SNP experiment on $MnWO_4$ was the last in a long line of (slightly less fruitful) experiments on the material, however I would like to thank all of those involved: Andrew Boothroyd and Prabakaran for supplying and cutting the samples. Dickon Champion for being really enthusiastic and helpful. Pascal Manuel for helping align the samples. Sean Giblin, Dennis Cowdery and all the lovely technical chaps at ISIS for helping to apply an electric field and ordering some silver pens. Matthias Gutmann, Kevin Knight and Winfried Kockelmann for ISIS instrument support. Sebatian Vial and Anne Stanault for D3 support.

Andrew, Zoso, Ross and Laura for being the Wills group. Caroline for printing responsibilities. Rosie Coates for her immense enthusiasm for science.

Betty P for supporting my cake habit. Gav 'n' Michael for light relief. Betty C for letting me escape to the country. Abby Fe for having the best wedding ever. Sam for holiday high jinx. Sophasaurus and me Dad for being related to me.

Contents

List of Tables

List of Figures

CHAPTER 1

Magnetism and Frustration

The ordered magnetic moments of individual atoms within a bulk gives rise to the observable, macroscopic magnetisation of materials. This phenomena is a fascinating example of an everyday effect due to the quantum mechanical nature of matter. This chapter will introduce the magnetic moment, describe the interactions between the individual moments, explore the bulk phenomena that are associated with these interactions and introduce the types structures that are formed.

1.1. The Magnetic Moment

The magnetic moment is a combination of two contributions: the spin, which can only be described with reference to quantum mechanics and the magnetic dipole perpendicular to the motion of the negatively charged electron, which can be described with reference to classical physics, [**1**]. The spin is usually responsible for what is termed the long range magnetic order and will be discussed after the classical contribution to the moment.

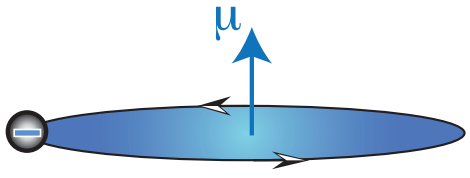

FIGURE 1.1. Schematic of an electron orbit giving rise to a magnetic moment, μ, the direction of the moment is with the blue arrow.

1.1.1. The Classical Contribution. A charged particle within an orbit, such as an electron, will produce a magnetic field in the direction perpendicular to the

plane of the orbit, with the orientation of the field dependent on the direction of the current flow. The magnitude of the magnetic dipole moment , μ, is dependent on the size of the charge on the orbiting body, which for an electron is e^-, the period of the orbit, $\tau = 2\pi r/\nu$, and the area the orbit sweeps out, πr^2. Thus, the moment due to the orbital motion is described by:

$$\mu = \frac{-e\pi r^2}{\tau} = -\frac{e\hbar}{2m_e} = -\mu_B \tag{1.1}$$

The orbital angular momentum $m_e\nu r$ of the electron in the ground state is equal to $\hbar$ and from this equation the Bohr magneton, μ_B, may be shown to have the value $\mu_B = 9.274 \times 10^{-24}\text{Am}^2$ [**1**].

The paths of the electron orbitals are more complex than the schematic in figure 1.1 and though the magnetic moment that arises from these orbitals may be considered classically, the orbitals themselves are described quantum mechanically, which will be discussed after the description of the spin.

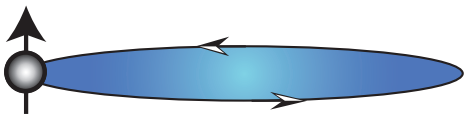

FIGURE 1.2. Schematic of the intrinsic spin of the electron, where the magnetism is localised on the electron is depicted by an arrow.

1.1.2. A Quantum Moment. The spin of an electron is most easily thought of as intrinsic angular momentum and is represented by the spin quantum number s. It can take the values m_s=$\pm 1/2$ and the moment has a component only along the axis $-g\mu_B m_s$, defined by a local field. The contribution from the spin to the overall moment is $\sqrt{s(s+1)}g\mu_B = \sqrt{3}g\mu_B/2$, where the g-factor has the value $g \approx 2$ in transition metals and μ_B is the Bohr magneton, [**1**].

The orientation of a combination of spins may be described using vector diagrams, shown in table 1.1. When two spin-$\frac{1}{2}$ particles are combined a single entity with spin

	$m_s = -1$	$m_s = 0$	$m_s = +1$
$S = 0$			
$S = 1$		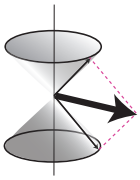	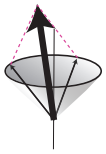

TABLE 1.1. The different combinations of spins to give the total magnitude of $\hat{\mathbf{S}}_{tot}$. There is single way to combine the vectors to give $s = 0$, hence a singlet state is formed. When $s = 1$ a triplet state is formed as there are three ways to combine the two spins to give $\hat{\mathbf{S}}^2_{tot}$=2. Whilst the relationship between the spins is maintained they can adopt any position on the surface of the cone and the angle to the azimuth is $\arccos(\frac{1}{\sqrt{3}})$ where the azimuth is defined when a magnetic field is applied. After reference [**3, 4**]

quantum number $s = 0$ or 1 is generated. $\hat{\mathbf{S}}^2_{tot}$, where $\hat{\mathbf{S}}_{tot}$ is the total spin operator, has the eigenvalue $s(s+1)$ and is therefore 0 or 2 for the cases $s = 0$ or 1. As the degeneracy of each state is $2s+1$ the $s = 0$ is a singlet state and the $s = 1$ is a triplet state, this is shown in table 1.1, [**3, 4**].

1.1.2.1. *The Pauli Matrices.* In order to allow the arbitrary orientation of the spin, described in table 1.1, it is useful to use the Pauli matrix notation,

$$\hat{\sigma}_x = \begin{pmatrix} 0 & 1 \\ 1 & 0 \end{pmatrix} \quad \hat{\sigma}_y = \begin{pmatrix} 0 & -\mathrm{i} \\ \mathrm{i} & 0 \end{pmatrix} \quad \hat{\sigma}_z = \begin{pmatrix} 1 & 0 \\ 0 & -1 \end{pmatrix} \tag{1.2}$$

The matrices may be combined as a vector,

$$\boldsymbol{\sigma} = (\hat{\sigma}_x, \hat{\sigma}_y, \hat{\sigma}_z) \tag{1.3}$$

and if the momentum operator is defined by $\hat{\mathbf{S}} = \frac{1}{2}\hat{\boldsymbol{\sigma}}$ and using the convention that angular momentum is measured in units of $\hbar$ and, hence, the angular momentum

associated with the electron is $\hbar\mathbf{S}$, the total spin angular momentum is defined as,

$$\hat{\mathbf{S}}_{tot} = \mathbf{i}\hat{S}_x + \mathbf{j}\hat{S}_y + \mathbf{k}\hat{S}_z, \tag{1.4}$$

where $\mathbf{i}$, $\mathbf{j}$ and $\mathbf{k}$ are Cartesian vectors. The vector coefficients in the spin $\frac{1}{2}$ case are restricted to have a half unit length, though the description can be generalized to the case of particles with $s > \frac{1}{2}$, and, indeed the description of the magnetic potential in the neutron scattering chapter, chapter 2, is dependent on this generality. The operator $\hat{\mathbf{S}}^2$ is given by:

$$\hat{\mathbf{S}}^2 = \hat{S}_x^2 + \hat{S}_y^2 + \hat{S}_z^2 \tag{1.5}$$

where $\hat{S}_\alpha^2$ ($\alpha = x, y, z$) is a unitary matrix with eigenvalue $\frac{1}{4}$ for $s = \pm\frac{1}{2}$ and the eigenvalue for $\hat{\mathbf{S}}^2 = \frac{3}{4}$, in the spin half case. The commutation relation between the spin operators is,

$$[\hat{S}_x, \hat{S}_y] = i\hat{S}_z \tag{1.6}$$

and the related cyclic permutations. The relationship above, combined with the observation that $\hat{S}_\alpha^2$ is unitary, indicates that the matrices form an antiunitary group. Each of the operators commute with $\hat{\mathbf{S}}^2$ to give,

$$[\hat{\mathbf{S}}^2, \hat{S}_\alpha] = 0, \tag{1.7}$$

so only one component of the vector and its magnitude can be known simultaneously.

The eigenvalues of the operators, $\hat{S}_x$, $\hat{S}_y$ and $\hat{S}_z$, specify a single spin state, m_S= +1/2 or m_S= -1/2, and can be represented by spinor notation. The notation can be understood with reference to a Riemann sphere shown in figure 1.3. The figure shows a vector $\mathbf{S}$ that runs from the origin to the surface of the sphere and a line from the end of $\mathbf{S}$ to the south pole. The value of q is the point the line intersects the

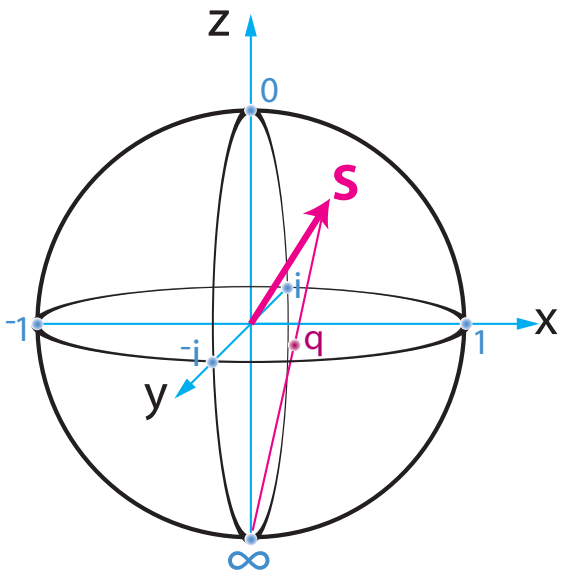

FIGURE 1.3. The Riemann sphere representation of the spin states of a spin-$\frac{1}{2}$ particle that represents the directions that are assigned to the Pauli matrices. The xy plane can be considered as an Argand diagram, the point, q, at which the line from **S** to the south pole intersects this plane gives $q = x + iy$. A measurement of the spin along **S** will always return a value of $+\frac{1}{2}$. After [**1**].

xy plane, where the plane is considered as an Argand diagram, and gives $q = x + iy$. The spinor representation of **S**, with reference to image 1.3, is given by,

$$\frac{1}{\sqrt{1+|q|^2}} \begin{pmatrix} 1 \\ q \end{pmatrix}. \tag{1.8}$$

The only diagonal matrix is in the z direction and hence the spin is usually thought of as either up or down in the direction of z, with corresponding eigenstates or $|\uparrow z\rangle$ or $|\downarrow z\rangle$. The spinors that describe these states are:

$$|\uparrow z\rangle = \begin{pmatrix} 1 \\ 0 \end{pmatrix} \qquad |\downarrow z\rangle = \begin{pmatrix} 0 \\ 1 \end{pmatrix} \tag{1.9}$$

The eigenstates of the spin in the directions x and y are degenerate and as such the spinors that represent these directions need to be normalised by division by $1/\sqrt{2}$,

$$
\begin{aligned}
|\uparrow x\rangle &= \tfrac{1}{\sqrt{2}}\begin{pmatrix}1\\1\end{pmatrix} \qquad |\downarrow x\rangle &= \tfrac{1}{\sqrt{2}}\begin{pmatrix}1\\-1\end{pmatrix} \\
|\uparrow y\rangle &= \tfrac{1}{\sqrt{2}}\begin{pmatrix}1\\i\end{pmatrix} \qquad |\downarrow y\rangle &= \tfrac{1}{\sqrt{2}}\begin{pmatrix}1\\-i\end{pmatrix}
\end{aligned}
\tag{1.10}
$$

A general state that is in an arbitrary direction is given by,

$$
|\psi\rangle = \begin{pmatrix}a\\b\end{pmatrix} = a|\uparrow_z\rangle + b|\downarrow_z\rangle \tag{1.11}
$$

The contribution to the magnetism from the spin arises due to the unpaired electrons, but the configuration of these electrons also influence the final magnetic order. Therefore, before we begin the discussion of the magnetic structures begins let us review the mathematics that gives rise to the other quantum numbers, n, l and m_l, which describe the structure and occupancy of the electronic orbitals.

1.1.3. The Orbitals. The orbitals may be considered in two separate parts: a radial part and an angular part. Let us begin with the radial part.

The radial part of an orbital can be characterised by $j_l(\beta_{n,l}r/a)$, in which r is the radius, a is a normalisation factor and j_l a Bessel function. The Bessel function is periodic and is terminated after an integer number of nodes such that $\beta_{n,l}$ is the n^{th} zero of the l^{th} Bessel function. The condition that the radial part has an integer number of nodes, denoted by the principle quantum number, n, introduces quantisation to the radial probability distribution of the occupied orbitals, [**6**].

The angular distribution of the orbitals is described with spherical harmonics, which can be thought of as the propagation of waves on the surface of a sphere and are described by normalised Legendre functions, $Y_l^{m_l}(\theta,\phi)$. The quantization, in this

$Y_l^{m_l}(\theta,\phi)$	$m_l=0$	$m_l=\pm1$	$m_l=\pm2$	$m_l=\pm3$
$l=0$	s			
$l=1$	p_z	$p_x,\ p_y$		
$l=2$	d_{z^2}	$d_{yz},\ d_{xz}$	$d_{x^2-y^2},\ d_{xy}$	
$l=3$	f_{z^3}	$f_{yz^2},\ f_{xz^2}$	$f_{xyz},\ f_{z(x^2-y^2)}$	$f_{y(3x^2-y^2)},\ f_{x(3y^2-x^2)}$

TABLE 1.2. The boundary surfaces of the real parts of the wavefunctions for the first four values of l. Note the cylindrical symmetry of the orbitals when depicted this way. The boundary surface indicates the region within which there is 90% probability of finding an electron, [**3**]

case, arises from the requirement that waves on this surface terminate at a node. To fulfill this requirement the quantum number, m_l, and the angular momentum quantum number, l, must be integers, with $l > 1$ and $|m| < l$ else the wavefunction becomes infinite at $\theta = 0$ and/or $\theta = \pi$, [**6**]. The simplest probability surfaces of the spherical harmonics are shown in table 1.2 and can be understood as the absolute difference between the surface of a sphere and a wave propagating on the surface of that sphere, [**3**].

When the radial and angular parts are combined in a polar coordinate system they are described by the following wavefunction,

$$\psi_{n,l,m}(r,\theta,\phi) = A_{n,l} j_l(\beta_{n,l} r/a) Y_l^{m_l}(\theta,\phi), \tag{1.12}$$

where the term $A_{n,l}$ is a normalisation factor.

The orbitals that may be occupied can be represented with a vector diagram, figure 1.4, in which the $2l+1$ values of m_l are represented as cones about the z axis. The

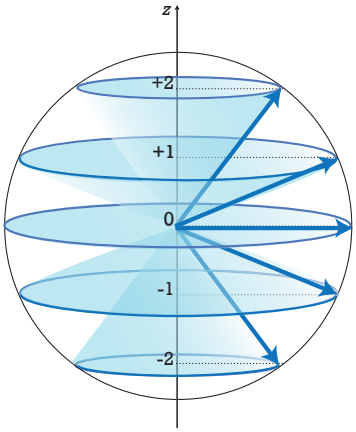

FIGURE 1.4. A vector representation of the m_l values of $l = 2$, where the radius of the circle is $\sqrt{l(l+1)}$. The cone-like representation indicates that if the z direction of the angular momentum is specified the xy components cannot be known. After [**3**].

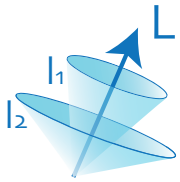

FIGURE 1.5. The total orbital angular momentum, L, is a sum over the vectors l_1 and l_2, where the vectors l are described in figure 1.4.

image represents the quantization of the quantum number m_l, its relation to l and the degeneracy of the x and y directions, that cannot be specified when the z component is known [**3**]. As the value of l increases the allowed orbitals will become more densely packed in the z direction, until the system appears continuous and classical.

For atoms with more than one electron, and assuming L-S coupling , the total orbital angular momentum, **L**, is given by a sum over the values of l, this can again be represented by a vector diagram, figure 1.5, which shows the degeneracy in the xy plane. The quantities n, l and m_l are the quantum numbers and, combined with the spin quantum number s, uniquely label the electron states , [**3, 6**].

1.1.4. Hund's Rules. The configuration that the electrons are most likely to adopt can be predicted using Hunds rules and described with the quantum numbers

n, l, m_l and s characterised in the preceding sections. Hund's rules allow us to predict the minimum energy combination of the total orbital angular momentum **L** and the total spin angular momentum **S** and hence the value of **J**, the total angular momentum, for the ground state, [**3**]. The rules state that:

(1) S needs to be maximised, to reduce the Coulombic energy, without contravening the Pauli principle.

(2) L then needs to be maximised, also reducing the Coulombic energy.

(3) J is then found, where $J = |L - S|$ if the shell is less than half full and $J = |L + S|$ otherwise.

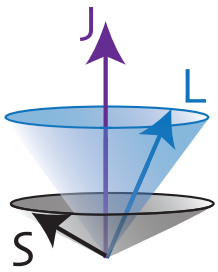

FIGURE 1.6. Vector representation of $L - S$ coupling where L is formed as in figure 1.5 and S is formed from the sum of spins as in figure 1.1

.

The rules assume that spin orbit coupling is weak and that L and S are good quantum numbers, a situation known as $L-S$, or Russell-Saunders coupling, shown in a vector diagram in figure 1.1.4. The magnitude of the magnetic moment can be calculated using Hund's rules is as follows:

$$\mu_{eff} = g_J \mu_B \sqrt{J(J+1)} \tag{1.13}$$

Where,

$$g_J = \frac{3}{2} + \frac{S(S+1) - L(L+1)}{2J(J+1)} \tag{1.14}$$

Where the g_J is the Lande g-value, μ_{eff} is the value of the effective moment, determined experimentally, and μ_B is the Bohr magneton that was established in equation 1.1.1.

The agreement between the magnetic moment determined by Hund's rules and the value determined experimentally is good when the spin orbit coupling is the most important contribution following the Coulombic interactions. The f-block metals are usually described by S-J coupling as the contracted outer orbitals do not interact strongly with the local environment. The transition metals, however, interact strongly with the local, crystalline environment, or crystal field, and the energy levels of otherwise degenerate orbitals can split and the total orbital angular momentum can quench, i.e. $L = 0$ and $J = S$.

1.1.5. The Crystal Field. The size and the nature of the crystal field depends on the symmetry of the local environment of magnetic site. When the local environment of the metal cation is tetrahedral the d_{z^2} and $d_{x^2-y^2}$ (or e_g) orbitals are lowered in energy, however, in an octahedral environment the d_{xy}, d_{xz} and d_{yz} (or t_{2_g}) orbitals are more favourable, where the orbitals can be seen in table 1.2, [**8**]. In both cases the orbitals become more favourable if they lie in the direction of the surrounding atoms and have the symmetry of the bonding environment.

In a strong crystal field the electrons adopt a low spin configuration and, where possible, form pairs in the lowest energy orbitals. In cases where the crystal field is weak the electrons behave in the opposite way, adopting a high spin configuration, singly occupying all the available orbitals. The interactions between the unpaired spins of the electrons in these orbitals enables the magnetic ordering to take place, let us now consider how these interactions are described.

1.2. Magnetic Interactions

The interactions that take place between electronic moments have many contributing factors. The interplay of these different interactions give rise to the different types of observed order that are observed. We will begin with a summary of the key types of interaction, found within insulators, and then examine the long range structures that emerge. First we will again consider the classical picture of magnetism with discussion of the dipolar interaction.

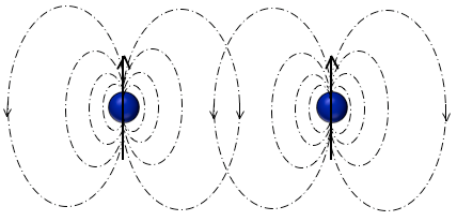

FIGURE 1.7. Schematic of the dipolar interaction showing the field lines of each of the atoms. The interaction leads to ferromagnetic ordering but is very weak and influences the final structure only in cases where the moment is large and the ordering temperature is low.

1.2.1. Dipolar Interaction. The dipolar interaction is the interaction that is most familiar on a macroscopic scale as it gives rise to observable magnetic fields. When the magnetic moment is small, however, the interaction is weak and is often the least important contribution for magnetic order. The decay of the magnetic dipolar field is proportional to $\frac{1}{r^3}$, which gives it a long range compared to the exchange interaction discussed in the subsequent subsection. The energy for the dipolar interaction, for two magnetic dipoles $\boldsymbol{\mu}_i$ and $\boldsymbol{\mu}_j$ seperated by $\mathbf{r}$ is given by,

$$E_{ij}^{dipole} = \frac{\mu_0}{4\pi r^3}[\boldsymbol{\mu}_i \cdot \boldsymbol{\mu}_j - \frac{3}{r^2}(\boldsymbol{\mu}_i \cdot \mathbf{r})(\boldsymbol{\mu}_j \cdot \mathbf{r})] \tag{1.15}$$

The interaction is generally insignificant as it is much weaker than the exchange interaction but can play an important role in materials that order at milliKelvin temperatures with large moments, such as the rare earth pyrochlores, [**35**].

1.2.2. Pairwise interactions. In order to describe the interaction between two electrons the spins need to be combined in a Hamiltonian, the most simple of which describes the pairwise interactions throughout the system.

$$\hat{H} = -\sum_{ij} J_{ij} \hat{\mathbf{S}}_i \cdot \hat{\mathbf{S}}_j. \tag{1.16}$$

where $\hat{\mathbf{S}}_i$ and $\hat{\mathbf{S}}_j$ are operators for the two particles i and j and J is the exchange integral and is the exchange constant between the i^{th} and the j^{th} spins. The interaction is between all the spins in the system, however, only the nearest neighbour and second nearest neighbour terms are usually significant. This effective Hamiltonian describes an Heisenberg magnet in which the spin may orient itself in any direction. Further terms are needed to describe the more sophisticated magnets that are described in the following sections, [**1**].

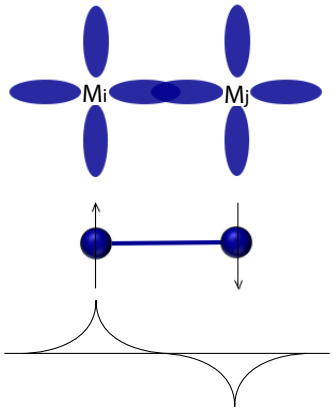

FIGURE 1.8. Image of the overlap of the orbitals on the neighbouring magnetic metal sites, M_i and M_j that gives rise to direct exchange. This is also represented as a schematic that indicates the direction of the magnetic moment on the atoms, represented by blue circles with arrows through them.

1.2.3. Direct Exchange. The quantum mechanical interaction between electrons on bonded magnetic ions is described as direct exchange and is due to the overlap of the electronic wavefunctions. For a spin half particle, such as an electron, the overall wavefunction must be antisymmetric. When the spatial part of the wave function is symmetric the spin part must be antisymmetric, or anti-aligned, and this arrangement is described by the antiferromagnetic exchange. If, however, the spatial

part is antisymmetric the spin part must be symmetric and the spins align parallel to give ferromagnetic exchange. The exchange interaction is ferromagnetic when $J > 0$ and corresponds to a singlet state and antiferromagnetic when $J < 0$ and gives rise to a triplet state, [**1**].

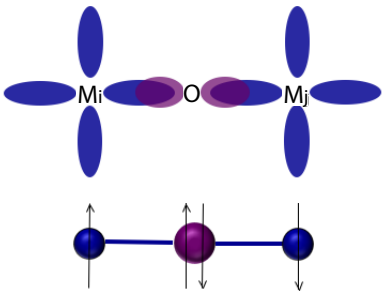

FIGURE 1.9. Image of the overlap of the orbitals on the magnetic metal sites, M_i and M_j mediated by an oxygen atom , O, that gives rise to superexchange. This is also represented as a schematic that indicates the direction of the vectors on the atoms, represented by blue circles and showing the preference for antiferromagnetic order.

1.2.4. Superexchange. In an ionic crystal the magnetic ordering is normally mediated by a non-magnetic ion to give a superexchange interaction. The strength of the superexchange interaction is dependent on the degree of orbital overlap. When the angle between the metal cations is 180° , the strength of the magnetic coupling is dependent on the type of bonding present, where σ-bonding will give rise to a larger superexchange interaction than a π-bonded system. When the cation-anion bonds are at 90° there is direct overlap of the d_{xy} (or d_{yz}, or d_{xz}) orbitals. Intermediate angles will tend to give less overlap and hence weaker exchange, [**7**]. Whether the bonding gives rise to antiferromagnetic or ferromagnetic exchange depends on the orbitals that are involved in the interaction, the bridging angles and the spin states of the involved metal ions.

1.2.5. Anisotropic Exchange Interactions. Anisotropic exchange arises when there is an exchange interaction, mediated by spin-orbit coupling, between the excited state of ion i and the excited state of ion j. The interaction, known as the

Dzyaloshinsky-Moriya (DM) interaction, when acting between two spins $\mathbf{S}_i$ and $\mathbf{S}_j$ gives the following term in the Hamiltonian,

$$\hat{H}_{DM} = \mathbf{D} \cdot \mathbf{S}_i \times \mathbf{S}_j \tag{1.17}$$

The term is minimized when $\mathbf{D}$ lies in the direction antiparrallel to the cross-product of the spins $\mathbf{S}_i$ and $\mathbf{S}_j$. The term, therefore, can give rise to a small canting of the moments. The canting can, for example, cause a small ferromagnetic component to arise perpendicular to the spin-axis of an antiferromagnetically ordered material and to the direction of $\mathbf{D}$, see figure 1.10. The vector $\mathbf{D}$ vanishes when there is a centre of inversion between the two sites i and j, [**1**]..

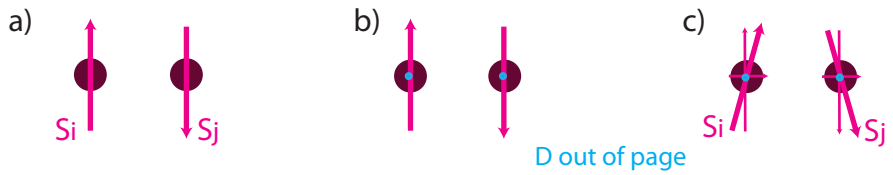

FIGURE 1.10. Image of the canting that occurs when there is a DM interaction in a simple antiferromagnet. a) Two spins, $\mathbf{S}_i$ and $\mathbf{S}_j$, are anti-aligned. b) $\mathbf{D}$ is out the page and perpendicular to the spin axis. c) To minimize the term the spins become canted and there is a ferromagnetic component to the magnetic structure that is perpendicular to both $\mathbf{D}$ and the spin axis.

1.2.6. Single Ion Anisotropy. When there is a large crystal field effect the orbital moment may be quenched. The crystalline environment, and the crystal field, tends to be anisotropic and this anisotropy is transfered to the overall spins when there is also large spin-orbit coupling. The effect of the single-ion anisotropy can be large and prevent the spins from aligning with an applied magnetic field, B. The following term is added to the Hamiltonian to describe this interaction:

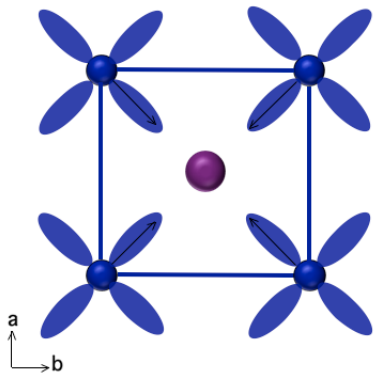

FIGURE 1.11. Schematic that indiates the restriction of the orbitals in a bonded system. This restriction gives rise to the single ion anisotropy and competes with the exchange interaction to give rise to frustrated, fluctuating structures.

$$\hat{H} = -D \sum_{i=1}^{N} (\boldsymbol{\delta}_i \cdot \mathbf{S}_i)^2, \tag{1.18}$$

where $\boldsymbol{\delta}_i$ is the anisotropy axis and D is a factor that determines the magnitude of the interaction.

1.2.7. Summary. The balance of these different interactions give rise to different preferential directions for the local ordering. Each of these interactions are represented by different terms in the Hamiltonian and the dominant terms will dictate the global order that is observed. Let us now consider the global patterns that emerge due to these interactions.

1.3. Magnetic Structures

The long range structure of magnetic materials is dictated by the interactions that were described in the previous section. The greater the variety of interactions that contribute substantially to the local order, and hence more terms that are present in the Hamiltonian, the more complex the long range structure will appear to be. This

section will begin with the paramagnetic case, in which the magnetic moments lack any long-range order, and then discuss the different types of order that may arise.

FIGURE 1.12. A paramagnetic solid is constructed from an array of ions that each have a magnetic moment, there is no bulk magnetism because the alignment of these moments is random and as such, over a large statistical sample will cancel to zero. The moments may be brought into alignment by the application of a magnetic field.

1.3.1. Paramagnetism. Paramagnetism is the term used to describe the disordered magnetism that is present in materials that have unpaired electrons, figure 1.12. A paramagnetic material has no net magnetization, but has the potential acquire a magnetization in an applied magnetic field. The lack of order on any length scale, represented by the random orientation of the arrows in figure 1.12, makes the paramagnetic phase equivalent, in terms of thermodynamics, to a material in the gas phase. The interactions between the nearest neighbours in the material are not strong enough to overcome the thermal fluctuations in the material and cause long range order, but again have the potential to do so as the temperature is reduced. The susceptibility, χ, of a paramagnet describes the response to an applied field and from this the effective moment, μ_{eff}, can be determined. In low magnetic fields the relation is described,

$$\chi = \frac{M}{H} \approx \frac{\mu_0 M}{B} = \frac{n\mu_0\mu_{eff}^2}{3k_{\mathrm{B}}T}, \tag{1.19}$$

where M is the magnetisation, H is the applied field, μ_0 is the permeability of free space, B is the induced magnetism, n is the number of magnetic moments per unit volume, k_{B} is the Boltzmann factor and T represents the temperature dependence.

The temperature dependence of χ is called the Curie law, which states that the magnitude of the susceptability is inversely proportional to the temperature, as given

in 1.3.1. This is true in the paramagnetic phase, but when the material reaches the point at which long range order sets in anomalies can be seen in the plot of the temperature dependance of the susceptibility. The transition to long range magnetic order, is equivalent, again in terms of thermodynamics, to the crystallization of a material. When a material crystalizes the translational symmetry is broken, whereas the magnetic order breaks the time reversal symmetry, [**1**]. Let us now consider the types of long range order that may arise, with reference to the Bloch wave formalism.

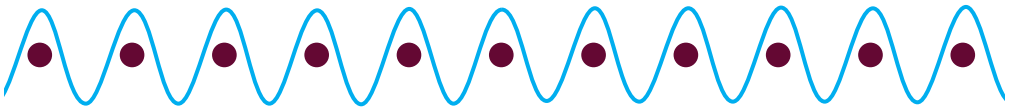

FIGURE 1.13. The Bloch wave formalism describes a periodic pattern in terms of the periodicity of the crystal lattice. The image here indicates a one-dimensional periodic structure of points and a wave which is periodic with that structure.

1.3.2. Bloch Waves. The magnetic structure of a material can be understood as a periodic pattern that is superposed onto that of the crystal lattice, [**9**]. This idea will be developed formally in the chapter that describes symmetry, chapter 3, however, the concept will be introduced in this section with reference to the different types of long range magnetic order that can be observed. The relationship between the periodicity of the wave and the crystal lattice is described by the Bloch wave formalism, where in a three-dimentional system, the relationship between a property at the position $\mathbf{r}$ is described by $\psi_{\mathbf{k}}(\mathbf{r})$ and at a position displaced by the vector $\boldsymbol{\tau}$ from $\mathbf{r}$, $\mathbf{r} + \boldsymbol{\tau}$ the property is described by,

$$\psi_{\mathbf{k}}(\mathbf{r} + \boldsymbol{\tau}) = e^{i\mathbf{k}\cdot\boldsymbol{\tau}}\psi_{\mathbf{k}}(\mathbf{r}), \tag{1.20}$$

where $\mathbf{k}$ is the wave vector and is in reciprocal units, $\boldsymbol{\tau}$ is a vector of integers that leaves the crystal invariant and $\mathbf{r}$ can be considered an arbitrary origin, [**10**].

The paramagnetic system described, in terms of the Bloch wave formalism, can be considered as many waves that have no phase coherence to give no overall moment

or long range order. The structures that are described subsequently can be described with spin density waves that are related to the lattice in progressively complex ways. The simple ferromagnet, has propagation vector, $\mathbf{k}$=0 and the property $\psi_{\mathbf{k}}$ is equivalent at all equivalent lattice sites, represented by the wave and arrows in figure 1.14. The simple antiferromagnet shown in figure 1.15 has $\mathbf{k}$=1/2 and the periodicity of the pattern of ordered moments is twice that of the lattice.

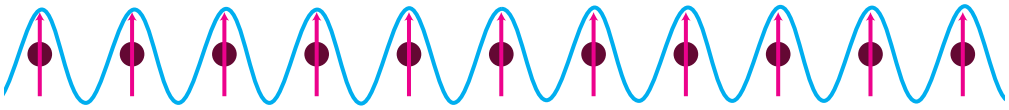

FIGURE 1.14. In a simple paramagnet the spins are parallel and the periodicity of the structure is equivalent to that of the lattice.

1.3.3. Ferromagnetism. A simple ferromagnet is characterised by spins that are aligned collinearly and in the same direction, figure 1.14. More complex ferromagnetic ordering schemes occur but the common factor is that order occurs spontaneously and can give rise to bulk magnetism, below the Curie temperature, T_C,

$$T_{\mathrm{C}} = \frac{g_j \mu_B (J+1) \lambda M_s}{3k_{\mathrm{B}}} = \frac{n\lambda\mu_{eff}^2}{3k_{\mathrm{B}}}. \tag{1.21}$$

The Curie temperature is the point at which the paramagnetic susceptibility goes to infinity. The value λ is a parameter that represents the molecular field and is directly proportional to the size of the exchange interaction J. M_s is the saturation magnetization.

If the transition occurs without an applied magnetic field, that breaks the symmetry of the system, there is high likelihood of domain formation, whereby there are regions of equivalent local order that are rotated with respect to the global axis system. Domain formation is analogous to formation of different crystallite twins during the crystallization process and increase the entropy of the system. The boundaries between the regions are not energetically favourable, but this is offset by the reduction in the field outside the crystal and the increase in entropy. The relationship

between the different regions of local order will be described in the chapter regarding symmetry, chapter 3.

When there is a single, or mono-domain, formed a ferromagnet will display a net bulk magnetism. Ferromagnetic order usually occurs in materials that have an exchange constant with $J > 0$ and are described by the Hamiltonian,

$$\hat{H} = -\sum_{ij} J_{ij}\mathbf{S}_i \cdot \mathbf{S}_j + g\mu_{\mathrm{B}} \sum_{j} \mathbf{S} \cdot \mathbf{B}. \tag{1.22}$$

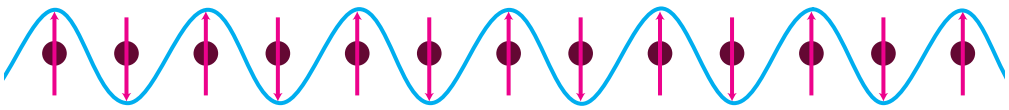

FIGURE 1.15. In a simple antiferromagnet the spins are anti-parallel, the periodicity is twice that of the lattice.

1.3.4. Antiferromagnetism. Antiferromagnetic order is the term applied to materials that have long range magnetic order, but the sum of the ordered moments is zero, $\sum_i S_i = 0$. Figure 1.15 is a representation of a one dimensional magnetic system, with an anti-collinear spin arrangement. If this system were constructed from an even number of sites the sum over all of the moments would be nil. Alternatively the structure can be considered as two, interpenetrating chains of spins that have equal and opposite spin order. Simple, three dimensional magnetic materials can, equivalently, be considered as two interpenetrating magnetic lattices with spins that are alligned in compensating directions. More complex antiferromagnets, including frustrated magnetic systems, can also be considered within this scheme, where the interpenetrating lattices are related by rotations other than 180°.

If we consider only the case of the simple antiferromagnet that is constructed from a positive, +, and negative, -, sublattice, the molecular field on each sublattice is,

$$B_+ = -|\lambda| M_- \tag{1.23}$$

and,

$$B_- = -|\lambda| M_+, \tag{1.24}$$

and gives the relation for the Neél temperature T_N, which is closely related to the Curie temperature, but with the order parameter λ replaced by $|\lambda|$,

$$T_{\mathrm{N}} = \frac{g_j \mu_B (J+1)|\lambda| M_s}{3k_{\mathrm{B}}} = \frac{n|\lambda|\mu_{eff}^2}{3k_{\mathrm{B}}}, \tag{1.25}$$

in the case of antiferrromagnetic materials the order parameter is negative, due to the negative exchange interaction $J < 0$.

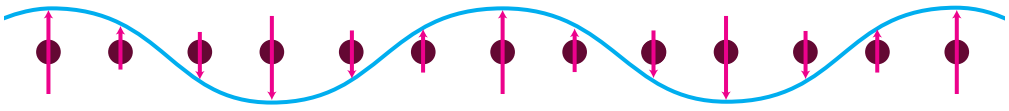

FIGURE 1.16. In a sinusoidal magnetic the spins have a magnitude that varies as a sine wave.

1.3.5. Sinusoidal Magnetism. Sinusoidal magnetic order can be considered as a special type of antiferromagnetic order, in which the frequency of the Bloch wave that describes the order does not have a simple relationship with the periodicity of the lattice. The size of the ordered moment is, therefore, sinusoidally modulated, which leads to a reduction in the observable moment size and no net magnetization.

1.3.6. Helical structures. Helical magnetic order arises in systems that have two competing ordering parameters which lie in orthogonal directions. This may for example be competition between the nearest neighbour in-plane ordering and the nearest neighbour out-of-plane ordering, [**1**]. Helical magnetic structures are chiral

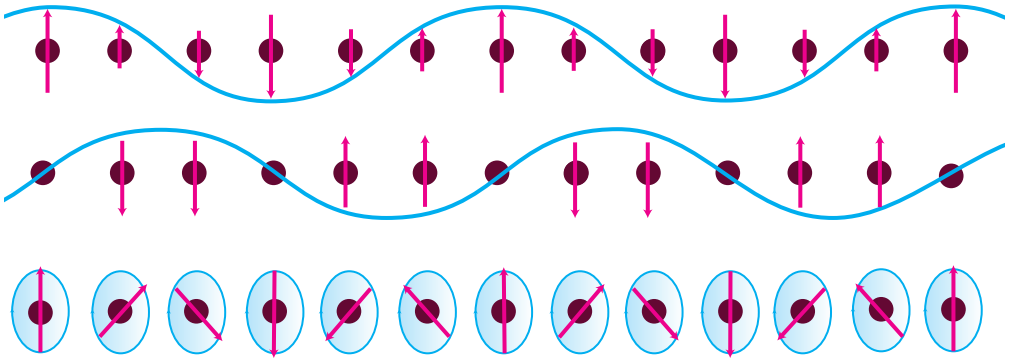

FIGURE 1.17. In a helical magnet the spins have an orientation that can be decomposed into two out of phase, orthogonal sine waves.

and the spiral that propagates in one direction cannot be brought into coincidence with one that propagates in the opposite direction by rotation or spatial inversion. This can be understood with reference to the description of the wave formalism at the start of the subsection. When a sine wave is rotated about the origin its phase is changed, this is not true in the case of a cosine like wave, unless the wave is orthogonal to the sine like component. As this is the case in a helical structure the rotation about any axis will leave the structure invariant.

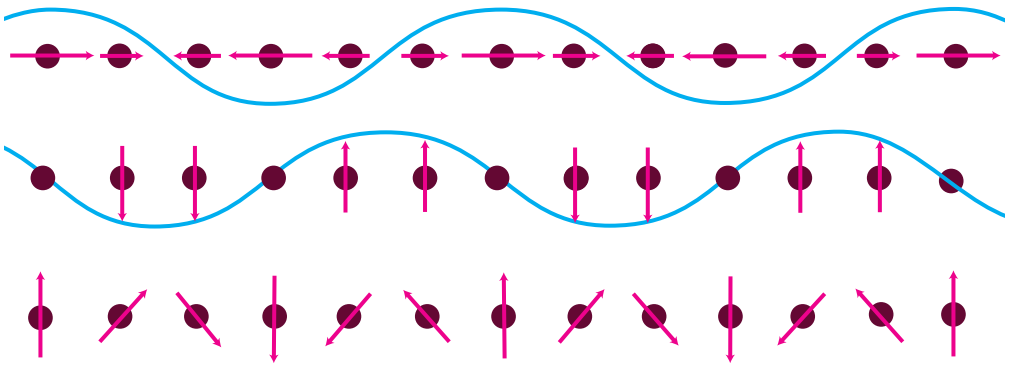

FIGURE 1.18. In a cycloidal magnet the spins can again be decomposed into two out of phase, orthogonal sine waves, but in this instance one of the waves is longitudinal.

1.3.7. Cycloidal Structures. Cycliodal order is also constructed from two out of phase components, which are oscillating in orthogonal directions. In the case of a cycloid, however, one of the components is longitudinal, which means that the

cycloidal structure is not truly chiral as the cycloidal type of order may be brought to coincide with the other handedness by rotation about the direction of propagation, followed by a translation by π. The operation may be performed as the component that is with **k** will be left unchanged by the rotation.

1.4. Magnetic Frustration

As has been described previously the magnetic order in materials arises due to several different types of interaction. In the examples given there is usually one type of order that dominates and this can be used to successfully model the final structure of the system. The more complex structures arise in situations where interactions compete and the structure is determined by more than one order parameter and the final structure is a compromise between them. The signature of frustration is a depression of the magnetic ordering temperature, compared to that expected from susceptibility measurements, θ_{CW}. This section will cover two very different frustrated systems: the first are the cycloidal multiferroic materials, in which frustration arises due to the competition between different exchange pathways; the second are the rare earth titanates, which are an archetype of geometric frustration.

1.4.1. Multiferroic materials. The common link between many of the recently discovered multiferroic materials is the presence of a cycloidal spin structure that, as discussed previously, arises when there is competition between orthogonal (super)exchange interactions, [**1, 12, 13**]. Multiferroic materials exhibit a simultaneous phase transition of the ferroelectric order, magnetic order and, frequently, a change in the lattice parameters, figure 1.19, [**12, 13**]. The phenomenon, and the progress that has been made in the field is discussed well in reference [**12**].

Ferroelectric materials are an electric analogue to ferromagnetic materials, and as such, below the transition temperature temperature a spontaneous electric dipole

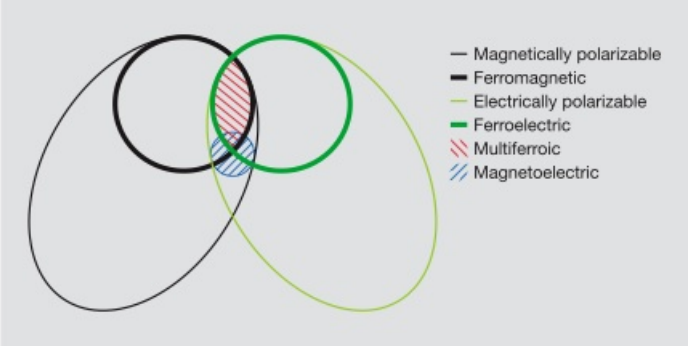

FIGURE 1.19. Schematic of the overlap between the different properties of material that display electric and magnetic phenomena. Ferromagnets form a subset of magnetically polarizable materials, such as paramagnets and antiferromagnets, and can show a bulk, net magnetization. Ferroelectrics show can show a spontaneous electric polarization and form a subset of all electrically polarizable materials (paraelectrics and antiferroelectrics). The red hatched area indicates multiferroic materials, in which there is both a spontanous magnetic order and electric polarization. The blue hatched area indicates magnetoelectrics in which the magnetic order may be controlled with an electric field or vice versa, after [**12**].

moment is observed. The electric dipole moment arises due to a distortion of the lattice that gives an asymmetric distribution of electron density about an atomic site [**14**]. In the case of the magnetoelastic multiferroics the distortion arises due to the magnetostriction, *i.e.*, a relaxation of the crystallographic structure that simultaneously minimizes the exchange and bonding energy, [**15**]. A microscopic model that gives rise to the displacement of the oxygen atom, was proposed by Sergienko and Dagotto, [**16**], and it suggests that the oxygens are displaced by an inverse Dzyaloshinsky-Moriya (DM) interaction [**17, 18**], such that the displacement is in the direction antiparallel to the cross-product of the spins on the atom sites $\mathbf{S}_i$ and $\mathbf{S}_j$.

The direction of the electric polarization is described by the relation,

$$\mathbf{P_e} = \frac{1}{V}\int d^3xP = \gamma'\chi_e[(\mathbf{S}_i \times \mathbf{S}_j) \times |\mathbf{k}|], \tag{1.26}$$

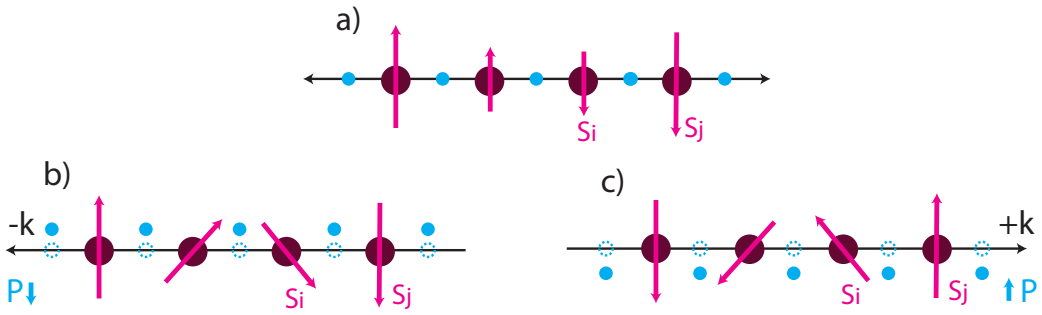

FIGURE 1.20. The movement of the oxygen atoms (in blue), with respect to the Mn ion sites (in purple). The image is a schematic to indicate the relative positions of the ions, with respect to the direction of electric polarization, the axis of rotation of the magnetic structure and the direction of propogation. The electric polarization **P** is the opposite direction to the displacement, but perpendicular to the direction of the propagation vector, **k** and the axis of rotation $\mathbf{S}_i \times \mathbf{S}_j$, after [**13**], to describe the electric polarisation in $RE\mathrm{MnO_3}$

where $\mathbf{S}_i$ and $\mathbf{S}_j$ are the spins that lie on neighbouring atom sites i and j as indicated in figure 1.20, where the equation is taken from the theory suggested by Mostovoy, [**20**].

The recent explosion of research in the area of multiferroics initially focused on the family of rare earth perovskite manganites $RE\mathrm{MnO_3}$, [**21, 22, 23**]. These materials display a cycloidal magnetic structure due to the competition between the nearest neighbour, intra-plane, J_1, and the next nearest neighbour, inter-plane J_2, Mn exchange interactions. Subsequently $Ni_3V_2O_8$, [**25**], and $MnWO_4$, [**26, 27, 28**], were demonstrated to also have a cycloidal structure and to exhibit multiferroic properties. The experimental evidence for the multiferroic nature of $MnWO_4$ will be described in the $MnWO_4$ results chapter, chapter 5.

1.4.2. Geometric frustration. Geometric frustration arises in systems that cannot simultaneously satisfy the pairwise interactions due to the crystallographic structure and first used with reference to magnetism in 1977, [**29, 30**]. A simple example of geometric frustration are spins on a triangular plaquette, if we place a

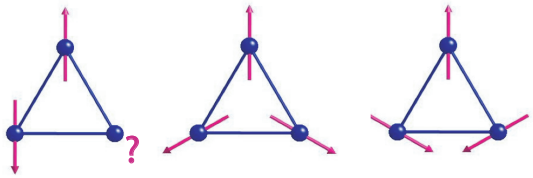

FIGURE 1.21. The possible arrangement of spins on a triangular plaquette. Figure a) indicates an antiferromagnetic arrangement between two ions. Figures b) and c) indicate the two equivalent solutions for the ground state structure.

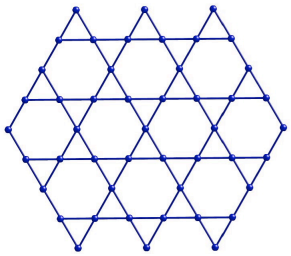

FIGURE 1.22. The kagomé lattice of corner sharing triangles.

moment on each of the corners of the triangle and assume that the exchange is antiferromagnetic, it can be understood from figure 1.21, that all of the pairwise exchange interactions cannot be satisfied. The free energy is equivalently minimised by the two structures shown, and neither of these fully satisfy the collinear requirement of a simple exchange interaction, [**31, 32**]. If a two-dimensional corner-sharing network of these triangles is generated (the kagomé lattice, figure 1.22) there will be as many possible ground state arrangements of the spins as there are triangles in the array.

If we consider the tetrahedron rather than a singular triangular plaquette it can be seen that if the bonding is antiferromagnetic the same situation arises as all the pairwise interactions cannot be simultaneously satisfied, figure 1.23. The *pyrochlore* structure (space group $Fd\bar{3}m$) of corner sharing tetrahedra, shown in figure 1.24, is analogous to a three dimensional array of kagomé lattices and again can give rise to magnetic structures with a macroscopically degenerate ground state manifold, [**33, 34**].

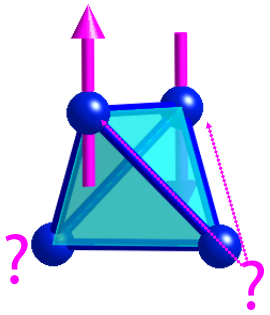

FIGURE 1.23. The competing interactions of an antiferromagnetic tetrahedron. The question marks indicate sites that cannot satisfy both the local exchange interactions.

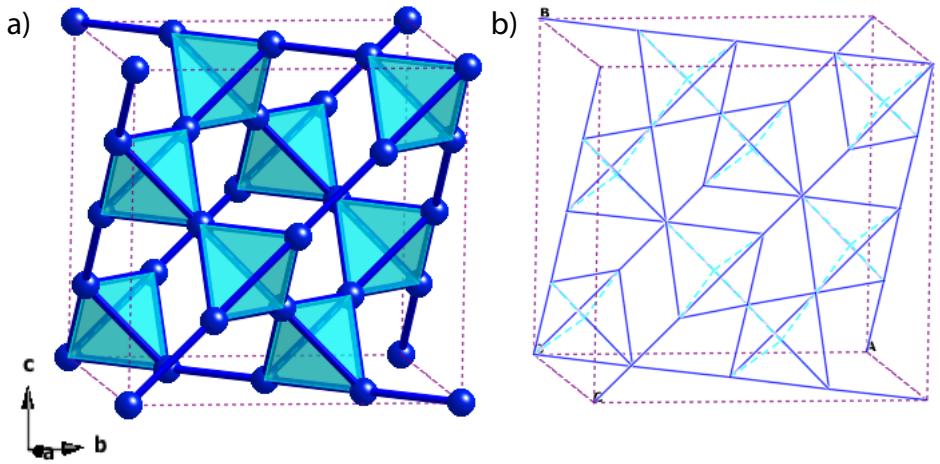

FIGURE 1.24. The pyrochlore lattice of vertex sharing tetrahedra, where figure a) shows the sites of the RE ions throughout the lattice and the tetrahedral relationship between them, and figure b) shows the local $\langle 111 \rangle$ axis within each the tetrahedra.

The array of rare earth (RE) sites in the family of rare earth titanates, $RE_2Ti_2O_7$ adopt the pyrochlore structure and includes many examples of different geometrically frustrated magnets [**35, 36, 37, 38**]. The RE^{3+} ions reside on the corner sites (16c), shown by the blue points in figure 1.24, the nearest atoms to these sites are eight oxygens, one above and below in the centre of the tetrahedra and then six further atoms that form a puckered ring in the plane perpendicular, [**39, 40**]. The distribution of the unpaired electrons in the surrounding orbitals on the electronic configuration of the ion and this gives rise to variation in the single ion anisotropy that is associated with each of the rare earth ions [**36**], when the spin orbit coupling

is large the single ion anisotropy is also large and this restricts the moment to specific directions.

When the moment is restricted to the local $\langle 111 \rangle$ direction, *i.e.* the direction that passes through a metal ion and the centre of the opposing face, figure 1.24.b, the order is said to be Ising-like as the only degree of freedom that the spin has is to parallel or anti-parallel to this axis. FeF_3 is an example of Ising antiferromagnet with the pyrochlore structure, in which order is observed at 15.5 K, thought to be stabilised by long-range interactions, [**41**]. The structure consists of all the spins pointing in or all the spins pointing out on each tetrahedron, figure 1.25.c.

When the exchange is ferromagnetic the moments on a single tetrahedron described by the two-in, two-out, spin ice structure, figure 1.25.a, is found in the rare earth titanates where RE = Ho and Dy, [**42, 43, 44, 45**]. These materials have been shown to have a macroscopically degenerate ground state manifold and do not exhibit any long range order at any temperature. The local order, of two-in and two-out is analogous to the proton disorder observed in ice [**46**], which gives rise to the name *spin ice* for these types of magnetic structures. The $Tb_2Ti_2O_7$ analogue also has local Ising anisotropy but exhibits a spin liquid type behaviour, where the structure continues to fluctuate to the lowest measured temperatures, [**47, 49**].

The single ion anisotropy may also act to restrict the moment to the XY plane. In this instance, when the exchange interaction in XY arrangement is ferromagnetic there is no frustration observed. This is trivially true for a collinear type XY magnet where the XY plane is perpendicular to the same cardinal directions, but long range order would also be observed if the XY plane is taken to be perpendicular to the local $\langle 111 \rangle$ axes, figure 1.25.b, [**50**]. When the spins are arranged antiferromagnetically there is no way to arrange the spins, in either the uniaxial or the local-axis case, that will give rise to an energetically favourable ground state, figure 1.25.d, [**48**]. When RE = Er the local structure that is observed is described by the local XY model and

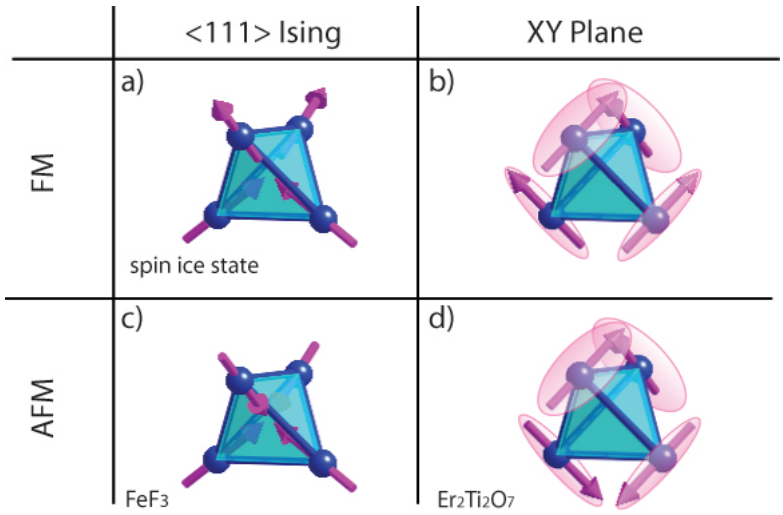

FIGURE 1.25. The different types of spin arrangement for a single tetrahedron of the pyrochlore lattice. a) The spin ice arrangement found in $RE_2Ti_2O_7$, RE = Ho and Dy, the pairwise interactions are not satisfied and no long range order is found. b) An example of a ferromagnetic structure restricted to the XY plane. c) The antiferromagnetic arrangement of spins found in FeF_3, with moments restricted to the local $\langle 111 \rangle$ axes. d) The XY antiferromagnetic arrangement that describes the spin arrangement in $Er_2Ti_2O_7$.

has also been shown to order below 1.4K. The structure that is adopted indicates that the ground state is selected by the entropically favourable order-by-disorder mechanism, [**50, 51, 52**].

The order-by-disorder mechanism was first discussed by Villain *et al*, [**54**]. The work describes an Ising system constructed from ferromagnetic chains, labelled A, that alternate with antiferromagnetic chains, labelled B. The structure has three exchange interactions, with values $0 < J_{AB} < |J_{BB}| < J_{AA}$. When T=0 and the number of atoms in the chains are even there is no long range order and there is degenerate ground state manifold that the system can explore. At higher temperatures, however, fluctuations occur in the antiferromagnetic chains, to give ferromagnetic excitations that link the ferromagnetic A chains and give long range ferromagnetic order, i.e. the order arises in A component of the system, due to the disorder of the B component. The order of the A component is the only one of the many of the structures that are

available in the ground state manifold that allows access to the many soft excitations in the B chains and hence is entropically favourable, [**48**].

References

[1] Blundell S, *Magnetism in Condensed Matter*, Oxford University Press, Oxford, (2001)

[2] Hladik J, *Spinors in Physics*, Masson, Paris (1996) Translated from French by J. Micheal Cole,

[3] Atkins P W and Friedman R S, *Molecular Quantum Mechanics*, Third Edition , Oxford University Press, Oxford, (1997)

[4] Atkins P W, *Physical Chemistry*, Seventh Edition , Oxford University Press, Oxford, (1997)

[5] Jordan T, *Quantum Mechanics in Simple Matrix Form*, John Wiley & Sons, New York, (1986) Dover reprint (2005)

[6] Griffiths D J, *Introduction to Quantum Mechanics*, Second Edition, Pearson Prentice Hall (2005)

[7] Goodenough J B, *Magnetism and the Chemical Bond*, John Wiley & Sons, Inc, (1963)

[8] Carlin R L C, *Magnetochemistry*, Springer-Verlag, (1986)

[9] Bloch F *Zeit, fur Physik*, **52** 555 (1928)

[10] Tinkham M, *Group Theory and Quantum Mechanics* McGraw-Hill, (1964)

[11] Feynman R P, Leighton R B, Sands M, *The Feynman Lectures on Physics: Commemorative Issue Vol 3*, World Student, (1963)

[12] Eerenstein W, Mathur N D and Scott J F *Nature* **759** (2006)

[13] Cheong S-W and Mostovoy M *Nature Materials* **6**, 13 (2007)

[14] Keve E T, Abrahams S C and Bernstein J L *J. Chem. Phys* **51** 4926 (1969)

[15] Radaelli P G, Vecchini C, Chapon L C, Brown P J, Park S and Cheong S-W **79**, 020404 (2009)

[16] Sergienko I A and Dagotto E *Phys. Rev. B* **97** 094434 (2006)

[17] Moriya T *Phys. Rev.* **120** 91 (1960)

[18] Dzyaloshinsky I *J. Phys. Chem. Solids* **4** 241 (1957)

[19] Taniguchi K, Abe N, Sagayama H, Ohtani S *Phys. Rev. B* **77** 64408 (2008)

[20] Mostovoy M *Phys. Rev. Lett.* **96** 067601 (2006)

[21] Kimura T, Ishihara S, Shintani H, Arima T, Takahashi S, Ishizaka K, and Tokura Y, *Phys. Rev. B* **68**, 060403(R) (2003).

[22] Goto T, Kimura T, Lawes G, Ramirez A P, and Tokura Y, *Phys. Rev. Lett.* **92**, 257201 (2004).

[23] Higashiyama D, Miyasaka S, Kida N, Arima T, and Tokura Y, *Phys. Rev. B* **70**, 174405 (2004).

[24] Aliouane N, Prokhnenko O, Feyerherm R, Mostovoy M, Strempfer J, Habicht K, Rule K C, Dudzik E, Wolter A U B, Maljuk A, Argyriou D N, *J. Phys.: Condens Matter*, **20**, 434215 (2008)

[25] Lawes G, Harris A B, Kimura T, Rogado N, Cava R J,Aharony A, Entin-Wohlman O, Yildirim T, Kenzelmann M, Broholm C, and Ramirez A P, *Phys. Rev. Lett.*, **95**, 087205 (2005).

[26] Arkenbout A H, Palstra T T M, Siegrist T, and Kimura T *Phys. Rev. B* **74**, 184431 (2006)

[27] Heyer O, Hollmann N, Klassen I *et al J. Phys.: Condens. Matter* **L471** (2006)

[28] Taniguchi K, Abe N, Ohtani S *et al Phys. Rev. Lett.* **97** 097203 (2006)

[29] Tolouse G, *Commun. Phys.*, **2** 115 (1977)

[30] Villain J, *J. Phys. C*, **10**, 1717 (1977)

[31] Wannier G H, Phys. Rev., **79** 357 (1950)

[32] Houtappel R M F, *Physica*, **16**, 425 (1950)

[33] Anderson P W, *Phys. Rev.*, **102**, 1008 (1956)

[34] Villain J, *Z. Phys. B.: Condens. Matt.*, **33**, 31 (1979)

[35] Gardner J S, Gingras M J P, Greedan J E, *Rev. Mod. Phys.*, **82**, 53 (2010)

[36] Greedan J E, *J. Mater. Chem.*, **11** 37 (2001)

[37] Ramirez A P, *Annu. Rev. Mater. Sci.*, **24**, 453, (1994)

[38] Bramwell S T, Field M N, Harris M J, Parkin I P, *J. Phys.: Condens. Mat.*, **12**, 483 (2000)

[39] Roth R S, *J. Res. Natl. Bur. Stand.*, **56**, 17 (1956)

[40] Knop O, Brisse F, Castelliz L, *Can. J. Chem.*, **47**, 971 (1965)

[41] Reimers J, Greedan J E, Stager V C, Bjorgvinnsen M, Subramanian M A, *Phys. Rev. B*, **43** 5692 (1991)

[42] Harris M J, Bramwell S T, McMorrow D F, Zeiske T, Godfrey K W *Phys. Rev. Lett.*, **79**, 2554 (1997)

[43] Bramwell ST, Harris MJ, den Hertog BC *et al*, *Phys. Rev. Lett.* **87** 047205 (2001)

[44] Fennell T, Petrenko O A, Fäk B *et al*, *Phys. Rev. B 70*, 134408 (2004)

[45] Fennell T, Petrenko O A, Fäk B *et al*, *Phys. Rev. B 72*, 224411 (2005)

[46] Pauling L *Phys. Rev.*, **57** 2680 (1935)

[47] Enjalran M, Gingras M J, Kao Y J, Del Maestro A, Molavian H R (2003)

[48] Bramwell S T, Gingras M J, Reimers J, *J. Appl. Phys.*, **75** 5523 (1994)

[49] Mirebeau I, Goncharenko I N, *J. Phys.: Condens. Matter* **17** S771 (2005)

[50] Champion J D M, Harris M J, Holdsworth P C W *Phys. Rev. B*, **68** 020401 (2003)

[51] Champion J D M, *Theoretical and Experimental Investigations of Frustrated Pyrochlore Magnets* , UCL

[52] Shirai M, *Experimental Investigations of Frustrated Antiferromagnets* , UCL

[53] Palmer S E and Chalker J T, *Phys. Rev. B*, **62** 488 (2000)

[54] Villain J, Bidaux R, Carton J-P and Conte R, *J. Phys.*, **41**, 1263 (1980)

CHAPTER 2

Neutron Scattering

When a wave impinges on a material that it couples with it is reflected, producing a new wavefront that is the Fourier transform of the scattering potential of the material. The process occurs for any type of wave, be that water, light or matter and the wavefront fully describes the scatterer. Some of this information may not be possible to interpret due to: interference effects; the thermal motion of the scatterer and, in the case of neutron scattering, the inability to measure the phase of the wave. The following sections describe how the neutron couples with matter, how a beam of particles can give rise to a diffraction pattern and how this pattern is changed when the neutron beam is spin polarized. The main texts that were consulted for this section were Squires [**1**], Lovesey [**2**] and Lovesey and Balcar [**3**].

2.1. The Neutron

The neutron is found in the nuclei of atoms and is only stable in this environment, the combination of quarks that generates the neutron gives rise to the properties outlined in table 2.1, [**1, 4**].

	Property	Value
1	mass	$m = 1.675 \times 10^{-27}$ kg
2	charge	0
3	spin	1/2
	magnetic dipole moment	$\mu_n = -1.913\mu_N \approx 0.001\mu_B$

TABLE 2.1. Properties of the neutron, where the nuclear magneton $\mu_N = 5.051 \times 10^{-27}\mathrm{JT}_1$

2.1.1. As a probe. These properties define the neutron as a scattering probe: the neutron mass gives a de Broglie wavelength at room temperature similar to solid and liquid interatomic distances, which allows diffraction from these materials; the energy of thermal neutrons is in the same range as condensed matter excitations, which facilitates their measurement; the neutron has no electric charge and interacts weakly with the atoms, which allows penetration of the bulk of the material; the moment of the neutron couples with a magnetic field, which gives data about magnetic structures. The neutron also couples with the strong force, which scales arbitrarily and allows identification of light atoms and differentiation of atoms with similar atomic number, Z. The main problem associated with neutron scattering is the long duration of experiments due to the weak coupling between the neutron and the scatterer and the dimness of neutron sources.

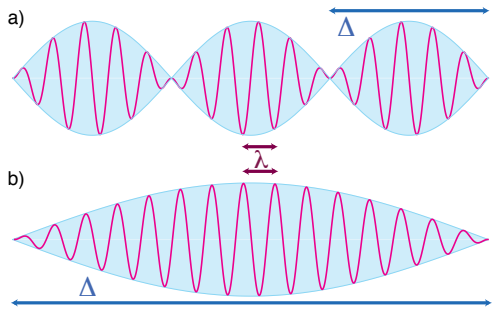

FIGURE 2.1. Schematic of matter waves, where λ is the de Broglie wavelength and Δ is the envelope of the particle. Neutrons, when considered as a wave are described by figure b.

a) A matter wave that would give rise to a particle with a well defined position due to the small envelope of the particle with respect to the de Broglie wavelength.

b) A matter wave that would give rise to a particle with well defined momentum due to the large envelope of the particle.

2.1.2. As a wave. Neutrons can be considered as a matter wave, figure 2.1, and the wavelength, λ, that is associated with each neutron of mass, m, and with velocity, v, is defined by the de Broglie relation, [**1**],

$$p = \frac{h}{\lambda}, \qquad p = mv. \tag{2.1}$$

The wavelength is inversely proportional to the momentum, p, of the related particle, with the Planck constant, h, as a scaling factor. The information limit is given by the Heisenberg uncertainty principle, $\Delta p \times \Delta x \geq h$, as to measure with accuracy Δx, the wavelength of the probe, λ needs to fullfil the relation $\lambda < \Delta x$, but also momentum of the order $h/\Delta p$, [**5**].

2.2. Scattering Process

This section will explore what happens when a wave meets an object with which it couples: light couples with the electronic charge cloud and neutrons couple with the strong force and the magnetic field.

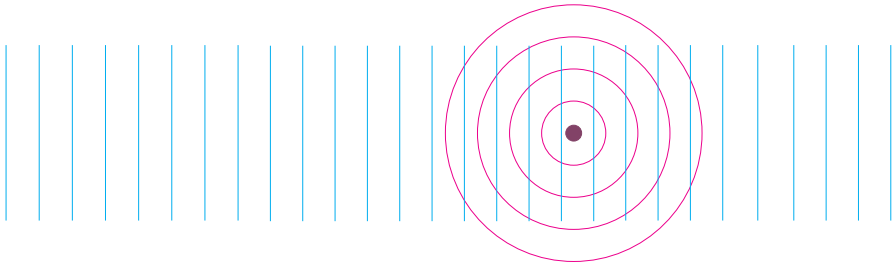

FIGURE 2.2. Spherical scattering (magenta) occurs when a plane wave (cyan) is reflected by a point (purple).

2.2.1. Interaction of a wave with an object. When a plane wave is incident on a object with which it couples, it is scattered equivalently in all directions, figure 2.2. The wavefront has the same shape as the object from which it has been scattered and the magnitude of the coupling is dependent on the coupling potential.

As stated, the neutron couples with the strong force, which binds the atomic nuclei, the magnetism, which is associated with the unpaired electrons and the nuclear spin. The magnitude of the neutron interaction is described by the potential, $\hat{V}(\mathbf{Q})$, and is constructed from the nuclear, $\hat{V}_N(\mathbf{Q})$, and the magnetic terms, $\hat{V}_M(\mathbf{Q})$, [**1, 2**].

$$\hat{V}(\mathbf{Q}) = \hat{V}_N(\mathbf{Q}) + \hat{V}_M(\mathbf{Q}), \tag{2.2}$$

where **Q** is the *scattering vector* and is the difference between the direction of the incident wave $\mathbf{k}_i$ and the final wave $\mathbf{k}_f$.

2.2.1.1. *Nuclear scattering.* The scattering from an isolated nucleus is isotropic and gives rise to a spherical wave, shown in figure 2.2. The properties of this wave are described by the wave equation, [**1**]:

$$\psi^{sc} = -\frac{b\exp(ikL)}{L} \tag{2.3}$$

where b is the scattering length and describes the magnitude of the coupling of the neutron with a nucleus, L is the distance of the crystal from the detector and k is a factor that defines the wavelength.

If we now consider the unit cell as the scattering object the reflected wave would be anisotropic and the potential would change with respect to the scattering direction, figure 2.3. The shape of the wavefront reflects the position and scattering length of the atoms in the cell. The coupling is given by the potential, $V_N = V_d(\mathbf{r} - \mathbf{R}_d)$, where the vector $\mathbf{r}$ is the location of the neutron and the vector $\mathbf{R}_d$ describes the location of the d^{th} nucleus within the unit cell. The potential for scattering to take place for

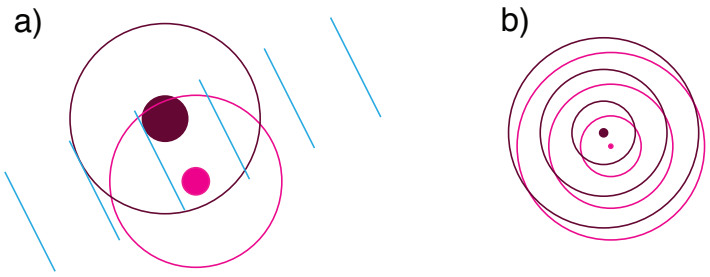

FIGURE 2.3. Anisotropic scattering occurs when the scattering object is non-spherical, the two points indicate two atoms that have different scattering lengths that combine to give anisotropic scattering.

a) The change in phase of the scattered radiation with respect to the incoming radiation and the scattering objects with different radii.

b) The observable wave front from the scattering object.

each atom is given by equation 2.4, [**1**].

$$V_{Nd} = \frac{2\pi\hbar^2}{m} b_d \tag{2.4}$$

where m is the mass of the neutron, the potential, V_{Nd}, is summed over all, d, atoms in the cell to give the nuclear structure factor, as a function of $\mathbf{Q}$,

$$F_{\mathrm{N}}(\mathbf{Q}) = \sum_d b_d \, \exp(i\mathbf{Q}\cdot\mathbf{d}) \, \exp(-W_d) \tag{2.5}$$

where W_d is the Fourier transform of the thermal motion of the atoms, termed the Debye-Waller factor, and will be discussed with respect to many body scattering, in section 2.3, [**1, 4**].

2.2.1.2. *Magnetic scattering.* Magnetic scattering from an atom is proportional to the magnitude of the total moment of that atom due to the electronic orbital motion and the nuclear and electronic spin. The coupling, in this instance, is between the component of the incident neutron moment, $\boldsymbol{\mu}_{\mathrm{n}}$, that is aligned with magnetic field, $\mathbf{B}$, about the atom. The scattering from neutrons that have a component aligned

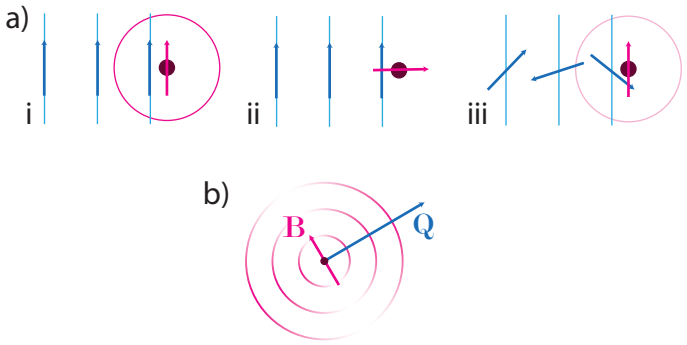

FIGURE 2.4. An illustration of the contributions to the anisotropy of magnetic scattering.

a) Demonstrates the outcome of equation 2.6 when the incident beam contains all spin orientations: i, Maximum scattering; ii, Minimum scattering and iii, Intermediate scattering.

b) Demonstrates the effect of on the magnitude of the scattering with respect to the different directions of incident radiation. The intensity of the scattering reflects the shape of the field about the atom.

with the local magnetic field is described by a wave equation that is analogous to equation 2.3, [**1**],

$$\psi^{sc} = -\frac{-\boldsymbol{\mu}_{\mathrm{n}} \cdot \mathbf{B} \exp(ikL)}{L} \tag{2.6}$$

Where the moment on the incident neutron, $\boldsymbol{\mu}_{\mathrm{n}} = -\gamma\mu_{\mathrm{N}}\boldsymbol{\sigma}$, in which the gyromagnetic ratio, $\gamma = 1.913$, $\boldsymbol{\sigma}$ is a vector of Pauli matrices and $\mu_{\mathrm{N}} = e\hbar/2m_p$ is the nuclear magneton where e is the proton charge and m_p is the proton mass. We will consider the moment that is associated with the atom, $\boldsymbol{\mu}_{\mathbf{B}}$, to be a sum of the electronic spin, $\mathbf{s}$ and angular momentum, $\mathbf{l}$, and will assume the nuclear spin contribution is negligible. The local field is, then, given by, [**1**],

$$\mathbf{B} = \mathbf{B}_S + \mathbf{B}_L \tag{2.7}$$

$$= \frac{\mu_0}{4\pi}\left\{\mathrm{curl}\left(\frac{\boldsymbol{\mu}_e \times \hat{\mathbf{R}}}{R^2}\right) - \frac{2\mu_B}{\hbar}\frac{\mathbf{p} \times \hat{\mathbf{R}}}{R^2}\right\} \tag{2.8}$$

where $\boldsymbol{\mu}_e = -2\mu_{\mathbf{B}}\mathbf{s}$ and $\mu_{\mathrm{B}} = e\hbar/2m_e$ and μ_{B} is the Bohr magneton, m_e is the mass of the electron and $\mathbf{s}$ is the spin angular momentum operator for the electron in units of $\hbar$. The term $\mathbf{R}$ is the distance from the electron to the point at which the field is measured and $\mathbf{p}$ is the momentum of the electron. The cross product terms in these relations give rise to the magnetic scattering only occuring from the component of the field, $\mathbf{B}$, that is perpendicular to the scattering direction, $\mathbf{Q}$. This leads to anisotropic scattering with respect to the direction of the incoming radiation, which is zero when $\mathbf{Q}$ is in the direction of the magnetization and at a maximum when $\mathbf{Q}$ is perpendicular, figure 2.4.b.

The magnetic structure factor, $\mathbf{F}_{\mathrm{M}}(\mathbf{Q})$, is the sum over all of the magnetic moments, $\boldsymbol{\mu}_d$, associated with the atoms, d, in the unit cell to give the local magnetization and may be calculated, [**6**],

$$\mathbf{F}_{\mathrm{M}}(\mathbf{Q}) = \mathrm{M}(\mathbf{Q}) = \sum_d \boldsymbol{\mu}_d \exp(i\mathbf{Q} \cdot \mathbf{r}_d) \tag{2.9}$$

The magnetic interaction vector, $\mathbf{M}_\perp(\mathbf{Q})$, is the part of the magnetic structure factor that lies in the plane perpendicular to $\mathbf{Q}$ and is measured in a neutron scattering experiment. The magnetic interaction vector is described mathematically by twice taking the cross product of the moment and the scattering plane:

$$\mathbf{M}_\perp(\mathbf{Q}) = \mathbf{Q} \times (\mathbf{M}(\mathbf{Q}) \times \mathbf{Q}) \tag{2.10}$$

2.2.1.3. *To summarise.* The number of scattered neutrons is described by the total scattering cross section, σ_{tot},

$$\sigma_{tot} = \frac{\text{(total number of neutrons scattered per second)}}{\Phi}, \tag{2.11}$$

where Φ is the flux of the incident neutrons. In the case of neutron diffraction from a single nuclear potential the scattering is isotropic, whereas, scattering from the unit cell is anisotropic. Magnetic scattering from a single ion is also isotropic, but varies in magnitude with respect to the direction of the incident wave, as only the part of the magnetic vector that lies in the plane perpendicular to $\mathbf{Q}$ contributes to the magnetic potential. The next section will consider the scattering from an array of scattering objects.

2.3. Many-body Scattering

Condensed matter can be described by an infinite array of atoms as volume of the sample is much much greater than the area probed by each neutron. The diffraction pattern is the sum of the Fourier transform of the regions probed by the scattered neutrons and, as such, the scattering pattern from a bulk material is the Fourier transform of the ensemble averaged structure. The pattern has the same symmetry as the lattice of the scatterer with the addition of centrosymmetry, if this is absent, as the inversion of phase that occurs when the incident beam is scattered in opposite directions, $\pm\mathbf{Q}$, cannot be observed. The interference effects due to these phase

changes can be observed and this gives rise to the diffraction pattern, in which a coherent relationship between the scattered waves gives rise to the measurable increase in intensity.

If the scatterer has discrete translational symmetry the scattering is *coherent* and displays maxima at discrete intervals to give the *reciprocal lattice*, figure 2.5. When the scatterer is randomly ordered the average structure and scattering will have no distinct features, figure 2.9, and the final scattering is described as *incoherent* scattering. In general the structure of real materials between the extremes of perfect order and complete disorder and the ensemble average will display features that are best described with probability density functions. Scattering from a probability distribution is most usually associated with amorphous, or locally ordered materials, such as glasses and frustrated magnets [**7, 8**], and gives *diffuse* scattering, figure 2.10, however, the thermal motion of nuclei and the magnetic form factor can also be thought of in these terms, figure 2.11.

In summary, the diffraction pattern is the Fourier transform of the ensemble average structure, where coherent scattering occurs when the crystal is the same in all parts, diffuse scattering occurs when it is similar and incoherent scattering occurs when the crystal is different in all parts. Let us begin by considering coherent scattering.

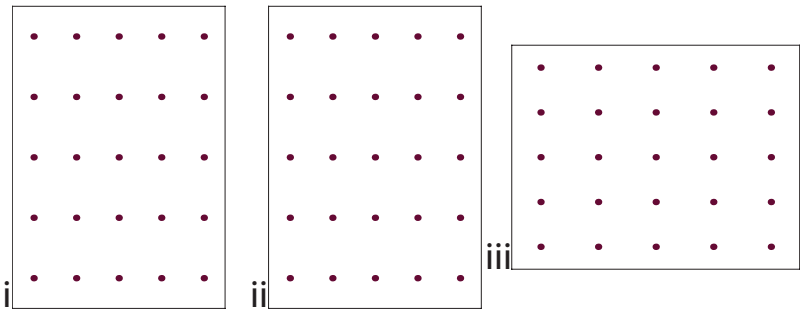

FIGURE 2.5. When the scatterer is static and has perfectly discrete translational symmetry the local structure, probed by the neutron, is the same as the ensemble average of the bulk, which gives a diffraction pattern of delta functions. (i) The local structure. (ii) The ensemble average. (iii) The diffraction pattern.

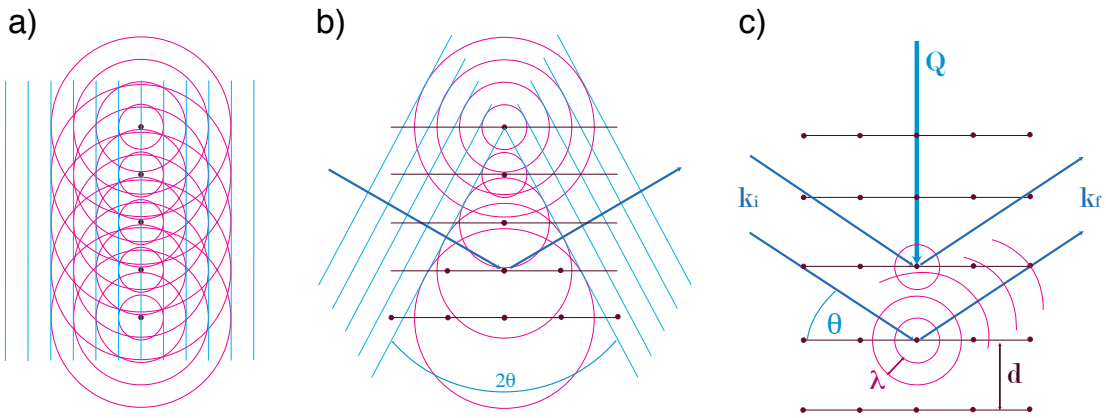

FIGURE 2.6. Illustration of the scattering from an ordered array of points.

a) When a plane wave (cyan) is incident on an array of points (purple) spherical scattering (magenta) occurs from all the points when the distance to from the points to the observer is large the scattering appears as a plane wave.

b) The incident wave (cyan, left) is related to the final wave (cyan, right) by the angle 2θ, where the final wave is a plane wave, which consists of coherent spherical wavefronts (magenta) and have been scattered by the purple points, that lie in the plane being probed (purple lines).

c) A schematic of the scattering process that shows the relationship between $\mathbf{Q}$, $\mathbf{k}_i$, $\mathbf{k}_f$ described in equation 2.12 and indicating the integer number, n, of wavelengths, λ, that are required to satisfy Braggs Law, equation 2.13.

2.3.1. Coherent Scattering. Scattering from an array of static identical points that have discrete translational symmetry gives rise to a perfectly coherent diffraction pattern, constructed from delta functions, figure 2.5, [**1**]. A one dimensional array is illustrated in figure 2.6a, in which the wavefronts, in magenta, show the maxima of the waves. When the distance from the array of points is large the scattered radiation appears as a plane wave, shown in cyan. The wavefront may be selected by changing the angle, θ, of the incoming radiation, $\mathbf{k}_i$, to the plane of scattering points. In the elastic case, which is the only case considered in this thesis, the scattered radiation, $\mathbf{k}_f$, is again in the direction θ away from the plane of scattering atoms. The total change in angle is the *scattering angle*, 2θ, and is illustrated in figure 2.6b. If one describes the direction of the incident and final radiation, $\mathbf{k}_i$ and $\mathbf{k}_f$, with vector

notation the value of **Q** that corresponds to the maximum scattering is found, figure 2.6c,

$$\mathbf{Q} = \mathbf{k}_i - \mathbf{k}_f. \tag{2.12}$$

Coherent scattering can occur only when there is an integer number, n, of wavelengths, λ, between equivalent planes with separation d, hence the requirement for discrete translational symmetry, illustrated in figure 2.6c and defined by Braggs Law, [**9, 10**],

$$n\lambda = 2d\sin\theta. \tag{2.13}$$

2.3.1.1. *The differential scattering cross section.* The differential scattering cross section gives the intensity of the scattering in the direction **Q**, described with polar coordinates, shown in figure 2.7 and described by the equation,

$$\frac{d\sigma}{d\Omega} = \begin{array}{c}(\text{number of neutrons scattered per second}\\ \text{into a small solid angle } d\Omega\\ \text{in the direction of } \theta,\ \phi) \ /\ \Phi\ d\Omega\end{array} \tag{2.14}$$

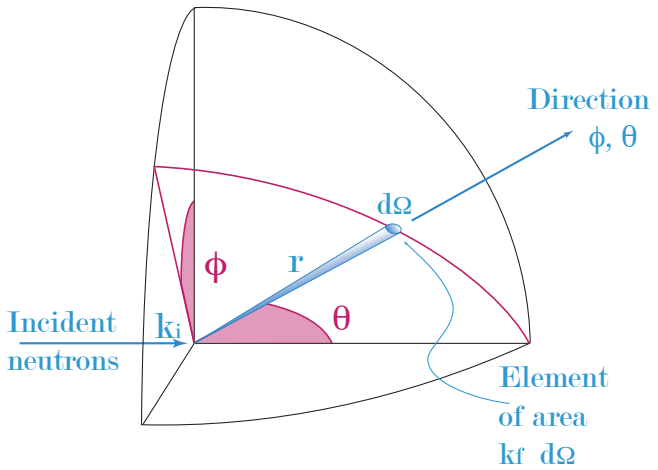

FIGURE 2.7. Geometry for a scattering experiment, showing the solid angle of scattering in the direction **Q** and the relation between **Q** and the scattering angles, θ and ϕ, after [**1**].

For strong elastic scattering to occur the scattering vector $\mathbf{Q}$ needs to be in the direction of a reciprocal lattice vector $\boldsymbol{\tau}_{hkl}$, where the set, $\{\boldsymbol{\tau}_{hkl}\}$, gives the reciprocal lattice. The values hkl are integers that define the Miller plane within the crystal to which vector is perpendicular. The relationship between $\mathbf{Q}$ and $\{\boldsymbol{\tau}_{hkl}\}$ is the Laue condition and may be defined,

$$\mathbf{Q} = \boldsymbol{\tau}_{hkl}, \qquad \boldsymbol{\tau}_{hkl} = h\mathbf{a}^* + h\mathbf{b}^* + h\mathbf{c}^*, \tag{2.15}$$

where the vectors $\mathbf{a}^*$, $\mathbf{b}^*$ and $\mathbf{c}^*$ are the basis vectors of the reciprocal lattice, [**11**], and are discussed in the symmetry chapter, chapter 3. The total *coherent* scattering can then be described as the set of delta functions that are non-zero when equation 2.15 is true, which is equivalent to the Fourier transform of the potential function. The differential cross section, therefore, for the coherent elastic case,

$$\left(\frac{\mathrm{d}\sigma}{\mathrm{d}\Omega}\right)_{coh\ el} = N\frac{(2\pi)^3}{\nu_0}\sum_{\boldsymbol{\tau}}\delta(\mathbf{Q}-\boldsymbol{\tau})|F(\mathbf{Q})| \tag{2.16}$$

where N is the number of atoms in the crystal, F is the structure factor and ν_0 is the volume of the unit cell, [**1**]. The Bragg condition and the Laue condition can be shown to be equivalent if one considers that $\mathbf{Q}{=}4\pi/\lambda\sin\theta$ and $\boldsymbol{\tau}_{hkl} = 2\pi/d_{hkl}$.

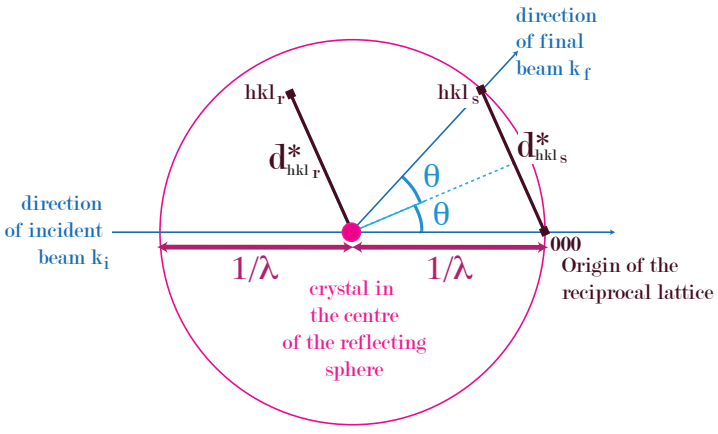

FIGURE 2.8. The Ewald sphere construction for a set of planes with the correct Bragg angle. The sphere, with radius r=1/λ, is drawn with the crystal at the centre. The vector between the origin and hkl$_s$ is equivalent to the vector between the crystal and hkl$_r$. The origin is fixed and the observable point hkl$_s$ is on the surface of the sphere, after [**12**].

2.3.1.2. *The Ewald sphere.* The Ewald sphere is a graphical representation of the Laue/Bragg condition where the reflections that satisfy these conditions fall on the surface of the sphere, [**12, 13**]. The construction allows the experimentalist to predict which peaks will be observable with a specific wavelength and crystal orientation. The application of the sphere can be easily understood with reference to figure 2.7 which describes the scattering geometry. One can imagine the Ewald sphere superposed onto the surface in the image, which would allow ready identification of the solid angle into which the crystal will scatter, when $\mathbf{Q}=\boldsymbol{\tau}$.

2.3.1.3. *The* **UB**-*matrix.* In an experimental situation the accessible reflections, and their positions, can be computed with the **UB**-matrix, a second rank tensor constructed from the **B**-matrix that converts the reciprocal lattice vector, $\mathbf{v}$ to crystallographic Cartesian axes,

$$\mathbf{v}_c = \mathbf{B}\mathbf{v}, \tag{2.17}$$

and the **U**-matrix that rotates the crystallograhic Cartesian axis system to the instrumental Cartesian axis system, [**14**]. The **B**-matrix can be found from the direct, $b, c,\ \alpha$, and reciprocal, $a^*,\ b^*,\ c^*,\ \beta^*,\ \gamma^*$, lattice parameters,

$$\mathbf{B} = \begin{pmatrix} a^* & b^*\cos\gamma^* & c^*\cos\beta^* \\ 0 & b^*\sin\gamma^* & -c^*\sin\beta^*\cos\alpha \\ 0 & 0 & 1/c \end{pmatrix} \tag{2.18}$$

where the crystallographic a axis is in the direction of the Cartesian x axis, the b axis in the xy plane and the c axis perpendicular to that plane. The instrument

can be imagined to have an axis system that is attached to the vertical shaft of the instrument, φ, such that when all instrumental angles are set to zero the z axis is vertical, the y axis is with the primary beam and x makes up the left hand set. The conversion of the crystallographic Cartesian axes to the instrumental axes then returns the vector $\mathbf{v}_\varphi$,

$$\mathbf{v}_\varphi = \mathbf{U}\mathbf{v}_c, \tag{2.19}$$

from which one can predict the position of the reciprocal lattice vectors in the real space axis system of the instrument.

FIGURE 2.9. A scatterer that is completely random will have an ensemble average that is equivalent in all places to give a featureless diffraction pattern. (i) The local structure. (ii) The ensemble average. (iii) The diffraction pattern.

2.3.2. Incoherent Scattering. Scattering from a material that has continuous translational symmetry gives incoherent scattering, figure 2.9, where the image shows a random distribution with respect to space. A random distribution of different atoms or isotopes on an organized lattice will also give incoherent scattering. This can be understood by considering figure 2.6.a, when the phase shift of the scattered waves are not equivalent the wavefront will never appear to be a plane wave. Neutron scattering experiments usually have a non-zero incoherent background due to the

random isotropic distribution and, above the transition temperature, the random orientations of the electronic and nuclear magnetic moments, [**1, 4**].

2.3.2.1. *The nuclear contribution.* The incoherent background that arises due to nuclear scattering is due to the different scattering lengths of the isotopes of equivalent elements and the difference in the scattering length from atoms of the same isotope that are in different spin states The incoherent scattering cross section is largest for hydrogen due to the substantial difference in the potential of the two spin states of the atom. Let us consider the case of incoherent scattering due to the mixing of different isotopes and assume that the distribution of isotopes is random and uncorrelated. The differential cross section, equation 2.3.1.1, is then the average pattern from all probed regions and may be written,

$$\left(\frac{\mathrm{d}\sigma}{\mathrm{d}\Omega}\right) \quad \approx \quad \overline{\left(\frac{\mathrm{d}\sigma}{\mathrm{d}\Omega}\right)}. \tag{2.20}$$

The nuclear scattering cross section is then the correlation between two atoms, m and n and the differential cross section, with respect to the nuclear scattering is,

$$\left(\frac{\mathrm{d}\sigma}{\mathrm{d}\Omega}\right) = \sum_m \sum_n b_n b_m \exp[\, i\, \mathbf{Q}.(\mathbf{r}_m - \mathbf{r}_n)], \tag{2.21}$$

where $\mathbf{r}$ is the position of the atoms m and n. As the sites are uncorrelated the ensemble average, $b_m\, b_n$, described in equation 2.3.2.1, may be replaced with $\overline{b_m\, b_n}$, which becomes $\bar{b}_m\, \bar{b}_n$, when $m \neq n$ and $\bar{b}_m^2$ when $m = n$, to give,

$$\left(\frac{\mathrm{d}\sigma}{\mathrm{d}\Omega}\right) = \sum_{m \neq n} b_m b_n \exp[\, i\, \mathbf{Q}.(\mathbf{r}_m - \mathbf{r}_n)] + \sum_{m=n} (\overline{b^2}_m - \bar{b}_m^2). \tag{2.22}$$

The first term is the coherent part of the scattering and describes the diffraction from two identical particles and the second term is the incoherent part of the scattering and describes the diffraction from two non-identical particles, [**1**]. The incoherent

part of the scattering is proportional to the variance of the crystal from the perfectly ordered state.

2.3.2.2. *The magnetic contribution.* The magnetic contribution to the incoherent scattering is due to the random orientation of the moments in a paramagnet and will disappear when the magnetic moments become ordered, [**4**]. The incoherent magnetic scattering decreases as a function of **Q** due to the magnetic form factor, discussed in the following section.

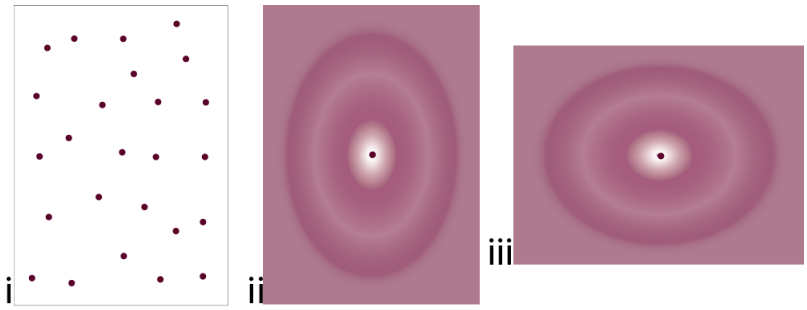

FIGURE 2.10. When the scatterer has short range order the ensemble average has maxima that correspond to the distance between a central atom and the expected positions of the nearest neighbours, which also gives a probability density distribution in the diffraction pattern. (i) The local structure. (ii) The ensemble average. (iii) The diffraction pattern.

2.3.3. Diffuse Scattering. Diffuse scattering arises when the ensemble average of scattering potentials contains a broad probability distribution. If the distribution arises due to the position of an atom with respect to it's nearest neighbours the ensemble average and diffraction would appear approximately as in figure 2.10, where the image 2.10.i shows the atoms that are probed in one region, and 2.10.ii shows the probability distribution that is observed for the ensemble average . Figure 2.10.ii indicates the probability of finding an atom local to the central atom, where the atom at the centre can be any atom within the bulk material. Diffuse scattering is typical of materials that have short range order, such as amorphous materials and frustrated magnets, [**7, 10**]. The diffraction patterns only show coherent scattering on the length scale of the atomic or magnetic correlations but are incoherent at longer length scales due to the lack of long range order.

A similar phenomenon can be observed in magnetic and nuclear scattering from a material that has long range order with fluctuations. The ensemble average of the moving particles gives a probability distribution about the lattice sites where the atoms would be in the ideal static crystal, figure 2.11. The atoms can no longer be considered point particles and hence, as the wavevector **Q** increases, the scattering becomes less intense and the peaks become broader. Magnetic scattering shows this more clearly due to the electron cloud being much larger than the ellipsoid of thermal motion.

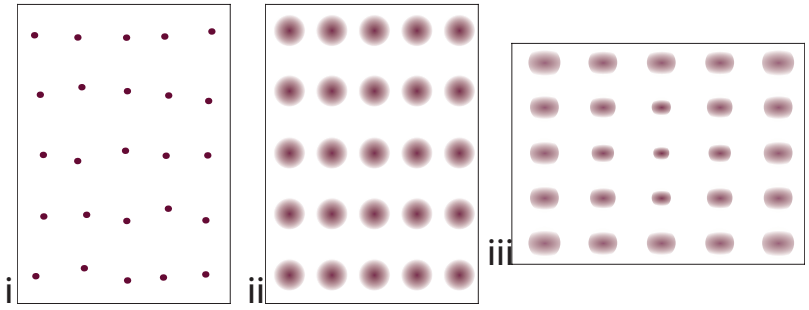

FIGURE 2.11. When the atoms are randomly displaced from the ideal lattice the ensemble average has maxima that correspond to the ideal locations of the atoms to give a probability density in the diffraction pattern, about the reciprocal lattice sites. (i) The local structure. (ii) The ensemble average. (iii) The diffraction pattern.

2.3.3.1. *Thermal motion.* The nuclear peaks in a diffraction pattern are never true delta functions, as would be expected for a static array of points with discrete translational symmetry, and instead have a Gaussian or Lorentzian distribution about the ideal peak position. The preferred direction of motion can be found from the relative peak intensities to and used to give an ellipsoid of motion. The shape of the ellipsoid reflects the range of motion available to the atom and from this the bond strength can be ellicited. The interpretation of this information from the diffraction pattern is given by the Debye-Waller factor, which models the thermal motion of the atoms within the scatterer,

$$W_d = \frac{\hbar}{4M_d N} \sum_s \frac{|\mathbf{Q} \cdot \mathbf{e}_{ds}|^2}{\omega_s} \langle 2n_s + 1 \rangle \tag{2.23}$$

where M_d is the mass of the atom d, $\mathbf{e}$ is the polarization vector with $s = j\,\mathbf{q}$ modes where j is the polarization index and takes values ($j = 1, 2, 3$) and ω_s is the angular frequency of mode s, [**1**].

2.3.3.2. *Electronic distribution.* The magnetic form factor is due to the distribution of the magnetization within an atom. In the ideal case the form factors are calculated from the radial wavefunctions of the electrons in the outer, open shells. More usually it is described with the dipole approximation that assumes that this distribution is spherically symmetrical, in this case the magnetic form factor is given by:

$$f(k) = \langle j_0(k) \rangle + (1 - 2/g)\langle j_2(k) \rangle \tag{2.24}$$

where g is the Landé splitting factor [**2, 15**]. From the perspective of diffuse scattering this can be understood as the decoherence of the waves that are scattered from the magnetization associated with the electrons in the extremal positions allowed within the electronic probability distribution. As the scattering angle θ increases the difference in path length of the scattering from these positions will increase until the scattered waves are out of phase. The values for the form factor coefficients are not easily calculable and as such have been tabulated in the International Tables, Vol C, [**16**].

2.3.4. Summary. Overall the Bragg scattering that is observed in a diffraction pattern is from the averaged structure of the crystal. If the scattering potential is equivalent in all the scattering planes, hkl, that contribute to the scattering vector $\mathbf{Q}_{hkl}$, the diffraction pattern consists of delta functions spaced by the reciprocal lattice vectors $\boldsymbol{\tau}_{hkl}$, if the potential is different in all the planes probed the scattering is featureless as there is no phase coherence. The overall pattern is the Fourier

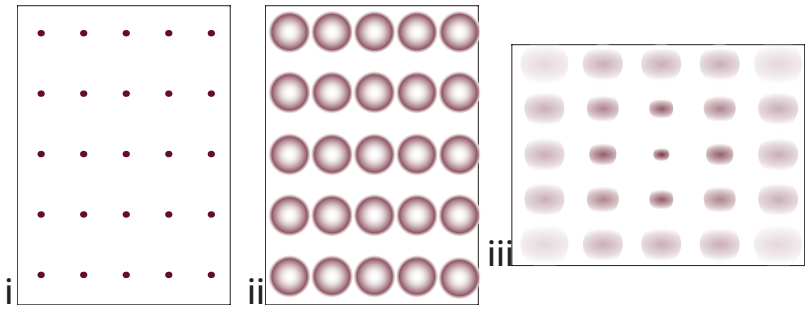

FIGURE 2.12. The outer electrons are in motion around the ideal lattice sites to give a decay in the intensity of the peaks as the distance from the origin increases. (i) The local lattice. (ii) The electronic distribution. (iii) The diffraction pattern.

transform of a convolution of the translational properties of lattice and the short range structure or basis.

The magnetic form factor is due to the distribution of the magnetization within an atom and are calcualted, the thermal effects are due to the motion of the nuclei about the atomic centres and can be found from the diffraction pattern.

In order to gather more information about the magnetic structure, and the distribution of the magnetization about the atomic centre polarized neutron techniques are frequently used. These techniques will be discussed in the next sections.

2.4. Polarized Neutron Scattering

As stated previously the neutron has spin and this allows it to couple with the magnetism that is perpendicular to the scattering direction. The earlier discussion only considered the total magnitude of the scattering and not the effect of the local field on the orientation of the neutron spin. This section will present a classical and a quantum mechanical picture of this interaction in the context of neutron polarimetry.

2.4.1. Neutron Polarimetry. The theory of polarized neutron scattering was well established by the mid sixties due to the independent work of Blume and Maleev,

[**17, 18, 19**]. Both authors developed the ideas of polarized neutron scattering introduced by Halpern and Johnson, [**20**], to consider the scattering that occurs when the polarization is oriented with any arbitrary direction and the orientation of the beam polarization is determined before and after the scattering event. A guide field is often used in neutron polarized neutron scattering instruments to maintain the orientation of the beam and stop precession about stray fields. The polarization, therefore, is dictated by the direction of the guide field and any information perpendicular to that field is lost. CRYOPAD (CRYOgenic Polarization Device) allows the arbitrary orientation of the beam before and after the sample, and overcomes the need for a guide field by shielding the sample from any stray magnetic fields with cryogenically cooled Meissner sheilding. The insert was developed by Francis Tasset and co-workers [**21, 22, 23, 24**].

The accuracy of the technique was improved by Tasset *et al* with the development of CRYOPAD II, [**25, 26**] and subsequently three third generation CRYOPAD inserts have been built, [**27**]. These devices are located at the ILL, where it has been deployed both on the triple axis spectrometer IN20 and the hot neutron source diffractometer D3, the CEA, where it is used on the triple axis spectrometer IN22, [**28**] and at JAERI, where it is used in conjunction with the triple axis spectrometer TAS-1, [**29**]. A similar device, named MuPAD, which has mu-metal shielding rather than cryogenically cooled Meissner screens has been developed at SINQ for use on the TASP three axis spectrometer, [**30**] and a copy of this device was built for use on HEIDi at FRM II. A summary of the currently operating inserts that allow spherical neutron polarization analysis is given in reference, [**33**].

2.4.2. CRYOPAD. The schematic shown in figure 2.13 represents the third generation CRYOPAD insert. The incident neutrons are polarized by a Cu_2MnAl Heusler crystal to give a polarization in the direction of motion $\mathbf{k}_i$. The beam then

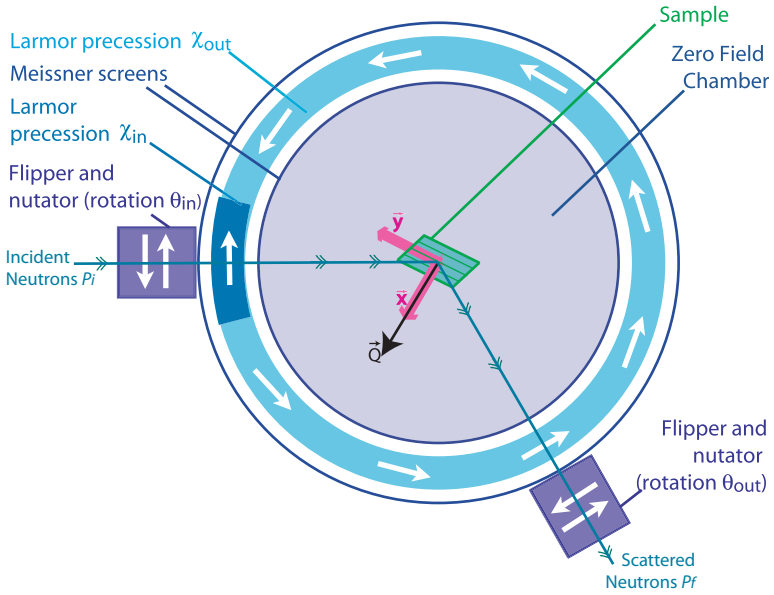

FIGURE 2.13. Diagram of the usual CRYOPAD axis system, where x is with $\mathbf{Q}$, z is with the instrument axis, φ and y makes up the right hand set. The progress of the neutron through the device is described below in figure 2.14 and in the text.

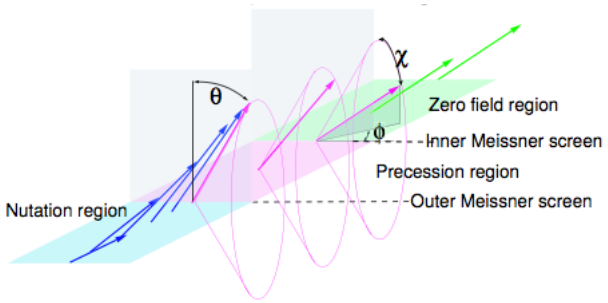

FIGURE 2.14. Schematic of the orientation process of the incident neutron beam. The neutron beam enters the nutation region with polarization in the direction of motion. The nutator contains a weak magnetic field that the neutron spin precesses about. The direction of the field is gradually changed until the neutron makes the angle θ with the vertical. The neutron beam then enters the precession region, which contains a perpendicular magnetic field that the neutron spin precesses about rapidly to move through the angle χ. The combination of the the two regions allows any arbitrary orientation of the polarization of the beam. The beam, with this orientation, then passes into the zero field region.

enters the nutation region, in which a magnetic field gradually changes from a direction parallel to the beam to a direction that is at an angle of θ_{in} to the vertical

direction, due to the mechanical change in the orientation of the coils. The nutation process is adiabiatic and the spin of the neutrons follows the gradual change in direction of the field, to give a polarization of the beam that is also aligned with θ_{in}. The direction of the spins may also be flipped by the spin flipper. At the exit of the nutator the neutrons cross the outer Meissner screen, which is transparent to neutrons and their polarization, [**21**], but shields the precession field from the nutator field. The Larmor precession region is created by an abrupt change in magnetic field which the neutron spin rapidly precesses about. The abrupt field change is due to a superconducting incident coil perpendicular to the direction of motion $\mathbf{k}_i$. This rapid change rotates the polarization of the beam through the angle χ_{in} such that any arbitrary orientation may be accessed. The Larmor precession abruptly ends when the inner Meissner screen is crossed and the neutron beam enters the zero field chamber. After this point the only significant field that the neutron encounters is within the sample. To minimise the field within the zero field chamber the Meissner shielding is surrounded by FeNi μ-metal above and below the scattering plane, this combination reduces the field within the chamber to 1-1.5mG when the insert is used on D3, [**33**].

As the neutron beam leaves the zero field chamber the process of precession and nutation occurs in reverse so that the components of the scattered polarization may be measured. To measure the magnitude of the polarization in the direction of x, for example, the polarization of the beam would be rotated from the direction $\mathbf{Q}$ to a direction that is parallel to the neutron analyser direction. The spin is then flipped so that the difference between the intensity of the spin-flipped and non spin-flipped components of the beam may be measured. The process is then repeated for the other cardinal directions and the difference in the intensity is then used to determine the polarization, as outlined in the previous section. The process is summarized in figure 2.14. CRYOPAD and MUPAD are in essence, 'zero-field' environments that

allow the arbitrary orientation of the polarization of the beam, before and after the sample

The final polarization is selected using an ^{3}He spin filter. ^{3}He works as a spin filter as the absorption cross-section for the different nuclear spin orientations is very large, ($\sigma \uparrow\downarrow$ [barn] $\approx 6000 \cdot \lambda$[Å]), compared to ($\sigma \uparrow\uparrow$ [barn] ≈ 5). Therefore only those neutrons with a spin component parallel to the ^{3}He nuclear spin will be detected as all of those with a component anti-parallel will be absorbed. The transmission, $T_\pm$ for both spin orientations through a cell with polarized ^{3}He is given by:

$$T_\pm = \exp\{-(1 \mp P_{He}) \cdot n_{He} \cdot \sigma_0 \cdot l\} \tag{2.25}$$

where P_{He} is the ^{3}He nuclear polarization, n_{He} is the number density of ^{3}He atoms σ_0 is the absorption cross section for unpolarized neutrons (σ_0[barn] $\approx 3000 \cdot \lambda$[Å]) and l is the length of the ^{3}He cell.

FIGURE 2.15. The effect of magnetic field of an atom (magenta) on the magnetic dipole moment of the polarized neutron beam (blue), the orientation of the field in both cases is indicated by the direction of the arrow.

i) The magnetic field has the same orientation as the polarization of the incident beam and there is no change in the orientation of the scattered beam.

ii) The magnetic field is out of the page, perpendicular to the incident beam, generating torque and producing a spin flip in the scattered beam.

2.4.3. Classical description of polarized scattering. The classical approach allows an intuitive understanding of the orientation of the spins in the neutron beam

after the scattering event. The magnetic part of the potential in the scattering plane can be considered a local magnetic field. The incoming beam with neutrons polarized in a specific direction will precess around the field due to the torque exerted by the magnetic field on a magnetic dipole. Figure 2.15 demonstrates the results with differently oriented incident polarized beams, where the polarization of the beam is indicated by the direction of the arrow. In image 2.15.i the orientation of the polarization remains unchanged as there is no torque when orientation of the polarization and the field are the same. In image 2.15.i the orientation of the polarization is flipped by 180° because the local field is perpendicular to the incoming beam polarization. Mathematically the torque on a magnetic dipole moment $\boldsymbol{\mu}$ in a magnetic field, $\mathbf{B}$, is described by the cross product,

$$\mathbf{T} = \boldsymbol{\mu} \times \mathbf{B}, \tag{2.26}$$

as such when $\boldsymbol{\mu}$ is in the same direction as $\mathbf{B}$ there is no torque generated and no change in the orientation of $\boldsymbol{\mu}$. If one allows the incoming neutron beam to have any arbitrary orientation, given by the vector $\mathbf{P}_i$, and arbitrary direction of the final polarization $\mathbf{P}_f$ is given by the Blume Maleev equations, [**17, 18, 19**],

$$\mathbf{P}_f = \frac{\mathbf{P}_f \sigma}{\sigma} \tag{2.27}$$

$$\begin{aligned} \sigma &= (NN^*) + (\mathbf{M}_\perp \cdot \mathbf{M}_\perp^*) \\ &\quad + (i\mathbf{P}_i \cdot (\mathbf{M}_\perp^* \times \mathbf{M}_\perp) + (\mathbf{P}_i \cdot (\mathbf{M}_\perp N^* + \mathbf{M}_\perp^* N)) \end{aligned} \tag{2.28}$$

$$\begin{aligned} \mathbf{P}_f \sigma &= (\mathbf{P}_i NN^*) \\ &\quad + (-\mathbf{P}_i(\mathbf{M}_\perp \cdot \mathbf{M}_\perp^*) + (\mathbf{M}_\perp(\mathbf{P}_i \cdot \mathbf{M}_\perp^*) + \mathbf{M}_\perp^*(\mathbf{P}_i \cdot \mathbf{M}_\perp)) \\ &\quad + (-i(\mathbf{M}_\perp^* \times \mathbf{M}_\perp)) \\ &\quad + (N\mathbf{M}_\perp^* + N^*\mathbf{M}_\perp - i(N\mathbf{M}_\perp^* - N^*\mathbf{M}_\perp) \times \mathbf{P}_i) \end{aligned} \tag{2.29}$$

Scattering	Contribution	Description
Nuclear	$\sigma_n = (NN^*)$	Intensity is modulus squared of the nuclear structure factor
	$\mathbf{P}_f\sigma_n = (\mathbf{P}_i NN^*)$	Incident polarization is unchanged
Magnetic	$\sigma_m = (\mathbf{M}_\perp \cdot \mathbf{M}_\perp^*)$	Intensity is modulus squared of the magnetic interaction vector
	$\mathbf{P}_f\sigma_m = (-\mathbf{P}_i(\mathbf{M}_\perp \cdot \mathbf{M}_\perp^*)$ $+(\mathbf{M}_\perp(\mathbf{P}_i \cdot \mathbf{M}_\perp^*)$ $+\mathbf{M}_\perp^*(\mathbf{P}_i \cdot \mathbf{M}_\perp))$	Components of polarization perpendicular to magnetic interaction vector are inverted
Magnetic 'chiral'	$\sigma_c = (i\mathbf{P}_i \cdot (\mathbf{M}_\perp^* \times \mathbf{M}_\perp)$	Intensity is dependent on orientation of incoming polarization
	$\mathbf{P}_f\sigma_c = (-i(\mathbf{M}_\perp^* \times \mathbf{M}_\perp))$	Polarization is generated in the direction of the scattering vector when $\mathbf{M}_\perp^* \neq \mathbf{M}_\perp$
Nuclear Magnetic interference	$\sigma_i =$ $(\mathbf{P}_i \cdot (\mathbf{M}_\perp N^* + \mathbf{M}_\perp^* N))$	Intensity depends on incident polarization when N and $\mathbf{M}_\perp$ are in phase
	$\mathbf{P}_f\sigma_i =$ $(N\mathbf{M}_\perp^* + N^*\mathbf{M}_\perp$ $-i(N\mathbf{M}_\perp^* - N^*\mathbf{M}_\perp) \times \mathbf{P}_i)$	Polarization is created along $\mathbf{M}_\perp$ when N and $\mathbf{M}_\perp$ are in phase. Incident polarization is rotated around $\mathbf{M}_\perp$ when N and $\mathbf{M}_\perp$ are π out of phase.

TABLE 2.2. Components of the Blume Maleev equations, after [**32**]

Where $\mathbf{M}_\perp$ is the magnetic interaction vector, $\mathbf{M}_\perp^*$ is the complex conjugate of the magnetic interaction vector and N and N^* is the nuclear structure factor and its complex conjugate respectively. The $\mathbf{Q}$ dependence of $\mathbf{M}_\perp$ and N has been omitted for clarity. Each of the different terms arise from different interference effects within the scattered beam and as such the contributions from them reveal different information about the scatterer. This information can be tabulated for clarity, see table 2.2, [**32, 33**].

The advantage of the equations derived by Blume and Maleev is that all input and output from the equations are classical vectors, however, the measurement is of the intensity of the beam in either spin flipped I^- or non-spin flipped, I^+ states.

2.4.4. Mathematical representation. The components of the vector that describes the final polarization, **P** is derived from the intensity of the spin-fip, I^-, and non-spin-flip, I^+, scattering,

$$P = \frac{I^+ - I^-}{I^+ + I^-}, \tag{2.30}$$

where I^+ and I^- is the intensity measured in the final S^+ and S^- channels respectively. The intensity is found from the differential cross-section that considers the polarization of the incident σ, and final beam, σ', and calculates the coupling of this polarization with the potential, $\hat{V}$,

$$\left(\frac{\mathrm{d}^2\sigma}{\mathrm{d}\Omega \mathrm{d}E'}\right) = \frac{k'}{k}\sum_{\sigma\sigma'} p_\sigma \sum_{\mu\mu'} p_\mu \times |\langle\sigma'\mu'|\hat{V}(\mathbf{Q})|\mu\sigma\rangle|^2 \ \delta(\hbar\omega + E_\mu - E'_\mu). \tag{2.31}$$

The relation includes the terms μ and μ' to indicate the change from one energy state to another, the energy of these states is indicated by E_μ and E'_μ and the final term describes the condition for energy conservation in the scattering process. The differential is a sum over all of the states that can participate in the scattering process and this is indicated by the sums over p_σ and p_μ, these represent the probability distribution of the initial states. In the purely elastic case $k' = k$ and it is assumed that the energy will be conserved and that there is no change in the state μ. Therefore we can simplify the cross section so that it has the form,

$$\left(\frac{\mathrm{d}\sigma}{\mathrm{d}\Omega}\right) = \sum_{\sigma\sigma'} p_\sigma \times |\langle\sigma'|\hat{V}(\mathbf{Q})|\sigma\rangle|^2, \tag{2.32}$$

where σ and σ' are spinors. Let us also assume that the probability of complete polarization for both σ and σ' is one, $p_\sigma = 1$, (in an experimental situation this is

not the case, however, the corrections for polarization can be applied as a prefactor to all subsequent equations), the calculation of the final polarization, P_f, may be written for each combination of incident spin and final spin,

$$P_f = \frac{|\langle\sigma'_+|V|\sigma\rangle|^2 - |\langle\sigma'_-|V|\sigma\rangle|^2}{|\langle\sigma'_+|V|\sigma\rangle|^2 + |\langle\sigma'_-|V|\sigma\rangle|^2} \tag{2.33}$$

where the $\mathbf{Q}$ dependence has, again, been omitted for clarity. In order that the potential may couple with the spin described by the Pauli spin matrices a more general potential than the one given in equation 2.2 is required. If we assume that there is no contribution to the magnetism from the nuclear spin this may be represented by,

$$\hat{V}(\mathbf{Q}) = \hat{V}_N(\mathbf{Q})\,\mathbf{1} + \hat{V}_M(\mathbf{Q}) \cdot \boldsymbol{\sigma} \tag{2.34}$$

where $\mathbf{1}$ is a 2×2 unitary matrix and $\boldsymbol{\sigma}$ is a vector of Pauli matrices. In this form the potential can be considered a rotational matrix that operates on the initial spin state σ to give the final spin state σ'. The measurement of the intensity of the neutrons with final spin states σ' reveals the rotational operation that has occured and from this the potential may be deduced.

If we consider just a single orientation of the polarization, say with the instrument axis, $\sigma = z^+$, and calculate the final polarization in the non-spin-flip $\sigma' = z^+$ and spin-flip channels, $\sigma' = z^-$, the description of the polarization given by Moon, Riste and Koeler, [**34**],

$$\langle \sigma'_{+}|\hat{V}(\mathbf{Q})|\sigma_{+}\rangle = N(\mathbf{Q}) + M_z(\mathbf{Q}) \tag{2.35}$$

$$\langle \sigma'_{-}|\hat{V}(\mathbf{Q})|\sigma_{+}\rangle = -(M_{\perp\, x}(\mathbf{Q}) + iM_{\perp\, y}(\mathbf{Q})) \tag{2.36}$$

The notation is consistent with that presented in the thesis and not with that presented in the paper. If we consider all of the components of the incident polarization simultaneously the result is a vector that is equivalent to the definition of the polarization given by Blume and Maleev,

$$\mathbf{P_f} = \frac{\mathrm{Tr}\cdot\hat{\rho}\langle\hat{V}^{\dagger}|\sigma|\hat{V}\rangle}{\mathrm{Tr}\cdot\hat{\rho}|\hat{V}|^2} \tag{2.37}$$

where $\hat{V}^{\dagger}$ is the complex conjugate transpose of $\hat{V}$, Tr$\cdot$ denotes the trace over neutron spin variables and $\hat{\rho}$ is a probability density matrix, [**35**], described by,

$$2\hat{\rho} = \mathbf{1} + \mathbf{P_i}\cdot\hat{\boldsymbol{\sigma}}. \tag{2.38}$$

From the expansion of equation 2.37 it is possible to derive the Blume Maleev equations, described in section 2.4.3. Both approaches can be constructed in matrix form to give a representation that relates the incident polarization $\mathbf{P}_i$ with the final polarization $\mathbf{P}_j$, where $i, j = x, y, z$ in this instance the symbol σ indicates the intensity of the final beam,

$$\mathbf{P}_{ij} = \left\langle \frac{\mathcal{P}_{ij}P_j + P_i^{''}}{Pj} \right\rangle \tag{2.39}$$

where $\mathcal{P}_{ij}$ is the i,j^{th} component of the polarization tensor, which is the representation most similar to that found from experiment. The interference terms of P'' arise from the calculation of the intensity and can all be deduced from the diagonal elements.

$$\mathcal{P} = \begin{pmatrix} \frac{(N^2-\vec{M}_\perp^2)}{\sigma_x} & \frac{I_{nz}}{\sigma_x} & \frac{I_{ny}}{\sigma_x} \\ \frac{-I_{nz}}{\sigma_y} & \frac{(N^2-\vec{M}_\perp^2+R_{yy})}{\sigma_y} & \frac{R_{yz}}{\sigma_y} \\ \frac{-I_{ny}}{\sigma_z} & \frac{R_{zy}}{\sigma_z} & \frac{(N^2-\vec{M}_\perp^2+R_{zz})}{\sigma_z} \end{pmatrix} \quad P'' = \begin{pmatrix} \frac{-I_{yz}}{\sigma} \\ \frac{R_{ny}}{\sigma} \\ \frac{R_{nz}}{\sigma} \end{pmatrix}$$

$$\begin{aligned} \sigma_x &= \vec{M}_\perp^2 + N^2 + P_x I_{yz} \\ \sigma_y &= \vec{M}_\perp^2 + N^2 + P_y R_{ny} \\ \sigma_z &= \vec{M}_\perp^2 + N^2 + P_z R_{nz} \\ \sigma &= \vec{M}_\perp^2 + N^2 + P_x I_{yz} + P_y R_{ny} + P_z R_{nz} \end{aligned}$$

$$\begin{aligned} N^2 &= NN^* & \vec{M}^2 &= \vec{M}\vec{M}^* \\ R_{ij} &= 2\Re(M_{\perp i}M_{\perp i}^*) & R_{ni} &= 2\Re(NM_{\perp i}^*) \\ I_{ij} &= 2\Im(M_{\perp i}M_{\perp i}^*) & I_{ni} &= 2\Im(NM_{\perp i}^*) \end{aligned}$$

References

[1] Squires G L, *Introduction to the Theory of Thermal Neutron Scattering*, Cambridge Universtiy Press, (1978), Reprinted by Dover Publications, New York, (1996)

[2] Lovesey S W, *Theory of Neutron Scattering from Condensed Matter* vol. 2, Oxford Universtiy Press, Oxford (1984) Reprinted 2003

[3] Balcar E & Lovesey S W, *Theory of Magnetic and Neutron and Photon Scattering*, Oxford Universtiy Press, Oxford (1989)

[4] Bacon G E, *Neutron Diffraction*, Clarendon Press, Oxford, (1975)

[5] Atkins P W & Friedman R S *Molecular Quantum Mechanics, third edition*, Oxford Universtiy Press, Oxford (1997) Reprinted 2003.

[6] Halpern O, Johnson M H *Physical Review*, **55**, 898, (1939)

[7] Ziman J M *Models of Disorder: The theoretical physics of homogeneously disordered systems*, Cambridge Universtiy Press, (1979)

[8] Fennell T *et al*, Magnetic Coulomb Phase in the Spin Ice $Ho_2Ti_2O_7$, *Science*, **415**, 326 (2009)

[9] Bragg W L *Proc. Roy. Soc. A* **89**, 248 (1913)

[10] Bragg W L *Proc. Roy. Soc. A* **89**, 468 (1914)

[11] Friedrich W, Knipping P, and Laue M, *Münch. Ber.*, (1912)

[12] Hammond C *The Basics of Crystallography and Diffraction*, 2nd edition, Oxford Universtiy Press, Oxford (2001)

[13] Ewald P P *PhD Dissertation*, *Ludwig Maximillian University of Munich* (1912)

[14] Busing W R & Levy H A *Acta Crystallographa*, **22**, 45, (1967)

[15] Editor E. Prince *International Tables of Crystallography Volume C: Mathematical, Physical and Chemical Tables, Section 6.1.2.4* Kluwer Academic Publishers, London, (2004)

[16] Editor E. Prince *International Tables of Crystallography Volume C: Mathematical, Physical and Chemical Tables, Section 4.4.5* Kluwer Academic Publishers, London, (2004)

[17] Izyumov Y. and Maleev S., *Soviet Phys. - JETP* **14** 1668 (1962)

[18] Blume M *Phys. Rev.* **130** 1670 (1963)

[19] Blume M., *Phys. Rev.* **133** A1366 (1963)

[20] Halpern O and Johnson M *Phys. Rev.* **55** 898 (1939)

[21] Tasset F, *Physica B* **156** 627 (1989)

[22] Nunez V, Brown P J, Chattopadhyay T, Forsyth J B and Tasset F *Physica B* **180** 903 (1992)

[23] Brown P J, Forsyth J B and Tasset F *Proc. R. Soc. Lond. A* 147 (1993)

[24] Tasset F, *J. Mag. Mag. Mat.* **129** 47 (1994)

[25] Tasset F, Lelièvre-Berna E, Roberts T, Bourgeat-Lami E, Pujol S, Thomas M *Physica B* **241** 177 (1998)

[26] Tasset F, Brown P J, Lelièvre-Berna E, Roberts T, Pujol S, Allibon J, Bourgeat-Lami E, *Physica B* **267** 69 (1999)

[27] Lelièvre-Berna E, Bourgeat-Lami E, Fouilloux P, *et al Physica B* **356** 131 (2005)

[28] Regnault L, Geffray B, Fouilloux P *et al Physica B* **350** e811 (2004)

[29] Takeda M, Nakamura M, Kakurai K, Lelièvre-Berna E, Tasset F, Regnault L-P *Physica B* **356** 136 (2005)

[30] Janoschek M, Klimko S, Gähler R, Roessli B, Böni P *Physica B* **397** 125 (2007)

[31] Lelivre-Berna E, Brown P, Tasset F, Kakurai K, Takeda M, Regnault L *Physica B* **397** 120 (2007)

[32] Tasset F *Physica B* **297** (2001)

[33] Lelivre-Berna E, Brown P, Tasset F, Kakurai K, Takeda M, Regnault L *Physica B* **397** 120 (2007)

[34] Moon R, Riste T, Koehler W *Phys. Rev.* **181** 920 (1969)

[35] McMaster W H, *Rev. Mod. Phys.* **33** 8 (1961)

CHAPTER 3

Symmetry

This chapter will introduce the concepts of group theory required to determine the magnetic structures discussed in this thesis, with reference to examples. Initially, point group symmetry will be described, with respect to the basis, and this will be developed to discuss space group symmetry and the lattice. These symmetry concepts will then be extended to consider the reciprocal lattice, [**1**], the first Brillouin Zone, [**2**], and the propagation vectors, [**3**], that lie within the zone. Once the concept of the propagation vector has been introduced it will be used to develop representational analysis, [**4**]. In order to understand how these ideas support analysis of magnetic structural data we will touch on the ideas of symmetry breaking and the Landau theory of second order phase transistions, [**5**]. Finally, we will return to application of these ideas by considering the domains that are frequently present in magnetic materials.

3.1. An Ordered Array

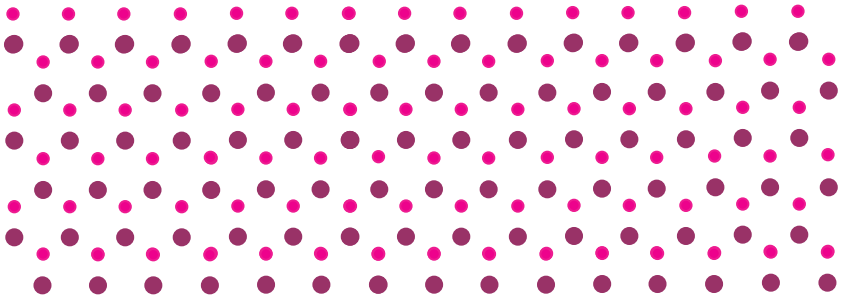

FIGURE 3.1. A two dimentional repeating pattern of dots.

A two dimensional repeating pattern, such as the one in figure, 3.1, can be considered as an array of identical tiles. An ideal crystal can be considered in a similar way, as

an infinite three dimensional pattern that is constructed of discrete units, which are congruent and completely fill the space. The pattern is a convolution of the repeating unit, the basis, and the discrete translations, the lattice, lattice⊗basis. There are an infinite number of different lattice and basis combinations for any repeating pattern and the one chosen depends on the aspect of the pattern that is most important to the observer, [**1, 6**].

3.2. The Basis

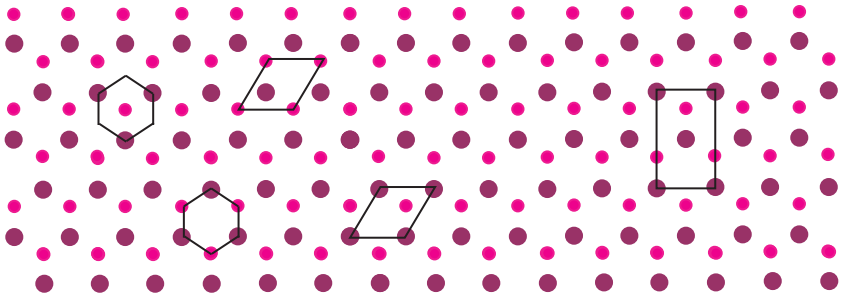

FIGURE 3.2. Examples of different units that can be repeated to generate the two-dimensional pattern of figure 3.1, the bases on the left are primitive as they contain a unique representation of each point in the pattern, the basis on the right is non-primitive as it contains more than one representation of the points in the pattern. The symmetry operations translate the points in the plane of the page as the pattern is two dimensional.

A selection of different bases for the pattern of figure 3.1 are shown in figure 3.2. The four unit cells on the left in figure 3.2 are primitive bases as they are all constructed of the minimum area that contains the information required to tile the pattern completely. All of the four units contain two complete, inequivalent dots and, indeed, any congruent shape that contains the two different dots could be used as a primitive basis, furthermore, the primitive cells contain only one lattice point.

The hexagonal units represent Wigner-Seitz cells and are constructed such that the edges of the cell are equidistant from equivalent points in the pattern. The 24 Voronoi polyhedra are found when this mode of construction is undertaken in three dimensions, [**1**]. The unit cell on the left is non-primitive as it contains more than one of

Operation Type	Symmetry Label	Symmetry Elements
Identity	E	E
Rotation	C_3	C_3^1 C_3^2
Reflection	σ_v	σ_1, σ_2, σ_3

TABLE 3.1. Symmetry elements associated with the C_{3v} point group.

the set of dots from which the pattern is constructed. Many of the bases that are used to describe crystalline structures are non-primitive to simplify the visualisation of the whole pattern.

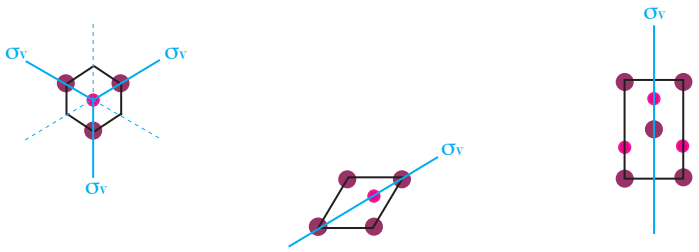

FIGURE 3.3. The symmetry that can be observed in the bases of figure 3.2. The lines represent vertical mirror planes, σ_v, that project from the page. The centre of the Wigner-Seitz cell is a three-fold rotational axis, C_3.

3.2.1. Point Group Symmetry. The symmetry that can be seen in the bases is described by the 32 point groups. This subsection will discuss the symmetry that is observed in this pattern and introduce some general aspects of group theory. The subsection has been written with reference to [**3, 7**]. The section will consider the symmetry that can be seen in the Wigner-Seitz cell of figure 3.2, as the cell reveals most clearly the symmetry of the point group in question.

3.2.1.1. *Symmetry Operations.* A symmetry operation is a manipulation of a pattern or image that leaves it unchanged. In the example of the Wigner-Seitz cell in figure 3.1 there are three types of symmetry operation that will leave the hexagonal unit indistinguishable: the identity operation, E; a rotation, C_3, about the central three-fold axis through either 120°, C_3^1, or 240°, C_3^2; and a reflection (or two-fold rotation followed by an inversion) σ_v, about one of the three mirror planes that intersect the rotational axis, σ_1, σ_2 or σ_3, [**7**]. The six symmetry elements form the

point group C_{3v}, summarised in table 3.1. The operations can be described with rotational matrices, shown in table 3.2 for the basis identified in figure 3.4.a, and the matrices abide by the rules of group theory, [**3, 8**]:

(1) The identity operation, E, is a member of the group.
(2) Every element in the group must have its inverse in the group such that $XX^{-1} = E$.
(3) The group is closed: the product of any two elements is a member of the group; the square of each element is in the group.
(4) The associative law of multiplication holds.

3.2.1.2. *Subgroups and Cosets.* The elements within any group, that contains an element other than the identity, may be decomposed into smaller *subgroups* that also obey all the rules of group theory, [**3**]. In the example of the C_{3v} group there exists five subgroups, summarised in table 3.2, and in general any element A of a group G may be multiplied with itself to form a periodic sequence, or subgroup, that will eventually return a unitary matrix, E,

$$A,\ A^2,\ A^3, \ldots A^{n-1},\ A^n = E. \tag{3.1}$$

The number of times, n, that this multiplication needs to occur before E is returned gives the order of the symmetry element A, [**3**], thus the the C_3 subgroup has order $n = 3$ and the σ_v subgroups have order $n = 2$.

The members of the group, G, that do not belong to the subgroup G_s form the left and right *cosets*, such that multiplication by an element from a coset X from the left

$$XS_2,\ XS_3,\ XS_g \quad \text{or right,} \quad S_2X,\ S_3X,\ S_gX \tag{3.2}$$

return only the other members of the coset and not one of the g members, S_g, of the subgroup, $G_S = E,\ S_2,\ S_3,\ S_g$, [**3**].

Element	Operation Matrices		Subgroup	Class	Character
E	$\begin{pmatrix} 1 & 0 & 0 \\ 0 & 1 & 0 \\ 0 & 0 & 1 \end{pmatrix}$	$\begin{pmatrix} 1 & 0 & 0 \\ 0 & 1 & 0 \\ 0 & 0 & 1 \end{pmatrix}$	E	E	3
C_3^1	$\begin{pmatrix} 0 & 0 & 1 \\ 1 & 0 & 0 \\ 0 & 1 & 0 \end{pmatrix}$	$\begin{pmatrix} 1 & 0 & 0 \\ 0 & -1 & 1 \\ 0 & -1 & 0 \end{pmatrix}$	E, C_3^1, C_3^2	C_3^1, C_3^2	0
C_3^2	$\begin{pmatrix} 0 & 1 & 0 \\ 0 & 0 & 1 \\ 1 & 0 & 0 \end{pmatrix}$	$\begin{pmatrix} 1 & 0 & 0 \\ 0 & 0 & -1 \\ 0 & 1 & -1 \end{pmatrix}$	E, C_3^1, C_3^2	C_3^1, C_3^2	0
σ_1	$\begin{pmatrix} 1 & 0 & 0 \\ 0 & 0 & 1 \\ 0 & 1 & 0 \end{pmatrix}$	$\begin{pmatrix} 1 & 0 & 0 \\ 0 & 1 & -1 \\ 0 & 0 & -1 \end{pmatrix}$	E σ_1	σ_1, σ_2, σ_3	1
σ_2	$\begin{pmatrix} 0 & 0 & 1 \\ 0 & 1 & 0 \\ 1 & 0 & 0 \end{pmatrix}$	$\begin{pmatrix} 1 & 0 & 0 \\ 0 & 0 & 1 \\ 0 & 1 & 0 \end{pmatrix}$	E σ_2	σ_1, σ_2, σ_3	1
σ_3	$\begin{pmatrix} 0 & 1 & 0 \\ 1 & 0 & 0 \\ 0 & 0 & 1 \end{pmatrix}$	$\begin{pmatrix} 1 & 0 & 0 \\ 0 & -1 & 0 \\ 0 & -1 & 1 \end{pmatrix}$	E σ_3	σ_1, σ_2, σ_3	1

TABLE 3.2. The matrix operations, subgroups, classes and characters of the group C_{3v}, where the matrices in the first column are for the basis $\mathbf{a}_1$, $\mathbf{a}_2$, $\mathbf{a}_3$, defined in figure 3.4.a and for those in the second column $\mathbf{a}_1$ oriented with $\mathbf{z}$.

3.2.1.3. *Characters and Classes.* The *character* χ of a symmetry element is the trace of the rotational matrix that describes the symmetry operation and all elements that have the same character belong to the same *class*, [**3**]. It can be seen, in table 3.2, that the C_{3v} group contains three different classes, which correspond to the three types of symmetry operation, E, σ and C.

3.2.1.4. *The irreducible representations and basis vectors.* Each symmetry operation may be represented by a rotational matrix where the matrix operates in the axis system defined by the *basis vectors* and the most simple matrices that describe these operations are the *irreducible representations*. When the basis vectors are in

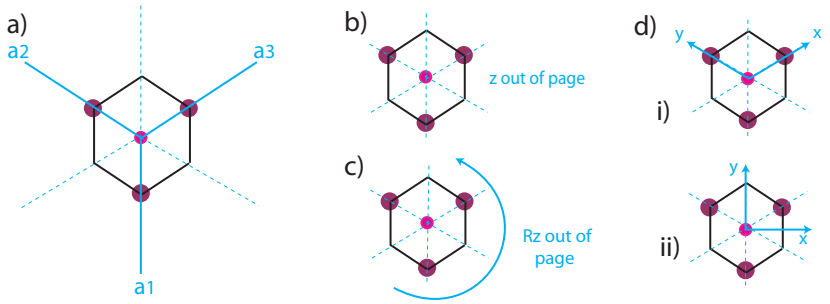

FIGURE 3.4. The different basis vectors that may be chosen to give the irreducible representations of C_{3v}

high symmetry directions the rotational matrices become block diagonal and these block diagonal matrices can be decomposed to give the irreducible representations, again this is illustrated with C_{3v} in the table 3.2. The basis that gives the matrices in the first column includes only vectors in the xy plane, whereas the operations in the second column are found when the $\mathbf{a}_1$ vector is with the 3-fold axis, [**3, 7**].

The redefinition of the basis vectors has produced a block diagonal matrix and this matrix can be decomposed into a one dimensional matrix, which describes the effects of the operations on a polar vector in the z-direction and a two dimensional matrix, that describes the effects of the operations applied to vectors that lie in the xy plane, where any two vectors may be used to define the plane, shown in table 3.3. The basis vectors that are associated with each IR are not unique, but the space that they describe is uniquely defined. The third irreducible representation corresponds to the effect of the operations upon an axial vector in the direction of **z**, [**7**].

3.2.1.5. *The great orthogonality theorem.* The great orthogonality theorem states that each of the, h, inequivalent, irreducible, unitary, matrix representations of a group are orthogonal to one another within the h-dimentional space of the symmetry group. The orthogonality of the IRs is described by the great orthogonality theorem, which allows you to decompose the a reducible representation into its IRs. [**3, 9**]:

$$\sum_R \Gamma^{(i)}(R)^*_{\mu\nu}\Gamma^{(j)}(R)_{\alpha\beta} = \frac{h}{l_i}\delta_{ij}\delta_{\mu\alpha}\delta_{\nu\beta}. \tag{3.3}$$

IR Figure	Γ_1 z (b)	Γ_2 R_z (c)	xy (d.i)	Γ_3 xy (d.ii)
E	(1)	(1)	$\begin{pmatrix} 1 & 0 \\ 0 & 1 \end{pmatrix}$	$\begin{pmatrix} 1 & 0 \\ 0 & 1 \end{pmatrix}$
χ	1	1	2	2
C_3^1	(1)	(1)	$\begin{pmatrix} -1 & 1 \\ -1 & 0 \end{pmatrix}$	$\begin{pmatrix} \frac{-1}{2} & \frac{\sqrt{3}}{2} \\ \frac{-\sqrt{3}}{2} & \frac{-1}{2} \end{pmatrix}$
C_3^2	(1)	(1)	$\begin{pmatrix} 0 & -1 \\ 1 & -1 \end{pmatrix}$	$\begin{pmatrix} \frac{-1}{2} & \frac{-\sqrt{3}}{2} \\ \frac{\sqrt{3}}{2} & \frac{-1}{2} \end{pmatrix}$
χ	1	1	-1	-1
σ_1	(1)	(-1)	$\begin{pmatrix} 1 & -1 \\ 0 & -1 \end{pmatrix}$	$\begin{pmatrix} -1 & 0 \\ 0 & 1 \end{pmatrix}$
σ_2	(1)	(-1)	$\begin{pmatrix} 0 & 1 \\ 1 & 0 \end{pmatrix}$	$\begin{pmatrix} \frac{1}{2} & \frac{-\sqrt{3}}{2} \\ \frac{-\sqrt{3}}{2} & \frac{-1}{2} \end{pmatrix}$
σ_3	(1)	(-1)	$\begin{pmatrix} -1 & 0 \\ -1 & 1 \end{pmatrix}$	$\begin{pmatrix} \frac{1}{2} & \frac{\sqrt{3}}{2} \\ \frac{\sqrt{3}}{2} & \frac{-1}{2} \end{pmatrix}$
χ	1	-1	0	0

TABLE 3.3. The operation matrices that correspond to the IRs of C_{3v}. It can be seen that the matrices are not unique but the trace of the matrices is equivalent for elements in the same class. The figure that is listed corresponds to the representation of the axis given in 3.4

Where, the summation is over all of the R symmetry elements A_1 to A_h, l_i is the dimensionality of the IR $\Gamma^{(i)}$. Each of the vectors that defines this space is labeled with three indices, the IR, i, (j) and the row and column terms of the matrices $\mu\,\nu$ ($\alpha\,\beta$). The number of orthogonal vectors h can be shown from this relation to give the dimensionality theorem, $\sum_i l_i^2 = h$, [**3**], which allows one to state the minimum number of basis vectors required for a point group. In our example $h = 6$ and we have seen that there are 3 IRs: two with dimension one and one with two dimensions. Since $2^2 + 1^2 + 1^2 = 6$ the dimensionality theorem tells us that we have found all of the IRs associated with the C_{3v} point group, [**3**]. The number of different IRs is equal to the number of classes in the group and the dimensionality l_i of each IR is equivalent to the number of elements that belong to that class.

Class	Edges	Angles
Triclinic	$\lvert a\rvert \neq \lvert b\rvert \neq \lvert c\rvert$	$\alpha \neq \beta \neq \gamma$
Monoclinic	$\lvert a\rvert \neq \lvert b\rvert \neq \lvert c\rvert$	$\alpha = \beta = 90° \neq \gamma$
Orthorhombic	$\lvert a\rvert \neq \lvert b\rvert \neq \lvert c\rvert$	$\alpha = \beta = \gamma = 90°$
Tetragonal	$\lvert a\rvert = \lvert b\rvert \neq \lvert c\rvert$	$\alpha = \beta = \gamma = 90°$
Cubic	$\lvert a\rvert = \lvert b\rvert = \lvert c\rvert$	$\alpha = \beta = \gamma = 90°$
Hexagonal	$\lvert a\rvert = \lvert b\rvert \neq \lvert c\rvert$	$\alpha = \beta = 90°, \gamma = 120°$
Rhombohedral	$\lvert a\rvert = \lvert b\rvert = \lvert c\rvert$	$\alpha = \beta = \gamma \neq 90°$

TABLE 3.4. The seven crystal systems.

3.3. The Lattice

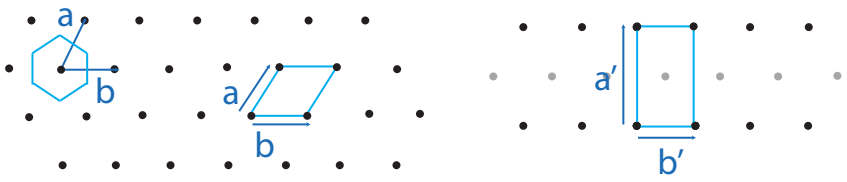

FIGURE 3.5. The lattices associated with each of the previously defined unit cells, the points in black indicate the lattice that is associated with the cell and those in grey indicate those that exist within the crytal.

The lattice describes the translational symmetry of the pattern that is shown in figure 3.1, with the different lattices that are associated with each of the cells shown in figure 3.5. The translational properties of a three-dimensional lattice, with lattice parameters **a**, **b** and **c**, are described by,

$$\boldsymbol{\tau} = x\mathbf{a} + y\mathbf{b} + z\mathbf{c}. \tag{3.4}$$

The relation gives the definition of the three dimensional repeating unit in crystallography, in which the edges are described by by a, b and c and the internal angles are α, β and γ. The most general description defines the triclinic unit cell, where $a \neq b \neq c$ and $\alpha \neq \beta \neq \gamma$ and none of the angles are equal to either 90° or 120°. The six special crystal classes describe the less general cells and are shown, with the triclinic cell in table 3.4.

3.3.1. The Bravais Lattices. When the crystal classes are combined with the types of cell, primitive, P, body centred, I and face centred, F or C, (this depends on whether the point is in all of the faces, F, or just those that are normal to the c axis, C) the fourteen Bravais lattices are produced, [**8, 10**]. A rigorous definition of the concept of the Bravais cell is given in reference [**8**], which gives the following rules for the selection of a particular crystal system:

(1) The form of the Bravais cell of a crystal must have one of the seven point groups of symmetry: $\bar{1}$, $2/m$, mmm, $\bar{3}m$, $4/mmm$, $6/mmm$, or $m3m$, depending the combination of symmetry operations that describe the crystal. As such the Bravais cell must correspond to the symmetry of the crystal.

(2) When the first requirement is satisfied, the number of right angles within a cell must be maximal.

(3) When the first two conditions are satisfied, the volume of the cell must be minimal.

The first requirement can prevent the primitive unit from representing the lattice.

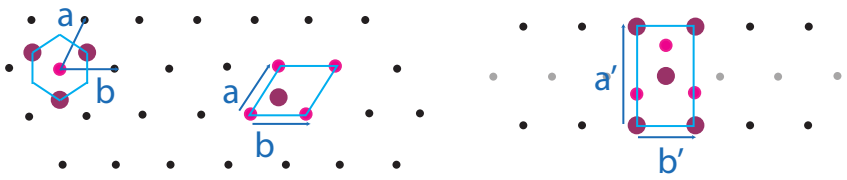

FIGURE 3.6. The combination of the bases and the lattices associated with each of the previously defined unit cells.

3.3.2. The Space Groups. The 230 space groups are generated from the combination of the rotations of the 32 point groups and the translations of the 14 Bravais lattices and are tabulated in the international tables, [**11**]. The symmetry operations that describe the symmetry elements of the space groups can be described with the

systematic notation of Wigner and Seitz, which are a combination of a rotation matrix, R, and a translational element, $\boldsymbol{\tau}$,

$$\{R|\boldsymbol{\tau}\}\mathbf{x} = R\mathbf{x} + \boldsymbol{\tau} = \mathbf{x}'. \tag{3.5}$$

where $\mathbf{x}$ and $\mathbf{x}'$ are 3 coordinate position vectors. The combination of the translational elements with the operations of the point groups give rise to glide planes (reflection translations) and screw axes (rotation translations). The elements of a space group abide by the group rules that were defined in the subsection 3.2.1 and, as such, IRs, subgroups and classes may be found for the space groups, [**12**]. Representational analysis finds the rotational symmetry of a periodic feature, such as the magnetic order, and then uses the Bloch wave formalism to describe the translational symmetry of that feature, [**4, 14, 15**], let us reconsider the Bloch wave from the perspective of its translational symmetry.

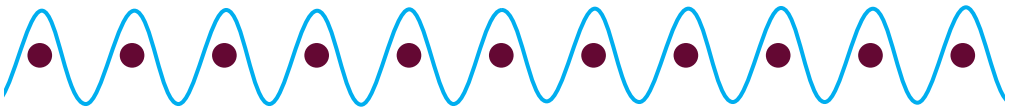

FIGURE 3.7. An image of a wave that is superposed onto the lattice, the top trace has the periodicity of the lattice and the lower trace has periodicity of twice the lattice.

3.3.3. The Symmetry of the Bloch wave. Bloch waves describe the periodic change of a property of a crystalline material and has been described, with reference to magnetism in section 1.3.2, and the Bloch wave formalism inherently represents the translational symmetry of the lattice and the periodicity of a Hamiltonian, [**13, 3**]. If a Hamiltonian has a periodicity it can be described by a cyclic set of symmetry operations, such as the group of rotations in subsection, 3.2.1, then the order of the group, h, corresponds to the periodic boundary conditions of the Hamiltonian. All eigenfunctions of this Hamiltonian must transform according to a representation, p, that belongs to the group and so solutions for the p^{th} representation, in the one

dimensional case, must have the property, [**3**],

$$\psi_p(x+a) = P_A\psi_v(x) = \Gamma^{(p)}(A)\psi_p(x) = e^{2\pi ip/h}\psi_p(x), \tag{3.6}$$

where A is a displacement of one period in the coordinates of a so that the at the displaced point P_A the wave $P_A\psi_v(x)$ is equivalent to the original wave $\psi_p(x+a)$, figure 3.7. The total wavelength is $L = ah$ and as such the above may be written,

$$\psi_p(x+a) = e^{2\pi ipa/L}\psi_p(x) = e^{2\pi ika}\psi_p(x) \tag{3.7}$$

In this one dimensional representation $k = 2\pi p/L$ and contains the information about the periodicity and has reciprocal length units. As the quantity k is directly related to the representation p the relation may be relabeled as $e^{2\pi ika}\psi_p(x)$ and this gives the Bloch theorem,

$$\psi_k(x) = u_k(x)e^{ikx}, \tag{3.8}$$

where $u_k(x)$ is periodic with period a. In a three-dimentional system the equation that describes this periodicity is

$$\psi_{\mathbf{k}}(\mathbf{r}+\boldsymbol{\tau}) = e^{i\mathbf{k}\cdot\boldsymbol{\tau}}\psi_{\mathbf{k}}(\mathbf{r}) \tag{3.9}$$

where $\mathbf{k}$ is the wave vector and $\boldsymbol{\tau}$ is the is a vector of integers that would give rise to a translation that leaves the crystal invariant. Let us now consider the reciprocal lattice formalism, within which $\mathbf{k}$ is described, [**10**].

3.4. The Reciprocal Lattice

The reciprocal lattice describes the diffraction patterns that are observed during scattering experiments and are the Fourier transform of the direct lattice, figure 3.8. The mechanism by which this happens is described in the neutron scattering chapter, chapter 2, here we will describe the mathematics.

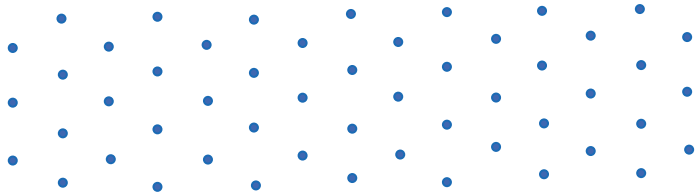

FIGURE 3.8. The reciprocal of the pattern of figure 3.1

The vectors of the reciprocal lattice, $\mathbf{n} = (\mathbf{a}^*, \mathbf{b}^*, \mathbf{c}^*)$, are normal to the planes of the direct lattice and the inverse of the length of the direct lattice vectors, $\mathbf{m} = (\mathbf{a}, \mathbf{b}, \mathbf{c})$,

$$\mathbf{m} \cdot \mathbf{n} = \delta_{\mathbf{m},\mathbf{n}} \tag{3.10}$$

where $\delta = 1$ when $\mathbf{m}$=$\mathbf{n}$ and $\delta = 0$ otherwise, figure 3.9, [**1**]. The definition of the reciprocal lattice points, which satisfies the above relation and ensures that the vectors are orthogonal is given by:

$$\mathbf{a}^* = \frac{\mathbf{b} \times \mathbf{c}}{V}, \quad \mathbf{b}^* = \frac{\mathbf{c} \times \mathbf{a}}{V}, \quad \mathbf{c}^* = \frac{\mathbf{a} \times \mathbf{b}}{V} \tag{3.11}$$

where, V is the volume of the unit cell. In order not to over generate the number of points in the reciprocal lattice the primitive unit cell must be used for the above equations. Space groups that are not based on a primitive unit cell, the F, C and I groups, lead to systematic absences in the diffraction pattern, which are listed in the International Tables, [**11**] and shown in grey in figure 3.9. The figure 3.9 also shows the different unit cells that are present in the reciprocal lattice, which correspond to the cells of the direct lattice shown in figure 3.6. The Wigner-Seitz cell, when defined with respect to the reciprocal lattice is termed the first Brillouin zone and it is within this zone that the unique, minimum values of the propagation vector $\mathbf{k}$ are found, [**3, 2**].

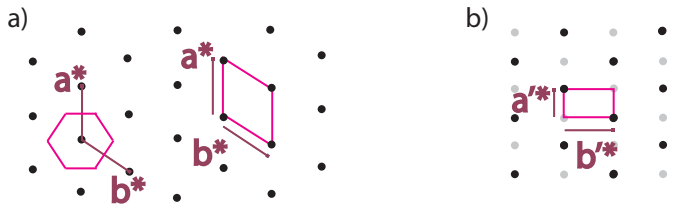

FIGURE 3.9. The lattices that would be observed in the diffraction data for primitive and non-primitive bases. Where the hexagonal primitive unit is equivalent to the first Brillouin zone.

3.4.1. The Brillouin Zone. The Wigner-Seitz cell in the reciprocal lattice gives the first Brillouin zone and it is used to describe the electronic structure, from which band theory arises, or the magnetic structure, which underpins representational analysis [**2, 4, 14**]. We will consider the symmetry of the **k** vector within this region.

The propagation vector **k**, describes the periodicity of a feature with respect to the translational symmetry of the lattice, described in the subsection about Bloch waves, 3.3.3. The wave vector **k**, falls within the first Brillouin zone of the reciprocal lattice as any position outside the first Brillouin zone may be related to one within the zone by an integer translation, **n**,

$$\psi_{\mathbf{k}}(\mathbf{r}+\boldsymbol{\tau}) = e^{i(\mathbf{k}+\mathbf{n})\cdot\boldsymbol{\tau}}\psi_{\mathbf{k}}(\mathbf{r}) \tag{3.12}$$

$$= e^{i\mathbf{k}\cdot\boldsymbol{\tau}}e^{i\mathbf{n}\cdot\boldsymbol{\tau}}\psi_{\mathbf{k}}(\mathbf{r}) \tag{3.13}$$

$$= e^{i\mathbf{k}\cdot\boldsymbol{\tau}}\psi_{\mathbf{k}}(\mathbf{r}) \tag{3.14}$$

3.4.2. The star of k. The star of **k**, $\{\mathbf{k}\}$, are the directions in which the propagation vector may propagate, that are energetically equivalent but distinguishable due to the discrete rotational symmetry of the lattice. In the case of C_{3v} a reciprocal vector **k**=z, or **k**=(0, 0, 0) remains unchanged under all operations of the group. Therefore, subgroup $G_{\mathbf{k}}$ contains all the elements of the group C_{3v} and $\{\mathbf{k}\}$ would

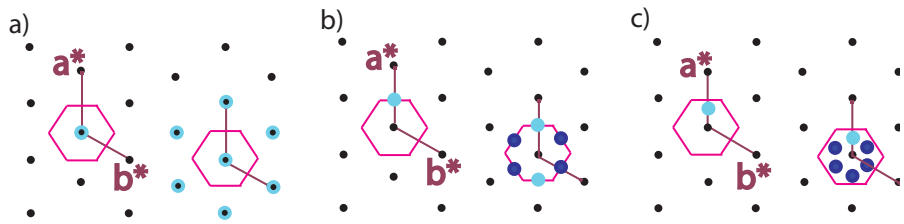

FIGURE 3.10. Examples of the observed diffraction patterns possible for the stars of the wave vector **k** in the C_{3v} example and in agreement with the rotational matrices of table 3.3. a) **k**=(0, 0, 0) left unchanged by all rotational operations and all scattering may be related by translational operations. b) When **k**=(1/2, 0, 0) the observed point lies on the zone boundary, the vector **k**=(-1/2, 0, 0) is related to the original point by a translation, indicated in blue, the rotationally related points are shown in purple and are generated by the other arms of the star. c) General point **k**=(a, 0, 0) gives six distinct, rotationally related **k** vectors.

consist only of the original vector **k**. Figure 3.10.a shows the magnetic scattering that would be observed for the case **k**=(0, 0, 0). The points are all related by integer lattice translations and as such no rotational symmetry operations are required to generate the different points.

A vector that is in the direction of x, that falls on the zone boundary, **k**=(1/2, 0, 0), figure 3.10.b, would be left unchanged only by the mirror plane σ_x and the identity E and hence the group $G_{\mathbf{k}}$ would contain two elements. The other four symmetry elements will generate either a vector in the direction of y or $-x-y$. The star of **k** has three arms, $L = 3$, where L is the number of arms, $\mathbf{k}_1$=**x**, $\mathbf{k}_2$= **y** and $\mathbf{k}_3$= **-x-y** and each arm has an associated little group $G_{\mathbf{k}_L}$ that contains two symmetry operations.

The figure 3.10.c shows an arbitrary position where all of the generated points are related by the rotations of G and not by translation. The six points are related by rotation, rather than translation and hence the star of **k** has six arms.

Overall, different arms of the star are generated by either a reflection or a rotation, and these two operations form a coset, g. The elements that generate $\mathbf{k}_L$ do not

contribute to the group $G_{\mathbf{k_L}}$ and, therefore G may be represented as consisting as a sum over the cosets g_L that generate the arms of the star $\{\mathbf{k}\}$, [**8**],

$$G_0 = G_{\mathbf{k}} + g_2 G_{\mathbf{k}} + ... = \sum_{L=1}^{l_k} g_L G_{\mathbf{k}}. \tag{3.15}$$

As the subgroup $G_{\mathbf{k}}$ abides by all of the rules of group theory it may also be broken down further into a set irreducible representations, Γ. Again there is associated with each IR a set of basis vectors, ψ, that define the axis system of the representation and in this instance these basis vectors will define the eigenspace of the modulated feature with propagation vector $\mathbf{k}$.

3.4.3. The Group $G_{\mathbf{k}}$. The little group $G_{\mathbf{k}}$ is the group of elements that leave $\mathbf{k}$ invariant when the star of $\mathbf{k}$, $\{\mathbf{k}\}$, is generated and $G_{\mathbf{k}}$ is a subgroup of G_0, the point group associated with the space group G, [**3, 9, 8**].

Consider the wave vector $\mathbf{k}$, described with respect to the reciprocal lattice, the directions of propagation that are equivalent, $\mathbf{k}'$, to the direction $\mathbf{k}$, can be found by applying the point group operations, R,

$$P_R \psi_{\mathbf{k}}(\mathbf{r}) = P_R u_{\mathbf{k}}(\mathbf{r}) e^{i\mathbf{k}\cdot\mathbf{r}} \tag{3.16}$$

$$= u_{\mathbf{k}}(\mathbf{R}^{-1}\mathbf{r}) e^{i\mathbf{k}\cdot\mathbf{R}^{-1}\mathbf{r}} \tag{3.17}$$

When the same orthogonal transformation is applied to both vectors in a scalar product the value of the product does not change and as such,

$$\mathbf{k}\cdot\mathbf{R}^{-1}\mathbf{r} = \mathbf{R}\mathbf{k}\cdot\mathbf{R}\mathbf{R}^{-1}\mathbf{r} = \mathbf{R}\mathbf{k}\cdot\mathbf{r}, \tag{3.18}$$

which gives,

$$P_R\psi_{\mathbf{k}}(\mathbf{r}) = u_{\mathbf{k}}(\mathbf{R}^{-1}\mathbf{r})e^{i\mathbf{Rk}\cdot\mathbf{r}}. \tag{3.19}$$

Thus it can be seen that the operation gives an eigenfunction that is still in Bloch form, but the direction has been rotated to the different, energetically equivalent direction **Rk**. The rotationally related vectors $\mathbf{k}'$ that are found from the operations of the point group generate cosets, termed the arms of the star of **k**, and are the degenerate directions of propagation for **k**, [**8, 3, 9**].

3.5. Representational Analysis

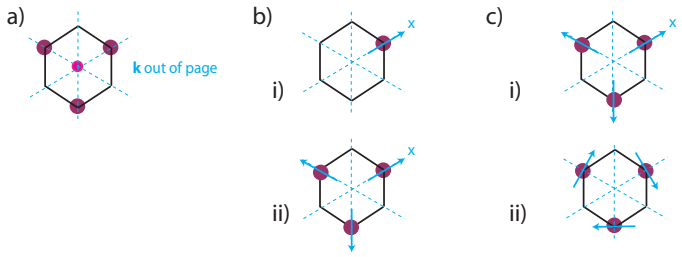

FIGURE 3.11. A representation of the process of the permutation rotation operation.

a) The propagation vector **k** is out of the page and the lines of mirror symmetry are indicated with dashed lines.

b) i. An atom and a vector is placed on a site ii. The atom and vector are permuted to generate the other, symmetry related atomic sites.

c) i. The second step is to rotate the generated set of vectors, which are shown again here. ii. The final set of vectors that are generated after the rotation step

Representational analysis was introduced by Bertaut to allow the description of all types of magnetic structures, including those that are incommensurate with the crystallographic unit cell, [**4, 14**]. The technique applies the operations of the little group $G_{\mathbf{k}}$ to a magnetic site to generate the equivalent atoms and then rotates the vectors on the generated atoms. The process is equivalent to that used to find the normal modes in molecular spectroscopy. The key difference arises when we consider the

infinite lattice for which any modulation of the structure needs to be described with a Bloch wave.

The first step of the process is the permutation Γ_{perm}, shown in figure 3.11.b, where the figure 3.11.b.i is the initial atom and the figure 3.11.b.ii shows the equivalent atoms that have been generated, to produce the orbit. The second step is to rotate the vectors on the atoms that have been produced to give the basis that is associated with each of the atom sites. The process is shown schematically in figure 3.11.c where the result of the first step is shown in 3.11.c.i and the final set of rotated axes is shown in 3.11.c.ii.

The process is described and demonstrated more fully in the paper of Bertaut, [**4, 14**], from which the mathematics that describes this process has been taken. The permutation rotation operation is given by the projection operator, which is said to project the basis vectors from the IRs,

$$a^{(v)} = g^{-1} \sum_{Cg} \chi^{\Gamma}(C_g)\chi^{(v)*}(C_g) \tag{3.20}$$

$$\Psi_{ij}^{(v)} = \sum_{Cg} D_{ij}^{(v)}(C_g) \cdot C_g\Psi. \tag{3.21}$$

where C_g is a symmetry operation of the space group G and $D^{(v)}(C_g)$ is the matrix representative of C_g, with matrix elements ij, in the representation $\Gamma^{(v)}$ and g is the number of symmetry elements in the group. Ψ are the spin components, whose linear combinations Ψ_{ij} for the basis of the irreducible representations.

The orientation of the moment in a real material is described by a sum over all basis vectors $\boldsymbol{\psi}$ that are associated with the IRs of the group, $\mathrm{G}_{\mathbf{k}}$. The basis that one uses to describe a magnetic structure may be either real or imaginary, where the imaginary part describes the phase relationship between the different atomic sites,

[**16**]. The direction of field local to an atom may be described by

$$\boldsymbol{\Psi}_d = \sum_i c_{id}\boldsymbol{\psi}_{id}, \tag{3.22}$$

where, c_{id}, is a weighting coefficient, $\boldsymbol{\psi}_{id}$, is the i^{th} basis vector of atom d and the sum returns a unit vector, $\boldsymbol{\Psi}_d$. The vector is summed over all d atoms in the unit cell and multiplied by the magnitude of the moment on each atom to give the overall magnetisation within the unit cell, the mathematical description of this is given in Appendix A.

The number of basis vectors that are included in this sum may be limited by the Landau theory of second order phase transitions.

3.6. Landau Theory

The phase transitions that a material undergoes may involve no change in symmetry, such as liquid gas transition; an abrupt change where there is no commonality between the symmetry of the initial phase and the final phase, such as the liquid-crystalline solid transition; or a gradual change in the properties such that a single phase is constantly present, [**5**]. The third type of transition is second order and there is a continuous change of one symmetry element. The continuous change is caused by one element becoming critical at the transition temperature. In the case of magnetic ordering the criticality manifests itself as correlations or fluctuations between the magnetic moments on all length scales. Landau theory of second order transitions states that this continuum affects one IR only and as such the order that emerges as the temperature is reduced will be described by one IR, [**17**]. The theory allows the assumption that in the case of second order phase transitions, and often in the case of first order phase transitions, only one IR will be required to describe the new structure and limits the parameters required to determine the final structure.

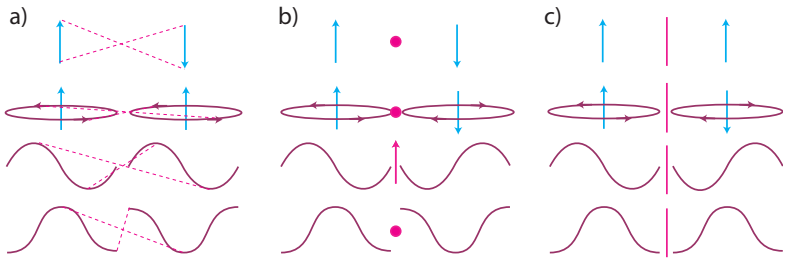

FIGURE 3.12. A comparison between the effects of symmetry operations on axial and polar vectors, sine waves and cosine waves.

a) Indicates the effect of inversion, and it can be seen that the cosine wave and the polar vector are both inverted, whilst the axial vector and the sine wave are left unchanged.

b) Indicates the effect of a rotation, where the points are rotational axes that are out of the plane of the page. When the sine wave lies in the plane of the loop it can be seen to transform as the axial vector.

c) Indicates the effect of a mirror operation, which is a combination of a rotation and an inversion, again it can be seen that the polar vector transforms as the cosine wave and the axial vector as the sine wave.

3.7. Domain Structures

Domain structures arise in all systems and are due to the symmetry breaking that occurs when order arises. In a crystallographic system, for example, the domains are the different crystallites that are formed during the crystallization process. These crystallites are ordered, and break the rotational and translational symmetry of the system, however, all of the crystallites taken together would not break break translational symmetry, as overall there would continue to be no long range order. The size of the crystallites usually depends on the growth rate and strength of the bonding.

Magnetic domains are in many ways equivalent to these crystallites, though when magnetic order occurs time inversion symmetry is broken rather than a spatial symmetry operation, [**5**, **18**] as magnetic moments are axial vectors and are inverted by the inversion of time rather than space, illustrated in figure 3.12. When the lattice axis system is degenerate the magnetic vectors may order in different but equivalent directions. For example, as in cubic or tetragonal systems, there are three directions

that must be equivalent (**a**, **b**, **c** and **a**, **b**, **a - b** respectively) but are distinguishable by a fixed observer.

The degeneracy manifests in several ways: with respect to the orientation of **k**, [**19**]; with respect to the orientation of the of the moments [**20**]; or with respect to direction of propagation of **k** in instances where +**k**≠- **k**, [**21**].

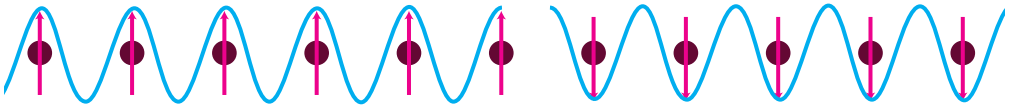

FIGURE 3.13. A simple ferromagnetic structure with two regions that are related by a 180° rotation.

3.7.1. Time inversion domains. When a material orders magnetically time inversion symmetry is broken, as magnetic moments are described by axial vectors and these are inverted by the inversion of time, rather than space. The global symmetry is maintained by the presence of 180° domains, in which the magnetic order in different regions of the crystal are in opposing directions, figure 3.13. Time inversion domains are always present when magnetic ordering occurs and cannot be distinguished by neutron scattering, [**18**].

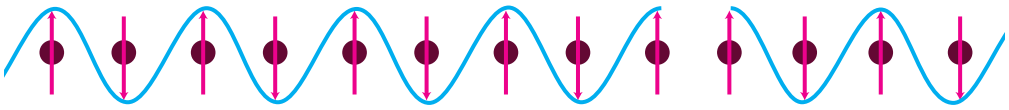

FIGURE 3.14. A simple anti-ferromagnetic structure is indistinguishable either side of local discontinuities.

3.7.2. Translational Domains. Translational domains are equivalent to 180° domains, in that the structure each side of the domain boundary is related by a 180° rotation. In this instance however the rotated structure is equivalent to the original structure when the origin of the lattice is translated and is readily understood with respect to simple anti-ferromagnetic materials as the time reversed structures are equivalent to the original structures if one moves to the next atom, 3.14. In a

diffraction experiment the domains would be indistinguishable, despite the existence of a domain boundary, [**18**].

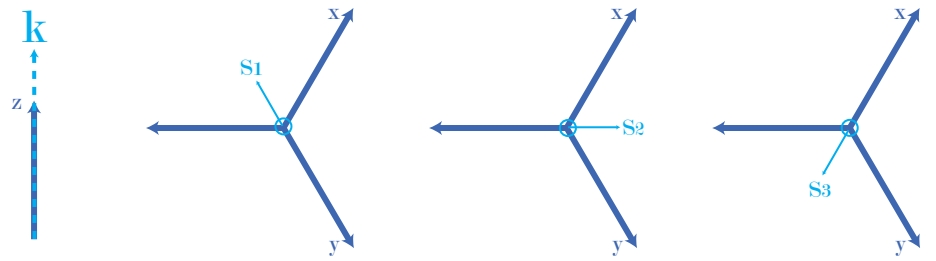

FIGURE 3.15. A schematic of the s-domains and the related spin structures for a crystal structure that is described by C_{3v} symmetry and a magnetic structure that propagates in the direction **k**=**z**

3.7.3. S-domains. S-domains arise when the lattice has degenerate directions, *e.g.*, the cubic and hexagonal lattices, and the moment lies in a direction that cannot be uniquely defined with the IR. In symmetry terms, this can be stated as follows: the subgroup of operations that leave the moment unchanged G_s is less than that of the space group, G.

This is readily illustrated by the C_{3v} point group, when the propagation vector, **k**, is in the direction of **z**, the little group $G_{\mathbf{k}}$ contains the same operations as G_0, figure 3.15. The group $G_{\mathbf{k}}$ can, therefore, be reduced to give the IRs of the C_{3v} group, shown in table 3.3. The IR Γ_1 does not apply to the magnetic moment as it describes a polar vector, the IR Γ_2 gives an axial vector in the direction of z which is left unchanged by the three-fold rotational symmetry, the IR Γ_3 describes a vector that lies in the xy plane and this vector will be changed by the rotation operation, shown in figure 3.15. The rotationally related structures are the S-domains and may be found by applying the crystallographic symmetry operations to a set of basis vectors. S-domains give rise to interference effects and cancellation in neutron diffraction experiments, [**20**].

3.7.4. k-domains. The arms of the star of **k** give rise to the **k**-domains, where the **k** vector may propagate in rotationally related, energetically equivalent, distinguishable crystallographic directions. The **k**-vectors that are shown in figure, 3.16, lie in the high symmetry directions of a Brillouin zone with C_{3v} symmetry. The different **k** are distinguishable in a diffraction pattern when they are not related by integer translations, as they will scatter to different points in reciprocal space, [**19**].

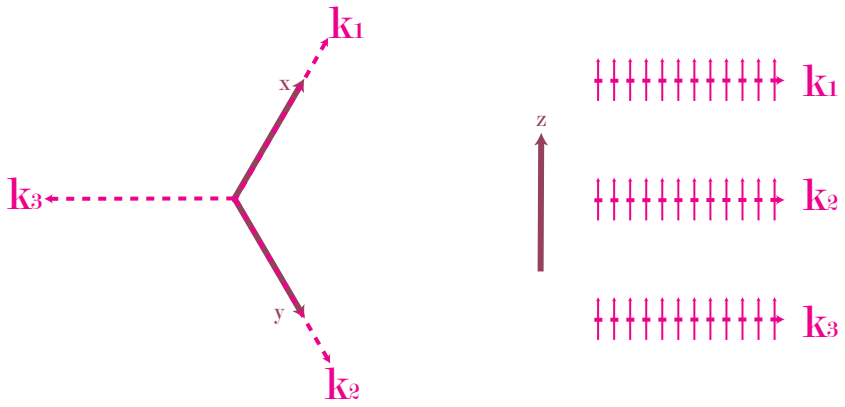

FIGURE 3.16. A schematic of the k-domains and the related spin structures for a crystal structure that is described by C_{3v} symmetry and a magnetic structure that propagates in the direction **k**=**x**.

3.7.5. Chiral-domains. Finally let us consider the degeneracy that is possible when $+\mathbf{k} \neq -\mathbf{k}$, which can be considered as a special type of **k**-domain. In this instance the directions of propagation for the vector **k** are distinguishable and arises in magnetic structures that are described by two orthogonal components with an out of phase relationship, *i.e.*, helical or cycloidal structures, described in the magnetism and frustration chapter, chapter 1.

The image shown, in figure 3.17, is of a cycloidal structure as this is clearer to represent on the page. The effect on the scattering due to the presence of these type of domains depends on the technique that is used to inspect them. When the incident beam is unpolarized the scattering to the points $+\mathbf{k}$ and $-\mathbf{k}$ will always be equivalent, regardless of the relative domain populations. When the beam is polarized and the domains are equally populated the scattering to the points $+\mathbf{k}$ and $-\mathbf{k}$ will again

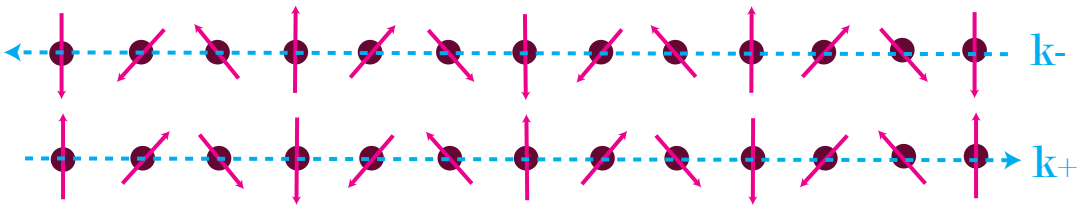

FIGURE 3.17. A schematic of the chiral-domains that arise when $+\mathbf{k} \neq -\mathbf{k}$. The orientation of the moments can be seen to be equal and opposite. These type of domains arise when the magnetic structure is helical or cycloidal as the sine and cosine components of the wave transform differently under rotation.

be equivalent and there will be no change in the intensity of the scattering that is dependent on the term $(-i(\mathbf{M}_{\perp}^{*} \times \mathbf{M}_{\perp}))$. This can be understood with reference figure 3.17, if the scattering that occurs with $\mathbf{Q}$ perpendicular to the direction of propagation, the intensity $+\mathbf{Q}$ would depend on the handedness observed from, say, the topside of both the structures, i.e. both types of handedness would contribute and this would sum to zero, the equivalent would be true in the case of **-Q** and all other scattering would be equal and opposite, [**21**]. In the case that there is only one domain present and the beam is polarised the scattering in the directions $+\mathbf{Q}$ and **-Q** would be different, as the observed handedness would change.

References

[1] Hammond C, *The Basics of Crystallography and Diffraction* Oxford University Press, Second edition, (2006)

[2] Kittel C, *Introduction to Solid State Physics*, 7th ed., John Wiley & Sons, Inc., (1996)

[3] Tinkham M, *Group Theory and Quantum Mechanics* McGraw-Hill, (1964)

[4] Bertaut E F, *Acta Crys.*, **A 24**, 217, (1968)

[5] Chaikin P M and Lubensky, *Principles of condensed matter physics.* , Cambridge University Press, Cambridge, (2007)

[6] Ladd M, *Symmetry And Group Theory In Chemistry*, Horwood Chemical Science Series, (1998)

[7] Ogden J S, *Introduction to Molecular Symmetry*, Oxford University Press, Second edition, (2006)

[8] Izyumov Y A, Naish V E and Ozerov R P, *Neutron diffraction of magnetic materials*, Consultants Bureau, Plenum Publishing Corporation, New York, (1991)

[9] Wigner E P, *Group Theory and its application to the quantum mechanics of atomic spectra*, Academic Press Inc, London, (1964)

[10] Bravais A, *Jounal de l'ecole polytechnique* **19** (1850)

[11] *International tables of Crystallography Volume A: Space-Group Symmetry*, Fifth Edition (2005) Edited by Theo Hahn

[12] Joshua S J, *Symmetry Principles and Magnetic Symmetry in Solid State Physics*, IOP Publishing, (1991)

[13] Bloch F *Zeit, fur Physik*, **52** 555 (1928)

[14] Bertaut E F, *J. Magn. Magn. Mat.*, **24**, 267, (1981)

[15] Kallel A, Boller H, Bertaut E F, *J. Phys. Chem. Solids,* **35** 1139 (1974)

[16] Wills A S, *J. Mater. Chem.* , **15**, 245, (2005)

[17] Landau L D, Lifshitz E M *Electrodynamics of Continuous Media* Pergamon Press, Oxford (1960)

[18] Blundell S, *Magnetism in Condensed Matter*, Oxford University Press, Oxford, (2001)

[19] *Methods of Experimental Physics; v 23, part C: Neutron scattering, Chapter 19. Magnetic Structures* Academic Press, London, (1987)

[20] Nunez V, Brown P J, Chattopadhyay T, Forsyth J B and Tasset F *Physica B* **180**, 903 (1992)

[21] Brown, P J, *Physica B*, **297**, 198, (2001)

CHAPTER 4

Spherical Neutron Polarimetry study of $Er_2Ti_2O_7$

4.1. Introduction

Erbium Titanate, $Er_2Ti_2O_7$, is one of the series of rare earth titanates $R_2Ti_2O_7$ that display a variety of exotic magnetic phenomena, that arise due to the balance of the single ion anisotropy, dipolar and exchange interactions, [**1, 2, 3, 4**]. The weighting and details of these contributions depends on the rare earth ion and gives different types of order or, indeed, prevents long range order from arising at all, [**5, 6, 7, 8, 9, 10**]. $Er_2Ti_2O_7$ is one of the members of the family in which long range order is observed, becoming an XY antiferromagnet at $T_N = 1.173$ K with the moments restricted to the local XY planes, [**3, 11**]. The details of the ordered magnetic structure gives insight to the balance of magnetic interactions and should enable the identification of the correct theoretical model.

This chapter will present the results from a polarimetry experiment that investigated the magnetic structure of $Er_2Ti_2O_7$. The analysis of the data was undertaken with recourse to group theory in order that the correct Hamiltonian could be determined and magnetic domain populations could be fitted. The chapter will begin with a review of the evidence that suggests that $Er_2Ti_2O_7$ orders with an antiferromagnetic XY structure. This will be followed with a discussion of the theories that are consistent with the XY model and the irreducible representations with which the theories correspond. The results of the polarimetry experiment will be presented, with an explanation of the purpose written data analysis routines and a discussion of the findings. The results have been published in reference, [**12**] and the approach to the data analysis was published in reference, [**13**]. A subsequent review of the findings

have revealed that the published result is not correct and the reasons for this will be discussed.

4.2. Experimental Literature Review

The pyrochlore mineral, $NaCaNbTaO_6F$, has the general structure $A_2B_2O_7$, where the larger Na and Ca ions reside on the A site and the smaller Nb and Ta reside on the B site, [**14**]. In 1956 Roth *et al.* determined that the rare earth titanate family of materials, $R_2Ti_2O_7$, have a structure that maps on to that of the pyrochlore, in which the tetravalent rare earth ions R^{3+} are found on the A site and the smaller, quadravalent Ti^{4+} are found in the B sites, [**15**]. The pyrochlore structure is stable when the Ahrens radius of the A atom, r_A, is greater than that of the B atom, r_B, within the range, $1.22< r_A/r_B <1.5$, [**16, 17**]. As the radius ratio $r_{Er^{3+}}/r_{Ti^{4+}} = 1.38$, falls within this range, $Er_2Ti_2O_7$, should order with the pyrochlore structure and, indeed, Knop *et al.* found this result with neutron and x-ray experiments described in reference, [**18**].

4.2.1. Structure and Bonding. The pyrochlore structure, best described by space group $Fd\bar{3}m$, consists of two interpenetrating arrays of corner sharing tetrahedra, which, in the case of $Er_2Ti_2O_7$, correspond to arrays of the Er^{3+} and Ti^{4+} ions, [**18**]. The lattice is face centred cubic, with $a = 10.04$ Å, and contains sixteen Er^{3+} ions on the 16*c* Wyckoff site, with unique position (0, 0, 0). The nearest neighbour of each Er^{3+} is found in the [110] direction, along the edge of the local tetrahedron with separation of 3.562 Å ($a\sqrt{2}/4$), mediated by an Er-O-Er bond with angle 109°, [**18**]. The eight O^{2-} ions that surround each Er^{3+} can be considered as a highly distorted cube, and a distinction can be made between the axial oxygen sites (in the 8*a* Wyckoff position with an Er-O_1 distance of 2.182 Å) and the six sites that form a puckered ring slightly above and below the equatorial plane (48*f* site, Er-O_2=2.471 Å), [**1, 16, 18**].

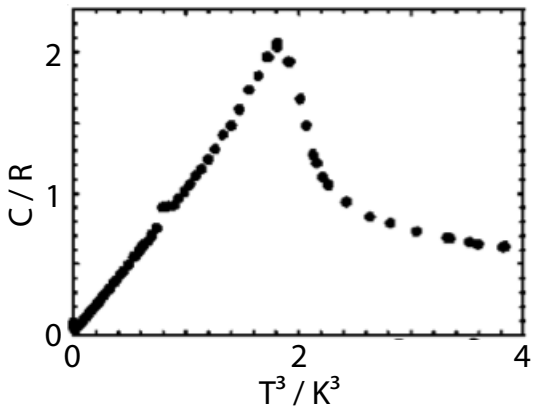

FIGURE 4.1. The heat capacity data collected by Champion *et al.*, for a powder $Er_2Ti_2O_7$ sample, from reference, [**11**]

.

4.2.2. Heat Capacity and Susceptibility. In 1966 Van Geuns made susceptibility measurements on $Er_2Ti_2O_7$ that indicated that the Curie-Weiss temperature of $\theta_{\rm CW} = -22$ K. Subsequently Blöte *et al.* measured the specific heat, which indicated an anomaly at T_N=1.25 K [**19**]. Blöte *et al* suggest that the ground state would correspond to $g_{\|} = 5.5$, *i*.e. an Ising one dimensional order or $g_{\perp} = 3.8$, *i*.e. an XY type two dimensional order, depending on which of the doublets corresponds to the ground state, [**19**]. The calculated entropy change during the transition to long range magnetic order, T_N=1.25K, was found to be ΔS $\approx$ 0.97 Rln 2, close to that of a material that has Kramers doublet ground state, [**19**]. The susceptibility measurements were repeated by Bramwell *et al.* and Dasgupta *et al.* in the temperature range 300 K to 50 K and from the data gave a Curie-Weiss temperature of θ_{CW}=-15.93 K and θ_{CW}=-13 K respectively, [**4, 21**]. Bramwell *et al.* also measured in the lower temperature range 50 K to 20 K and found that this returned θ_{CW}=-22.3 K, in agreement with the value attributed to van Geuns, but argued that the data could not exclude strong antiferromagnetic exchange coupling as proposed by Blöte, [**4**].

4.2.3. Neutron Diffraction and Crystal Field Measurements. To confirm whether the magnetic interactions are dominated by antiferromagnetic exchange or

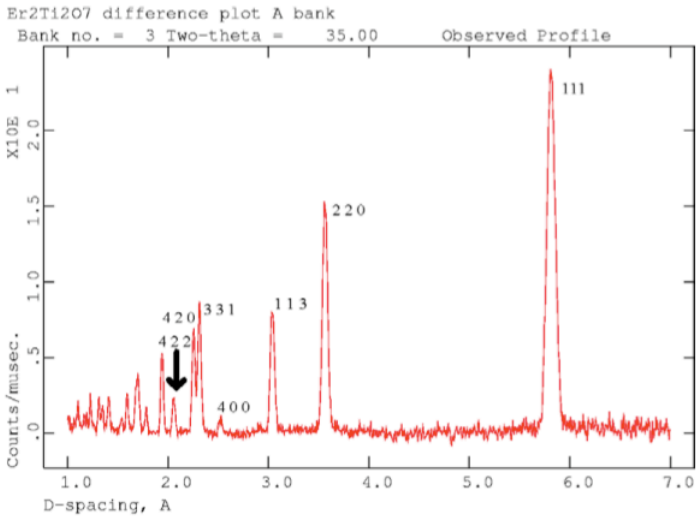

FIGURE 4.2. Magnetic diffraction pattern of $Er_2Ti_2O_7$, obtained by subtracting a high temperature scan (4.85 K) from a low temperature scan (50 mK) measured on Polaris at ISIS. The low multiplicity magnetic Bragg peaks are indexed, after, [**28**]

the crystal field effects and determine whether the magnetic order is best described with a uniaxial Ising model or a local XY model crystal electric field measurements and neutron diffraction experiments were undertaken by Champion *et al.*, [**11**]. The calculation of the crystal field supports the prediction of a single ion Kramers doublet ground state and has a wave function of the form,

$$\psi_0 = -0.5428|-11/2\rangle - 0.2384|-5/2\rangle + 0.5628|1/2\rangle + 0.3876|7/2\rangle - 0.426|13/2\rangle. \quad (4.1)$$

The result corresponds to moments of 3.8 μ_B perpendicular and 0.12 μ_B parallel to the local $\langle 111 \rangle$ axis, indicating that the moments lie in the local XY planes, [**11, 22**]. The lowest lying excited state is separated by 6.41 meV (75 K) from the ground state, much more the 10 cm-1 (14 K) suggested by Blöte *et al.*. The diffraction pattern, shown in figure 4.2, again indicates the XY nature of the structure, due to the presence of the (1, 1, 1) peak, which would be absent if the local anisotropy gave rise to an Ising $\langle 111 \rangle$ antiferromagnet. The refined moment is 3.0 μ_B, in the ordered state, below T_N=1.73 K, in approximate agreement with the crystal field calculations

and the reduction by 0.8 μ_B is attributed to zero-point fluctuations, [**11, 22, 28**]. The Bragg peaks associated with the magnetic scattering were coincident with those from the nuclear scattering, and hence the magnetic structure has propagation vector $\mathbf{k}$={0, 0, 0}, ($\mathbf{k}$=0).

The XY type order is further supported by the polarized neutron study of Mirebeau *et al.*, that measured the magnetic site susceptibility of $Er_2Ti_2O_7$ with respect to temperature, [**23**]. The polarized neutron flipping ratios are visualized as magnetic ellipsoids that surround the magnetic sites, and are analogous to the thermal ellipsoids that can be found from neutron scattering from ordered nuclei. The investigation by Mirebeau *et al.* indicated that at low temperature the XY anisotropy was present, but that the moment is not entirely restricted to the XY plane. Above 100 K the magnetic density distribution is spherical, [**23**]. The investigation by Mirebeau *et al.* agrees with the low temperature observations of Blöte *et al.* and Champion *et al.*, [**19, 11**], which indicate that the ground state is XY like and the high temperature susceptibility measurements by van Geuns, which indicate that the Er^{3+} is Heisenberg like, [**20, 19**].

4.3. Theoretical Literature Review

4.3.1. Original study of an XY pyrochlore. The initial study of the magnetic order that is expected in a classical Heisenberg pyrochlore lattice antiferromagnet with local planar anisotropy was completed in 1994, by Bramwell *et al.*, [**24**]. The spins are restricted to the XY planes associated with the corner sites of a tetrahedron, $\mathbf{S}_1$, $\mathbf{S}_2$, $\mathbf{S}_3$, and $\mathbf{S}_4$, where the numbers correspond to the corner sites shown in figure 4.3. For the system to be antiferromagnetic the sum over the four sites must be zero, $\sum_i \mathbf{S}_i = 0$. The model meets this condition by stating that the antiferromagnetic exchange is between two sets of two spins, $\mathbf{S}_1$-$\mathbf{S}_4$ and $\mathbf{S}_2$-$\mathbf{S}_3$ with the rest of the exchange interactions ignored, this gives the ground state structure found by

Bramwell *et al.*, and shown in 4.3.b. The two sets of spins, $\mathbf{S}_1$-$\mathbf{S}_4$ and $\mathbf{S}_2$-$\mathbf{S}_3$, are allowed to flip independently and the related spin flip structure is shown in figure 4.3.c, the inversion of the moments for each of these structures gives a four-fold degenerate structure and a twelve-fold degenerate ground state, when the rotational symmetry of the tetrahedron is included.

When all of the tetrahedra in the pyrochlore are considered, $\mathbf{S}_1$-$\mathbf{S}_4$ and $\mathbf{S}_2$-$\mathbf{S}_3$ can be thought to form infinite antiferromagnetic rods. In the model the rods are uncorrelated and give rise to a structure described as 'uniaxial nematic' in which the entropy per spin approaches zero in the thermodynamic limit as $N^{-2/3}$ but the spins remain disordered over the tetrahedra, [**24**].

Monte Carlo calculations were used to determine whether the structure could order and a first order transition to a magnetically ordered state at $T/J = 0.06$ was observed, [**24**]. The order was described with wave vector $\mathbf{k}$=0 and it was thought to arise due to thermally induced coupling between the rods, *i*.e. the transition to an ordered state occurs via an order-by-disorder transition.

4.3.2. The Champion state. The Hamiltonian that describes the combination of antiferromagnetic exchange and single ion anisotropy is given by,

$$\mathscr{H} = -\mathsf{J}\sum_{\langle i,j\rangle} \mathbf{S}_i \cdot \mathbf{S}_j - D\sum_{i=1}^{N} (\boldsymbol{\delta}_i \cdot \mathbf{S}_i)^2, \tag{4.2}$$

where the first term describes the antiferromagnetic exchange and the second term describes the single ion anisotropy, [**11, 27**]. The antiferromagnetic condition is satisfied when the sum of the moments over each tetrahedron is zero, so that the first term becomes $\sum_i \mathbf{S}_i = 0$. When the second term is non-zero, $D < 0$, the moment is restricted to the local XY plane, perpendicular to i^{th} $\langle 111\rangle$ axis where the atom site i=1, 2, 3 or 4, is described by δ_i, [**11**]. The study by Champion *et al.*. determined that three additional ground states would satisfy the Hamiltonian, shown in figure

4.3.c, d and e, to give four possible ground states, I to IV, [**28**]. State I is the starting point of the Bramwell model, and state II is generated, within this model, when the spins on site 2 and 3 are flipped, , [**24**]. States II and III are related by a rotation of 90° is applied to each of the sites, about the local ⟨111⟩ axes. State IV is disordered and there is no simple relationship between this state and the other states found.

To determine which of the states, I to IV, best describe the ground state of an ideal XY antiferromagnetic pyrochlore single-spin flip Monte Carlo simulations were performed , [**11, 27, 28**]. The most favourable ground state was found to be described by the eigenvectors of state III, which allows access to zero frequency modes over the planes perpendicular to **a** and **c - b**, in the Brillouin zone, where the axes are that of the primitive rhombohedral unit cell, [**27**]. The other ground states that were investigated gave rise to microscopic number of zero modes at specific points within the plane, and are less favoured by the order-by-disorder mechanism, [**27, 28**]. The model indicates that the transition to the long range ordered ground state is first order and does not capture the behaviour of the specific heat, [**11, 27**].

4.3.3. Exchange and Dipolar Interactions. The classical Heisenberg pyrochlore with antiferromagnetic exchange and dipolar interactions was studied by Palmer and Chalker, [**29**], where the internal energy is described by,

$$U_{int} = \frac{\mathsf{J}_{ex}}{2} \sum_{i \neq j} \mathbf{S}_i \cdot \mathbf{S}_j + \frac{\mathsf{J}_{dd}}{2} \sum i \neq j [\mathbf{S}_i \cdot \mathbf{S}_j - 3(\mathbf{S} \cdot \hat{\mathbf{r}}_{ij})(\mathbf{S} \cdot \hat{\mathbf{r}}_{ij})] \tag{4.3}$$

This combination of interactions gave rise to a structure that agrees with state I of the four XY states, though there is no requirement, within the Hamiltonian, for the moments to lie in the local XY planes. The state that is selected in this instance can therefore be considered the energetically favoured state and has been shown to be stable with respect to thermal fluctuations rather than selected by them.

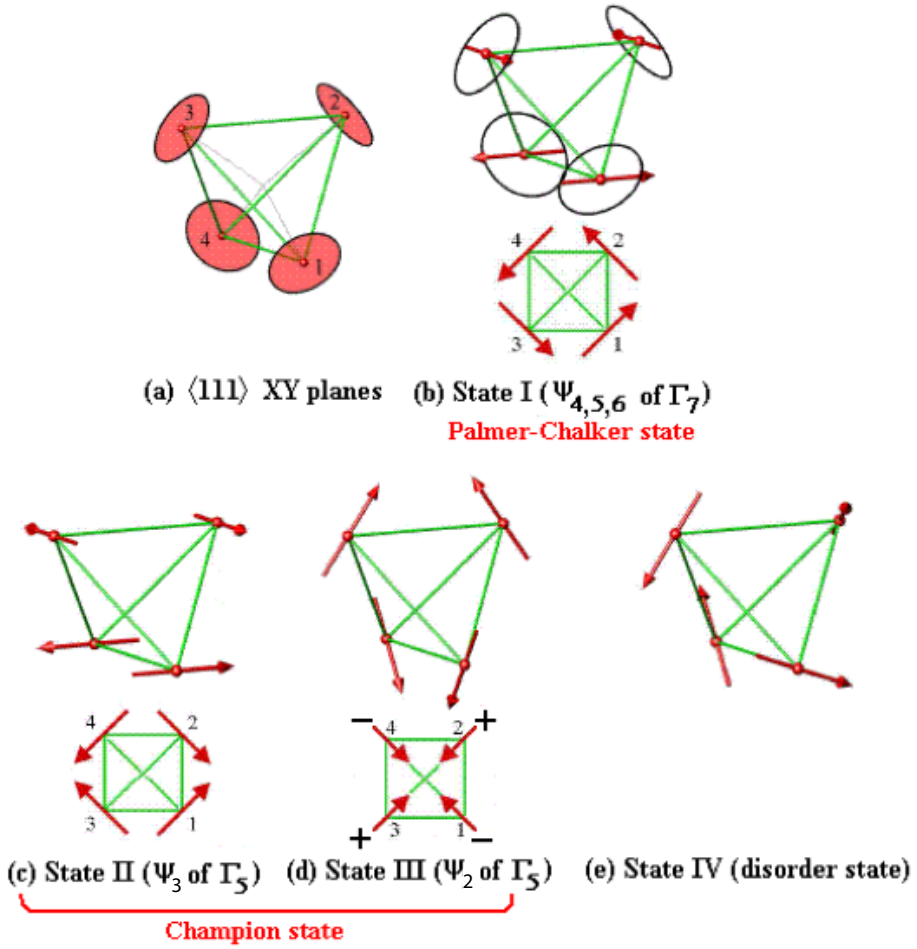

FIGURE 4.3. An illustration of the order possible in the XY antiferromagnet pyrochlore, with respect to one tetrahedron.
a) The local XY planes for the corner sites of the tetrahedron are shown in red and local $\langle 111 \rangle$ axis are shown in grey and connect to the centre of the tetrahedron, note that an oxygen atom is located at this site.

b) - e) The states that satisfy the Hamiltonian of equation 4.2, where:
b) The order found in dipolar model for a Heisenberg antiferromagnet determined by Palmer and Chalker, [**29**], and one of the twelve degenerate structures suggested by Bramwell *et al.*. for the 'uniaxial nematic' structure, [**24**].

c) When two of the spins are flipped state II is found and hence agrees with one of the twelve structures suggested by Bramwell *et al.*. The state is indistinguishable experimentally from the Champion ground state.

d) State III is found by a 90° rotation of the spins of state II about the local $\langle 111 \rangle$ axis. This state is favoured by the order-by-disorder mechanism suggested by Champion *et al.*, [**11, 27, 28**].

e) A disordered state that has no simple relation to states I to III. Image after, [**22, 28**]

4.3.4. The Hamiltonian and the Symmetry. The restrictions to the magnetic order that are imposed when a Hamiltonian is selected are equivalently described by the symmetry operations of the space group that describes the magnetic structure. The sets of restrictions that correspond to different Hamiltonians correspond to the sets of symmetry operations within an irreducible representation, [**30**]. The eigenvectors of Champion eigenstate agree with the basis vectors $\boldsymbol{\psi_2}$ of the IR Γ_5. The Palmer Chalker state is described by the discrete set of basis vectors that belong to the Γ_7 irreducible representation.

4.4. The symmetry of $Er_2Ti_2O_7$

The pyrochlore structure is highly symmetric, best described by cubic space group $Fd\bar{3}m$ and the antiferromagnetic structure of $Er_2Ti_2O_7$ has propagation vector $\mathbf{k}$={0, 0, 0}, $\mathbf{k}$=0 hence forth, [**11, 31**]. The single propagation vector gives rise to one $\mathbf{k}$-domain and the little group $G_{\mathbf{k}}$ contains all of the operations of the group G_0, minus the inversion operation.

The Er^{3+} magnetic ions in $Er_2Ti_2O_7$ reside on the 16*c* site and have symmetry equivalent positions 000(1), $\frac{3}{4}\frac{1}{4}\frac{1}{2}$(2), $\frac{1}{4}\frac{1}{2}\frac{3}{4}$(3) and $\frac{1}{2}\frac{3}{4}\frac{1}{4}$(4), the twelve further positions are related by the pure translations (0, $\frac{1}{2}$, $\frac{1}{2}$), ($\frac{1}{2}$, 0$\frac{1}{2}$) and ($\frac{1}{2}$, $\frac{1}{2}$, 0). All the sites have the point symmetry $\bar{3}m$, hence they have three-fold rotational symmetry, a centre of inversion and are at the convergence point of three planes of mirror symmetry. This section will present the different irreducible representations that are found for $Er_2Ti_2O_7$ and their associated domains.

4.4.1. The Irreducible Representations. The point group G_0 associated with the space group $G = Fd\bar{3}m$ is equivalent to the octahedral point group O_h, shown in table 4.1, where the notation follows that of Kovalev, [**32**]. The group $G_{\mathbf{k}}$, is found when the operations of G_0 are applied to the vector $\mathbf{k}$ and when these operations are

O_h	E	$8C_3$	$6C_2$	$6C_4$	$3C_4^2$	i	$8S_6$	$6\sigma_d$	$6S_4$	$3\sigma_h$
Γ_1	1	1	1	1	1	1	1	1	1	1
Γ_2	1	1	1	1	1	-1	-1	-1	-1	-1
Γ_3	1	1	-1	-1	1	1	1	-1	-1	1
Γ_4	1	1	-1	-1	1	-1	-1	1	1	-1
Γ_5	2	-1	0	0	2	2	-1	0	0	2
Γ_6	2	-1	0	0	2	-2	1	0	0	-2
Γ_7	3	0	-1	1	-1	3	0	-1	1	-1
Γ_8	3	0	-1	1	-1	-3	0	1	-1	1
Γ_9	3	0	1	-1	-1	3	0	1	-1	-1
Γ_{10}	3	0	1	-1	-1	-3	0	-1	1	1

TABLE 4.1. The character table of the octahedral point group, O_h, where the symbol C indicates a rotation, S_n is an inversion rotation, where n is the index of the rotation, and σ indicates a mirror plane, which can be thought of as a two-fold rotation followed by an inversion.

applied to the unique atom at site (0, 0, 0) the basis vectors shown in table 4.2 are generated. Both of these calculations were performed using SARAh, [**33**].

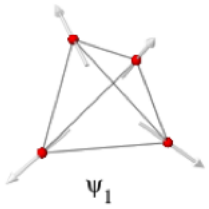

FIGURE 4.4. The basis vectors that define the orientation of the spins that are generated using the Γ_3 irreducible representation. It can be seen that they will be invariant under rotations about any of the {111} axis or any reflection about any {110} axis, where these lie along the edges of the tetrahedron.

4.4.2. Domain structures of Γ_3. The magnetic structure that is generated with Γ_3 corresponds to that found in the ordered phase of FeF_3, which is a geometrically frustrated antiferromagnet that orders at 15.5K, [**34**]. The irreducible representation Γ_3 is one dimensional and gives rise to the antiferromagnetic arrangement of spins shown in figure 4.4. The structure could exhibit domains in which the spins are inverted by 180° across the domain boundary, a translation of half the magnetic unit cell would bring the structure back into agreement, and as such they are termed translational domains. A translational domain is found only in antiferromagnets and

Γ	Basis Vector	Atom: (Site) 1: (0, 0, 0)			2: (0, .75, .75)			3: (.75, 0, .75)			4: (.75, .75, 0)		
Γ_3													
	ψ_1	2	2	2	2	$\bar{2}$	$\bar{2}$	$\bar{2}$	2	$\bar{2}$	$\bar{2}$	$\bar{2}$	2
Γ_5													
	ψ_2	2	$\bar{1}$	$\bar{1}$	2	1	1	$\bar{2}$	$\bar{1}$	1	$\bar{2}$	1	$\bar{1}$
	ψ_3	0	$\sqrt{3}$	$-\sqrt{3}$	0	$-\sqrt{3}$	$\sqrt{3}$	0	$\sqrt{3}$	$\sqrt{3}$	0	$-\sqrt{3}$	$-\sqrt{3}$
Γ_7													
	ψ_4	0	1	$\bar{1}$	0	$\bar{1}$	1	0	$\bar{1}$	$\bar{1}$	0	1	1
	ψ_5	$\bar{1}$	0	1	1	0	1	1	0	$\bar{1}$	$\bar{1}$	0	$\bar{1}$
	ψ_6	1	$\bar{1}$	0	$\bar{1}$	$\bar{1}$	0	1	1	0	$\bar{1}$	1	0
Γ_9													
	ψ_7	2	0	0	2	0	0	2	0	0	2	0	0
	ψ_8	0	1	1	0	$\bar{1}$	$\bar{1}$	0	$\bar{1}$	1	0	1	$\bar{1}$
	ψ_9	0	2	0	0	2	0	0	2	0	0	2	0
	ψ_{10}	1	0	1	$\bar{1}$	0	1	$\bar{1}$	0	$\bar{1}$	1	0	$\bar{1}$
	ψ_{11}	0	0	2	0	0	2	0	0	2	0	0	2
	ψ_{12}	1	1	0	$\bar{1}$	1	0	1	$\bar{1}$	0	$\bar{1}$	$\bar{1}$	0

TABLE 4.2. Basis vectors for the space group F d -3 m:2 with $\mathbf{k}_{-55} = (0,\ 0,\ 0)$.The decomposition of the magnetic representation for the Er^{3+} site $\Gamma_{Mag} = 0\Gamma_1^1 + 0\Gamma_2^1 + 1\Gamma_3^1 + 0\Gamma_4^1 + 1\Gamma_5^2 + 0\Gamma_6^2 + 1\Gamma_7^3 + 0\Gamma_8^3 + 2\Gamma_9^3 + 0\Gamma_{10}^3$

.

is equivalent to the 180° domains found in ferromagnets. In this example the boundary would be abrupt as the spins are Ising like and as such restricted to the local $\langle 111 \rangle$ axes. The boundaries would generate layers in which there are ferromagnetic defects within the anti-ferromagnetic structure.

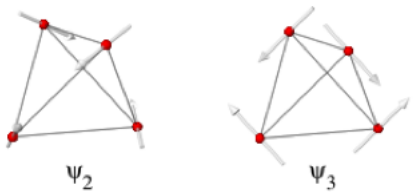

FIGURE 4.5. The basis vectors that define the orientation of the spins that are generated using the Γ_5 irreducible representation. It can be seen that they will be invariant under rotations about any of the {111} axis but no longer with respect to a reflection about the 110 plane.

4.4.3. Domain structures of Γ_5. The irreducible representation that corresponds to Γ_5 gives rise to an XY type ordered arrangement where the XY plane is defined by the basis vectors shown in 4.5 and corresponds to state II and state III described in 4.3. A linear combination of these two vectors will give all the possible orientations of the vector in the plane, whilst imposing the restriction that the symmetry operations that define Γ_5 must remain true. Another way to consider the restriction is that one may orient a spin vector anywhere in the XY plane on the atom about the origin and then apply the transformation and permutation operations to find the orientation of the moments on the other atoms, *i.e.* the orientation of the moment in the local XY plane is continuously degenerate but the translational symmetry is not.

Let us consider the basis vectors that are given by SARA*h*, in table 4.2 and shown in figure 4.5. The rotationally related S-domains for each of the basis vectors are given in table 4.3. The S-domains are found by applying the crystallographic symmetry operations of G to the magnetic structure and arise when the crystallographic axis system is degenerate. In this example domain 1, domain 2 and domain 3 are indistinguishable when viewed down the a, b and c axis respectively.

Domain	Basis Vector	Atom: (Site) 1: (0, 0, 0)			2: (0, .75, .75)			3: (.75, 0, .75)			4: (.75, .75, 0)		
Domain 1	$\boldsymbol{\psi}_2$	2	$\bar{1}$	$\bar{1}$	2	1	1	$\bar{2}$	$\bar{1}$	1	$\bar{2}$	1	$\bar{1}$
	$\boldsymbol{\psi}_3$	0	$\sqrt{3}$	$\bar{\sqrt{3}}$	0	$\bar{\sqrt{3}}$	$\sqrt{3}$	0	$\sqrt{3}$	$\sqrt{3}$	0	$\bar{\sqrt{3}}$	$\bar{\sqrt{3}}$
Domain 2	$\boldsymbol{\psi}_2$	$\bar{1}$	2	$\bar{1}$	$\bar{1}$	$\bar{2}$	1	1	2	1	1	$\bar{2}$	$\bar{1}$
	$\boldsymbol{\psi}_3$	$\bar{\sqrt{3}}$	0	$\sqrt{3}$	$\bar{\sqrt{3}}$	0	$\bar{\sqrt{3}}$	$\sqrt{3}$	0	$\bar{\sqrt{3}}$	$\sqrt{3}$	0	$\sqrt{3}$
Domain 3	$\boldsymbol{\psi}_2$	$\bar{1}$	$\bar{1}$	2	$\bar{1}$	1	$\bar{2}$	1	$\bar{1}$	$\bar{2}$	1	1	2
	$\boldsymbol{\psi}_3$	$\sqrt{3}$	$\bar{\sqrt{3}}$	0	$\sqrt{3}$	$\sqrt{3}$	0	$\bar{\sqrt{3}}$	$\bar{\sqrt{3}}$	0	$\bar{\sqrt{3}}$	$\sqrt{3}$	0

TABLE 4.3.
Table of basis vectors calculated for the S-Domains in Γ_5.

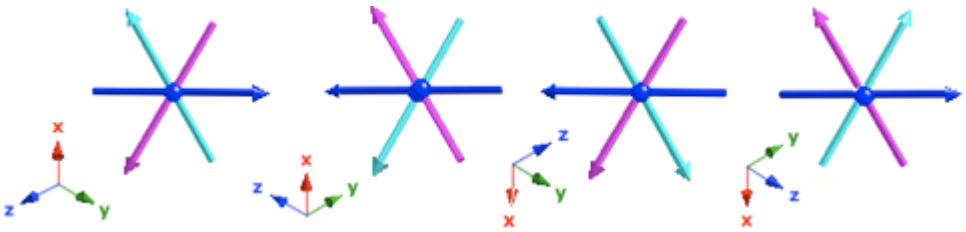

FIGURE 4.6. The relationship between the basis vectors of the IR Γ_7 changes from site to site, thus, if we wish the moments to remain the same size on each site the basis vectors cannot be combined in a linear combination. The the variation of the size of the moment around the sites of the tetrahedron will not break the symmetry.

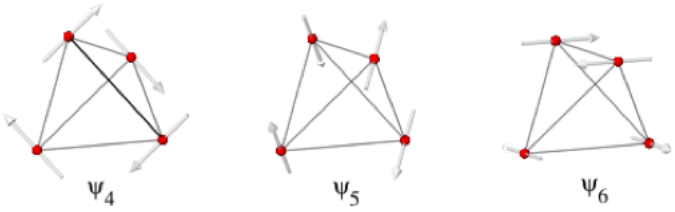

FIGURE 4.7. The basis vectors that define the orientation of the spins that are generated using the Γ_7 irreducible representation. It can be seen that they will be invariant under rotations about any of the {111} axis but no longer with respect to a reflection about the 110 plane.

4.4.4. Domain structures of Γ_7. The irreducible representation that describes Γ_7 is three dimensional, but again restricts the magnetic moment to the XY plane. The set of basis vectors gives the structure shown in figure 4.6 that corresponds to state I of the possible theoretical structures, shown in figure 4.3.b. When the restriction that the magnitude of the moments is equivalent on the Er^{3+} sites is applied the basis vectors cannot be combined in a linear combination as the basis vectors do not have a consistent relationship, shown in figure 4.6. The symmetry of this set of basis vectors is, therefore, not continuous within the XY plane and the group forms a discrete set of vectors $\boldsymbol{\psi}_4$, $\boldsymbol{\psi}_5$ or $\boldsymbol{\psi}_6$.

The rotationally related domains are described by the complete set of basis vectors and these were the vectors that were used to represent the S-domains for this structure, along with the time reversed counterparts.

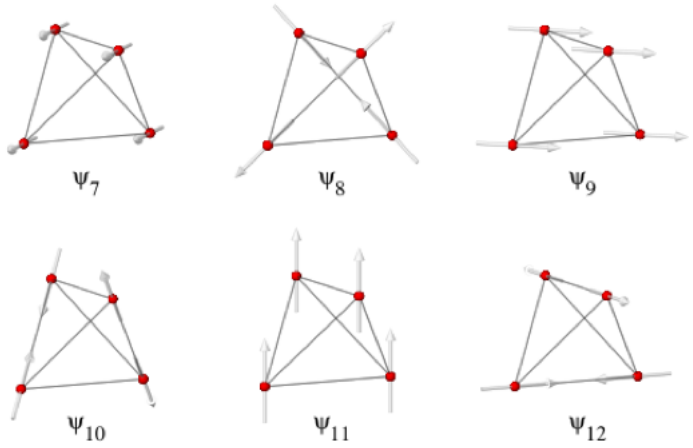

FIGURE 4.8. The basis vectors that define the orientation of the spins that are generated using the Γ_9 irreducible representation.

4.4.5. The domain structures of Γ_9. The irreducible representation, Γ_9 contains six basis vectors, which do not lie in the XY plane. A linear combination of the propogation vectors give rise to a ferromagnetic structures that can either be aligned with the crystallographic axis system, **a**, **b** or **c** ($\boldsymbol{\psi}_7$, $\boldsymbol{\psi}_9$ or $\boldsymbol{\psi}_{11}$), with the local $\langle 110 \rangle$ axis ($\boldsymbol{\psi}_8$, $\boldsymbol{\psi}_{10}$ or $\boldsymbol{\psi}_{12}$) or with the local $\langle 111 \rangle$ axis ($\boldsymbol{\psi}_7+2\boldsymbol{\psi}_8$). The final arrangement will return the spin ice structure, where the spins are ferromagnetically ordered and restricted to the local $\langle 111 \rangle$. The vectors that lie in the directions **a**, **b** or **c** convert from one to another by a threefold rotation, and, if the order is a single vector, say $\boldsymbol{\psi}_7$ that the S-domains are described by $\boldsymbol{\psi}_9$ and $\boldsymbol{\psi}_{11}$, or say $\boldsymbol{\psi}_8$ that the domains are described by $\boldsymbol{\psi}_{10}$ and $\boldsymbol{\psi}_{12}$.

4.5. Comparison of Experimental Results and Theoretical Predictions

The data presented in the paper of Champion *et al.* supports the Champion model for the magnetic structure, which corresponds to the Γ_5 IR, [**11**], however, a plot of the evolution of the (2, 2, 0) reflection indicates that the transition is strongly second order, which disagrees with the strongly first order transition seen in the simulations, [**27, 28**]. The Champion model identifies that the order is specifically described by the $\boldsymbol{\psi}_2$ basis vector of Γ_5 but the basis vector that describes the order cannot be

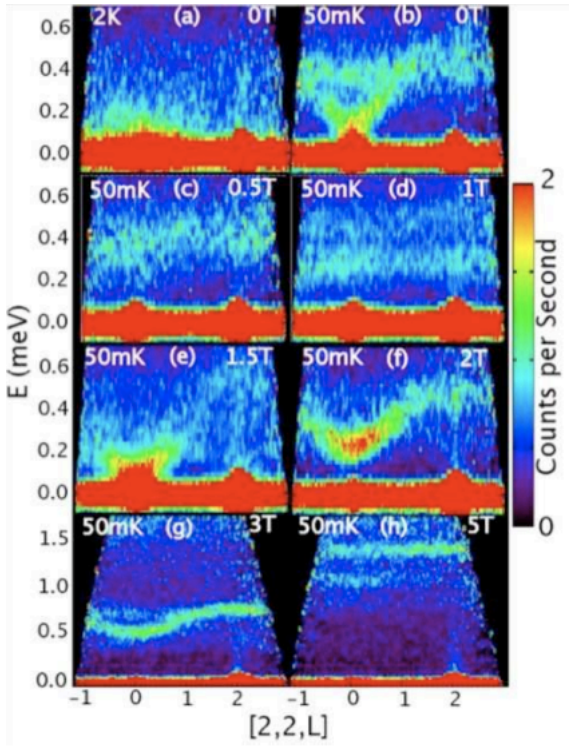

FIGURE 4.9. The dispersion of spin waves is shown along the [2,2,L] line in reciprocal space, joining the (2, 2, 0) and (2, 2, 2) wavevectors, where Bragg scattering characteristic of the low temperature states in high and low magnetic fields is observed. a) shows data at T=2 K and H=0, while b) - h) show data at T=50 mK and applied field as indicated, [**41**].

determined from unpolarised diffraction data due to the presence of S-domains. In order to try and distinguish between the two structures a 0.5 T magnetic field was applied to a single crystal of $Er_2Ti_2O_7$ in the [1 $\bar{1}$ 0] direction. The field caused an increase by a factor of 1.9 in the counts of the (2, 2, 0) peak, which led the authors to conclude that a monodomain with the $\boldsymbol{\psi}_2$ ground state had been formed. Work by Ruff *et al.* indicates that this change in the magnitude is accompanied by the elimination of a soft mode in reciprocal space, shown in figure 4.9, which they interpret as a qualitative change in the magnetic ground state, [**41**]. The inelastic measurements by Ruff *et al.* agree with inelastic measurements that were made in zero field by Champion and co-workers, [**11**], which are ungapped at the Brillouin zone centre. Finally, there is evidence from a μSr experiment performed by Lago *et al.*, [**42**], that there is component of the magnetism that remains dynamic to 20 mK, which is unaccounted for in either of the models.

Overall the previous work indicates that the static order is described by the Γ_5 irreducible representation, which agrees with the theoretical model put forward by Champion *et al.*. The theory of Champion *et al.* suggests that the order is properly described by only the $\boldsymbol{\psi}_2$ basis vector and this cannot be determined with diffraction techniques, in an attempt to make this distinction a neutron polarimetry experiment was performed. This technique was thought to be suited to the task as it typically allows an unambiguous description of the magnetic order and is conducted in zero-field so that the magnetic structure will remain unperturbed.

4.6. Experimental Details

The purpose of the experiment was to confirm that long range order found in $Er_2Ti_2O_7$ is described by the Γ_5 IR, as suggested by the Champion model and determine the coefficients of the basis vectors, $\boldsymbol{\psi}_2$ and $\boldsymbol{\psi}_3$, that best describe this ground state structure. The experiment was performed with CRYOPAD on D3 at the ILL on the $\approx$ 8 mm sample used in the experimental study by Champion *et al.*, [**11**]. The experimental arrangement will be discussed in this section.

4.6.1. Sample Environment. The polarimetric measurements were taken with neutrons of wavelength 0.825 Å at a temperature of 50 mK, well below the magnetic ordering temperature, T_N=1.2 K, the temperature was achieved by the sample being placed within a dilution refrigerator. Measurements were taken with the crystal in two orientations, the first set of data were collected with the [001] zone axis vertical and the second set with the crystal oriented with the [$\bar{1}$10] zone axis vertical. The orientation was performed on Orient Express at the ILL after which the sample glued on to a standard pin with epoxy resin. The initial orientation allows access to all odd and all even $hk0$ reflections; the latter orientation allows access to the hhl set of reflections, where all of the accessible reflection indices are even. Twenty five reflections were measured in the [001] orientation and 33 in the [$\bar{1}$10] orientation,where

the (2, 2, 0), (4, 4, 0), (6, 6, 0) and (0, 0, 4) were measured in both orientations, to give a total of 55 different reflections.

4.7. Data Analysis

The raw data were corrected for detector efficiency by the standard set of CRYOPAD routines within the IGOR PRO software suite that supported the instrument at that time. Mathematica routines, written by the author, calculated, and corrected for, the decrease in the efficiency of the ^{3}He cell, based on the magnitude of the polarization measured at non-magnetic reflections. Mathematica routines were also written by the author to fit the coefficients of the basis vectors to the corrected data and to plot the both the experimental and calculated data. The calculation of the magnetic structure was based on the both the Champion model and Palmer Chalker model for the sake of completeness.

This section will outline the routines that were written to calculate the polarization matrices and the corrections made to compensate for the depolarization of the ^{3}He cell during the experiment. Let us begin by considering the origin of the experimental error in CRYOPAD type experiments

4.7.1. Polarimetry errors and ^{3}He depolarisation. The data that is collected from a polarimetry experiment is subject to several sources of error, [**35**], which will be discussed in this section. The greatest contributions are from the beam polarization and the angular error introduced during the experiment. We will consider the latter first.

When mounting a crystal at the ILL the orientation is usually completed using the single crystal Laue diffractometer Orient Express, after which it is glued onto a pin, attached to the sample stick and inserted into the sample environment, within

CRYOPAD. The process introduces angular error in the form of the tilt of the sample environment with respect to the CRYOPAD insert. The orientation of the crystal is likely to introduce an error of the same magnitude. These errors will combine to give a systematic error of $\approx 0.2°$, which cannot readily be corrected for, but can be accounted for in the calculation of the model polarization matrix by considering the minimum and maximum offset for each reflection.

The polarization of the beam is equivalent to the probability that one will find the neutron in the desired spin state, p_σ that is included in equation 2.32. The cause of this error arising is due to:

(1) The incomplete polarization of the beam by the Heusler crystal
(2) The inefficiencies of the flippers, nutators and precession coils
(3) Stray fields within the 'zero'-field chamber
(4) The incomplete polarization, and subsequent depolarization of the ^{3}He analyser cell.

Let us consider these points in turn with reference to CRYOPAD. The Heusler crystal efficiency is, on average, 98%, where the de-polarization of the beam is due to inhomogenities within the monochromating array or demagnetization of the Heusler crystals [**35**]. The efficiency of the flippers has been measured and modelled and the systematic error of the precession coils is calculated to be in the order of 0.02° and the nutators to be in the order of 0.01°. The variations of the energy of the incident neutron beam could lead to imperfect rotation by these coils, where the fluctuations are compentsated for by a constant switching of the of the final measurement direction. The stray fields within the chamber have been calculated in the case of CRYOPAD on D3 to be $1 - 1.5$mG, which would cause an error of approximately 0.1°. Other polarimeters tend to show larger fields in the zero field region due to problems with cooling the superconducting shielding efficiently, the location of the instrument with respect to other high field equipment and the manner in which the

shielding is constructed. Again these errors are systematic and are often negligible with respect to the statistical error of the neutron count rate or the systematic error introduced by mounting the sample.

The depolarization of the ^{3}He cell, however, is not a negligible contribution to the reduction of the polarization in the beam. In the ideal case the rate of the depolarization is due to the dipolar interaction of the He atoms within the cell The actual relaxation time, however, is usually dependent on the number of paramagnetic impurities and the interaction of the gas within the cell with the walls of the gas cell, [**36, 37, 38, 39**]. The relaxation of the cell can be modeled as an exponential where the polarization within the cell P_{He} at time, t is given by,

$$P_{He}(t) = P_0 \exp(-t/\tau) \tag{4.4}$$

where τ the relaxation rate and P_0 is the initial polarization, [**36**]. The polarization of the ^{3}He within the cell is not measured directly, instead the intensity of the spin flip and non-spin flip scattering is measured to give the transmission of the cell in each state,

$$T_{\pm}(P_{He}) = \exp\{-(1 \mp P_{He})\, n_{He}\, \sigma_0\, l\} \tag{4.5}$$

where n_{He} is the number density of the ^{3}He atoms, σ_0 is the absorption cross section, (σ_0 [barn] ≈ 3000) from which the total transmission,

$$T_n(P_{He}) = \frac{T^+ + T^-}{2} = \exp(-O)\cosh(OP_{He}) \tag{4.6}$$

and the polarization of the beam, P_n,

$$P_n(P_{He}) = \frac{T^+ - T^-}{T^+ + T^-} = \tanh(OP_{He}) \tag{4.7}$$

are found, where the value $T^{\pm}$ is the transmission of the cell, and is equivalent to the intensity of the beam that will pass through the polarized cell, [**36**]. The value

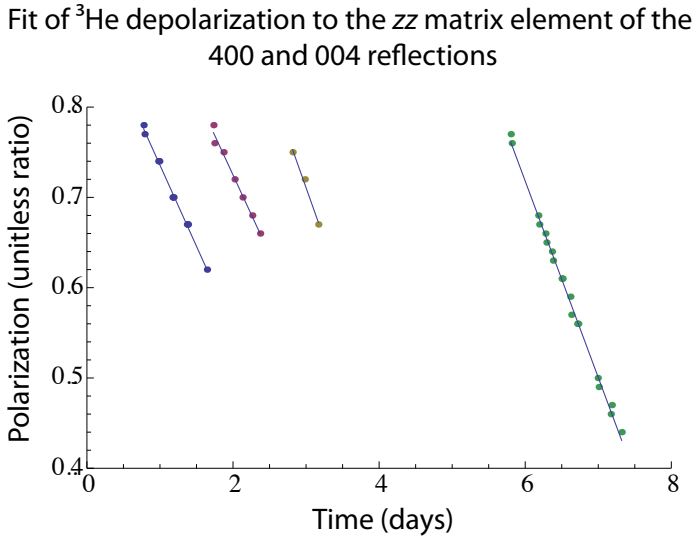

FIGURE 4.10. The rate of change of the polarization measured in the zz channel at the reference nuclear peaks, $\{0, 0, 4\}$. The different lines indicate the different cells that were used during the experiment.

$O = n_{He}\,\sigma_0\,l$ is the opacity of the filter and may be defined

$$O = 0.0732\,l\,\lambda\,p_{He}, \tag{4.8}$$

where 0.0732 is a factor to compensate for the units of l the length of the cell in centimeters, λ the wavelength of the beam in and p_{He} the pressure of the He in bar. If we replace transmission with the intensity of the scattered beam the equation is the same as that used to find the value of the elements of the polarization matrix:

$$P_{ij} = \frac{I^+ - I^-}{I^+ + I^-} \tag{4.9}$$

In order to correct for the decrease in polarization, with respect to time, the peaks with no magnetic component may be measured and the fit to this data used to normalize the polarization of all other reflections.

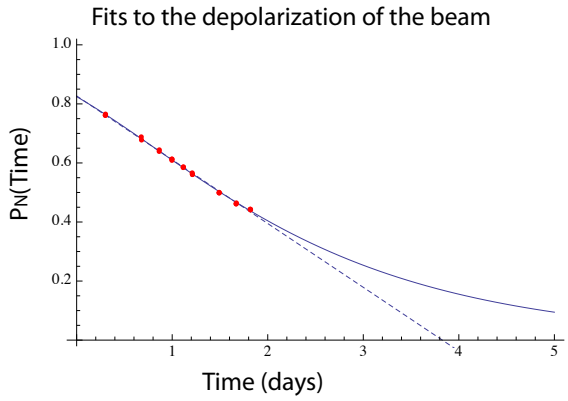

FIGURE 4.11. The rate of change of the polarization measured in the zz channel at the reference nuclear peaks, $\{0, 0, 4\}$ for the final ^{3}He cell. Where the red points are the experimental data the dashed line is the linear fit and the solid line a hyperbolic tan fit. The fitted values are included in the text.

4.7.2. Calculation of the depolarization rate. The fit to the polarization of the beam was made in Mathematica with a routine written by the author. The reflections that have no magnetic contribution fulfill the condition $h_{4p}k_{4q}l_{4r}$, where p, q and r are integers, of these the (4, 0, 0) and (0, 0, 4) reflections were used to measure the polarization. The zz element of the matrix was used for the fit as the polarization of the beam is only rotated about the axis χ to be oriented in the z direction and as such the instrumental error is minimised. The (4, 0, 0) and (0, 0, 4) reference reflections were grouped by the Mathematica routine such that within each group the measured polarization decreased, when the polarization was found to increase a new group was started, where the increase in the polarization indicates a new ^{3}He cell being inserted. The routine then makes a linear fit to each group, with respect to time and polarization, and returns the equations for each of the fits. The measured polarization is then divided by the value expected, at that time, for a non-magnetic peak. The routines are included in Appendix C.

The plot of the beam polarization during the $Er_2Ti_2O_7$ experiment is shown in 4.10 with the calculated fit. The best fit that was found to the data was linear, despite the exponential decay of the polarization within the cell. This is due to the combination of the hyperbolic tan function, equation 4.7, that describes the polarization of the

beam, with the exponential that describes the decay rate of the polarization of the cell, equation 4.4,.

$$P_n(t) = \tanh\{OP_0 \exp(-t/\tau)\} \tag{4.10}$$

In the region of useful beam polarization (approximately 80% to 40%) the function is very well approximated by a linear fit, as shown in figure 4.11, where the fit made with equation 4.10 is shown in a solid line and the linear fit with a dashed line. The fitted values are $\tau = 1.989$, and $O = 1.17$ and $P_0 = 1$. The experimental values that describe the cell were not recorded, however, the wavelength was $\lambda = 0.834$ Å and the pressure in the cell is usually in the region of 1.2 bar. When the values are input into equation 4.8 the fitted value for O would indicate that the cell had length 15.5 cm, which is approximately half the length of the ^{3}He cell used. The polarization of the ^{3}He within the cell at the start of the measurements, P_0 is set to 1 as the value for O and the value for the initial polarization cannot be refined simultaneously, with the values given the initial efficiency of the cell $P_n(0) = 0.84$.

The expected transmission can also be calculated using the fitted values and this is shown in figure 4.12. The plot on the left is the measured intensity of the non-spin-flip and spin-flip scattering compared to the calculated transmission, and the plot on the right is the again the measured intensity, but now compared to the transmission divided by an arbitrary factor of two. The plots indicate that the general features of the transmission are in agreement but the scale is incorrect.

4.7.3. Calculation of the polarization matrices. The polarisation matrices were calculated in Mathematica in a routine written by the author and compared to experimental values. The routines were written with reference to the mathematics in

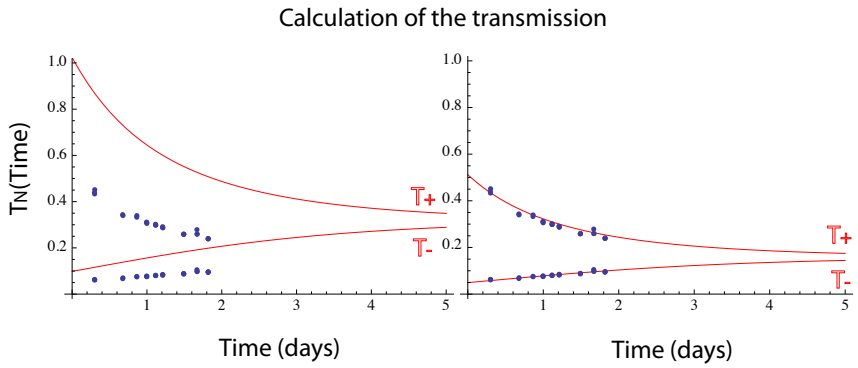

FIGURE 4.12. The rate of change of the measured intensity of the non-spin-flip (upper traces) and spin-flip (lower traces) in the zz channel at the reference nuclear peaks, $\{0, 0, 4\}$ for the final ^{3}He cell. The lines are calculated from the fit made to the measured polarization of the beam. The lines in the plot on the left is generated from equation 4.5 and lines in the plot on the right are reduced by an arbitrary factor of two.

chapter 2, the outline of the process is as follows, the Mathematica notebooks that are associated with these calculations are included in Appendix C.

4.7.3.1. *Calculation of the magnetic form factor.* The magnetic structure factor was calculated with the basis vectors calculated in SARA*h* as input:

- A sum is made over the i basis vectors $\boldsymbol{\psi_i}$ that have been selected for the calculation, for a single atom, where each of the basis vectors is multiplied by a coefficient that is input by the user, c_i,

$$\sum_i c_i \boldsymbol{\psi_i} \tag{4.11}$$

- The basis vectors were normalised with respect to the first basis vector of the set that is included in the sum.

$$\boldsymbol{\Psi} = \frac{\sum_i c_i \boldsymbol{\psi_i}}{\sum_i c_i \boldsymbol{\psi_1}} \tag{4.12}$$

- The normalised basis vector sum $\mathbf{\Psi}'_d$ for the atom d is then multiplied by the phase of the magnetic structure within the unit cell, where the propagation vector is $\mathbf{k}$ and the centering translations are $\mathbf{t}_d$,

$$\mathbf{\Psi}'_d = \mathbf{\Psi}_d \exp -2\pi i \mathbf{k} \cdot \mathbf{t}_d \tag{4.13}$$

- A sum is made over all of the atoms d, at position $\mathbf{r}_d$ in the unit cell and multiplied by the phase change that occurs on scattering, where the scattering vector is $\mathbf{Q}$ and the atom site is d,

$$\mathbf{\Psi}''_d = \sum_d \mathbf{\Psi}'_d \exp 2\pi i \mathbf{Q} \cdot \mathbf{r}_d \tag{4.14}$$

- The vector is then multiplied by the moment, μ_n, the form factor f_n and the factor $\gamma r_0/2 = 0.2695 \times 10^{-12} cm$ ($r_0 = e^2/m_e c^2$ being the classical electron radius, [**43**]) and a final sum is then made over the different types of magnetic atoms n in the unit cell,

$$\mathbf{M}(\mathbf{Q}) = 0.2695 \sum_n \mu_n f_n \mathbf{\Psi}''_n \tag{4.15}$$

4.7.3.2. *Calculation of the magnetic interaction vector.* The magnetic interaction vector was determined for each reflection with respect to the CRYOPAD axis system, the rotational matrices for this operation are described in this section.

- The crystallographic axes, a, b, c, with internal angles α, β and γ are converted to orthogonal axis with the rotational matrix,

$$P_{abc\,to\,orth} = \begin{pmatrix} a\sin\beta + a\sin\gamma - a & 0 & 0 \\ a\cos\gamma & b & 0 \\ a\cos\beta & 0 & c \end{pmatrix} \tag{4.16}$$

- The matrix P is normalized and used to generate a matrix that converts to the CRYOPAD axis system, where each row in the matrix below corresponds to a vector and the final matrix is a vector of these vectors,

$$Q_{orth\,to\,xyz} = \begin{pmatrix} \mathbf{Q}\hat{\cdot}P \\ z\hat{\cdot}P \times \mathbf{Q}\hat{\cdot}P \\ z\hat{\cdot}P \end{pmatrix} \tag{4.17}$$

- The $P_{abc\,to\,orth}$ matrix is used to convert $\mathbf{M}(\mathbf{Q})$ to from the crystallographic the orthogonal axis system,

$$\mathbf{M}(\mathbf{Q})_{orth} = \mathbf{M}(\mathbf{Q}) \cdot P_{abc\,to\,xyz} \tag{4.18}$$

- The $Q_{orth\,to\,xyz}$ matrix is then used to rotate the vector $\mathbf{M}(\mathbf{Q})_{orth}$ to the equivalent position, but described using the CRYOPAD axis system,

$$\mathbf{M}(\mathbf{Q})_{xyz} = Q_{orth\,to\,xyz} \cdot \mathbf{M}(\mathbf{Q})_{orth} \tag{4.19}$$

- The scattering vector $\mathbf{Q}$, in the CRYOPAD axis system, is along the x axis and as such the magnetic interaction vector found by taking twice the cross product of the vector $\mathbf{M}(\mathbf{Q})_{xyz}$ and the vector (1, 0, 0):

$$\mathbf{M}(\mathbf{Q})_{\perp\,xyz} = (1,0,0) \times (\mathbf{M}(\mathbf{Q})_{xyz} \times (1,0,0)) \tag{4.20}$$

There is a general explanation of rotation and transformation of vectors and matrices in appendix B.

4.7.3.3. *Calculation of the polarization matrices.*

- The polarization matrices are calculated using Blume's equations, such that the terms of equation 2.4.3 are replaced with the calculated $\mathbf{M}\perp(\mathbf{Q})_{xyz}$, the experimentally determined value for N and $\mathbf{P}$ a vector description of the incident polarization,

$$\mathbf{P}_f = \frac{\mathbf{P}_f\sigma}{\sigma} \tag{4.21}$$

$$\begin{aligned}\sigma &= (NN^*) + (\mathbf{M}_\perp \cdot \mathbf{M}_\perp^*) \\ &\quad + (i\mathbf{P}_i \cdot (\mathbf{M}_\perp^* \times \mathbf{M}_\perp) + (\mathbf{P}_i \cdot (\mathbf{M}_\perp N^* + \mathbf{M}_\perp^* N))\end{aligned} \tag{4.22}$$

$$\begin{aligned}\mathbf{P}_f\sigma &= (\mathbf{P}_i NN^*) \\ &\quad + (-\mathbf{P}_i(\mathbf{M}_\perp \cdot \mathbf{M}_\perp^*) + (\mathbf{M}_\perp(\mathbf{P}_i \cdot \mathbf{M}_\perp^*) + \mathbf{M}_\perp^*(\mathbf{P}_i \cdot \mathbf{M}_\perp)) \\ &\quad + (-i(\mathbf{M}_\perp^* \times \mathbf{M}_\perp)) \\ &\quad + (N\mathbf{M}_\perp^* + N^*\mathbf{M}_\perp - i(N\mathbf{M}_\perp^* - N^*\mathbf{M}_\perp) \times \mathbf{P}_i)\end{aligned} \tag{4.23}$$

where,

$$\mathbf{M} \perp = \mathbf{M} \perp (\mathbf{Q})_{xyz}, \quad N = N_{expt}, \tag{4.24}$$

$$\mathbf{P}_{i\,x} = (1,0,0), \quad \mathbf{P}_{i\,y} = (0,1,0), \quad \mathbf{P}_{i\,z} = (0,0,1) \tag{4.25}$$

- In order to calculate the structure in which domains are present the final polarization, $\mathbf{P}_f^s$, for each of the s domains was multiplied by the intensity of the scattering from that domain σ^s and a coefficient that indicates the volume fraction, c_s. The sum is then divided by the total intensity, expected for the domain combination $\sigma^{s\,tot}$, [**40**] ,

$$\mathbf{P}_f = \frac{\sum_s c_s \mathbf{P}_f^s \sigma^s}{\sigma^{s\,tot}} \tag{4.26}$$

$\mathbf{P}_f$ returns a vector that is directly comparable to the experimental value recorded when $\mathbf{P_i}$=x, y or z.

4.7.3.4. *Plot of experimental and calculated data.* The data were plotted in a routine, again written by the author in Mathematica, that plots the calculated and experimental matrices in in the position in reciprocal space of the reflection that has been measured. The position is found by designating the axis system and then dividing the point in reciprocal space by the axes. Due to the quantization of the plot, whereby the plot is broken down in to squares, only the integer part of the postion is retained. The central value of the matrix is assigned this position and the other terms of the matrix are plotted with respect to this central position, the routine is included in Appendix C. The results will be presented with respect to these plots and the comparison will be made, initially, by considering how the atoms contribute to the magnetic interaction vector.

4.8. Results

Data were recorded in the magnetically ordered phase at 50 mK in two orientations, where either the [0, 0, 1] or [1, $\bar{1}$, 0] directions are vertical. These orientations allow access the (0, 0, 1) and (1, $\bar{1}$, 0) planes respectively. The presentation of the results

will follow the progression of the experiment and present the results from the [0, 0, 1] orientation first.

4.8.1. The experimental matrices observed in the [0, 0, 1] orientation. The 25 reciprocal lattice points that were inspected in the [0, 0, 1] orientation must fall within the (h, k, 0) scattering plane where h and k are even, due to the extinction conditions of the $Fd\bar{3}m$ space group.

The experimental polarisation matrices for the data set recorded with the crystal in the [0, 0, 1] orientation are shown in figure 4.8.1. The position of the 3×3 squares of colour indicate the point in reciprocal space that the polarisation matrices were recorded. The colours within the squares indicate the value recorded in each of the channels of the polarisation matrices, where the orange indicates a value of 1 and the blue indicates a value of -1. The incident polarisation is positive in all cases.

Let us first consider the matrices at the positions $h_{4p}, k_{4q}, 0$, where p and q are integers. The polarization matrix for reflection (4, 0, 0) is shown in table, 4.4, the values in the matrix are approximately unitary along the diagonal of the matrix, where the errors are between 0.8% in the xx channel and 1.4% in the zz channel. The off-diagonal elements, for a nuclear only peak should all be zero, as all the off diagonal terms are due to interference between the magnetic contribution and either the nuclear contribution or with itself. The non-zero off diagonal terms represent systematic errors and are not unusual in a CRYOPAD experiments, [**44**], in the matrix presented the errors are $yz = -1.3\%$, $zx = 1.3\%$ and $zy = 8\%$. The last term is of a significant size, but this size is consistent for all measurements of the nuclear peaks, regardless of the orientation. This implies that the error is due to the instrument rather than a feature of the sample.

The magnetic contribution may be zero, either because the magnetic moment lies in the direction of scattering, **Q**, or because there is no net magnetism related to

Reflection	Polarisation Matrix
$(4,0,0)$	$\begin{pmatrix} 1.008\ (0.002) & 0.000\ (0.003) & 0.000\ (0.003) \\ 0.000\ (0.003) & 1.011\ (0.002) & -0.013\ (0.003) \\ 0.013\ (0.003) & 0.080\ (0.003) & 1.014\ (0.002) \end{pmatrix}$

TABLE 4.4. The polarization matrices observed for the 4 0 0 reflection, with positive incident polarization, the output is approximately a 3×3 identity matrix which is indicative of purely nuclear scattering.

'Family'	Reflections, **Q**	Magnetic structure factors
1	$h_{4p}k_{4q}l_{4r}$	$\mathbf{m}_1+\mathbf{m}_2+\mathbf{m}_3+\mathbf{m}_4$
2	$h_{4p\pm2}k_{4q\pm2}l_{4r}$, $h_{4p}h_{4p}l_{4q\pm2}$	$\mathbf{m}_1-\mathbf{m}_2-\mathbf{m}_3+\mathbf{m}_4$
3	$h_{4n\pm1}h_{4n\pm1}l_{4n\pm1}$	$\mathbf{m}_1-\mathbf{m}_2-\mathbf{m}_3-\mathbf{m}_4$
4	$h_{4n\pm1}h_{4n\pm1}l_{4n\mp1}$	$\mathbf{m}_1+\mathbf{m}_2+\mathbf{m}_3-\mathbf{m}_4$

TABLE 4.5. The different 'families' of magnetic reflections that can be accessed with the [001] and [1$\bar{1}$0] orientations, where p, q and r are integers. The 'family' indicates those reflections that have the same magnetic structure factors, with respect to the vectors on the atomic positions, $\mathbf{m}_1$, $\mathbf{m}_2$, $\mathbf{m}_3$, and $\mathbf{m}_4$. The relationship is due to the phasing introduced on scattering and is found from $\exp(i2\pi\mathbf{Q}.\mathbf{r}_d)$, where $\mathbf{Q}$ is the scattering vector and $\mathbf{r}_d$ is the position of atom d.

this site. In order to determine which is the correct description the other members of this family of magnetic reflections must also be considered. In the former case magnetic scattering would be observed at the (0, 4, 0) position in reciprocal space, as it is perpendicular to the (0, 0, 4) position and the magnetic moment would now lie in the y direction, with respect to the CRYOPAD axes. If there is no magnetic contribution to any of the reflections that belong to the $h_{4p}, k_{4q}, 0$ family it can be understood that these reflection indices are non-magnetic.

The experimental data that is plotted in the matrix map in figure 4.8.1, shows, at the (4, 0, 0) position of reciprocal space, a matrix that has an orange colour along the diagonal of the matrix, where the orange indicates a value of one. Furthermore, the experimental data indicate that all of the positions $h_{4p}, k_{4q}, 0$ have orange along the diagonal of the matrix, which indicates that the reflections are non-magnetic.

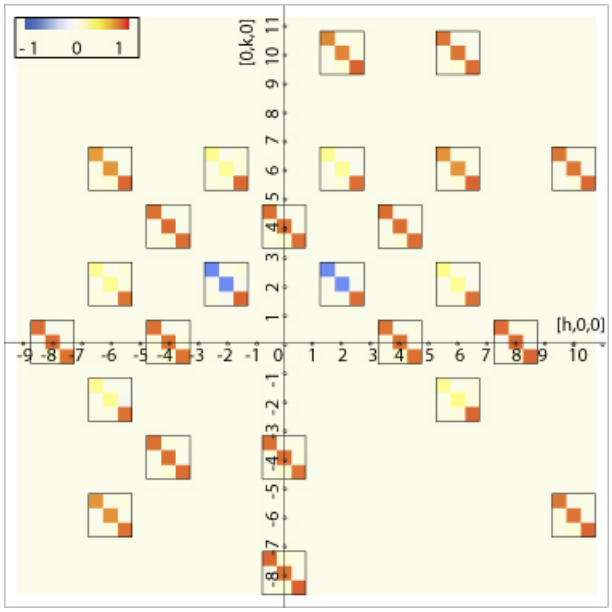

FIGURE 4.13. A colour map of each of the polarisation matrices for the [0, 0, 1] orientation shown with respect to the position of the scattering in reciprocal space. The incident polarisation is positive for the x, y and z channels. The matrices that are plotted at the {4, 0, 0}, {8, 0, 0} and {4, 4, 0} positions are diagonal with elements equal to one. The polarization is therefore unchanged on scattering and reflections indicate that there is no magnetic contribution to these peaks. The reflections at the $h_{4p\pm2}k_{4q\pm2}0$ belong to family 2 and have scattering only in the diagonal channels and is unitary in the zz channel. The difference in colour of the zz channel and xx and yy channels for the reflections of family 2 diminish as $\mathbf{Q}$ increases.

The reflections with the indices $h_{4p}k_{4q}0$, where p and q are integers belong to the same family of reflections, where a family has equivalent contributions to the scattering from each of the atomic sites. In the case of $Er_2Ti_2O_7$, with the d atomic positions defined as $m_1 : (0,0,0)$, $m_2 : (\frac{1}{2},\frac{3}{4},\frac{1}{4})$, $m_3 : (\frac{1}{4},\frac{1}{2},\frac{3}{4})$, $m_4 : (\frac{3}{4},\frac{1}{4},\frac{1}{2})$ the phase shift on scattering for each atomic sites is $\mathbf{Q}.\mathbf{r}_d = 0$ or 2π, hence $\exp(i2\pi\mathbf{Q}.\mathbf{r}_d) = 1$ for all atoms. For the family h_{4p}, k_{4q}, l_{4r}, labelled family 1 in table 4.5, the reflections are all non-magnetic, which agrees with the stipulation for an antiferromagnet on the pyrochlore lattice for the sum over the atoms $\mathbf{k}$=0, $\sum \mathbf{m}_d = 0$, where d=1 to 4. From this relation it may be inferred that the sum of the moments on the sites $\mathbf{m}_1$, $\mathbf{m}_2$ and $\mathbf{m}_3$ are equal and opposite to $\mathbf{m}_4$.

$$\mathbf{m}_1 + \mathbf{m}_2 + \mathbf{m}_3 + \mathbf{m}_4 = 0 \tag{4.27}$$

hence,

$$\mathbf{m}_4 = -(\mathbf{m}_1 + \mathbf{m}_2 + \mathbf{m}_3) \tag{4.28}$$

The above relation may be substituted into the magnetic structure factor for the second family of reflections, $h_{4p\pm2}, k_{4q\pm2}, l_{4r}$ and $h_{4p}, h_{4p}, l_{4q\pm2}$,

$$\mathbf{M(Q)} = \mathbf{m_1} - \mathbf{m_2} - \mathbf{m_3} + \mathbf{m_4} \tag{4.29}$$

to give,

$$\mathbf{M(Q)} = -\mathbf{2}(\mathbf{m_2} + \mathbf{m_3}). \tag{4.30}$$

Therefore, the reflections that have the indices $h_{4p\pm2}$, $k_{4q\pm2}$, l_{4r} and h_{4p}, h_{4p}, $l_{4q\pm2}$, will return information from the moments on the atoms at the positions $m_2 : (\frac{1}{2}, \frac{3}{4}, \frac{1}{4})$ and $m_3 : (\frac{1}{4}, \frac{1}{2}, \frac{3}{4})$.

Polarization matrices for the reflections (2, 2, 0), (6, 2, 0) and (6, 6, 0), recorded in the [0, 0, 1] orientation which are described by $h_{4p\pm2}$, $k_{4q\pm2}$, l_{4r}, and hence belong to family 2, are shown in 4.6. The values recorded in the xx and yy channels for the (2, 2, 0) reflection, greater than zero for the (±6 ±2 0) reflection and slightly less than one in the (±6 ±6 0) reflection. The increase of the value in the xx and yy channels as $\mathbf{Q}$ increases is due to the magnetic form factor, as the relative strength of the magnetic spin-flip scattering decreases with respect to the non-spin-flip nuclear scattering.

Spin-flip scattering in the xx and yy channels, but not in the zz channel occurs when the magnetic interaction vector, $\mathbf{M(Q)}_\perp$ is in the direction of the $\mathbf{z}$ axis of the CRYOPAD axes system. The $\mathbf{z}$ axis of the crystal is in the direction [0, 0, 1], which

Reflection	Polarisation Matrix
$(2,2,0)$	$\begin{pmatrix} -0.827\,(0.005) & 0.013\,(0.004) & -0.013\,(0.004) \\ -0.013\,(0.005) & -0.816\,(0.004) & -0.040\,(0.004) \\ -0.000\,(0.005) & -0.013\,(0.005) & 1.017\,(0.004) \end{pmatrix}$
$(6,2,0)$	$\begin{pmatrix} 0.325\,(0.009) & 0.027\,(0.009) & -0.027\,(0.009) \\ 0.000\,(0.009) & 0.299\,(0.008) & 0.027\,(0.009) \\ 0.000\,(0.009) & 0.041\,(0.009) & 1.008\,(0.008) \end{pmatrix}$
$(6,6,0)$	$\begin{pmatrix} 0.869\,(0.012) & 0.014\,(0.014) & 0.028\,(0.013) \\ 0.028\,(0.014) & 0.870\,(0.012) & 0.014\,(0.014) \\ 0.000\,(0.014) & 0.070\,(0.014) & 1.040\,(0.011) \end{pmatrix}$

TABLE 4.6. The polarization matrices observed for the 220, 620 and 660 reflections. The polarization is less than one in the xx and yy channels and one in the zz channel for all of the reflections, $xx \approx yy < zz$. The polarization in the xx channel increases as $\mathbf{Q}$ increases, (2, 2, 0)<(6, 2, 0)<(6, 6, 0).

indicates that the scattering is due to a moment that lies in the crystallographic **c** direction. All of the matrices that correspond to family 2, seen in figure 4.8.1, have the pattern $xx \approx yy < zz$, which indicates that the magnetic moment is consistently along **c**.

Consideration of the basis vectors of the Γ_5 and Γ_7 IRs allows us to determine which IR describes the magnetic structure from the knowledge that $\mathbf{M}(\mathbf{Q})_\perp$, lies in the direction of **c**. The table 4.7, lists the basis vectors that are associated with the atomic sites $m_2 : (\frac{1}{2}, \frac{3}{4}, \frac{1}{4})$ and $m_3 : (\frac{1}{4}, \frac{1}{2}, \frac{3}{4})$ for the Γ_5 and Γ_7 IRs. The table also includes the basis vectors of the domains s that are found when the rotations of space group G are applied. The final column shows the sum of the two basis vectors and gives the Fourier sum of the moments that are observed for the reflections of family 2.

The Γ_5 IR consists of the basis vectors $\boldsymbol{\psi}_2$ and $\boldsymbol{\psi}_3$ and the sum of the basis vectors for atoms $d = 2$, 3 would give a moment that is parallel or anti-parallel to the direction

Basis Vector	Domain	Site 2			Site 3			Sum		
$\boldsymbol{\psi}_2$	1	$\frac{2}{\sqrt{6}}$	$\frac{1}{\sqrt{6}}$	$\frac{1}{\sqrt{6}}$	$\frac{-2}{\sqrt{6}}$	$\frac{-1}{\sqrt{6}}$	$\frac{1}{\sqrt{6}}$	0	0	$\frac{2}{\sqrt{6}}$
	2	$\frac{-1}{\sqrt{6}}$	$\frac{-2}{\sqrt{6}}$	$\frac{1}{\sqrt{6}}$	$\frac{1}{\sqrt{6}}$	$\frac{2}{\sqrt{6}}$	$\frac{1}{\sqrt{6}}$	0	0	$\frac{2}{\sqrt{6}}$
	3	$\frac{-1}{\sqrt{6}}$	$\frac{1}{\sqrt{6}}$	$\frac{-2}{\sqrt{6}}$	$\frac{1}{\sqrt{6}}$	$\frac{-1}{\sqrt{6}}$	$\frac{-2}{\sqrt{6}}$	0	0	$\frac{-4}{\sqrt{6}}$
$\boldsymbol{\psi}_3$	1	0	$\frac{-1}{\sqrt{2}}$	$\frac{1}{\sqrt{2}}$	0	$\frac{1}{\sqrt{2}}$	$\frac{1}{\sqrt{2}}$	0	0	$\frac{2}{\sqrt{2}}$
	2	$\frac{-1}{\sqrt{2}}$	0	$\frac{-1}{\sqrt{2}}$	$\frac{1}{\sqrt{2}}$	0	$\frac{-1}{\sqrt{2}}$	0	0	$\frac{-2}{\sqrt{2}}$
	3	$\frac{1}{\sqrt{2}}$	$\frac{1}{\sqrt{2}}$	0	$\frac{-1}{\sqrt{2}}$	$\frac{-1}{\sqrt{2}}$	0	0	0	0
$\boldsymbol{\psi}_4$	1	0	$\frac{-1}{\sqrt{2}}$	$\frac{1}{\sqrt{2}}$	0	$\frac{-1}{\sqrt{2}}$	$\frac{-1}{\sqrt{2}}$	0	$\frac{-2}{\sqrt{2}}$	0
	2	0	$\frac{1}{\sqrt{2}}$	$\frac{-1}{\sqrt{2}}$	0	$\frac{1}{\sqrt{2}}$	$\frac{1}{\sqrt{2}}$	0	$\frac{2}{\sqrt{2}}$	0
$\boldsymbol{\psi}_5$	1	$\frac{1}{\sqrt{2}}$	0	$\frac{1}{\sqrt{2}}$	$\frac{1}{\sqrt{2}}$	0	$\frac{-1}{\sqrt{2}}$	$\frac{-2}{\sqrt{2}}$	0	0
	2	$\frac{-1}{\sqrt{2}}$	0	$\frac{-1}{\sqrt{2}}$	$\frac{-1}{\sqrt{2}}$	0	$\frac{1}{\sqrt{2}}$	$\frac{2}{\sqrt{2}}$	0	0
$\boldsymbol{\psi}_6$	1	$\frac{-1}{\sqrt{2}}$	$\frac{-1}{\sqrt{2}}$	0	$\frac{1}{\sqrt{2}}$	$\frac{1}{\sqrt{2}}$	0	0	0	0
	2	$\frac{1}{\sqrt{2}}$	$\frac{1}{\sqrt{2}}$	0	$\frac{-1}{\sqrt{2}}$	$\frac{-1}{\sqrt{2}}$	0	0	0	0

TABLE 4.7. The normalised basis vectors for IRs Γ_5 and Γ_7, found for the atoms on sites 2 and 3 for each of the rotationally related domains. The first column of vectors corresponds to the atom site 2, the second to atom site 3 and the third column to their sum.

of **c** for all of the rotationally related domains, the same sum with moments described by $\boldsymbol{\psi}_3$ gives a moment in the direction of **c** for two of the rotationally related domains and no observable moment for the final domain, the sum of the basis vectors over atoms $d = 2$, 3 for each of the domains is shown in table, 4.7.

The basis vectors of the Γ_7 IR, when summed over atoms $d = 2$, 3 would give two non-zero results, where the sum would produce a moment vector in the direction of **-b** for the $\boldsymbol{\psi}_4$ set of basis vectors and in a moment in the direction of **a** for the $\boldsymbol{\psi}_5$ set of basis vectors. The basis vectors for the sites two and three and their sums are shown in table 4.7.

Input	Polarisation Matrix
$\boldsymbol{\psi}_2$	$\begin{pmatrix} -0.60 & 0.00 & -0.79 \\ 0.00 & -0.60 & -0.79 \\ 0.00 & 0.00 & 1.00 \end{pmatrix}$
$\boldsymbol{\psi}_3$	$\begin{pmatrix} -0.85 & 0.00 & -0.53 \\ 0.00 & -0.85 & -0.53 \\ 0.00 & 0.00 & 1.00 \end{pmatrix}$
expt	$\begin{pmatrix} -0.827\,(0.005) & 0.013\,(0.004) & -0.013\,(0.004) \\ -0.013\,(0.005) & -0.816\,(0.004) & -0.040\,(0.004) \\ -0.000\,(0.005) & -0.013\,(0.005) & 1.017\,(0.004) \end{pmatrix}$

TABLE 4.8. The calculated and experimental polarization matrices observed for the 220 reflections. The polarization is less than one in the xx and yy channels and one in the zz channel for all of the reflections, $xx \approx yy < zz$. The polarization in the xz and yz channels is non-zero for the calculated matrices.

As the data indicate that the moment is in the c direction, the magnetic structure must be described by the Γ_5 IR. Let us now turn our attention to the basis vectors that belong to this IR and the calculation of the polarization matrices.

4.8.2. The calculated polarization matrices for the [0, 0, 1] orientation. The experimental polarisation matrices indicates that the moment must be descirbed by the Γ_5 irreducible representation, which consists of two basis vectors $\boldsymbol{\psi}_2$ and $\boldsymbol{\psi}_3$, the calculated plots for the basis vectors, $\boldsymbol{\psi}_2$ and $\boldsymbol{\psi}_3$, of domain 1 are shown in figures 4.14 and 4.15 respectively. Calculated matrices for the (2, 2, 0) reflection for domain 1 of ψ_2 and ψ_3 are shown in table 4.8, with the experimental value, for reference.

The matrices in table 4.8 were calculated following the steps outlined in section, 4.7.3, with a moment size of 3.0, as found in the paper of Champion *et al*. The agreement between the calculated polarization matrices is reasonably good along the diagonal elements, following the pattern, $xx \approx yy < zz$. The xx and yy elements of $\boldsymbol{\psi}_2$ are

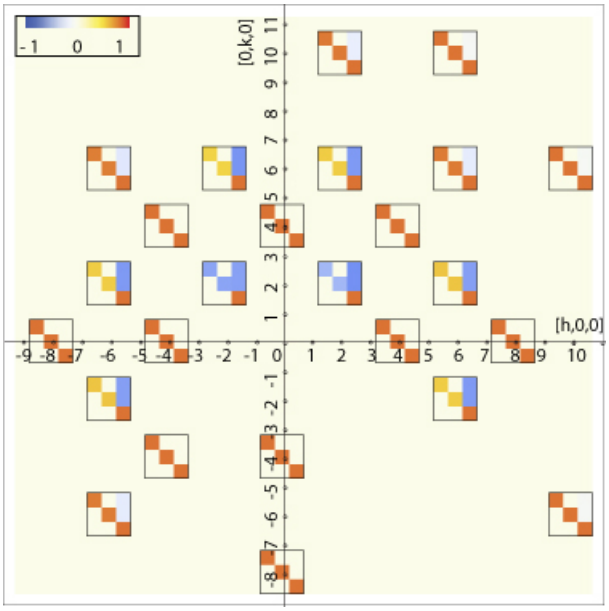

FIGURE 4.14. The plot of the calculated polarisation matrices for $\boldsymbol{\psi_2}$, domain 1. The diagonal elements have the pattern $xx = yy < zz$, which indicates that the magnetic interaction vector is in the c direction. The off diagonal elements are in the P_f=z channel is non-zero, which disagrees with the experimentally observed plots.

larger than those of $\boldsymbol{\psi}_3$ because, for domain one, the magnetic interaction vector is larger for $\boldsymbol{\psi}_3$ than $\boldsymbol{\psi}_2$, by a ratio of $\frac{1}{\sqrt{6}}$ to $\frac{1}{\sqrt{2}}$, from table, 4.7.

The calculated matrices have off-diagonal elements that are not observed in the experimental data. The non-zero matrix elements for P_f=z arises due to interference from the nuclear and magnetic scattering, described as $\frac{R_{nz}}{\sigma}$, in section 2.2.4.3 in the chapter on neutron scattering, chapter 2. The matrices for all of the reflections measured in the [0, 0, 1] orientation are shown in 4.14 and 4.15 for $\boldsymbol{\psi}_2$ than $\boldsymbol{\psi}_3$ respectively. The plots indicate that the pattern of non-zero elements in the P_f=z column is repeated for all reflections that have a magnetic contribution.

The calculated plot for the basis vectors, $\boldsymbol{\psi_2}$ and $\boldsymbol{\psi_3}$, that includes the domain averaging and with a moment size of 3.0 $\boldsymbol{\mu}_B$ is shown in is shown in table 4.9 and figure 4.16. The calculated matrices and plots are in reasonably good agreement with the experimental matrices and data plots as all of the matrices have the pattern $xx = yy < zz$ and there are no off-diagonal elements.

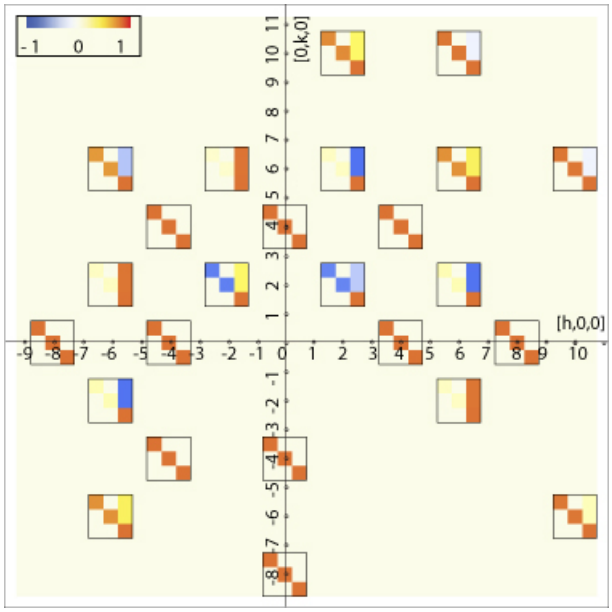

FIGURE 4.15. The plot of the calculated polarisation matrices for $\boldsymbol{\psi_3}$, domain 1. The diagonal elements have the pattern $xx = yy < zz$, which indicates that the magnetic interaction vector is in the c direction. The off diagonal elements are in the P_f=z channel is non-zero, which disagrees with the experimentally observed plots and the magnetic scattering is stronger in the diagonal elements of the matrix than that observed for $\boldsymbol{\psi_2}$, domain 1.

Input	Polarisation Matrix
$\boldsymbol{\psi}_2$	$\begin{pmatrix} -0.78 & 0.00 & 0.00 \\ 0.00 & -0.78 & 0.00 \\ 0.00 & 0.00 & 1.00 \end{pmatrix}$
$\boldsymbol{\psi}_3$	$\begin{pmatrix} -0.78 & 0.00 & 0.00 \\ 0.00 & -0.78 & 0.00 \\ 0.00 & 0.00 & 1.00 \end{pmatrix}$
expt	$\begin{pmatrix} -0.827\,(0.005) & 0.013\,(0.004) & -0.013\,(0.004) \\ -0.013\,(0.005) & -0.816\,(0.004) & -0.040\,(0.004) \\ -0.000\,(0.005) & -0.013\,(0.005) & 1.017\,(0.004) \end{pmatrix}$

TABLE 4.9. The calculated and experimental polarization matrices observed for the 220 reflections, for each of the basis vectors that belong to the Γ_5 IR. The different domains that are listed in table 4.7 and their time reversed counterparts are averaged over as described in section, 4.7.3 of this chapter. The polarization is less than one in the xx and yy channels and one in the zz channel for all of the reflections, $xx \approx yy < zz$. The matrices are all diagonal and the matrices generated by $\boldsymbol{\psi}_2$ and $\boldsymbol{\psi}_2$ are equivalent.

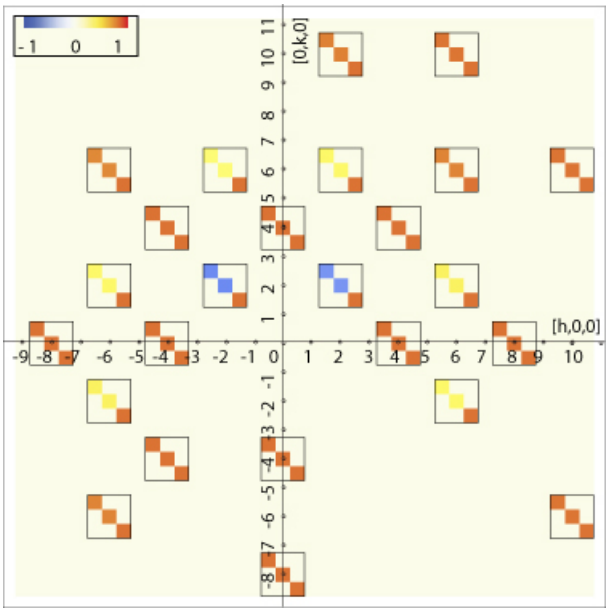

FIGURE 4.16. The calculated plot for both $\boldsymbol{\psi_2}$ and $\boldsymbol{\psi_3}$ of Γ_5 when domain averaging is included in the description of the magnetic structure. The magnetic interaction vector can be understood to lie in the direction of the CRYOPAD z axis which is the [0, 0, 1] crystallographic direction.

The matrices calculated for $\boldsymbol{\psi_2}$ and $\boldsymbol{\psi_3}$ are equivalent and indicate that the values returned for the different basis vectors is equal when the domain averaging is taken into account.

For completeness the Γ_7, domain averaged calculated matrix map is plotted. The calculated data show that the magnetic interaction vector lies consistently in the xy plane, as is indicated in the table 4.7, where only the component in the y direction can be detected. The data calculated for the Γ_7 IR serve to underline that the magnetic structure is best described by the Γ_5 IR.

4.8.3. Summary for [0, 0, 1] orientation. The data that was collected in the [0, 0, 1] orientation for the the set of reflections that belong to family one indicated that the sum over the moments on the tetrahedra sum to zero, confirming that the structure is antiferromagnetic. The data collected for the reflections that correspond the second family indicate that the observed moment lies in the direction of **c** and hence the magnetic structure is described by the Γ_5 irreducible representation. The

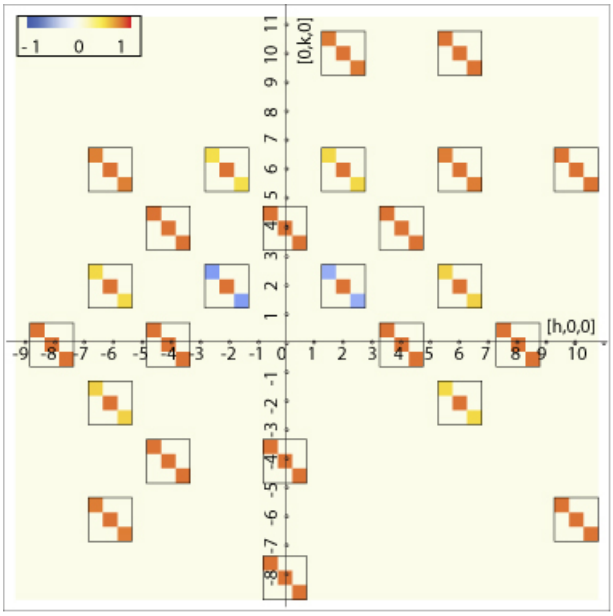

FIGURE 4.17. The calculated plot for the domain averaged description of Γ_7 where the domains included in the average include the basis vectors $\boldsymbol{\psi_4}$, $\boldsymbol{\psi_5}$ and $\boldsymbol{\psi_6}$ and their time reversed counterparts. The plots does not agree well with the experimental data as the matrix elements do not follow the pattern $xx = yy < zz$. The data indicates instead that the magnetic interaction vector lies in the CRYOPAD y direction.

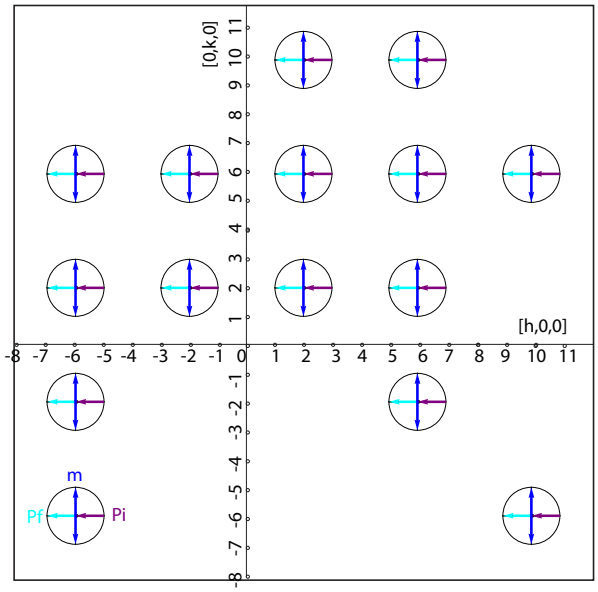

FIGURE 4.18. Representation of the magnetic interaction vector that is observed for each of the magnetic reflections inspected in the 001 plane. The incident polarization is shown by the arrow pointing into the circle and the final polarisation is shown by the arrow pointing outward, where the polarization is described for the magnetic scattering only. The double pointed arrow indicates the moment.

correspondence between the plots of the experimental data and the data calculated for the Γ_5 IR, when domain averaging is included, is very good. The plot of the calculated values for the domain averaged structure indicate that the basis vectors of $\boldsymbol{\psi}_2$ and $\boldsymbol{\psi}_3$ are indistinguishable in this orientation.

4.8.4. The experimental polarization matrices for the $[1\bar{1}0]$ orientation.

The experimental data that was gathered in the $[1\bar{1}0]$ orientation is shown in plot 4.19, where the incident polarisation is positive in all the channels. The reflections that can be seen at positions $h_{4p}k_{4q}l_{4r}$ correspond to those that are non-magnetic and again can be seen to return matrices that are diagonal with no reduction in polarisation in any of the channels.

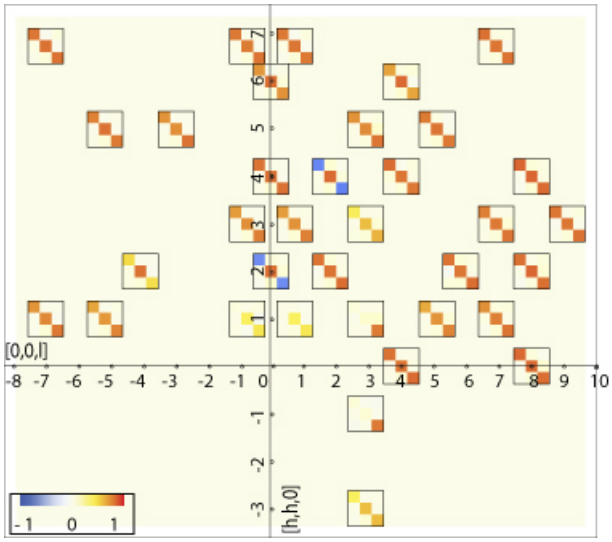

FIGURE 4.19. A colour map of each of the polarisation matrices for the $[1\bar{1}0]$ orientation shown with respect to the position of the scattering in reciprocal space. The incident polarisation is positive for the x, y and z channels. The matrices for the set of reflections with $h_{4p}h_{4p}l_{4q}$ are diagonal and unitary. The matrices at positions $h_{4p\pm2}$, $h_{4p\pm2}$, l_{4q} and h_{4p}, h_{4p}, $l_{4q\pm2}$ are diagonal and unitary in the yy channel. The matrices for the set of reflections $h_{4n\pm1}$, $h_{4n\pm1}$, $l_{4n\pm1}$ and $h_{4n\pm1}$, $h_{4n\pm1}$, $l_{4n\mp1}$ are again diagonal and have $xx < yy < zz$.

The reflections that can be seen at the positions $h_{4p\pm2}$, $h_{4p\pm2}$, l_{4q} and h_{4p}, h_{4p}, $l_{4q\pm2}$ that correspond to family two can be seen to have a reduction in the polarization of the xx and zz channels. The pattern now indicates that the magnetic interaction

Reflection	Polarisation Matrix (Error)
$(2, 2, 0)$	$\begin{pmatrix} -0.821\ (0.005) & 0.053\ (0.006) & -0.026\ (0.006) \\ -0.026\ (0.006) & 1.008\ (0.004) & 0.080\ (0.006) \\ -0.027\ (0.006) & 0.106\ (0.006) & -0.823\ (0.005) \end{pmatrix}$
$(2, 2, \bar{4})$	$\begin{pmatrix} 0.602\ (0.012) & -0.014\ (0.012) & -0.014\ (0.012) \\ 0.027\ (0.012) & 1.000\ (0.010) & -0.027\ (0.013) \\ 0.027\ (0.012) & 0.069\ (0.012) & 0.576\ (0.011) \end{pmatrix}$
$(4, 4, 2)$	$\begin{pmatrix} -0.862\ (0.020) & 0.097\ (0.023) & 0.000\ (0.023) \\ 0.014\ (0.022) & 1.017\ (0.024) & 0.056\ (0.022) \\ 0.014\ (0.021) & 0.084\ (0.022) & -0.893\ (0.022) \end{pmatrix}$

TABLE 4.10. The polarization matrices observed for the (2, 2, 0), (2, 2, $\bar{4}$) and (4, 4, 2) reflections. The matrices are all diagonal, which indicates that there is domain averaging. The polarization matrices imply the magnetic interaction vector is in the y direction, as $xx \approx zz < yy$.

vector lies in the xy plane, with the strongest magnetic contribution to the matrices observed in the [h, h, 0] direction and a much weaker contribution to the matrices observed in the directions that are toward [0, 0, l]. The comparison between the matrices recorded at the points [4, 4, 2] and [2, 2, 4] demonstrate the difference between the moment observed along the two different axes, table 4.10. The table also includes the polarization matrix recorded for the [2, 2, 0] position, which may be compared to the matrix included in table 4.6 the difference indicates that the observed moment has the same magnitude, but now lies in the **y** direction of the CRYOPAD axis system. The pattern is indicative of a magnetic interaction vector that lies in the crystallographic direction **c** which agrees with the observation made from the data gathered in the [0, 0, 1] orientation.

The experimental matrices recorded at the $h_{4n\pm1}$, $h_{4n\pm1}$, $l_{4n\pm1}$ and $h_{4n\pm1}$, $h_{4n\pm1}$, $l_{4n\mp1}$ reciprocal lattice points return values in polarization channels which can be described $xx < yy < zz$. The pattern implies that the orientation of the magnetic interaction vector mostly lies in the **z** direction for reflections that belong to families three and

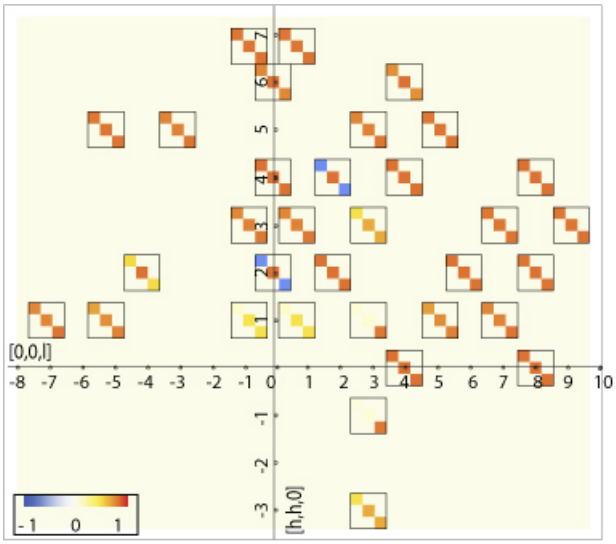

FIGURE 4.20. The matrix map of the calculated matrices for the reflections that investigated in the (1, $\bar{1}$, 0) scattering plane. The calculations were performed with a magnetic structure that was described by $\boldsymbol{\psi}_2$ and $\boldsymbol{\psi}_3$ with averaging over all domains. The incident polarisation is positive in all channels. The calculated data plotted is in good agreement with the experimental data plotted in figure 4.19.

four. The matrices observed at points [1, 1, 3] and [1, 1, $\bar{3}$] return values of zero of the xx and yy channels and are positive in the zz channel. The matrices for these reflections indicate that the magnetic interaction vector lies in the direction of **z** and that the magnetic and nuclear scattering has an equivalent intensity. The reduction in the magnitude of the magnetic scattering due to the form factor can again be observed, and is most clearly seen in the increase of the matrix values of the reciprocal lattice points with $[h, h, h]$, where $h = 2p + 1$.

4.8.5. The calculated polarization matrices for the [1, $\bar{1}$, 0] orientation.

The previous set of reflections has established that the structure must be described by the Γ_5 IR, with domain averaging. The plot of the data calculated for the basis vectors $\boldsymbol{\psi_2}$ and $\boldsymbol{\psi_3}$ with equally populated domains and with a moment magnitude of 3.0 μ_B is shown in figure 4.20. The data is plotted on a single map as the values that are returned for the polarization matrices are again equivalent for the two basis vectors, once domain averaging has been taken into account. The plot of the data

indicates that, with the inclusion of the different possible domains, the matrix maps are virtually equivalent for the experimental and calculated data.

4.8.6. Summary for the [1, $\bar{1}$, 0] orientation. The polarization matrices that have been recorded in the [1, $\bar{1}$, 0] orientation again confirm that the Γ_5 irreducible representation correctly describes the magnetic structure of $Er_2Ti_2O_7$. The data also indicates that there are rotationally related domains present in the sample and that these are equally populated. The polarization matrices that were calculated using both the $\boldsymbol{\psi}_2$ and $\boldsymbol{\psi}_3$ fitted the data extremely well, when the domain averaging was included in the calculations.

4.8.7. Data analysis methodology. A comparison of the calculated data and the experimental data was made to determine the goodness of fit, using the equation,

$$\chi = \frac{1}{q\ m\ n} \sum_{q} \sum_{m,\,n} (\mathbf{P}_{f\ expt_{q,m,n}} - \mathbf{P}_{f\ calc_{q,m,n}})^2 \tag{4.31}$$

where, m is the direction of the incident polarization, $\mathbf{P}_i$, and m = (x, y or z) and n is the direction of the final polarization, $\mathbf{P}_f$, n= (x, y or z). The basis vectors that describe the data belong either to $\boldsymbol{\psi}_2$ or $\boldsymbol{\psi}_3$ where they are indistinguishable when the domain averaging from equally populated domains is taken into account. The only free variable is, therefore, the magnitude of the magnetic moment and the best fit is given by a moment of $3.5\mu_B$ which agrees well with the value that is expected from the crystal field measurements, $3.8\mu_B$, and moment found from the diffraction data, 3.0 μ_B, [**11**]. The RMS average difference for calculated and experimental data sets is 0.005, which is less than the average statistical error for the matrix elements, 0.01.

Previously it was stated by the author, [**35**], that the magnetic structure was described by the ψ_2 basis vector, whereas the discussion of results above indicates that this distinction cannot be made. The mistake arose due to the way in which the basis vectors are combined in a linear combination, the details of which will be outlined below. The basis vectors that are associated with the different models, and a linear combination of them were used as input to the program. The coefficients of the basis vectors, and the S-domains that are associated with them, were varied at random to find the best fit to the data. It was established, by randomly varying the S-domain populations the that volume fraction of each of the S-domains were equivalent and the coefficients of the basis vectors were the only free variables. The data also indicate that the order was described by the Γ_5 IR, where an explanation for this statement has been given in the results section. The Γ_5 IR contains only two basis vectors, ψ_2, ψ_3,and the sum of the absolute value of the coefficients, is unity,

$$|c_2| + |c_3| = 1 \tag{4.32}$$

The input for the coefficients was found by considering one variable, c_2, as, $|c_2| = 1-|c_3|$. Polarization matrices were calculated for this variable in the range -1< c_2 <1 and compared to the experimental data. The error arose as the correct statement for the relationship between the coefficients is the following,

$$|c_2|^2 + |c_3|^2 = 1 \tag{4.33}$$

The coefficients in the original calculations did not include the normalization required to ensure that the linear combination of the basis vectors does not have a length greater than unity.

4.9. Discussion of Results

To gain insight to the reason for the indistinguishability of the different basis vectors the intensity that is recorded in the xx, yy and zz channels will be determined for the magnetic interaction vectors that are observed in each of the domains for family two.

4.9.1. The calculation of the matrix elements. As stated in the introduction to polarimetry and neutron scattering the elements of the polarization matrix are found from the ratio of the difference and the sum of the intensity of the spin flip and non-spin flip channels for each of the matrix elements,

$$P_f = \frac{I^+ - I^-}{I^+ + I^-}, \tag{4.34}$$

where I^+ and I^- is the intensity measured in the final S^+ and S^- channels respectively. Where the intensity may be found from the relation,

$$I = |\langle \sigma' | V | \sigma \rangle|^2, \tag{4.35}$$

where the values σ and $\sigma\prime$ indicate the initial and final polarization and are represented by spinors and V is the potential. In the case that there is no scattering from the nuclear spin the potential is described by the inner product of a vector of Pauli matrices and the magnetic interaction vector summed with a 2×2 identity matrix multiplied by nuclear contribution to the scattering,

$$\hat{V}(\mathbf{Q}) = \hat{V}_N(\mathbf{Q})\,\mathbf{1} + \hat{V}_M(\mathbf{Q}) \cdot \boldsymbol{\sigma} \tag{4.36}$$

In the case of the magnetic reflections that are observed in the [0, 0, 1] orientation, which have a magnetic component in the **z** direction, of the CRYOPAD axis system,

Domain	$\mathbf{M}_\perp$	I^+	I^-	$\frac{I^+-I^-}{I^++I^-}$
1	$0\ 0\ \frac{2}{\sqrt{6}}$	$\lvert n\rvert^2+\frac{2nm^*}{\sqrt{6}}+\frac{2n^*m}{\sqrt{6}}+\frac{2\lvert m\rvert^2}{3}$	0	1
2	$0\ 0\ \frac{2}{\sqrt{6}}$	$\lvert n\rvert^2+\frac{2nm^*}{\sqrt{6}}+\frac{2n^*m}{\sqrt{6}}+\frac{2\lvert m\rvert^2}{3}$	0	1
3	$0\ 0\ \frac{-4}{\sqrt{6}}$	$\lvert n\rvert^2-\frac{4nm^*}{\sqrt{6}}-\frac{4n^*m}{\sqrt{6}}+\frac{8\lvert m\rvert^2}{3}$	0	1
Total	$0\ 0\ 0$	$3\lvert n\rvert^2+4\lvert m\rvert^2$	0	1

TABLE 4.11. The calculated intensity for the positive and negative channels of the final polarization for the $\boldsymbol{\psi}_3$ basis vector. The positive intensity recorded for the each of the domains is different. After the interference terms have cancelled the sum contains only n^2 and m^2 terms.

the nuclear contribution the potential may be written,

$$V = \begin{pmatrix} n+m_z & 0 \\ 0 & n-m_z \end{pmatrix} \tag{4.37}$$

From 4.9.1, the intensity of the scattering that is incident in the z direction and measured in the $+z$ direction is found from the complex conjugate transpose of,

$$\begin{pmatrix} 1 & 0 \end{pmatrix} \begin{pmatrix} n+m_z & 0 \\ 0 & n-m_z \end{pmatrix} \begin{pmatrix} 1 \\ 0 \end{pmatrix} \tag{4.38}$$

Similarly, the intensity of the scattering that is incident in the z direction and measured in the $-z$ direction is found from the complex conjugate transpose of,

$$\begin{pmatrix} 0 & 1 \end{pmatrix} \begin{pmatrix} n+m_z & 0 \\ 0 & n-m_z \end{pmatrix} \begin{pmatrix} 1 \\ 0 \end{pmatrix} \tag{4.39}$$

The normalized magnetic interaction vectors are shown in table for $\boldsymbol{\psi}_2$ and $\boldsymbol{\psi}_3$ in table 4.7, and the calculated intensities in the positive and negative channels are shown in table 4.11 and 4.12 respectively.

As each domain contributes separately to the rotation of the neutron polarization the sum over the scattering from the different domains is made after the intensity is found for each of the different structures. After the intensity is calculated the nuclear

Domain	$\mathbf{M}_\perp$	I^+	I^-	$\frac{I^+-I^-}{I^++I^-}$
1	$0\ 0\ \frac{2}{\sqrt{2}}$	$\lvert n\rvert^2 + \frac{2nm^*}{\sqrt{2}} + \frac{2n^*m}{\sqrt{2}} + 2\lvert m\rvert^2$	0	1
2	$0\ 0\ \frac{-2}{\sqrt{2}}$	$\lvert n\rvert^2 - \frac{2nm^*}{\sqrt{2}} - \frac{2n^*m}{\sqrt{2}} + 2\lvert m\rvert^2$	0	1
3	$0\ 0\ 0$	$\lvert n\rvert^2$	0	1
Total	$0\ 0\ 0$	$3\lvert n\rvert^2 + 4\lvert m\rvert^2$	0	1

TABLE 4.12. The calculated intensity for the positive and negative channels of the final polarization for the $\boldsymbol{\psi}_3$ basis vector. The positive intensity recorded for the each of the domains is different. After the interference terms have cancelled the sum contains only n^2 and m^2 terms. The total intensity in the positive channel is equivalent to that found for ψ_2, table 4.11

and magnetic interference terms of each of the domains continue to have opposing signs, hence when the contributions from the different domains are summed to give the overall value in I^+ channel is $3|n|^2 + 4|m|^2$. Due to the cancellation of the nuclear and magnetic interference the intensity in the positive channel can seen to be equivalent for the basis vectors $\boldsymbol{\psi}_2$ and $\boldsymbol{\psi}_3$ and the value returned in the zz element of the polarization matrix is always unity.

The process may be repeated for the xz and yz channels, which were shown to be non-zero when the magnetic structure is described by one domain, table 4.8 and figures 4.14 and 4.15. These channels return the values that correspond to the magnetic and nuclear interference only, $\frac{2nm^*}{\sqrt{2}} + \frac{2n^*m}{\sqrt{2}}$ and $-\frac{2nm^*}{\sqrt{2}} - \frac{2n^*m}{\sqrt{2}}$, in table 4.12, and described as $\frac{R_{nm}}{\sigma}$ in the general matrix in section 3.2.4.3 in chapter 3. From the relation above it can be seen that these terms will cancel.

The magnitude of the magnetic scattering in the xx and yy channels can also be seen to be dependent on the domain considered, table 4.8 and figures 4.14 and 4.15 and this is due to the size of the magnetic interaction vector, which is different for each of the domains, tables 4.11 and 4.12. The total scattering, when the sum over the domains is taken into account is dependent only on the absolute values of the nuclear

and magnetic scattering $|n|^2$ and $|m|^2$, which allows one to determine the IR but not the basis vector.

4.10. Conclusion

The analysis and fit of the ^{3}He decay indicates that when fitting to an element of the polarization matrix the correct function to describe the polarization of the cell is a hyperbolic tan function. This may be fitted with as a line in the region of usefulness for a ^{3}He cell, which is approximately 80% to 40%. The linear fit can be seen to describe the measurements well. The transmission is not fitted so well, as though the features are reproduced the scale is not correct in the calculated data.

The systematic errors that arise in polarimetry tend to be large as evidenced by the presence of off-diagonal terms in the matrices that should contain only nuclear scattering. When there is only nuclear scattering it should not possible for any off-diagonal elements to be non-zero, if these elements are non-zero it is due to an incorrect orientation of the polarization. In order to be certain that these off-diagonal elements are due only to errors in the orientation of the polarization and not to a feature of the sample it may be better to calibrate CRYOPAD at the beginning of experiments with a standard sample that is known not to have any magnetic properties.

The Γ_5 irreducible representation describes the magnetic structure and would agree with an order-by-disorder transition. The basis vectors that describe the structure cannot be determined when balanced S-domains are present as the continuous rotational symmetry of the XY planes is indistinguishable from the rotational symmetry of the different domain orientations, i.e. the global symmetry has not been broken. It is impossible using any sort of bulk probe to make a distinction between them, and all diffraction techniques report the averaged structure. The S-domains arise

due to degeneracy of the cubic crystallographic structure and are indicative of it. The result published in the JPCM paper, which indicated that the basis vectors were distinguishable, was incorrect. The error arose due to an incorrect normalization of the different basis vectors that prevented the proper cancellation of the interference terms.

The matrix plot of the data is a useful interpretive tool as it allows the visualization of the magnetic structure with respect to the position in reciprocal space. From these plots a large amount of information may readily be inferred, such as the orientation of the magnetic interaction vector and the decrease in the intensity of the magnetic peaks due to the form factor.

Further work on $Er_2Ti_2O_7$ could determine the effect of the application of a magnetic field on the magnetic structure as this will select one of the basis vectors preferentially, though the information that is gained by this experiment would still not give a conclusive answer as to the low temperature structure. Measurements of the magnetic susceptibility by Mirebeau *et al.*, [**23**], and the crystal field measurements, [**22**], indicate that there is a low-lying Ising component to the structure. The work by Mirebeau *et al* shows that the susceptibility is almost spherical at high temperatures, becoming flatter at lower temperatures as the restriction of the moment to the XY plane increases. The measurement of this component, that was not observed in the polarimetry experiment, may well give further insight to the low temperature magnetic order and the fluctuations observed by Lago *et al*, [**42**].

References

[1] Ramirez A P, *Annu. Rev. Mater. Sci.*, **24**, 453, (1994)

[2] Greedan J E, *J. Mater. Chem.*, **11** 37 (2001)

[3] Gardner J S, Gingras M J P, Greedan J E, *Rev. Mod. Phys.*, **82**, 53 (2010)

[4] Bramwell S T, Field M N, Harris M J, Parkin I P, *J. Phys.: Condens. Matt.*, **12**, 483 (2000)

[5] Reimers J, Greedan J E, Stager V C, Bjorgvinnsen M, Subramanian M A, *Phys. Rev. B*, **43** 5692 (1991)

[6] Harris M J, Bramwell S T, McMorrow D F, Zeiske T, Godfrey K W *Phys. Rev. Lett.*, **79**, 2554 (1997)

[7] Bramwell ST, Harris MJ, den Hertog BC *et al*, *Phys. Rev. Lett.* **87** 047205 (2001)

[8] Fennell T, Petrenko O A, Fäk B *et al*, *Phys. Rev. B*, *70*, 134408 (2004)

[9] Fennell T, Petrenko O A, Fäk B *et al*, *Phys. Rev. B*, *72*, 224411 (2005)

[10] T. Fennell *et al*, *Science*, **415**, 326 (2009)

[11] Champion J D M, Harris M J, Holdsworth P C W, et al., *Phys. Rev. B*, **68**, 020401(R) (2003)

[12] Poole A, Wills A S, Leliévre-Berna E, *J. Phys.: Condens. Matter* **19** 452201 (2007)

[13] Poole A, Leliévre-Berna E, Wills A S, *Physica B*, **404**, 2535 (2009)

[14] von Gaertner H R, *Neues Jb Mineralog. Geol. Palaontol. Beilage-Bd Abt. A*, **61**, 1 (1930)

[15] Roth R S, *J. Res. Natl. Bur. Stand.*, **56**, 17 (1956)

[16] Knop O, Brisse F, Castelliz L, *Can. J. Chem.*, **47**, 971 (1965)

[17] Scherbakova L G, Mamsurova L G, Sukhanova G E *Russian Chemical Reviews*, **48**, 423 (1979)

[18] Knop O, Brisse F, Castelliz L, Sutarno, *Can. J. Chem.*, **43**, 2812 (1965)

[19] Blöte H W J, Weilinga R F, Huiskamp H, *Physica* , **43** , 549 (1969)

[20] van Geuns *Phd Thesis, University of Lieden* (1966) *citation taken from,* [**19**]

[21] Dasgupta P, Jana Y and Ghosh D, *Solid State Comms.*, **139**, 424 (2006)

[22] Shirai M, *Experimental Investigations of Frustrated Antiferromagnets* , UCL

[23] Cao H, Gukasov A, Mirebeau I, Bonville P, Decorse C, Dhalenne G, *Phys. Rev. Lett.*, **103**, 056402 (2009)

[24] Bramwell S T, Gingras M J, Reimers J, *J. Appl. Phys.*, **75** 5523 (1994)

[25] Villain J, Bideaux R, Carton J.-P, Conie R, *J. Phys*, **41**, 1263, (1980)

[26] Blundell S, *Magnetism in Condensed Matter*, Oxford University Press, Oxford, (2001)

[27] Champion J D M, Holdsworth P C W, *J. Phys.: Condens. Matter* **19** S665 (2004)

[28] Champion J D M, *Theoretical and Experimental Investigations of Frustrated Pyrochlore Magnets* , UCL

[29] Palmer S E, Chalker J T, *Phys. Rev. B*, **62** 488 (2000)

[30] Tinkham M, *Group Theory and Quantum Mechanics* McGraw-Hill, (1964)

[31] McMorrow D F, Zeiske T, Bramwell S T, Harris M J, King P J C *J. Magn. Magn. Mat.*, **177**, 757, (1998)

[32] O.V. Kovalev, *Irreducible Representations of the Space Groups,* Gordon and Breach, New York, (1965)

[33] Wills A S, *Physica B* **276**, 680 (2000), program available from

`www.ccp14.ac.uk`

[34] Reimers J, Greedan J E, Stager V C, Bjorgvinnsen M, Subramanian M A, *Phys. Rev. B*, **43** 5692 (1991)

[35] Leliévre-Berna E, Brown PJ, Tasset F, *Physica B* **397** 138 (2007)

[36] Batz M, Beaßler S, Heil W, Otten E W, Rudersdorf J, Schmiedeskamp J, Sobolev Y, Wolf M, *J. Res. Natl. Inst. Stand. Technol.*, **110**, 293 (2005)

[37] Heil W, Humblot H, Otten E, Schafer M, Sarkau R, Leduc M *Phys. Lett. A* **201** 337 (1995)

[38] Heil W, Dreyer J, Hofmann D, Humblot H, Lelievre-Berna E, Tasset F *Physica B* **267** 328 (1999)

[39] Newbury N, Barton A, Cates G, Happer W, Middleton H *Phys. Rev. A* **48** 4411 (1993)

[40] Izyumov Y A, Naish V E and Ozerov R P, *Neutron diffraction of magnetic materials*, Consultants Bureau, Plenum Publishing Corporation, New York, (1991)

[41] Ruff J P C, Clancy J P, Bourque A, White M A, Ramazanoglu M, Gardner J S, Qiu Y, Copley J R D, Johnson M B, Dabkowska H A and Gaulin B D *Phys. Rev. Lett.*, **101**, 147205 (2008)

[42] Lago J, Lancaster T, Blundell S J, Bramwell S T, Pratt F L, Shirai M and Baines C, *J. Phys.: Condens. Mat.*, **17**, 979, (2005)

[43] Shirane G, Shapiro S M, Tranquada J M, *Neutron Scattering with a Triple-Axis Spectrometer*, Cambridge University Press, (2002)

[44] Finger T, Senff D, Schmalzl K, Schmidt W, Regnault L P, Becker P, Bohatý L, Braden M, *J. Phys.: Conf. Ser.*, **211** 012001(2010)

CHAPTER 5

Spherical Neutron Polarimetry Study of MnWO4

5.1. Introduction

Manganese Tungstunate, $MnWO_4$, is a multiferroic material, [**1, 2**] with a spontaneous electric polarization that occurs simultaneously with a second order phase transition into a cycloidal, antiferromagnetic phase, [**3, 4, 5**]. $MnWO_4$ also exhibits coupling between these types of order such that an applied magnetic field induces a change in the direction of the electric polarization, [**5, 6, 7**] and the application of an electric field will produce a change in the magnetic domain populations, [**1, 10, 9**].

This chapter will present the results from a neutron polarimetry experiment that investigated the magnetic structure of $MnWO_4$ and response of the electric structure to an applied electric field. The results of the latter part of the experiment were published in reference, [**10**]. The chapter will begin with a review of the literature that describes the magnetic structure, the group theory and the multiferroic properties, this will be followed with a explanation of the experimental set-up to allow an electric field to be applied across the sample, a presentation of the neutron polarimetry measurements and a discussion of the results.

5.2. Literature Review of Magnetic Structure determination

The magnetic structure of $MnWO_4$ was originally determined in 1969 by H. Dachs, E. Stoll and H. Weitzel, [**11**] from neutron diffraction experiments. Dachs *et al* identified that the material underwent a magnetic phase transition at T_N =7.5 K to become

a collinear antiferromagnet with wave vector $\mathbf{k}$=($\pm\frac{1}{4}$, $\frac{1}{2}$, $\frac{1}{2}$). The magnetic structure proposed by Dachs *et. al.* differs from the other transition metal tungstunates, TMWO$_4$ (TM = Ni, Co and Fe), which have wave vector $\mathbf{k}$=($\pm\frac{1}{2}$, 0, 0), despite all analogues adopting the wolframite crystallographic structure, [**11**]. The wolframite structure is monoclinic and is best described by the space group $P2/c$, the TM ions reside on the $2f$ site, which is a two-fold rotational center. The crystal structure has inversion centers that in the face-centered positions, shown in pink on in figure 5.1. Dachs *et al* attribute $\mathbf{k}$=($\pm\frac{1}{4}$, $\frac{1}{2}$, $\frac{1}{2}$) propagation vector to strong antiferromagnetic exchange in the z direction found in MnWO$_4$, and not observed in the other members of the TMWO$_4$ family. The exchange pathways and crystallographic structure are shown in figure 5.1 and the material is characterized by layers of manganese at the centre of distorted oxygen octahedra, separated by tungsten atoms, stacked perpendicular to **b**. Due to the ground state structure, Lautenschläger *et al* expanded on the initial research in order to explore the possibility that MnWO$_4$ was an example of the axial-next-nearest-neighbour Ising (ANNNI) model, [**7**].

5.2.1. Magnetic structure. The ANNNI model describes structures that have ferromagnetic exchange, J, between the nearest neighbour atoms within a layer and antiferromagnetic exchange between the first layer and the nearest and next nearest layers, J_1, J_2, [**13**]. When $J_2 > J_2/2$ the ANNNI model predicts the ground state observed by Dachs in MnWO$_4$, [**11**], where there is a first order transition at T<6.8 K into a sinusoidally ordered phase with two moments up followed by two moments down, as shown in figure 5.2. The structure is collinear and commensurate (CC), where the moments are at an angle of $\approx 35^\circ$ to the a axis and fully in the ac plane, however, this structure repeats antiferromagnetically in the perpendicular direction, which disagrees with the requirement for J to be ferromagnetic within the ANNNI model, [**13**].

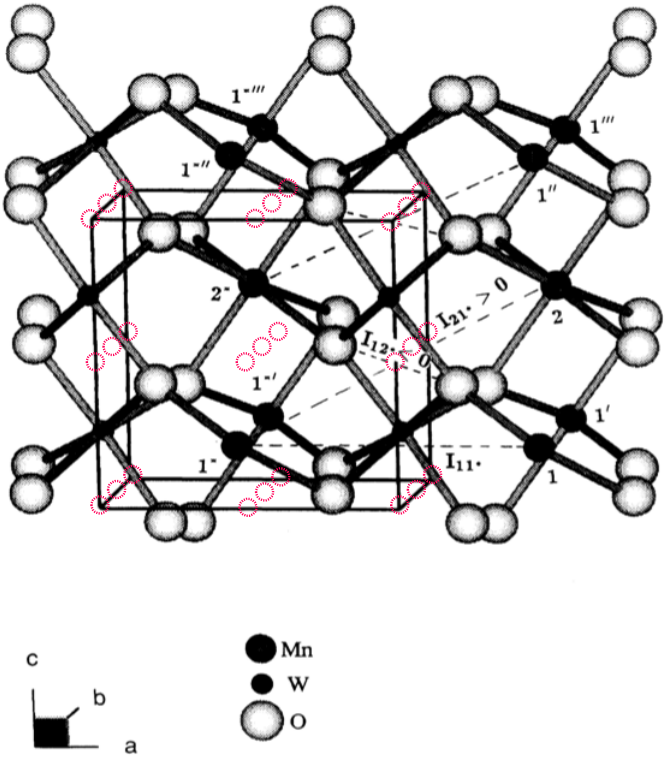

FIGURE 5.1. The structure of $MnWO_4$ with the exchange pathways shown with the dashed lines. The structure forms layers of Mn and W, which are surrounded by oxygen octahedra. The numbers 1, 2 indicate the Mn^{3+} in a single unit cell. The symbols *, $'$ and $''$ indicate progression in the a, b and c directions, respectively. The open dashed circles indicate the positions of the inversion centers. After, [**7**].

The ANNNI model also predicts that the commensurate ground state is preceded by a collinear modulated structure that locks in to rational multiples of 2π. The specific heat measurements undertaken by Lautenshlager *et. al.*, described in reference [**7**], and shown in figure 5.3, indicate that $MnWO_4$ undergoes three magnetic phase transitions at 6.8 K, 12.6 K and 13.4 K, two more than been identified previously from susceptibility measurements, [**14**]. Thus, Lautenschläger *et. al.* disproved the ANNNI model, but the work revealed that $MnWO_4$ had an unusual phase diagram, with an incommensurate magnetic structure, that had not been observed previously.

Lautenschläger *et. al.*, undertook neutron diffraction experiments on both powder and single crystal samples to determine the magnetic structure of the higher temperature phases. The neutron diffraction data collected from the powder sample

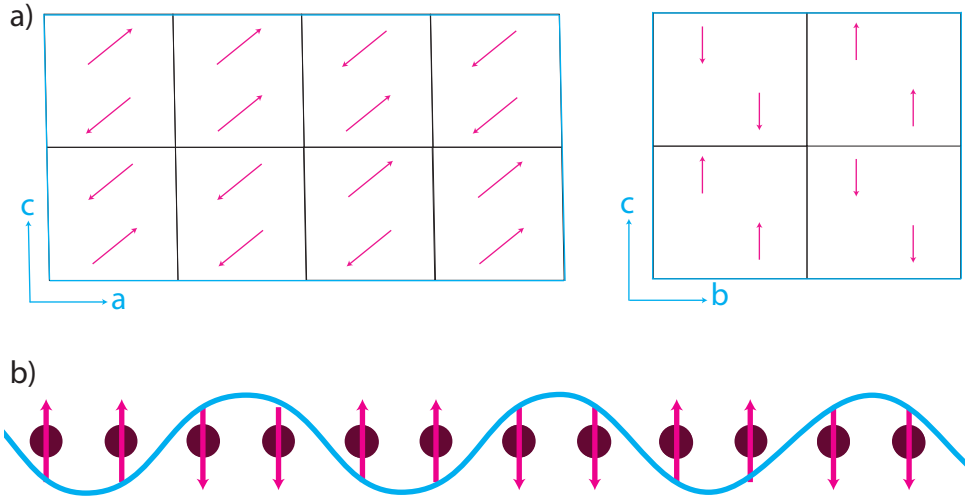

FIGURE 5.2. The magnetic structure of $MnWO_4$ in the collinear commensurate phase, CC (AF1). a) The magnetic structure is described by two upward moments followed by two downward moments in the *ac* plane, and is antiferromagnetic in the *b* direction. b) The pattern of moments can be described by a sine wave.

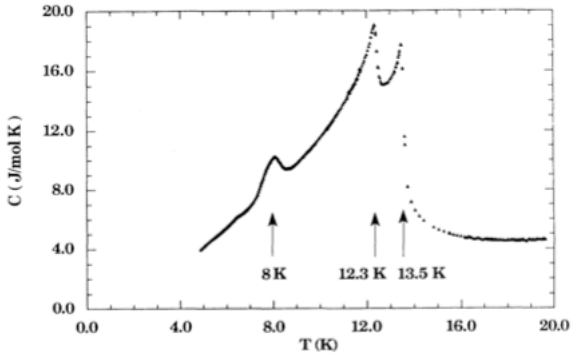

FIGURE 5.3. Specific heat of $MnWO_4$ showing the two second order phase transitions at 13.5K and 12.3K and the first order phase transition at 8K. After, [**7**].

indicated the wave vector for both of the high temperature phases was incommensurate with $\mathbf{k}$=($\pm$0.214, $\frac{1}{2}$, 0.457), where $\mathbf{k}$-vector allows only sinusoidal or cycloidal magnetic structures, [**7**].

The phase transition that occurs at 13.4 K is second order and the magnetic structure found between 13.4 K and 12.6 K is incommensurate and collinear, the ICC (AF3) phase. The moments lie in the *ac* plane, $\approx 35^\circ$ from the *a* axis with a sinusoidal amplitude modulation. The transition at 12.6 K is again second order and leaves

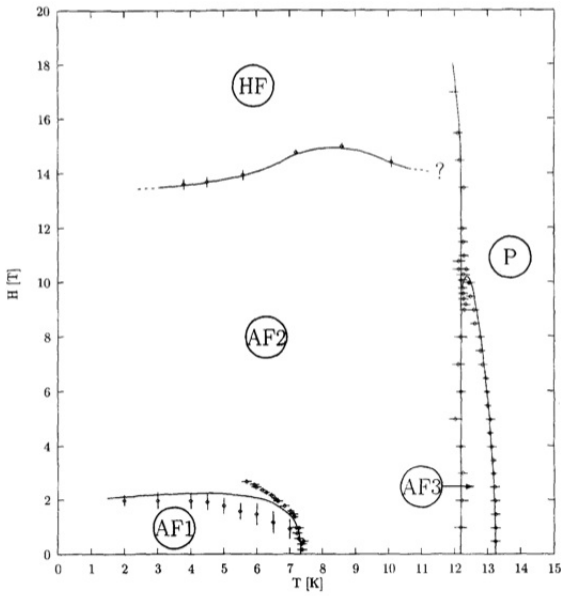

FIGURE 5.4. Magnetic phase diagram of $MnWO_4$, determined from susceptibility and magnetization measurements in applied magnetic fields, with a magnetic field applied parallel to the *ac* or easy direction, after, [**15**].

the **k**-vector is unchanged, the magnetic structure is cycloidal with an additional component in the *b* direction that is out of phase with that in the *ac* plane, [**7**], thus the phase is incommensurate and non-collinear ICNC (AF2). From the susceptibility and magnetization measurements in applied magnetic fields a phase diagram was generated, figure 5.4, where the data is plotted with respect to temperature and applied magnetic field, [**15**]. An interesting point to note is that the magnetic field is applied along the easy direction, *i.e.* 35° from the *a* axis in the *ac* plane, and stabilizes the cycloidal structure, ICNC (AF2).

As the temperature decreases $MnWO_4$ undergoes a first order phase transition from the incommensurate collinear antiferromagnetic ICNC to a commensurate collinear CC (AF1) ground state. The temperature of this first order transition is slightly sample dependent, [**7**] and occurs at $\approx$ 7 K.

Lautenschläger *et. al.* suggest that the selection of the easy direction the CC (AF1) and ICC (AF3) phases is due to single ion anisotropy. The competition between the anisotropy and the isotropic exchange interactions give rise to the incommensurate

propagation vector, [**7**]. The cycloidal structure arises as the frustrated moments saturate. As the temperature is further reduced the importance of the single ion term increases and the saturated moments again fall in line with the easy direction in the *ac* plane, $\approx 35^{\circ}$ from the *a* axis. The argument for the presence of single ion anisotropy, despite the isotropic, high spin, d^5 arrangement of the outer electrons, is supported by the inelastic magnetic scattering, [**16, 17**], which shows a small gap at the centre of the Brillioun Zone, and an asymmetric response to an applied magnetic field, [**17**].

5.2.2. The Symmetry of $MnWO_4$. Group theory was employed by Lautenschläger *et. al.* to determine the incommensurate magnetic structures found in the ICC (AF3) and ICNC (AF2) phases, [**7**]. Furthermore, the breaking of inversion symmetry is a unifying theme in incommensurate ferroelectric magnets, [**19, 20, 21, 22, 23**]. Let us, therefore, review the approach taken by Lautenschläger *et. al.* to the symmetry analysis of $MnWO_4$, [**7**].

The crystallographic structure of $MnWO_4$ is best described by the space group $P2_1/c_1$, which contains the operations,

$$G = \{\ (x, y, z),\ \ (x, \bar{y}, z + \frac{1}{2}),\ \ (\bar{x}, \bar{y}, \bar{z}),\ \ (\bar{x}, y, \bar{z} + \frac{1}{2})\ \}.$$

The magnetic structure of the CC (AF1) phase, the ICC (AF3) phase and the ICNC (AF2) phase can all be described with the general propagation vector $\mathbf{k}$=(k_x, $\frac{1}{2}$, k_z), which is left invariant by the operations of the little group,

$$G_{\mathbf{k}} = P_c = \{\ (x, y, z),\ \ (x, \bar{y}, z + \frac{1}{2})\ \}.$$

these operations can be used to generate the two positions of the Mn^{2+} ions,

$$\mathbf{r}_{Mn_1} = \begin{pmatrix} 0.5 \\ y \\ 0.25 \end{pmatrix}, \quad \mathbf{r}_{Mn_2} = \begin{pmatrix} 0.5 \\ -y \\ 0.25 + \frac{1}{2} \end{pmatrix},$$

which are related by a glide reflection, or an inversion about the origin. For both the atoms to fall within the first unit cell of the space group, $P2_1/c_1$, a translation by (0, 1, 0) must be applied to Mn_2. When the returning operation and the translation (0, 0, $\frac{1}{2}$) are combined with $\mathbf{k}$=(k_x, $\frac{1}{2}$, k_z) it is found that the moment on the second atom is related to Mn_1 by a phase of $a = e^{-i\pi k_z}$. The final magnetic structure is a combination of the permutation representation Γ_{perm}, which describes the relationship between the sites and the axial vector representation Γ_{axial}, that describes the relationship between the moments on those sites. The combination of the two representations gives the overall representation for the magnetic structure, $\Gamma_{mag} = \Gamma_{perm} \times \Gamma_{axial}$.

$$\Gamma_{perm}[(x,y,z)] = \begin{pmatrix} 1 & 0 \\ 0 & 1 \end{pmatrix}, \quad \Gamma_{perm}[(x,\bar{y},z+\tfrac{1}{2})] = \begin{pmatrix} 0 & -a^2 \\ -1 & 0 \end{pmatrix}$$

$$\Gamma_{axial}[(x,y,z)] = \begin{pmatrix} 1 & 0 & 0 \\ 0 & 1 & 0 \\ 0 & 0 & 1 \end{pmatrix}, \qquad \Gamma_{axial}[(x,\bar{y},z)] = \begin{pmatrix} -1 & 0 & 0 \\ 0 & 1 & 0 \\ 0 & 0 & -1 \end{pmatrix}$$

Γ_{mag} may be decomposed into the two irreducible representations of $G_{\mathbf{k}}$ according to $\Gamma = 3\Gamma_1^1 + 3\Gamma_2^1$. The associated basis vectors are given in table 5.1.

A linear combination of the basis vectors will describe the possible magnetic structures. The components of the basis vectors indicate that the relationship between the magnetic moments is described by a cosine function, $m_{j\alpha}(\mathbf{r})$, that is dependent on the position of the atom with respect to the propagation of the magnetic structure $\mathbf{k}$. The position of the atom is described with refrence to the unit cell under inspection

Representation	Basis Vector	Mn_1			Mn_2		
	ψ_1	1	0	0	a*	0	0
Γ_1^1	ψ_2	0	1	0	0	-a*	0
	ψ_3	0	0	1	0	0	a*
	ψ_4	1	0	0	-a*	0	0
Γ_2^1	ψ_5	0	1	0	0	a*	0
	ψ_6	0	0	1	0	0	-a*

TABLE 5.1. The basis vectors that describe the phase relationship of the atoms within the unit cell, where $a = e^{-i\pi k_z}$, [**7**].

and the position in the lattice is described by $\mathbf{R}_l = l_1\mathbf{a} + l_2\mathbf{b} + l_3\mathbf{c}$, where l_n is an integer.

$$m_{j\alpha}(\mathbf{r}) = m_{j\alpha}^{(0)} \cos(2\pi\mathbf{k}\cdot\mathbf{R}_l + \phi_{j\alpha}), \quad \alpha = x, y, z \tag{5.1}$$

The phase relationship between the atoms $j = 1, 2$ is given by $\phi_{2\alpha} = \phi_{1\alpha} + \pi k_z$ and the amplitude $m_{j\alpha}^{(0)}$ in the a, c direction is restricted to $m_{1\,x,z}^{(0)} = \pm m_{2\,x,z}^{(0)}$ and in the y direction as $m_{1\,y}^{(0)} = \mp m_{2\,y}^{(0)}$.

The realization of a sinusoidal wave rather than a helical wave is dependent on the amplitude m and phase ϕ that is chosen. For a sinusoidal structure to arise the coefficient for the component in the b direction must be zero whereas a helical structure will arise if all of the components have non-zero coefficients.

The group theory derived by Lautenschläger *et. al.*, [**7**] was developed further in the work by Harris, [**20**], which indicates that by also considering the inversion symmetry the phase relationship between the different basis vector components, for a variety of mutliferroic materials, is fixed. The application of the inversion symmetry leaves the free energy invariant, but does not leave the propagation vector **k** invariant. This combination acts to fix the phase of the basis vectors within each IR to give the basis vectors in table 5.2, and coefficients for these Fourier components are all real.

Representation	Basis Vector	Mn_1			Mn_2		
	ψ_1	1	0	0	a*	0	0
Γ_1^1	ψ_2	0	i	0	0	-ia*	0
	ψ_3	0	0	1	0	0	a*
	ψ_4	-i	0	0	ia*	0	0
Γ_2^1	ψ_5	0	1	0	0	-a*	0
	ψ_6	0	0	-i	0	0	ia*

TABLE 5.2. The basis vectors that describe the phase relationship of the atoms within the unit cell with the inversion symmetry taken into account, where $a = e^{-i\pi k_z}$, [**20**].

5.2.3. Summary of Magnetic Structure. The magnetic structures in the low temperature commensurate phase, CC (AF1), and the high temperature incommensurate phase, ICC (AF3), are both sinusoidal. The intermediate ICNC (AF2) phase was determined to have a cycloidal structure, which arises due to a component of the magnetic structure in the b direction that emerges during the second order phase transition and is described by a separate irreducible representation.

5.3. Literature Review of $MnWO_4$ as a Multiferroic Material

As stated previously, multiferroic materials are defined as materials that have a phase in which there is simultaneous ferroelectric, (anti)ferromagnetic and ferroelastic order. In some of these materials the ordering is coupled, such that the electric polarization may be controlled with the application of an electric field and the magnetic structure may be controlled with the application of an electric field. This section will review the evidence that $MnWO_4$ is a multiferroic in which there is coupling between the magnetic order and the electric polarization.

5.3.1. Evidence of Simultaneous Phase Transitions. In 2006 three papers were published on $MnWO_4$, from separate groups, that showed a change in the capacitance of the sample during the phase transition from the ICC (AF3) to the ICNC (AF2), phase, [**4, 3**] as well as an increase in the electric polarization, [**5**]. All of the groups indicated that there is a simultaneous ferroelectric and antiferromagnetic transition at ≈12.5 K. The figures of 5.5, which are taken from the work of Taniguchi *et. al.*, [**5**], and show the temperature equivalence of the change of the magnetic susceptibility in the b direction, an anomaly in the dielectric constant and the spontaneous electric polarization also found parallel to **b**. A comparison of the data with the specific heat measurements, shown in figure 5.3, indicate the temperature of the transitions correspond with the observed specific heat anomalies. The change of the susceptibility in the a direction and c direction can clearly be seen to agree with the first peak observed in the specific heat, whereas the spike in the dielectric constant agrees with the temperature at which the second peak occurs. The electric polarization, shown in 5.5.c, indicates that the magnitude of the electric dipole is temperature dependent and increases as the temperature decreases until the first order phase transition into the CC (AF1) phase.

The ferroelastic nature of the ICNC (AF2) phase was demonstrated by Chaudhury and co-workers, [**24**], where figure 5.6 shows that as the temperature decreases the lattice increases in the direction of c, whilst the a direction decreases. The difference in the response of the lattice parameters demonstrates the anisotropy of the magnetically ordered phase. The transition temperatures indicated in the plot can be seen to be in agreement with those in figures 5.5 and 5.3.

Further work by Taniguchi *et. al.* supported the change in the crystallographic structure with the observation of incommensurate superlattice peaks in the multiferroic phase, [**25**]. The x-ray diffraction experiment performed by the Taniguchi group indicated that super lattice peaks appeared for each of the magnetic phases, at a position

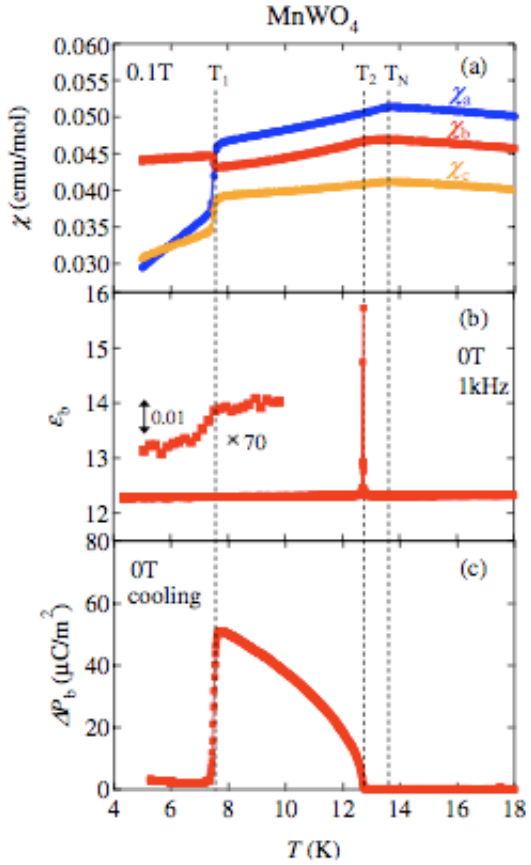

FIGURE 5.5. The data indicate that there is a simultaneous transition into an electrically polarized and magnetically ordered phase. a) The magnetic susceptibility in the different crystallographic directions. b) The dielectric constant, which indicates a sharp feature at the second phase transition. c) The magnitude of the electric polarization can be seen to be significant only in the cycloidal phase and increases as the temperature decreases, from, [**5**].

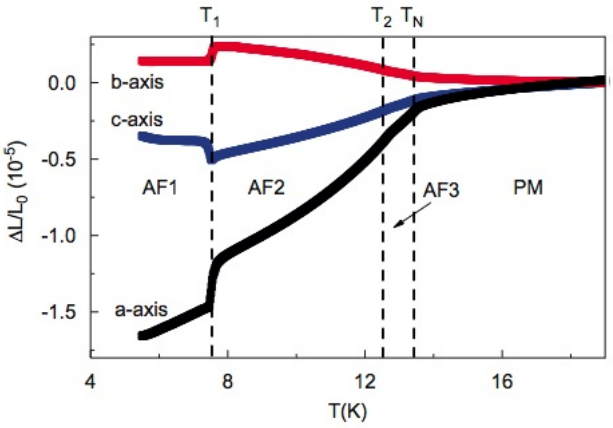

FIGURE 5.6. The change of the lattice parameters with respect to the temperature. The different rates of change in the length of the parameters shows the anisotropy of the interaction, [**24**].

twice that of the magnetic propagation vector. The intensity of the peaks was much less in the IC phases (AF3, AF2) than those observed in the CC phase (AF1) phase and intensity of the peaks increased as the temperature was lowered, in rough agreement with the increase of the electric polarization. The observations indicate that these structural changes occur due to exchange striction, [**29**], which agrees with the mechanism proposed by Chapon *et. al.* with respect to the manganate multiferroics, [**26**].

5.3.2. Evidence of Change in the Electric Polarization with Applied Magnetic Field. Taniguchi *et. al.* also demonstrate that the application of a magnetic field parallel to the **b** direction causes the electric polarization to flop from the *b* to the *a* direction, [**5**]. The figure, 5.7.a, shows the measurements of the polarization in a magnetic field applied parallel to **b** at 10.7 K. The magnitude of the electric polarization decreases as the magnetic field increases until, at field of 10.7 T, the direction of the electric polarization changes so that it is with **a**, a sharp feature is also observed in the measurements of the dielectric constant. The phase diagram of the electric polarization is similar to, but not the same as, that recorded by Ehrenberg *et. al.* who determined the magnetic phase diagram with a magnetic field applied parallel to **b**, figure 5.7, [**7, 15**]. The magnetic phase diagram indicates that there is no obvious change in the magnetic structure when the polarization flop region is entered, and, indeed, Harris suggests that the electric polarization that is observed in this phase can not be described by symmetry arguments, [**20**].

The coupling between the electric polarizability and the magnetic field in the ICNC (AF2) phase was further demonstrated by Kundys *et al*, [**28**], with measurements of the electric polarization with respect to applied field, figure 5.8 and temperature, figure 5.9. The figure 5.8 indicates that there is a simultaneous increase in the applied magnetic field and decrease in the magnitude of the electric polarizability, in agreement with the observations of Taniguchi *et. al.*, [**5**]. The magnitude of the

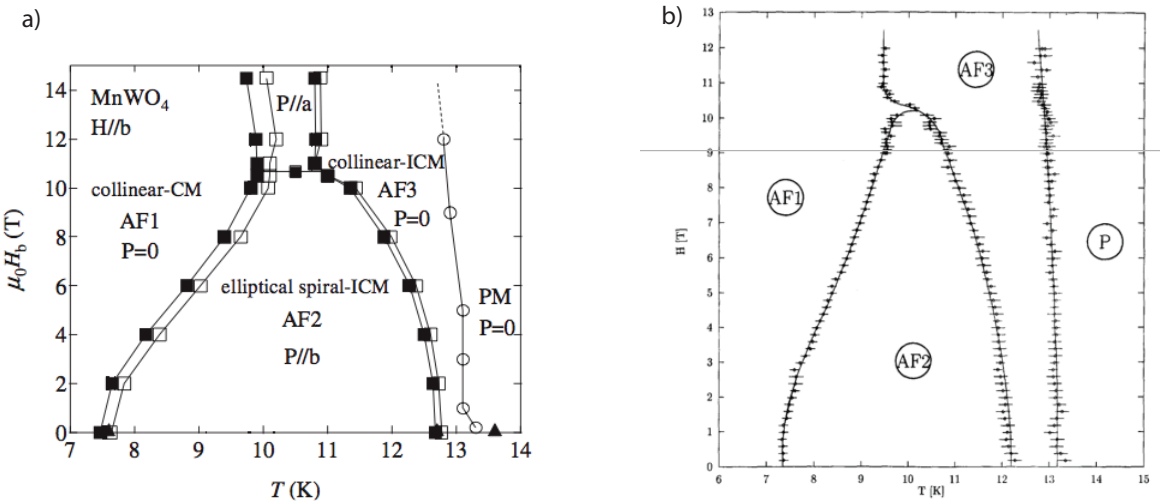

FIGURE 5.7. Phase diagrams of $MnWO_4$ with a magnetic field applied $\|\mathbf{b}$. a) The phases of the electric polarization, [**5**]. b) The magnetic structure phase diagram, determined from neutron diffraction and susceptibility measurements, [**7, 15**].

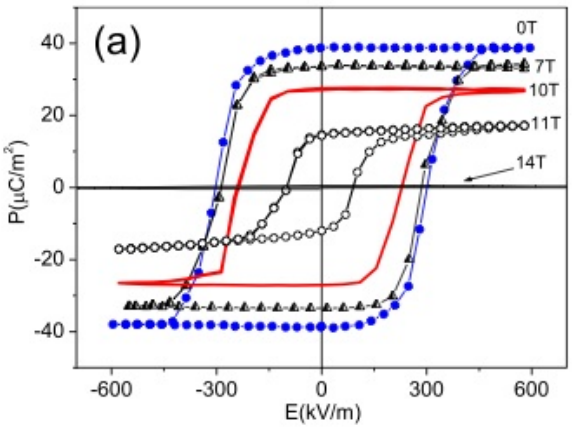

FIGURE 5.8. The change of the electric polarization with respect to the applied magnetic field recorded at 10K. The plots indicate that the magnitude of the electric polarization in the b direction can be controlled with a magnetic field, after , [**28**].

electric polarization and the magnitude of the magnetic field that is required to invert it is seen to be temperature dependent, figure 5.9, which is in agreement with the plot of the electric polarization shown in figure 5.5.

5.3.3. Evidence of Control of the Magnetic Domain Population with an Applied Electric Field. Several groups have identified, by different means,

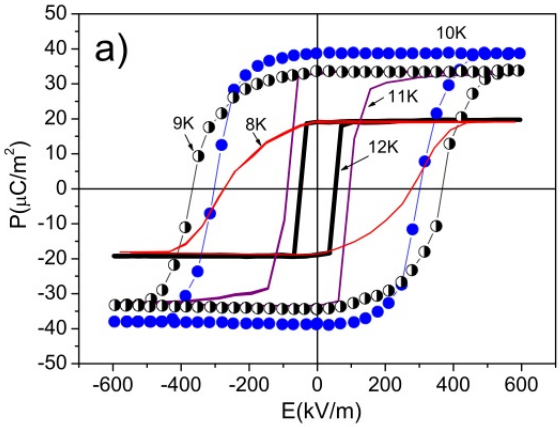

FIGURE 5.9. The change of the electric polarization with respect to temperature recorded at 0T. The plots indicate that the magnitude of the polarization and the coercive electric field is dependent on the temperature, after , [**28**].

during the course of our investigation, the ability to control the magnetic structure of $MnWO_4$ with the application of an electric field, [**10, 9, 31, 8**]. Sagayama *et. al.* measured the difference in the scattered intensity of neutron beam that had initial polarization parallel to and antiparallel to the direction of the scattering vector, **Q**, [**10**], where the scattered intensity directly correlated with the induced electric polarization. The sample was cooled in an electric field, which selects a single handedness of chiral domain, with +**k** or -**k**. The population of each handedness domain can be determined from the change in intensity due to the change in sign of the chiral, polarization dependent term of the scattering cross section described in table 2.2. When both domains are equally populated this term cancels, however, when only one of the chiral domains is populated intensity is only observed at the corresponding position in **Q**-space, i.e. at *hkl* +**k** or -**k**, [**33**]. By applying a poling electric field, where by a small electric field is applied to the sample whilst cooling, to make one domain more energetically favourable, Sagayama *et al* demonstrated that there was coupling between the electric polarization and the magnetic order. The analysis revealed that onset of the electric polarization occurred at the same temperature of the onset of the cycloidal magnetic structure, but, the magnitude of the electric dipole did not directly correlate to the ellipticity. Meier *et. al.* measure the optical second

harmonic generation (SHG) in order to directly observe the magnetic and electronic domains present in the material, [**9**]. The domains were shown to overlap perfectly and a mono-domain was created when an electric field was applied, the group concluded that the domains are most accurately described as hybrid 'magneto-electric' domains due to intrinsic link between the two properties. Finally, after the results of this thesis were published, Finger *et. al.* published an extensive neutron polarimetry investigation of $MnWO_4$ the results of which agree with the work that will be presented in the experimental section, [**31, 8**].

5.3.4. Summary. The experiments indicate that there is a simultaneous phase transition that gives rise to both magnetic order and electric polarization, and furthermore the electric polarization may be controlled with a magnetic field. The relationship between the two types of order can be understood if one considers the charge density cloud to be slightly asymmetric where the asymmetry is caused by the magnetic structure, and this gives rise to a small spontaneous dipole moment. The direction of the asymmetry may be selected for by inducing a dipole in a specific direction by the application of an electric field, and, as such the magnetic structure may be manipulated. The application of a magnetic field will cause the magnetic structure to deform and this gives the observed change in the direction of the spontaneous electric polarization.

5.4. Experimental Details

The purpose of the experiment was to determine unambiguously the magnetic structure in each of the ordered magnetic phases and to demonstrate the response of the magnetic domain population, in each of these phases, to an applied electric field. The experiment was carried out with CRYOPAD on D3 at the ILL. The sample growth and experimental arrangement will be discussed in this section.

5.4.1. Sample Growth. The sample was grown by Boothroyd *et al* in the Clarendon Laboratory, Oxford, where the single crystals of $MnWO_4$ were grown by the floating-zone method. High purity powders of $MnCO_3$ and WO_3 mixed in stoichiometric ratio and ground in a zirconia ball mill. The mixed powder was calcined at 800°C for 24 hr under CO_3 /CO gas flow. Further sintering was performed at 900°C in air with intermediate grinding. After confirming the single-phase purity of the compound, compressed rods of 10 mm diameter and 100 mm length were prepared and sintered at 1040°C for 24 hr in a vertical sintering furnace. Single crystals were grown in a four-mirror optical floating-zone furnace (Crystal Systems Inc.). The molten zone was scanned at a speed of 35 mm/hr with counter-rotation of the feed and seed rods at 25 rpm. The growth was initiated on a polycrystalline rod the first time, and subsequent runs were seeded with a single crystal from the previous run.

Single crystals were cleaved from the zone-melted boule. The phase purity and structure of the grown crystals were confirmed by powder x-ray diffraction and the crystalline quality of the crystals was checked by x-ray and neutron Laue patterns respectively. Thermogravimetric analysis of a sample of ground crystal confirmed the stoichiometric oxygen content.

5.4.2. Sample Preparation and Environment. The crystals that were grown for the experiment were checked for quality and oriented at ISIS. The cardinal directions of the crystal were identified and the sample was cut and polished to give faces perpendicular to the b direction The final dimensions of the crystal were 7.12×2.49×3.94mm where the separation between the polished ac faces was 2.49mm. The cutting and polishing of the crystal was completed by the Boothroyd group in Oxford.

The sides of the crystal were then carefully masked with PTFE tape and gold was sputtered onto the polished ac faces at the LCN, so that an electric field could be applied across the sample, the faces were polished, as well as cut, to improve the

homogeneity of the applied electric field. The conducting surface was applied directly to the crystal to achieve the maximum electric field across the sample. The crystal was then oriented with the [1, 1, 1] axis vertical on Orient Express at the ILL, such that the $(h, k, \bar{l})$ scattering plane could be inspected, and glued to a regular sample pin with Stycast epoxy resin. In this orientation those reflections with inner product $(h, k, \bar{l})\cdot$ (1, 1, 1) will fall in the scattering plane. The magnetic reflections do not fall in the scattering plane as they cannot fulfill this condition (CC $\mathbf{k}= (\frac{1}{4}, \frac{1}{2}, \frac{1}{2})$ and IC $\mathbf{k}= (\pm 0.214, \frac{1}{2}, 0.457)$. Instead they fall slightly above and slightly below the scattering plane, but can detected due to the broadness of the peaks in the vertical direction.

The pin was attached to a goniometer, which was attached to a sample stick adapted to allow the application of high voltage electric fields. An insulated copper wire was soldered onto each of the gold surfaces with indium solder to apply the electric field across the sample, indium solder was used as it has a low melting point and is less likely to disrupt the gold surface. One of the wires was connected to the high voltage equipment, via an insulated wire that ran the length of the stick, and the other wire was connected to the stick itself, which acted as the earth. The sample was then placed in an alumnium foil bag and the stick was inserted in an orange cryostat. The incident wavelength was $\lambda = 0.843$ Å.

As the measurement included the application of an electric field on the crystal, the pressure in the sample space is an important parameter. The breakdown voltage of gases is dependent on: the pressure, the temperature, the nature of the surface, particles in the gas and the electrode field. In an effort to allow the temperature to be controlled whilst avoiding electrical discharge, the pressure was maintained at ambient , [**39, 40**].

Data were recorded at 6 K, 8.6 K and 13 K to determine the magnetic structure in the CC (AF1) phase, ICNC (AF2) and ICC (AF3) respectively. A temperature

scan was recorded from 13 K to 6 K to observe the evolution of the structure and an electric field was applied at 6 K, 10 K, 11 K 12 K and 13 K to observe the effect on the domain populations.

5.5. Data Analysis

The raw data were corrected for detector efficiency and ^{3}He depolarization with the standard CRYOPAD routines, written by Jane Brown, to give the standard 3×3 polarization matrices. Due to the elevation of the peaks from the scattering plane a further correction was made to the matrix components by a purpose written Mathematica routine. The corrected data was then plotted, again in a purpose written Mathematica routine, given in appendix C. The calculation of the polarization matrices was based on the magnetic structure proposed by Lautenshlager *et. al.*, [**7**], and completed in Mufit, [**41**] (appendix D). The results were collated in an Excel spreadsheet and compared to the corrected experimental data.

This section will outline the corrections made to the data to compensate for the elevation of the reflections and the approach taken to the generation of the calculated matrices. Before the calculations are described a summary of the expected experimental matrices for a chiral magnetic structure will be presented.

5.5.1. Theory of Chiral Terms. The neutron polarimetry technique allows the polarized moments of the neutron beam to be arbitrarily oriented using a combination of two rotations corresponding to the spherical coordinate system, [**34, 35**]. All components of the polarization matrix, with polarization axes defined with **x** parallel to the scattering vector **Q**, **z** with the zone axis of the crystal and **y** completing the right handed cartesian set, are recorded, section 2.4.1. The polarization matrix is the experimental quantity that is most closely related to the polarization tensor form of the Blume Maleev equations, fully described in, [**36, 37**]. In the purely magnetic

case, when the incident polarization is positive, the matrix that should be observed has the form,

$$\mathcal{P} = \begin{pmatrix} -1 & 0 & 0 \\ B & A & C \\ B & C & -A \end{pmatrix} \tag{5.2}$$

Where xx is unity with opposite sign to the incident polarization as all the intensity is spin flip and $yx = zx = B$, $yy = -zz = A$ and $yz = zy = C$. A simple way to understand the relationship between the A and C components, when B=0, is shown in table 5.3 and is described by the matrix,

$$\begin{pmatrix} \cos\alpha & \sin\alpha \\ \sin\alpha & -\cos\alpha \end{pmatrix} \tag{5.3}$$

Where the angle α is the angle made between the incident and final polarization vectors. Half of the angle α will give the angle of the magnetic interaction vector with respect to the zone axis, θ. The matrix that describes the position of the magnetic interaction vector is equivalent to the sum of the σ_y and σ_z Pauli matrices where the matrix coefficients, $\hat{V}_M(\mathbf{Q})_y$ and $\hat{V}_M(\mathbf{Q})_z$ are real. A two by two matrix with $\alpha/2$ is the rotational matrix that gives the final polarization.

The perpendicular sine and cosine components of the cycloidal magnetic structure, when they lie perpendicular to the $\mathbf{Q}$, give rise to a non-zero 'chiral term' as polarization is generated in the $\mathbf{x}$ direction. This effect is described by the cross product between the magnetic interaction vector and its complex conjugate in the Blume Maleev equations,

$$\mathbf{P}_{f_{chiral}} = -i(\mathbf{M}_{\perp}^{*} \times \mathbf{M}_{\perp}). \tag{5.4}$$

Polarisation Diagram $P_i = y$	P_f	Polarisation Diagram $P_i = z$	P_f	Matrix Representation
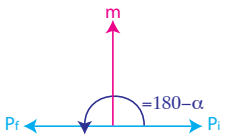	$yy = -1$ $yz = 0$	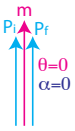	$zy = 0$ $zz = 1$	$\begin{pmatrix} -1 & 0 \\ 0 & 1 \end{pmatrix}$
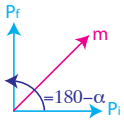	$yy = 0$ $yz = 1$	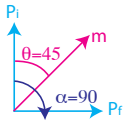	$zy = 1$ $zz = 0$	$\begin{pmatrix} 0 & 1 \\ 1 & 0 \end{pmatrix}$
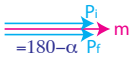	$yy = 1$ $yz = 0$	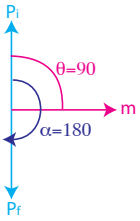	$zy = 0$ $zz = -1$	$\begin{pmatrix} 1 & 0 \\ 0 & -1 \end{pmatrix}$

TABLE 5.3. Representation of the matrix elements for the magnetic moment in various orientations.

As described by Jane Brown in reference, [**43**], the idealized experimental arrangement would have both M_y or the M_z perpendicular to **Q** in this instance the polarization tensor described in section 2.4 has the simplified form:

$$\mathcal{P} = \begin{pmatrix} -1 & 0 & 0 \\ B & A & 0 \\ B & 0 & -A \end{pmatrix} \text{ or } \mathcal{P} = \begin{pmatrix} -1 & 0 & 0 \\ -B & A & 0 \\ -B & 0 & -A \end{pmatrix} \tag{5.5}$$

With the terms,

$$A = \frac{M_1(\mathbf{k})^2 - M_2(\mathbf{k})^2}{M_1(\mathbf{k})^2 + M_2(\mathbf{k})^2} \text{ and } B = \frac{2M_1(\mathbf{k})^2 M_2(\mathbf{k})^2}{M_1(\mathbf{k})^2 + M_2(\mathbf{k})^2} \tag{5.6}$$

The A component of the matrix gives the ellipticity of the cycloid and is unity when the structure is spherical and the sine and cosine components have equivalent magnitudes. The B component is the chiral term of the matrix, the magnitude

is dependent on the population of each of the 'chiral' domains, ± **k**; when ± **k** are equally populated B=0; when the magnetism is ordered as a single **k** domain and the structure is spherical B will have a magnitude of one, with the sign of B dependent on the handedness of **k**. In general the matrix element B is always non-zero when there is a real and imaginary part of the magnetic interaction vector perpendicular to **Q** and its value is dependent on the population of the ±**k** domains that are present and the ellipticity of the structure, [**43**]. The A component is dependent only on the ellipticity, as such the ellipticity may be determined by fitting the A terms and the population of the **k** domains determined by using mixing ratios to determine the B component.

5.5.2. Corrections to orientation error in the scattering data. A simple way to correct for magnetic scattering lying above and below the scattering plane is to use the **UB** matrix, section 2.3.1.3, and calculate the direction of the reciprocal vector that is under inspection in the instrumental axis system,

$$\mathbf{h}_{xyz} = \mathbf{UB}\,\mathbf{h}_{hkl}, \tag{5.7}$$

The **UB** matrix for crystal is,

$$\mathbf{UB} = \begin{pmatrix} 0.1705 & -0.09438 & -0.03123 \\ 0.03879 & 0.09414 & -0.16347 \\ 0.11154 & 0.11154 & 0.11154 \end{pmatrix},$$

which can then be used to find the angle ρ of the elevation of the vector $\mathbf{h}_{xyz}$ and to generate a matrix that will rotate the polarization (x, y, z) to a direction approximately equivalent to the ideal instrument coordinate system (X, Y, Z),

$$\rho_{\mathbf{h}_{xyz}} = \sin^{-1}\left[h_z/\sqrt{(\mathbf{h}_{xyz}\cdot\mathbf{h}_{xyz})}\right] \tag{5.8}$$

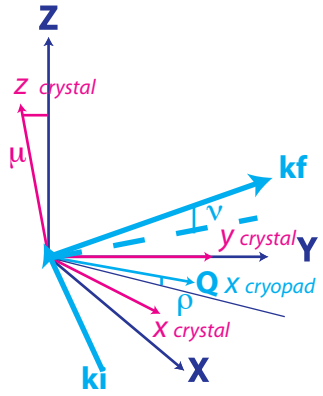

FIGURE 5.10. Diagram of the usual CRYOPAD axis system, x, y, z and the instrument axis system X, Y, Z. The angle μ is the maximum difference between the z axis of the sample and the z axis of the instrument. ρ is the angle between the scattering vector and the scattering plane. The angle ν is the elevation of the detector required to be at the optimum position to measure $\mathbf{k}_f$.

$$\mathbf{A} = \begin{pmatrix} a_{\mathrm{X}x} & a_{\mathrm{X}y} & a_{\mathrm{X}z} \\ a_{\mathrm{Y}x} & a_{\mathrm{Y}y} & a_{\mathrm{Y}z} \\ a_{\mathrm{Z}x} & a_{\mathrm{Z}y} & a_{\mathrm{Z}z} \end{pmatrix} = \begin{pmatrix} \cos\left(\rho_{\mathbf{h}_{xyz}}\right) & 0 & -\sin\left(\rho_{\mathbf{h}_{xyz}}\right) \\ 0 & 1 & 0 \\ \sin\left(\rho_{\mathbf{h}_{xyz}}\right) & 0 & \cos\left(\rho_{\mathbf{h}_{xyz}}\right) \end{pmatrix}$$

The matrix is then applied to the intensity of each of the reflections in each of the channels to determine the amount of the scattering that has been recorded in the 'wrong' polarization channel, [**42**].

5.5.3. Calculation of Model Polarization Matrices. The calculated polarization matrices were generated in the Mufit program, [**41**], which calculates the expected output from a neutron polarimetry experiment following the procedure outlined in the neutron scattering chapter. The matrices are generated by finding the spin flip and non-spin flip intensity in each of the channels and finding the ratio of the sum and the difference, as outlined in section 2.4. An example of an input file for Mufit is included in appendix D

The program defines the standard polarimetry axis system X, Y, Z by taking the scattering vector (**Q**) of the reflection under inspection and any other vector that

lies in the scattering plane. The cross product of these two vectors is then found and this is assumed to be the zone axis of the crystal, and this calculation is made for each reflection. In cases where the magnetic scattering lies in the scattering plane the same vector may be used to find the zone axis for all reflections, in the case where **Q** lies above or below the plane this can be seen to return a different zone axis for each reflection. Hence a suitable vector was calculated and used as input for each of the reflections in order for the zone axis to remain equivalent in all cases.

Different models were systematically compared to the experimental data in each of the magnetic phases, and the best match used as a starting model for the refinement. The results of these refinements are presented in the following section.

5.6. Results and Discussion

Data were recorded in each of the magnetic phases, with and without an electric field and a temperature sweep was made with to observe the evolution of the magnetic structure. The results will follow the progression of the experiment and begin with a description of the magnetic structures that were observed without an applied electric field. The first phase that will be considered is the high temperature ICC (AF3) phase, which occurs between 13.5K and 12.5K. Nuclear reflections were periodically measured to check the polarization and were used by the CRYOPAD routine to correct the for the change of the polarization of the ^{3}He cell and then removed from the data set.

5.6.1. The magnetic structure of the ICC (AF3) phase. The eight reciprocal lattice points that were inspected in the high temperature incommensurate collinear phase of $MnWO_4$ are shown in the figure 5.11. The map is of the (h, k, $\bar{l}$) scattering plane, where the magnetic reflections are above or below the plane and as such the positions of the points shown in the map are approximate.

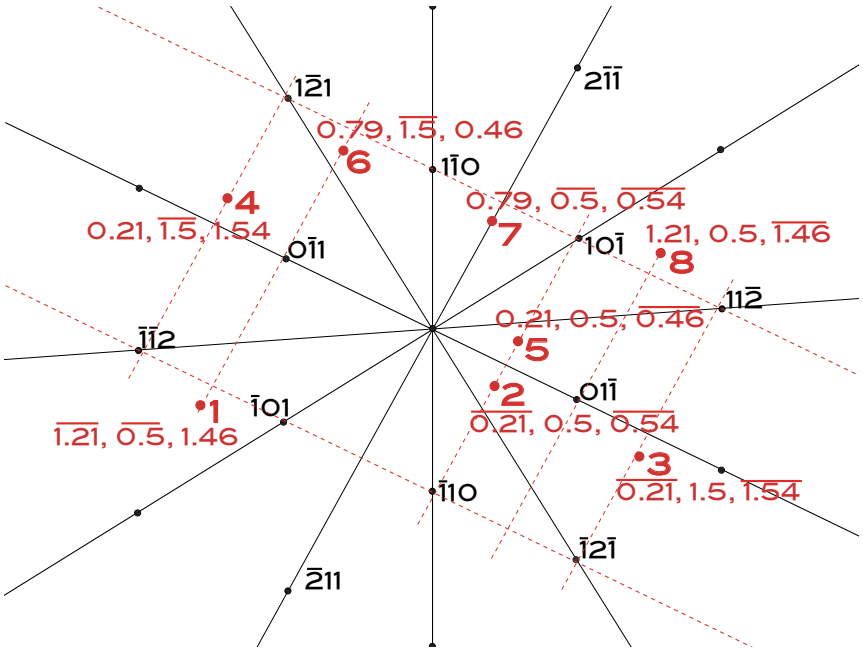

FIGURE 5.11. A map of the scattering plane that is accessed when the crystal is oriented with the [1, 1, 1] zone axis. The points marked in red are the magnetic reflections that were inspected to determine the magnetic structure of the ICC (AF3) phase.

The experimental matrices shown in figure 5.11 have positive incident polarization such that the incoming polarization for the top row of the matrix is with $+x$, the centre row is with $+y$ and the bottom row is with $+z$. Data were also collected with incident polarization with negative incident polarization where all the data is collated in appendix G. The data tables in the appendices G, F, E include the experimental data corrected for the elevation of the magnetic reflections with the experimental error, the matrices calculated by Mufit that give the best fit to this data, the difference between the calculated and fitted data for each of the channels and the RMS average of the difference for each of the different incident polarizations, x, y and z. The difference and the RMS average were calculated in excel. Before we consider the structural information that can be seen in the matrices a comparison between the data with positive and negative incident polarization will be made.

When the incident polarization x is parallel to the scattering vector $\mathbf{Q}$ the experimental matrices recorded in the with $P_i = +ve$ are equal and opposite to the matrix

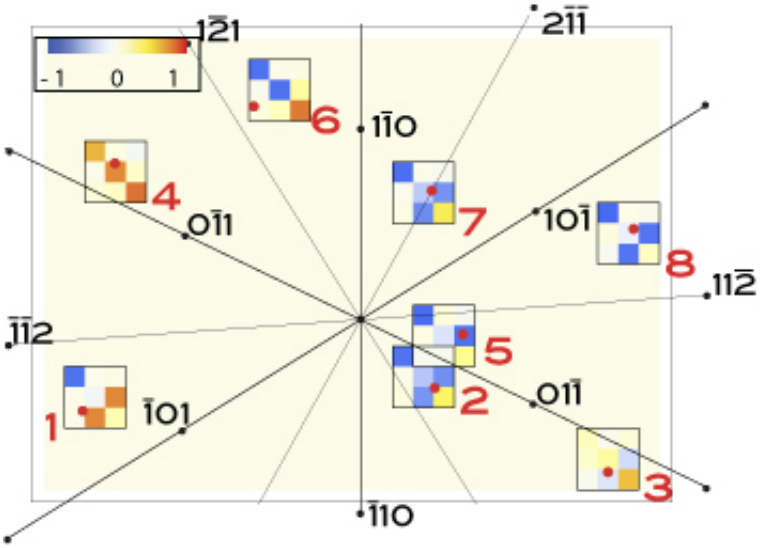

FIGURE 5.12. The values of the experimental matrices in the ICC (AF3) phase where the values of the matrices are represented by the colours indicated in the scale. The matrices are in the position in reciprocal space at which the reflection appears, as indicated by the numbered point, where the number corresponds to the map in figure 5.11 and the tables in appendix G.

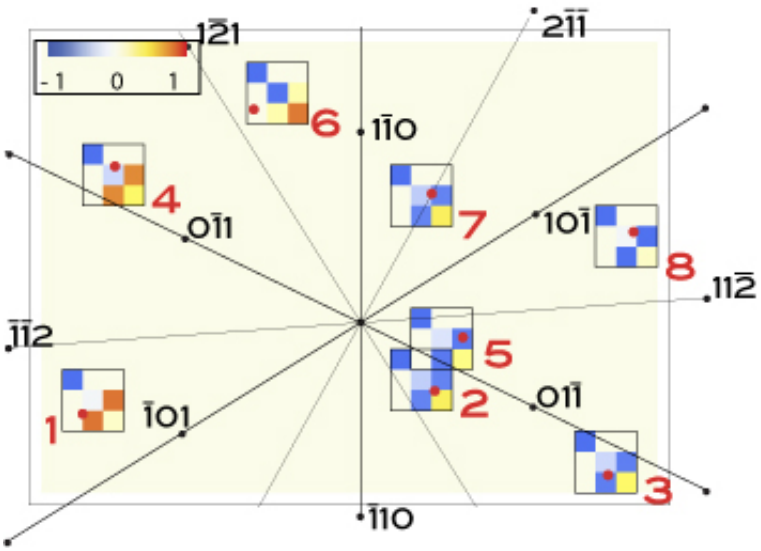

FIGURE 5.13. The matrix map of the calculated ICC (AF3) value, fitted with Mufit, where the matrix values are represented by the colours indicated in the scale. The matrices are in the position in reciprocal space at which the reflection would appear, as indicated by the numbered point, where the number corresponds to the map in figure 5.11 and the tables in appendix G. The model of the magnetic structure used to generate the values is a sinusoidal wave which is elevated by 34.9° from the *a* direction in the *ac* plane. Comparison with plot 5.12 indicates that the fit is good for all reflections, except those labelled 3 (-0.21, 1.5, -1.54) and 4 (0.21, -1.5, 1.54), a discussion of this difference is given within the text.

recorded with $P_i = -ve$. Furthermore, the values that are recorded in each of the polarization channels for purely magnetic scattering, would appear as described in subsection 5.5.1, such that $xx = \pm 1$, $yx = zx = B$, $yy = -zz = A$ and $yz = zy = C$.

A comparison of the experimental matrices of point 1 (1.21, 0.5, -1.56) with $P_i = +ve$ and $P_i = -ve$ is shown in table 5.4. The final polarization for incident polarization $P_i = +ve$ is $yy = -0.14$ and $zz = 0.23$, whereas the final polarization for incident polarization $P_i = -ve$ is $yy = 0.18$ and $zz = -0.12$. The values for C within each matrix are not equal and opposite indicating that the corrections made were not sufficient to compensate entirely for the out of plane magnetic reflections. The values of yy and zz are transposed in the $P_i = +ve$ and $P_i = -ve$ matrices, as is expected, and indicate that the error is consistent with respect to the polarization of the incident beam.

Overall the data indicate that the corrections made to compensate for the elevation of the magnetic scattering above and below the plane were not sufficient to return the ideal magnetic matrices. Let us turn our attention to the structural information that can be observed in the data.

The average of the experimental data with $P_i = +ve$ and $P_i = -ve$, is shown in the table 5.5 to compensate for the error previously described. A calculated polarization matrix for a magnetic structure that has a moments that lie in ac plane and make an angle of θ=34.9° to the a axis is also shown in the table 5.5. It can be seen that when the average of the experimental matrices is taken the symmetry of the matrix has been regained and the difference between the experimental and calculated matrices is small.

The points 3 (-0.21, 1.5, -1.54) and 4 (0.21, -1.5, 1.54) show quite poor agreement but consideration of the experimental matrices indicates that there is nuclear scattering

Reference (Reflection)	Polarization Value
1_{expt} $(-1.21, -0.5, 1.46)$ $P_i = +ve$	$\begin{pmatrix} -0.99\ (0.027) & -0.01\ (0.029) & 0.02\ (0.029) \\ 0.00\ (0.029) & -0.14\ (0.029) & 0.92\ (0.028) \\ -0.00\ (0.029) & 0.92\ (0.027) & 0.23\ (0.029) \end{pmatrix}$
1_{expt} $(-1.21, -0.5, 1.46)$ $P_i = -ve$	$\begin{pmatrix} 0.97\ (0.026) & 0.02\ (0.029) & -0.02\ (0.029) \\ -0.08\ (0.028) & 0.18\ (0.029) & -0.94\ (0.026) \\ -0.08\ (0.029) & -0.93\ (0.029) & -0.12\ (0.029) \end{pmatrix}$
1_{expt} $(-1.21, -0.5, 1.46)$ $difference$	$\begin{pmatrix} -0.02\ (0.053) & 0.01\ (0.058) & 0.00\ (0.058) \\ 0.08\ (0.057) & 0.04\ (0.058) & 0.02\ (0.054) \\ 0.08\ (0.058) & 0.01\ (0.056) & -0.100\ (0.058) \end{pmatrix}$

TABLE 5.4. The corrected experimental polarization matrices for point 1 (1.21, 0.5, -1.46) with positive $P_i = +ve$ and negative, $P_i = -ve$, incident polarization. The difference between the matrices indicates that error due to the elevation of the scattering above and below the plane is still present as in the ideal case the elements of the different matrices would all have the same magnitudes, but with opposing signs. The error in the zz channel is greater than that of the statistical experimental error.

Reference (Reflection)	Polarization Value (Error)
1_{expt} $(1.21, 0.5, -1.46)$ $average\ P_i = \pm$	$\begin{pmatrix} \mp 0.98\ (0.037) & 0.01\ (0.041) & 0.00\ (0.041) \\ 0.04\ (0.040) & \mp 0.16\ (0.041) & \pm 0.93\ (0.038) \\ 0.04\ (0.041) & \pm 0.93\ (0.040) & \pm 0.17\ (0.041) \end{pmatrix}$
1_{calc} $(1.21, 0.5, -1.46)$ $P_i = \pm ve$	$\begin{pmatrix} \mp 1.00(0.02) & 0.00(0.01) & 0.00\ (0.00) \\ 0.00\ (0.04) & \mp 0.14\ (0.02) & \pm 0.99\ (0.06) \\ 0.00\ (0.04) & \pm 0.99\ (0.06) & \pm 0.14\ (0.03) \end{pmatrix}$

TABLE 5.5. The average of the polarization matrices with incident polarization in positive and negative directions, $P_i = +ve$ and $P_i = -ve$, for point 1 (1.21, 0.5, -1.46). The average matrix shows the symmetry that is expected in the purely magnetic case. The matrix that is calculated from the model with θ=34.9° is in close agreement with the averaged experimental matrix.

incident at the same point in reciprocal space, which interferes with the magnetic scattering. There are three reasons that this can be stated unequivocally:

Reference (Reflection)	Polarization Value $(\text{Error})_{expt}$ $(\text{Difference})_{calc}$
3_{expt} $(-0.21, 1.5, -1.54)$	$\begin{pmatrix} 0.187\,(0.067) & -0.015\,(0.069) & 0.070\,(0.065) \\ 0.117\,(0.085) & 0.271\,(0.074) & -0.403\,(0.067) \\ -0.043\,(0.064) & -0.313\,(0.073) & 0.711\,(0.068) \end{pmatrix}$
3_{calc} $(-0.21, 1.5, -1.54)$	$\begin{pmatrix} -1.00\,(1.19) & 0.00\,(-0.02) & 0.00\,(0.07) \\ 0.00\,(0.12) & -0.42\,(0.69) & -0.91\,(0.51) \\ 0.00\,(-0.04) & -0.91\,(0.60) & 0.42\,(0.29) \end{pmatrix}$

TABLE 5.6. The polarization matrices for point three. The matrix indicates that there is both nuclear and magnetic contributions to the scattering at this point in reciprocal space.

(1) The value of the xx component of the matrix is positive, which is not possible if the incident polarization is with **Q** and positive and the scattering is purely magnetic, as all of the scattering should be spin flip.

(2) The yy and zz terms both have the same sign, which again is not possible if the scattering is purely magnetic.

(3) The outgoing x, y and z channels for each incident x, y and z polarization do not give a unit vector, as is the case for purely magnetic scattering when no domains are present. As there is no cancelation of the polarization the incident unit vector should only be rotated and the length should not change.

.

The experimental values for the point 3 is shown in table 5.6 and indicate that the calculated matrices for the magnetic contributions to three and four are correct, as the diagonal elements increase in magnitude $xx < yy < zz$ and the yz and zy components have the correct sign.

The figures 5.13 and 5.12 indicate the symmetry that one would expect to observe in the polarization matrices with respect to their position in reciprocal space. Let us briefly consider the plots for points 1(-1.21, -0.5, 1.46) and 8 (1.21, 0.5, -1.56). The

Reference (Reflection)	Polarization Value
1_{expt} $(-1.21, -0.5, 1.46)$	$\begin{pmatrix} -0.990\ (0.027) & -0.008\ (0.029) & 0.023\ (0.029) \\ 0.003\ (0.029) & -0.142\ (0.029) & 0.923\ (0.028) \\ -0.000\ (0.029) & 0.924\ (0.027) & 0.233\ (0.029) \end{pmatrix}$
8_{expt} $(1.21, 0.5, -1.46)$	$\begin{pmatrix} -1.041\ (0.037) & 0.007\ (0.041) & -0.050\ (0.040) \\ 0.041\ (0.044) & -0.224\ (0.043) & -0.966\ (0.040) \\ -0.056\ (-0.043) & -0.970\ (0.042) & 0.153\ (0.046) \end{pmatrix}$

TABLE 5.7. The experimental polarization matrices for points 1 (-1.21, -0.5, 1.46) and 8 (1.21, 0.5, -1.56). The reflections form a Friedel pair and experimental matrices indicate the symmetry. The value of point 1, channel yy is equivalent to the value of point 8, channel zz. The difference between the values of yy and zz within each of the matrices is indicative of the elevation of the reflections from the scattering plane.

plot indicates that the terms yz and zy are equal but opposite, whereas the diagonal components yy and zz are equivalent in the two matrices. This indicates that the moment lies at a point that is almost equidistant from both the y and z directions, as defined by CRYOPAD, and hence nearly all of the scattering is spin flip.

The aspects that are equal and opposite are due to the reflections being rotated through 180°, and the direction of the incident y polarization is inverted, $\mathbf{y}_1$=-$\mathbf{y}_z$. This is tabulated in table 5.7 and represented graphically in 5.14, which shows the position of the calculated magnetic interaction vector with respect to the direction of the incident polarization and the calculated final polarization. The position of the magnetic interaction vector is generated by Mufit, but may also be calculated by finding the normalized difference between the incident and final polarization vectors. The plot shows the position of the magnetic interaction vector when observed from different positions in reciprocal space. The magnetic interaction vector plotted at point 6 (0.79, -1.5, 0.46) indicates the vector is in the direction of z the zone axis, [1, 1, 1], whereas at points 1(-1.21, -0.5, 1.46) and 8 (1.21, 0.5, -1.56) the magnetic interaction vector is in the direction yz.

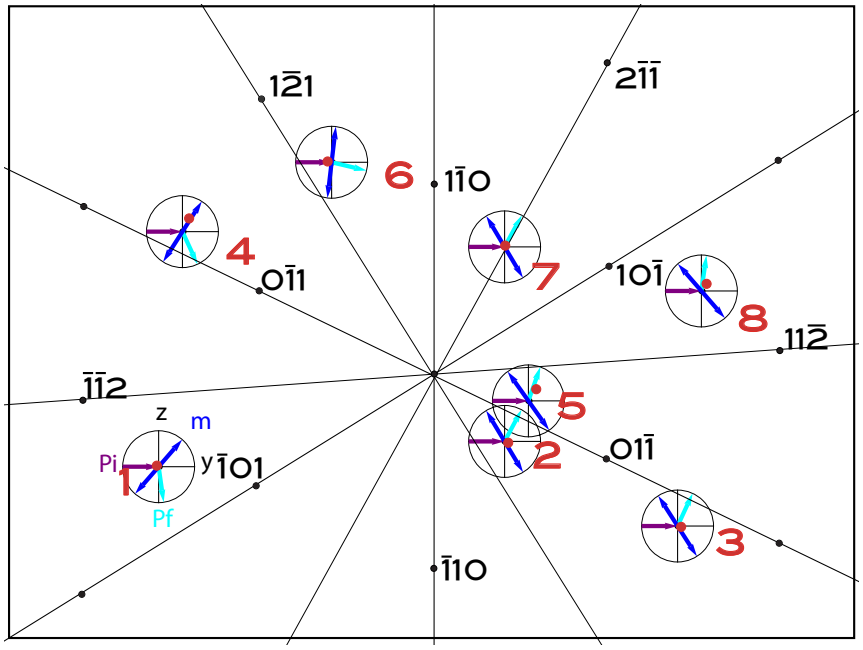

FIGURE 5.14. The measured and calculated polarization for incident polarization with +y. The experimental incident and final polarization is shown with the purple lines, where the error is indicated by the dashed lines either about the final polarization. The vector that describes the best fit to the data is shown in cyan and thus the calculated moment in the scattering plane is shown in magenta.

The best fit is tabulated with the structures determined in reference, [**7**]. The best fit of the orientation of the moment can be seen to agree well with that described by Lautenschläger *et al* , using a single IR. The phase relationship between the two atomic sites cannot be determined from neutron polarimetry, as in the sinusoidal case this leads to a reduction in the magnitude of the moment. Purely magnetic polarization matrices are not sensitive to the magnitude of the moment, only its orientation, which is equivalent on both atomic sites. A comparison of the data is shown in table 5.8.

5.6.2. The magnetic structure of the ICNC (AF2) phase. The reciprocal map of the points that were inspected in the ICNC (AF2) phase with positive incident polarization is shown in figure 5.15, where the number associated with each reflection on the map corresponds to the data tables in the appendix F. The best fit was found by comparing the polarization matrices calculated by Mufit for different

	Technique	T(K)	$\|\mathbf{m}\|$ (μ_B)	$\phi(^\circ)$	m_x	m_y	m_z
1	powder (D1B)	12.7	2.3(1)	35.0			
2	single crystal (DN4)	13.3	2.1(1)	34.8			
3	polarimetry (D3)	13.0		34.9	0.82	0.00	0.57

TABLE 5.8. The refined values for the position of the moment in the ICC (AF3) phase, recorded at the temperatures indicated. The angle ϕ is the angle from the **a** axis of the moment in the ac plane and $|\mathbf{m}|$ (μ_B) is the magnitude of the moment. The angular description of the moment is converted into the vector used as input into for the Mufit program, m_x, m_y, m_z for the polarimetry data. The values for the non-polarized data, 1 and 2, are taken from, [**7**] and can be seen to agree well with refined structure calculated from the polarimetry data.

starting models and then using the best model as the starting point for the refinement. Following a brief description of the experimental polarization matrices the calculated data for each of the starting models will be presented

The experimental matrices indicate that the magnetic structure is composed of two, perpendicular, out of phase spin density waves, to give a cycloid or a helix, and that there is an imbalance in the populations of the associated +**k** and -**k** domains. The evidence for these observations is that the yx and zx matrix elements are non-zero in the experimental polarization matrices, i.e. in figure 5.15 the elements with final polarization in the direction of x are blue or orange, and that the magnitude of the yy, yz, zy and zz is reduced compared to that found in the ICC (AF3) phase. The cycloidal or helical structure is expected, but the imbalance in the domain populations in zero field is not. The magnetic structures when defined by +**k** and -**k** should be energetically equivalent and as such when there is no perturbation to the symmetry of the system the domains that are associated with two structures are expected to be equally populated.

For completeness the first model used for to fit the data was that of the sinusoidal structure found in ICC (AF3), where the magnetic structure is sinusoidal and the

moments make an angle of 34.9° to the a direction in the ac plane. A comparison between the plots 5.15 and 5.16 shows that the fit of the calculated data to the experimental data is poor. There are three observations that can be made with the fit of the data:

(1) The value of yx and zx matrix elements are zero in the calculated polarization matrices and non-zero in the experimental polarization matrices.
(2) The magnitude of the yy, yz, zy and zz matrix elements in the calculated plots is greater than that of the experimental polarization matrices.
(3) The sign of the terms is consistent between the two plots.

Item 1 and 2 are indicative that the model is missing an additional out of phase component in the magnetic structure and item 3 indicates that the new structure is related to that of the higher temperature phase.

To improve the fit to the data the polarization matrices were calculated using a model that included an imaginary component in the direction of the b axis. The matrix map of the calculated matrices is shown in figure 5.18. The best fit to the data was found when the imaginary component was 0.85 of the magnitude of the component in the ac plane, which indicates that the structure is slightly elliptical. The ratio of the two components agrees well with the range of values found by Lautenschläger *et al* , where a comparison is made in between the literature values and the experimentally determined values in table 5.11.

The yy, yz, zy and zz channels of the calculated matrices agree well with those found from experiment, which indicates that the magnetic structure is correct, but the magnitudes of the 'chiral' terms are in poor agreement.

Point 8 (-0.786, 1.5, -0.457), however, is fitted well and is consistent between figures 5.16, 5.17 and 5.18, for reference see table 5.10. The equivalence between the

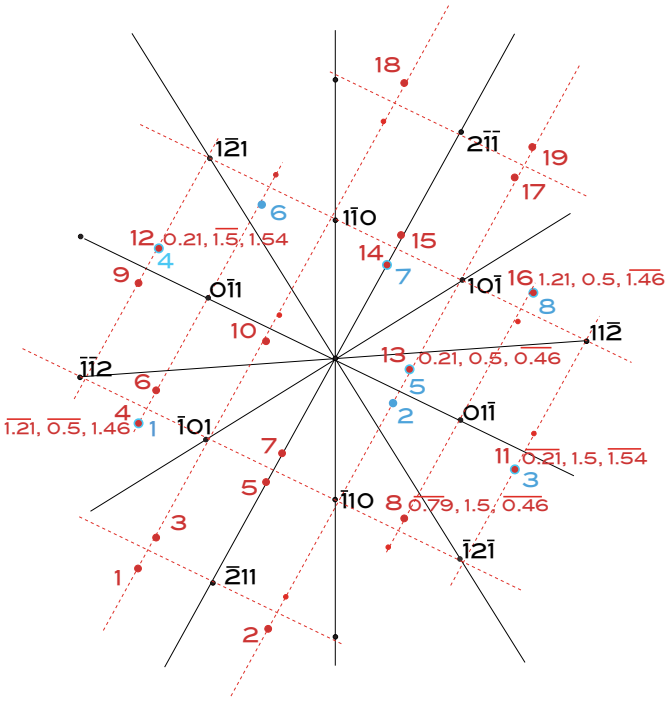

FIGURE 5.15. The reciprocal lattice points that were inspected in the ICNC (AF2) phase are shown in red and the points in the ICC (AF3) phase are shown in blue. The dashed red lines are a guide to indicate the position of the magnetic scattering with respect to the nuclear scattering, those that are above the dashed lines that run parallel to $(0\bar{1}1)$ are $+\mathbf{k}$ positions and those below the line are -**k** positions.

experimental and calculated matrix indicates that there is virtually no imaginary contribution to the magnetic interaction vector for this value of **Q**.

The introduction of the imaginary component to the magnetic structure highlights a different aspect of the symmetry of polarization matrices. The points that form the Friedel pairs in the reciprocal map, that were previously seen to give equal and opposite matrix elements can be seen to have equivalent values for the 'chiral' term of the polarization matrix. Consider, for example, points 10 (-0.214, -0.5, 0.457) and 13 (0.214, 0.5, -0.457), the matrix elements have a similar magnitude but opposite sign for the terms with final polarization in the channels $yy \approx -zz \approx 0.2$, and $yz \approx zy \approx 0.35$, whereas the 'chiral' terms are approximately equivalent in sign and magnitude $yx \approx yz \approx 0.5$.

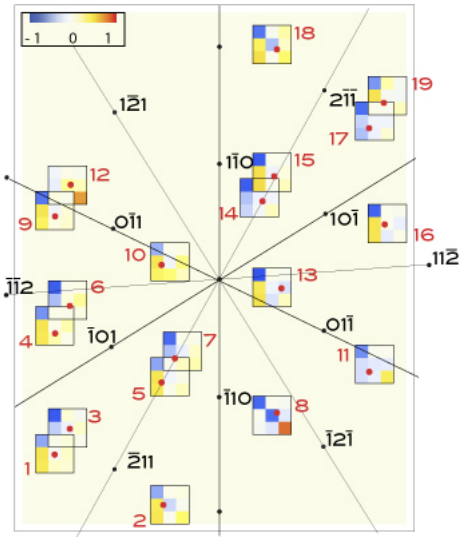

FIGURE 5.16. The matrix map of the data recorded in the ICNC (AF2) phase. The colours indicate the values of the polarization matrices in the respective positions in reciprocal space. The points indicate the approximate positions of the reciprocal lattice points associated with each matrix. The matrices can all be seen to have a non-zero 'chiral' component, despite the data being recorded in zero field and neither 'chiral' domain being energetically favourable.

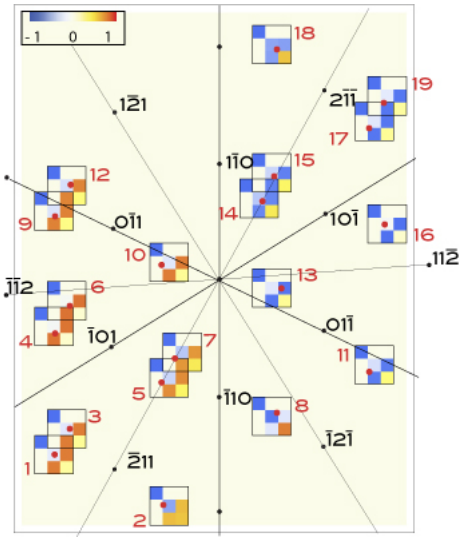

FIGURE 5.17. A matrix map calculated for reflections measured in the ICNC (AF2) phase. The colours indicate the values of the polarization matrices in the respective positions in reciprocal space. The points indicate the approximate positions of the reciprocal lattice points associated with each matrix. The model for the magnetic structure used to generate the map is collinear and equivalent to that found in the ICC (AF3) phase. The matrices can be seen to have the same sign in the yy, yz, zy and zz channels, but the magnitude of the values are larger than those found experimentally. Furthermore there is no component in the 'chiral' channels.

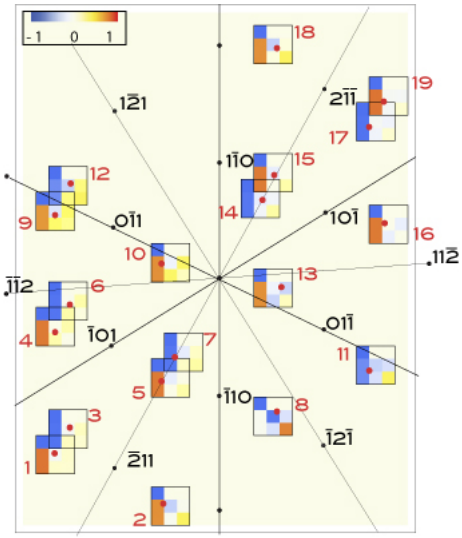

FIGURE 5.18. A matrix map calculated for reflections measured in the ICNC (AF2) phase. The colours indicate the values of the polarization matrices in the respective positions in reciprocal space. The points indicate the approximate positions of the reciprocal lattice points associated with each matrix. The model used for the magnetic structure is a cycloidal monodomain with ellipticity equal to 0.85. The values found in the yy, yz, zy and zz channels are equivalent to the experimental matrices but the magnitude of the 'chiral' term is larger than that found experimentally.

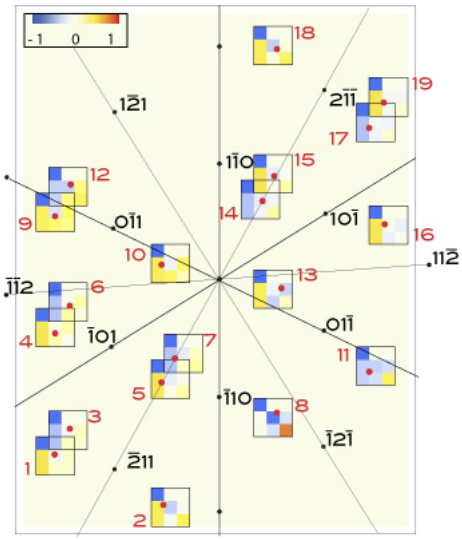

FIGURE 5.19. A matrix map calculated for reflections measured in the ICNC (AF2) phase. The colours indicate the values of the polarization matrices in the respective positions in reciprocal space. The points indicate the approximate positions of the reciprocal lattice points associated with each matrix. The model used for the magnetic structure is a cycloidal monodomain with ellipticity equal to 0.85 and relative domain populations of 0.25 -**k** 0.75 -**k**. The fit of all of the matrix elements can be seen to be in good agreement with those found from experiment, except for point 12 (-0.21, 1.5, -1.54) due to the nuclear scattering incident at this position, discussed with respect to the ICC AF3 phase (in the maps for the higher temperature phase this reflection is labelled point 4).

Reference (Reflection)	Polarization Value $(\text{Error})_{expt}$ $(\text{Difference})_{calc}$
8_{expt} $(-0.786, 1.5, -0.457)$	$\begin{pmatrix} -1.05\,(0.01) & -0.03\,(0.01) & -0.08\,(0.01) \\ -0.04\,(0.01) & -1.01\,(0.01) & -0.28\,(0.01) \\ -0.09\,(0.01) & -0.3\,(0.01) & 1.01\,(0.01) \end{pmatrix}$
8_{calc} $(-0.786, 1.5, -0.457)$	$\begin{pmatrix} -1.00\,(0.05) & 0.00\,(-0.03) & 0.00\,(-0.08) \\ 0.00\,(-0.04) & -0.95\,(-0.06) & -0.30\,(0.02) \\ 0.00\,(-0.09) & -0.30\,(0.00) & 0.95\,(0.06) \end{pmatrix}$

TABLE 5.9. The polarization matrices for point 8 (-0.786, 1.5, -0.457). The experimental matrix was recorded at 8.6 K in the ICNC (AF2) phase and the calculated matrix was generated for a collinear model for the magnetic structure. The agreement between the calculated and experimental plots is good, though slightly greater than experimental error, despite the expectation of a non-collinear magnetic structure in the ICNC (AF2) phase.

Reference (Reflection)	Polarization Value
10_{expt} $(-0.214, -0.5, 0.457)$	$\begin{pmatrix} -0.63\,(0.00) & -0.02\,(0.00) & 0.02\,(0.00) \\ 0.53\,(0.00) & -0.16\,(0.00) & 0.34\,(0.00) \\ 0.45\,(0.00) & 0.38\,(0.00) & 0.18\,(0.00) \end{pmatrix}$
13_{expt} $(0.214, 0.5, -0.457)$	$\begin{pmatrix} -1.16\,(0.00) & -0.01\,(-0.01) & -0.06\,(0.01) \\ 0.52\,(-0.01) & -0.19\,(-0.01) & -0.33\,(0.01) \\ 0.56\,(-0.01) & -0.33\,(0.01) & -0.21\,(0.01) \end{pmatrix}$

TABLE 5.10. The polarization matrices for points 10 (-0.786, 1.5, -0.457) and 13 (0.214, 0.5, -0.457) The experimental matrices was recorded at 8.6 K in the ICNC (AF2) phase the values of the matrices demonstrate that the sign of the xx, yx and zx components of the matrices are equivalent for the Friedel pairs, whilst all other elements undergo a reversal of sign.

The symmetry of the matrices reflects the geometry of the experiment, such that when one observes the same point at **Q** and -**Q** the CRYOPAD axes **x** and **y** are reversed and **z** remains the same. The magnetic structure appears reversed as the direction of the component that is detected in the direction **y** remains unchanged

when viewed from the opposite position. The component that is measured in the x channels, however, are inverted when viewed from opposing sides, which, when combined with the inversion of the direction of **x**, gives rise to the equivalence of the signs for the 'chiral' components.

The chiral components may also be seen to be equal and opposite for the positions that are generated from +**k** and -**k** vectors. To the left of the direction that point 8 (-0.786, 1.5, -0.457) makes with the origin the chiral terms of the matrices above the lines are negative and those below the lines are positive (points 1 to 10 (-0.786, 1.5, -0.457) and point 12), this pattern is inverted when we look to the right of this line. As we move through reciprocal space away from this line more of the imaginary component will fall in the plane perpendicular to **Q** and as such the magnitude of the chiral or phase term increases and the magnitude of the yy, yz, zy and zz terms decrease.

The final fit to the data used a model that also included domain mixing ratios of 0.25 +**k** 0.75 -**k**, where the values were calculated by fitting the chiral term to that of the experimental data.

In summary the ratio of the real and imaginary components agrees well with that described by Lautenschläger *et al* , where the component in the ac plane is 34.9 ° to the a axis, equivalent to that found in the sinusoidal phase with a component in the direction of b that is 0.85 times the magnitude of the perpendicular component, a comparison is given in 5.11. The ±**k** domains are unequally populated and have a ratio of 1:3.

5.6.3. The magnetic structure of the CC (AF1) phase. The final, lowest temperature phase of $MnWO_4$ is the collinear commensurate phase CC (AF1). The matrix map of the experimental data recorded in this phase can be seen in 5.23 and the fit to that data can be seen in figure 5.24, where the magnetic reflections are

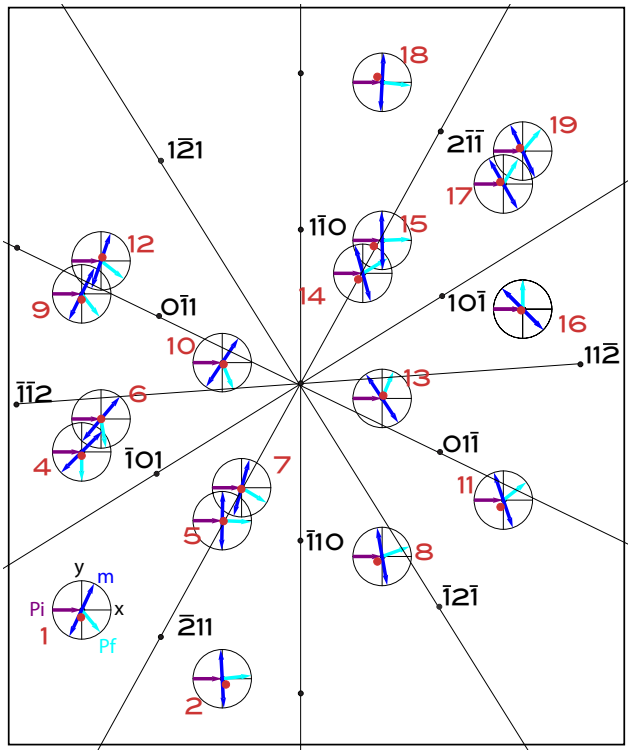

FIGURE 5.20. Position of the incident polarization, in purple, the calculated polarization, in cyan, and the orientation of the moment, in blue, in the plane perpendicular to **Q** that generates this rotation.

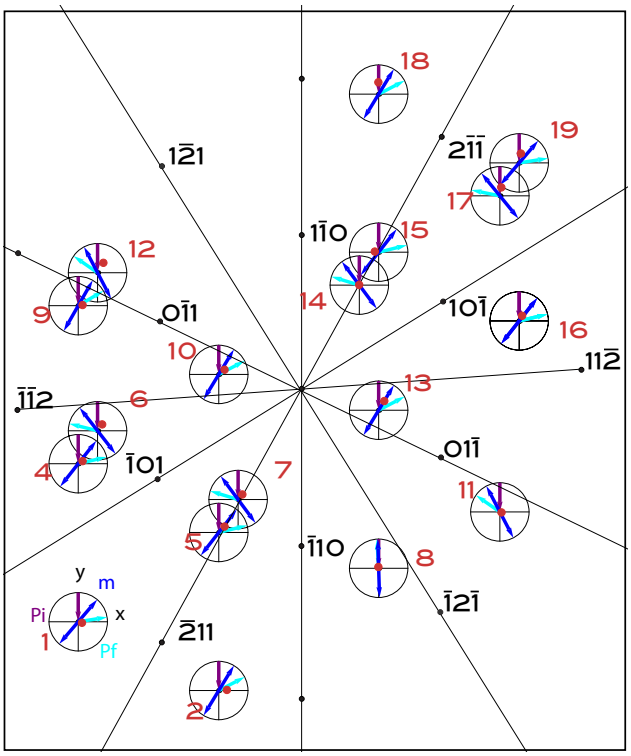

FIGURE 5.21. Position of the incident polarization, in purple, the calculated polarization, in cyan, and the phase difference, in blue, between the real and imaginary components of the moment that generates the rotation.

	Technique	T(K)	$\|\mathbf{m}\|$ (μ_B)	$\phi(^\circ)$	p	m_x	m_y	m_z
1	powder (D1B)	9.4	3.9(1)	35.9	0.99			
2	single crystal (D10)	9.2	4.8(5)	34.6	0.78			
3	single crystal (DN4)	9.5	4.1(1)	33.9	0.82			
4	polarimetry (D3)	8.6		34.9	0.85	0.82	i0.85	0.57

TABLE 5.11. The refined values for the position of the moment in the ICNC (AF2) phase, where the data were collected at the temperatures indicated. The magnitude of the moment $|\mathbf{m}|$ (μ_B) is given for the literature results. The angle ϕ is the angle from the **a** axis in of the moment in the ac plane and the value p indicates the relative magnitude component in the b direction. The vector that was used as input to Mufit, m_x, m_y, m_z, is given in the final column. The agreement between the polarimetry data and that found in previous experimental work are seen to agree well. The values for the non-polarized data, 1, 2 and 3 are taken from, [**7**].

those shown in 5.22. Appendix E contains all of the experimental data, with the best fit to the data the difference between the fit and the experimental matrices and the RMS average. The fit of the data in the CC (AF1) phase again agrees well with the structure published initially by Dachs, [**11**] and subsequently confirmed by Lautenschläger *et al*, [**7**], with the moment, again, lying in the ac plane making an angle of 34.7° to the a axis, there is no component in the b direction. This section will begin by discussing the experimental reasons for the poor fit that is observed for some of the reflections in this phase.

The map of the reciprocal space shown in figure 5.22 indicates the magnetic reflections that were measured in the CC (AF1) phase, where colour of the points indicate different experimental conditions. The points that are shown in red were measured at 5 K, whereas those in blue were measured at 6 K after an electric field had been applied. The points that also have a black outline were measured at the beginning of the experiment with an incorrect **UB** matrix that was generated with a [1, 1, $\bar{1}$] zone axis, where the reflection indices have been corrected for the change in the zone axis, hence the measured points were described as being in the (h, k, l)

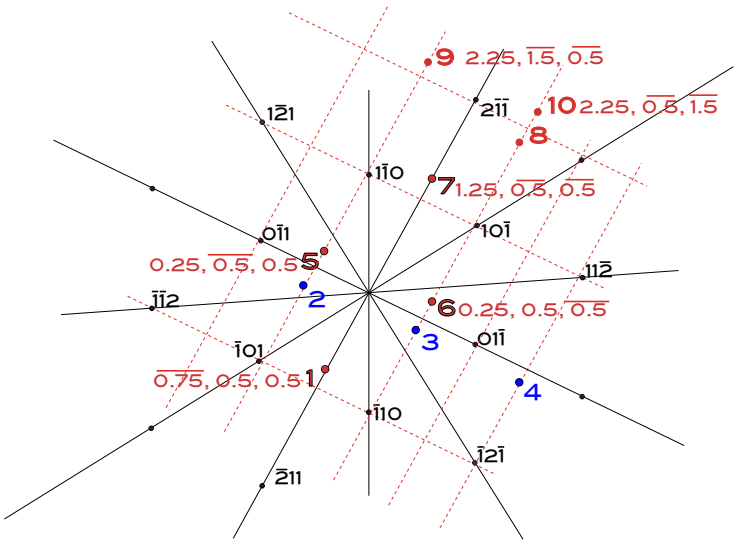

FIGURE 5.22. The reciprocal lattice points that were inspected in the CC (AF1) where the colour of the points indicates the conditions under which they were measured, as described in the text. The dashed red lines are a guide to indicate the position of the magnetic scattering with respect to the nuclear scattering, those that are above the dashed lines that run parallel to $(0\bar{k}, k)$ are +**k** positions and those below the line are -**k** positions.

The reflections that fit the proposed structure best are those that were measured with the correct **UB** matrix (reflections numbered 2, 3, 4, 8, 9, 10), which was generated using points that lie above and below the $(h, k, \bar{l})$ scattering plane. These points were measured at different temperatures, such that 2, 3 and 4 were measured at 6 K and the points 8, 9 and 10 were measured at 5 K. The fit of the structure to the experimental matrices, however, remains good despite this change in temperature, which can be understood in that the polarization matrices, in the purely magnetic case are sensitive to the orientation of the moment and not the magnitude. As the temperature is lowered we would expect the magnitude of the moment to increase, but the structure and hence the orientation of the moment to remain the same. The effect of the electric field can also be seen to make no difference to the magnetic structure.

The points that were measured with the incorrect **UB** matrix, which was generated from points that were labelled as being in the (h, k, l) plane rather than the $(h, k,$

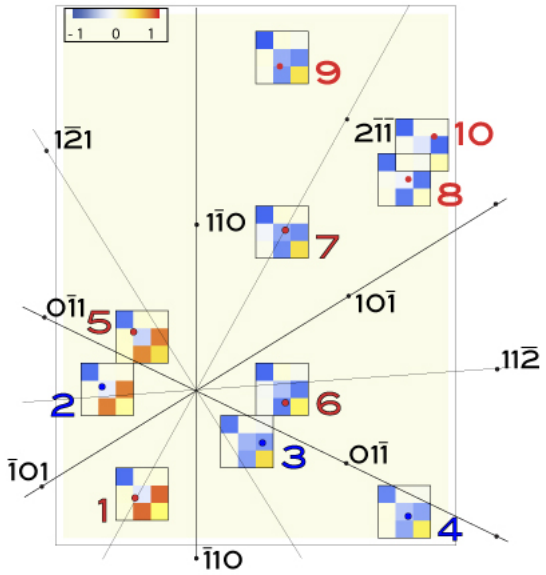

FIGURE 5.23. The matrix map of the experimental data collected in the CC (AF1) phase with positive incident polarization. The colours indicate the values of the polarization matrices in the respective positions in reciprocal space. The points indicate the approximate positions of the reciprocal lattice points associated with each matrix. The reflections numbered 2, 3, 4, 8, 9, 10 were collected with a **UB** matrix generated for reflections found in the (h, k, $\bar{l}$) plane, whereas those labelled 1, 5 and 7 were collected with a **UB** matrix generated for a crystal oriented to find the (h, k, l) scattering plane.

$\bar{l}$) orientation do not agree with the calculated matrices as well as those that were measured subsequently. The points are included in order that there is a complete map of the moment with respect to the angle of observation.

The inversion of the sign of l should return the correct reciprocal lattice vector for the reflection that was observed at the position inspected. As the lattice points were labelled incorrectly and from this initial error the **UB** matrix generated was wrong due to the monoclinic unit cell. If the crystal were cubic, the different directions would be indistinguishable. The reflections could be found at the positions calculated using the incorrect matrix as the β=91.1°, very close to 90°. A comparison of the position of three reflections that were calculated with both the (h, k, l) plane and the (h, k, $\bar{l}$) plane are shown in table 5.12, where the angles that describe the position of peaks are: gamma, the position of the detector in the scattering plane; omega, the rotation of the sample, and nu the position of the detector out of the scattering plane.

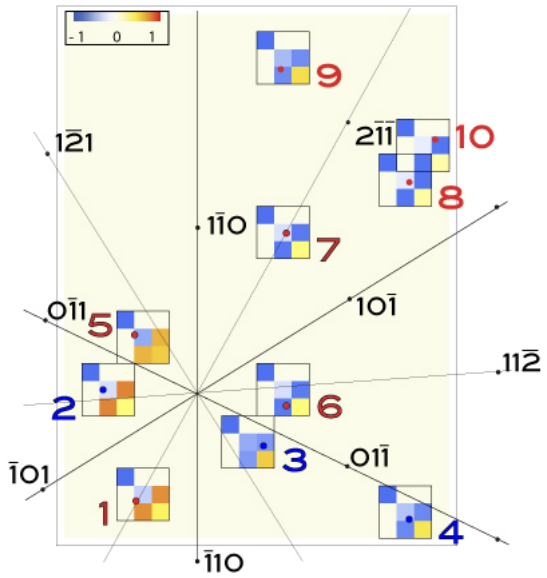

FIGURE 5.24. A matrix map calculated for the CC (AF1) phase with positive incident polarization. The colours indicate the values of the polarization matrices in the respective positions in reciprocal space. The points indicate the approximate positions of the reciprocal lattice points associated with each matrix. The model used to calculate these points has a moment that lies in the *ac* plane where the angle of the moment is 34.7° from the *a* axis and no component in the *b* direction. The matrices of the reflections numbered 2, 3, 4, 8, 9, 10 agree with the experimental data more closely than those numbered 1, 5 and 7.

The (0 1 1) peak is 1° wide at the half maximum position, shown in figure 5.26, less than the difference in omega of the calculated positions of the peaks using **UB** matrix 1 and **UB** matrix 2. The measurement of polarization matrices on D3 is a measurement of the background, the peak and then the background. In order to optimize this measurement an omega scan is conducted before the measurement of the matrices. The omega scan has two purposes, to determine whether there is a peak present at the specified position and to optimize the position of the peak measurement. The background measurements are always made at the same distance each side of the peak. Thus in those cases where the peak is near to the calculated position the peak maximum will be found, and this was case for the (0 1 1) and (-0.75 -0.5 -1.5) peaks which are approximately 0.3° in omega from the calculated position, less than the width of the peak. The magnetic peaks of the incommensurate phase

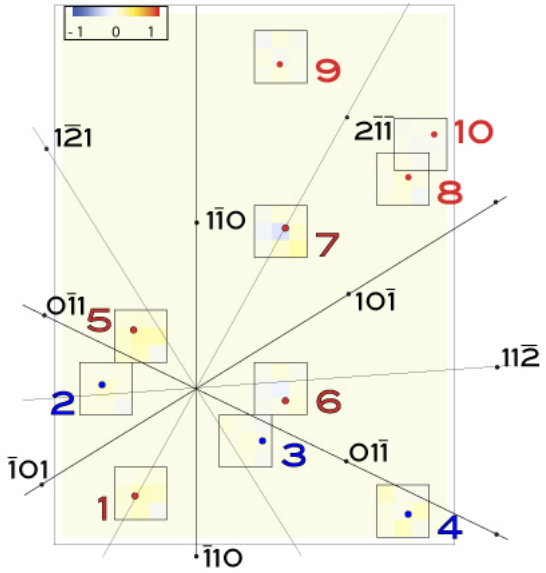

FIGURE 5.25. A matrix map of the difference between the calculated and experimental values for the CC (AF1) phase. The colours indicate the magnitude of the difference between the polarization matrices in the respective positions in reciprocal space. The points indicate the approximate positions of the reciprocal lattice points associated with each matrix. The difference can seen to be greater for the reflections numbered 1, 5 and 7.

UB matrix	h	k	l	$gamma$	$omega$	nu
1	0.	1.	1.	−12.558	−82.762	0.
2	0.	1.	−1.	−12.558	−82.504	0.
$diff$				0.	0.258	0.
1	−0.75	−0.5	−1.5	−16.636	59.808	−1.303
2	−0.75	−0.5	1.5	−16.396	60.105	1.318
$diff$				0.24	0.297	0.015
1	0.21	−1.5	−1.46	−18.646	100.111	−0.891
2	0.21	−1.5	1.54	−19.3	98.939	1.355
$diff$				0.654	1.172	0.464

TABLE 5.12. The angles that describe the detector and sample positions where **UB** matrix 1 was the original, incorrect matrix calculated for a sample oriented with the [1 1 $\bar{1}$] direction upward the **UB** matrix 2 had the [1 1 1] direction upward. The value $diff$ is the difference of the absolute values of the angles. All the instrument angles change for out of plane reflections. The **UB** matrices are included in Appendix H, along with a more comprehensive table of reflections.

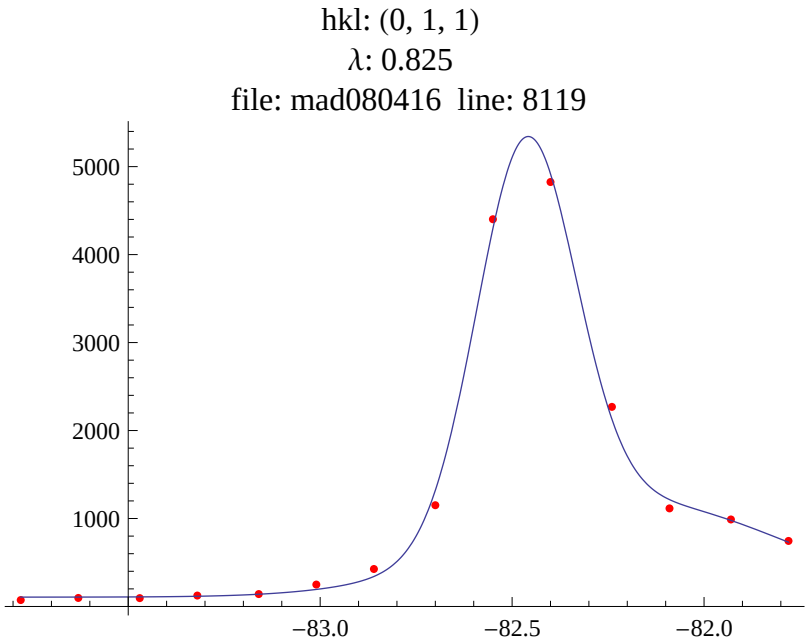

FIGURE 5.26. Omega scan of the (0 1 1) peak. The peak has been fitted with two Gaussian functions where the main peak is centered at -82.46°. This is in good agreement with the position of the peak calculated with the second **UB** matrix. The peak 1° wide at the half maximum position.

could not be found as the shift in omega is much larger, due to the change in the l component of hkl.

A comparison of the experimental and calculated values generated for the points 5 (0.25, -0.5, 0.5) and 2 (-0.25, -0.5, 0.5) is given in table 5.13.

The orientation of the refined moment, which makes an angle of 34.7° to the a axis and lies in the ac plane, is nearly equivalent to that of the ICC (AF3) phase where the moment lies 34.9° to the a axis. The value calculated from the best fit to the polarization data roughly agrees with previous experimental work, though there is a range of orientations for the moment in this phase, see ref [**7**] for a complete list. The equivalence of the orientation of the moment in the ICC (AF3) phase and the CC (AF1) phase is highlighted in the following section that discusses the evolution of the ellipticity with respect to the reduction in temperature.

Reference (Reflection)	Polarization Value $(\text{Error})_{expt}$ $(\text{Difference})_{calc}$
2_{expt} $(-0.25, -0.5, 0.5)$	$\begin{pmatrix} -0.99\,(0.01) & 0.\,(0.01) & 0.02\,(0.01) \\ 0.02\,(0.01) & -0.24\,(0.01) & 0.95\,(0.01) \\ 0.02\,(0.01) & 0.95\,(0.01) & 0.27\,(0.01) \end{pmatrix}$
2_{calc} $(-0.25, -0.5, 0.5)$	$\begin{pmatrix} -1.00\,(0.01) & 0.00\,(0.02) & 0.00\,(0.01) \\ 0.00\,(0.02) & -0.36\,(0.12) & -0.93\,(0.02) \\ 0.00\,(0.02) & -0.93\,(0.02) & 0.36\,(0.05) \end{pmatrix}$
5_{expt} $(0.25, -0.5, 0.5)$	$\begin{pmatrix} -0.95\,(0.01) & 0.07\,(0.02) & 0.04\,(0.02) \\ 0.11\,(0.02) & -0.44\,(0.02) & 0.96\,(0.01) \\ 0.11\,(0.02) & 0.91\,(0.02) & 0.58\,(0.02) \end{pmatrix}$
5_{calc} $(-0.786, 1.5, -0.457)$	$\begin{pmatrix} -1.00\,(0.05) & 0.00\,(0.07) & 0.00\,(0.04) \\ 0.00\,(0.11) & -0.66\,(0.21) & 0.75\,(0.19) \\ 0.00\,(0.11) & 0.75\,(0.16) & 0.66\,(-0.08) \end{pmatrix}$

TABLE 5.13. The polarization matrices for points 5 (-0.786, 1.5, -0.457) and 2 (-0.25, -0.5, 0.5) of plots 5.23 and 5.24. The matrices are a comparison between the experimental values and the values calculated for the magnetic structure, the fit of the data for point 2 is better than that for point 5.

	Technique	T(K)	$\lvert\mathbf{m}\rvert$ (μ_B)	$\phi(^\circ)$	m_x	m_y	m_z
1	powder (D1B)	1.5	4.5(1)	39.0			
2	single crystal (D10)	1.7	5.6(5)	36.6			
3	single crystal (DN4)	5.2	4.5(1)	37.5			
4	polarimetry (D3)	5		34.7	0.81	0	0.59

TABLE 5.14. The refined values for the orientation of the moment in the CC (AF1) phase at the temperatures, T, indicated. The magnitude of the moment, $|\mathbf{m}|$ (μ_B), for the refined data is given in the second column and the angle ϕ is the angle from the **a** axis in of the moment in the ac plane. This is converted into the vector used as input into for the Mufit program m_x, m_y, m_z. The values for the non-polarized data, 1, 2 and 3 are taken from, [**7**].

5.6.4. Phase diagram with respect to temperature observed by polarimetry. The refined structures found for each of the phases were used as starting models to fit the polarization matrices that were recorded for the (0.786, 0.5, 0.457) reflection recorded during a sweep of the temperature from the 13 K to 6 K. The (0.786, -0.5, -0.543) reflection was chosen as it was the strongest magnetic reflection that was observed in the ICNC (AF3) phase and had a clear chiral response. The reflection corresponds to point 14 in the ICNC (AF2) phase and point 7 in the ICC (AF3) phase matrix plots. As only one reflection was recorded at each temperature no refinement could be undertaken and as such polarization matrices were systematically calculated for different values of p, the proportion of the moment along b when the ac component is unitary. The calculations were tabulated and an inspection was made to find the best fit at each temperature.

The matrices for the moments observed in the ICC (AF3) and CC (AF1) phase can be seen to be virtually equivalent and this is indicative of the orientation of the moments in these two phases also very nearly equivalent, which can be seen in the table 5.15. Both of the matrices clearly indicate that there is no component in the yx and zx channels, which indicates the sinusoidal nature of the structure. As the temperature decreases from 12.4K the magnitude of the imaginary component increases, which can be determined from the yy, yz, zy, zz, as well as the magnitude of the 'chiral' term. These matrix elements diminish in magnitude as the imaginary component increases, due to interference effects. The magnitude of the 'chiral' component is seen to increase, but not at the rate that one would expect if there was a single domain present, which can be inferred as the elements in the different x, y and z channels do not return a unit vector. The orientation of the magnetic moment can be fitted with the real component making an angle of 34.9 ° to the a axis and the magnitude of the imaginary component in the direction of **b** increasing, where the fitted value of **b** is shown in the final column of table 5.15. The ratio of the positive and negative domains is slightly different to that measured for the ICNC (AF2)

Temperature	Experimental Matrix	Calculated Matrix	Calculated Single Domain Matrix	Magnitude of im_y
7.03				0.00
7.42		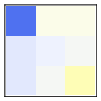		0.85
7.81	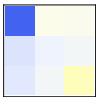	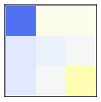		0.84
9.02	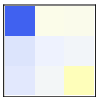			0.83
11.00	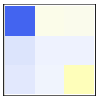	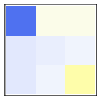		0.78
12.02	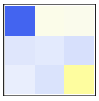	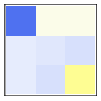		0.63
12.40				0.50
12.80				0.00

TABLE 5.15. Experimental and calculated matrices for the (0.786, -0.5, -0.543) reflection at the temperatures indicated. The starting model that was used to calculate the polarization matrices had a unitary component in the *ac* plane, 34.9° from the *a* axis, equivalent to the structure that was found in the ICC (AF3) phase. The im_y contribution to the magnetic interaction vector was found by systematically increasing the value of im_y and comparing the output to the experimental data. The domain ratio that was used for the calculation was 0.35 +**k** to 0.65 -**k**. The extrapolated matrices for a monodomain of +**k** is shown in the third column and the magnitude of the imaginary component is shown in the final column.

dataset, where the ratio of +**k** to -**k** was 25:75, whereas in this data set the population of the chiral domains is better described by +**k** to -**k** 35:65. The fit of the data is in general very good, though there is some evidence of the polarization that one would wish to measure in the xx channel is being recorded in the zx channel, due to the misalignment of the sample and this can be understood from the experimental matrix plotted for the data at 7.42K, as the zx component is less than the yx component.

In order to fit the data the magnitude of the imaginary component can be seen to increase, which indicates the change in the elipticity of the cycloid, the change in the magnitude of this component is indicated in the final column of table 5.15 and plotted in figure 5.27. The plot may be compared to the polarization measured by Taniguchi *et al* and Arkenbout *et al*, [**5, 3**], shown in figure 5.28, which indicates the magnitude of the polarization with respect to temperature. Both the sets of experimental data indicate that the polarization increases as the temperature decreases, reaching a maximum of $\approx 58\mu\mathrm{C/m}^2$ before the sharp transition to the low temperature CC (AF1) phase. The rapid rate of the initial part of the curve can also be seen in the curve that describes ellipticity, however the continuous increase of the polarization cannot be observed in the plot of the magnitude of the imaginary component, 5.27, which indicates that the increase in the electric polarization is mostly dependent on the increase of the overall magnitude of the moment. The experiments performed by Sagayama *et al* that measured the intensity of the scattering in the $+x$ and $-x$ channels with respect to applied electric field also indicate this result, [**10**].

As discussed with respect to the ICNC (AF2) phase the matrix elements that correspond to yy, yz, zy and zz are equivalent for both the $+\mathbf{k}$ and -**k** domains. From the fit to these elements one can extrapolate the matrices that would be expected if there were a mono-domain of $+\mathbf{k}$ present, where the calculated matrices are shown in column three of table 5.15. These calculated matrices will be used subsequently to compare the data collected in an applied electric field.

5.6.5. Multiferroic coupling with respect to field and temperature. The data gathered in the applied electric field are shown in the table 5.16, where the magnitude of the 'chiral' components of the matrices indicate that monodomains of each handedness were induced. In the positive applied field the strongly red elements of the yx and zx components arise when the structure is described entirely by cycloids that propagate with $+\mathbf{k}$, as described previously in the table 5.15. The xx and zx

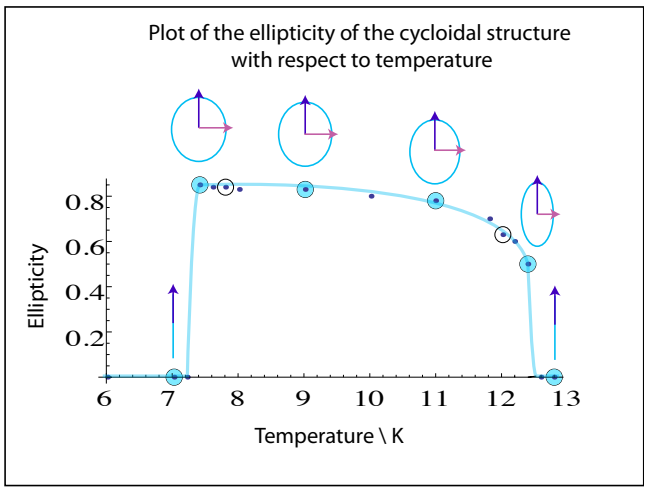

FIGURE 5.27. A plot of the fitted relative magnitudes of the imaginary component. The circled points are those included in the table above, the filled circles are those that correspond to the ellipses drawn on the plot. The component in the direction **ac** is a unit vector, shown in purple and the imaginary component is shown in pink in the horizontal direction.

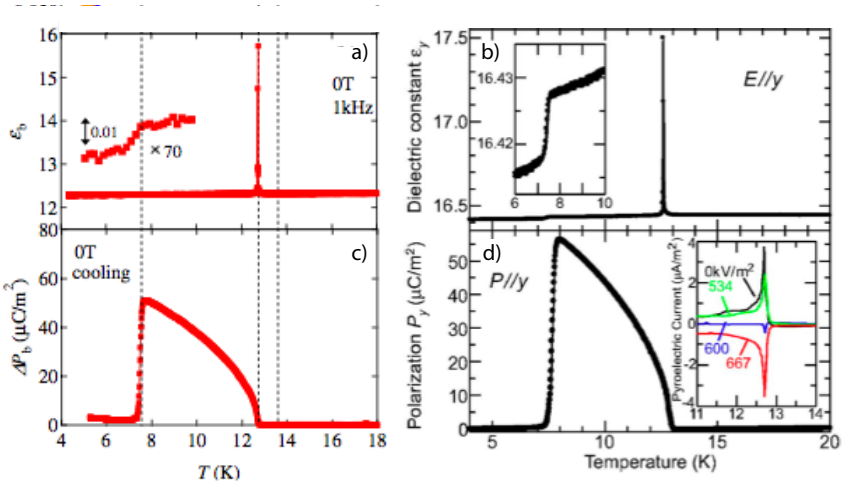

FIGURE 5.28. Data that indicates the electric polarization of $MnWO_4$. a) and b) Plots of the dielectric constant observed in $MnWO_4$ with respect to temperature, repeated from figure 5.5 for convenience. c) and d) The magnitude of the electric polarization with respect to temperature. The images a) and c) are from reference , [**5**] and plots b) and d) are from, [**3**].

elements again show the signature of missallignment in that there is intensity recorded in the wrong channels to give an increase in the value of xx and a reduction in the value of zx. The matrices are well described by the orientation of the moment was found using with the data that was collected during the temperature sweep at 12

Electric Field	Incident polarization	Experimental Matrix	Calculated Matrix	Difference Matrix
+450	+y			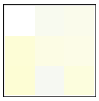
	-y			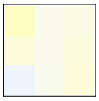
-450	+y	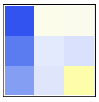	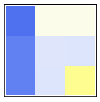	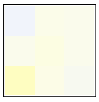
	-y			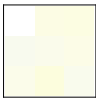

TABLE 5.16. Matrices indicating the goodness of fit when there is the structure is a monodomain of +**k**, when a positive field is applied, and -**k**, when a negative field is applied. The data were collected at 12K for the (0.786, -0.5, -0.563) reflection. The component of the moment in the *ac* plane is unitary and makes an angle of 34.9° with the *a* axis and the imaginary component in the *b* direction that is has relative magnitude of 0.63.

K, with an imaginary component with magnitude 0.63 and real component that lies 34.9° from the **a** axis in the *ac* plane.

The matrices recorded in negative applied field can be seen to be roughly equivalent to those measured in positive applied field, with an inversion of the sign of the 'chiral' terms, the matrices overall indicate that there is a monodomain of -**k**.

The matrices were recorded at the extremes of the hysteresis curve shown in 5.29 and as such the curves unambiguously indicate that the application of an electric field generates a chiral monodomain and that the reversal of this field inverts the handedness of the monodomain structure. The magnitude of the electric field required to generate the reversal of the domain population increases as the temperature decreases, with a coercive field of 100kV/m required at 12 K and ≈210kV/m required at 11 K. The coercive field at 10K was not determined due to field breakdown, but other studies have indicated that there is a reversal of the electric polarization when an electric field of 600kV/m is applied to a sample cooled in a poling electric field to

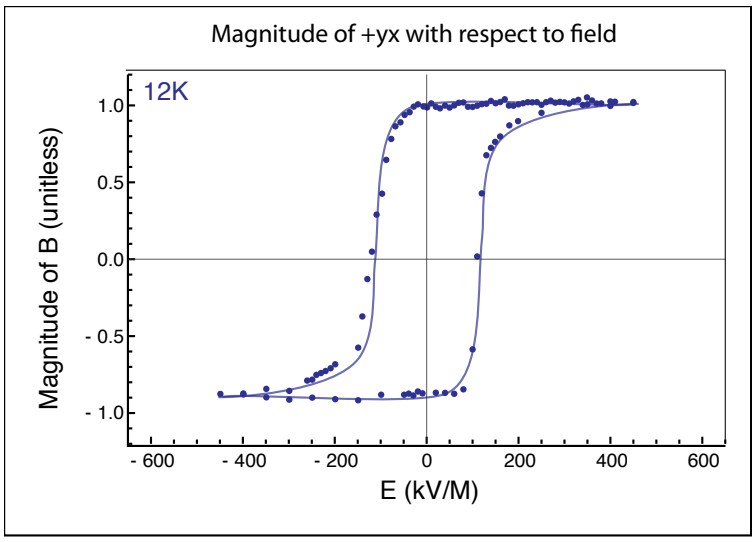

FIGURE 5.29. Hysteresis of the chiral term B in the polarization matrices of $MnWO_4$ recorded at 12K plotted with respect to electric field. The coercive field is 100kV/m the magnetic structure at the extremes of the hysteresis have an ellipticity of 1:0.63 real:imaginary.

ensure that a single handedness is selected, at 10 K, [**3**], which would agree reasonably well with the data shown in figure 5.30. The increase in the magnitude of the field required to invert the sign of the chirality is inidicative of the increase of the electric polarization as the temperature decreases and the increased order present in the sample.

There is no indication that there is any chirality or magnetoelectric coupling present in the sinusoidal CC (AF1) and ICC (AF3) phases as the application of a poling electric field whilst cooling made no change to the polarization matrices at 7K and 13K.

5.7. Conclusion

The magnetic structure of $MnWO_4$ has been shown to agree well with that described in the paper of Lautenschläger *et al* and is unambiguously shown to be a cycloidal in the ICNC (AF2) phase. The response to the electric field has been demonstrated and the transition in to an unbalanced chiral phase is clearly observed even without

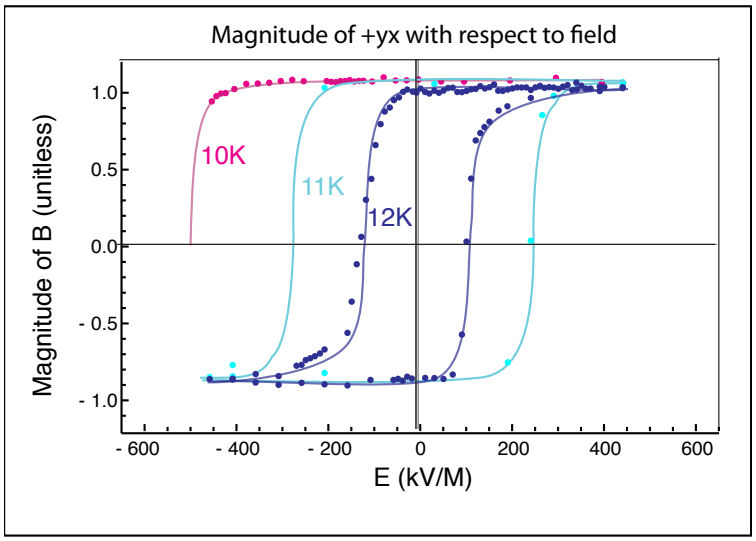

FIGURE 5.30. Hysteresis of the chiral term in the polarization matrices of $MnWO_4$ recorded at 12K, 11K and 10K plotted with respect to electric field. The size of the coercive field can be seen to increase as the temperature decreases.

an applied electric field. This observation implies that there is a domain imbalance when there is no applied electric field and this fits with the idea that there is a degree of pinning to defects within these materials to generate the ferroelectric domains, [**9**]. The magnitude of the elipticity in the multiferroic phase has been shown to increase as the temperature decreases and this reflects the increase of the electric polarization as the temperature decreases, but cannot describe it fully. This observation agrees with other experimental work that has measured the response of the magnetic structure to an applied electric field, that was published after this study commenced, [**10, 8, 31**]. The domain population and hence the magnetic structure have been shown to be controlled by the application of an electric field. There is no indication that the other phases have a chiral magnetic structure and they do not respond to the application of an electric field.

The polarimetry technique allows the direct observation of the non-collinear term, which enabled this study to be undertaken. The advantage of measuring the 'chiral' components of the polarization matrices, as opposed to the change in scattered intensity of an incident beam polarized in the direction of $\pm\mathbf{Q}$ (polarization analysis)

is the reduction in error that arises from extinction and absorption. The polarization matrices return a ratio of the final intensity and the absorption and extinction errors cancel. This is not in the case in polarization analysis and as such the absolute structure is more difficult to extrapolate. The advantage of the polarization analysis technique is that the magnitude of the moment may be found, as shown in the work of Sagayama *et. al.*, [**10**].

The application of group theory in this instance informed the original structure determination and has informed much of the theoretical work that has been completed on multiferroic materials. The breaking of inversion symmetry when the systems magnetically order allows the distortions to occur which gives rise to the electric polarization.

References

[1] Eerenstein W, Mathur N D and Scott J F *Nature*, **442**, 759 (2006)

[2] Cheong S W and Mostovoy M, *Nature Materials* **16**, 14 (2007)

[3] Arkenbout A H, Palstra T T M, Siegrist T, and Kimura T *Phys. Rev. B* **74**, 184431 (2006)

[4] Heyer O, Hollmann N, Klassen I *et al J. Phys.: Condens. Matter*, **L471**, (2006)

[5] Taniguchi K, Abe N, Ohtani S *et al Phys. Rev. Lett.*, **97**, 097203, (2006)

[6] Kimura T, Goto T, Shintani H, Ishizaka K, Arima T and Tokura Y *Nature*, **426**, 55 (2003)

[7] Chu Y-H, Martin L W, Holcomb M B, *et al Nature Materials*, **7**, 478, (2008)

[8] Sagayama H, Taniguchi K, Abe N, Arima T, Soda M, Matsuura M and Hirota K *Phys. Rev. B*, **77**, 220407 (2008)

[9] Brown P J, Forsyth J B and Tasset F, *Solid State Sciences*, **7** 682 (2005)

[10] Poole A, Wills A S, Brown P J *J Phys.: Conf. Series* **145** 012074 (2008)

[11] Dachs H, Stoll E and Weitzel H *Z. Krist.*, **125** 120-129 (1967)

[12] Lautenschläger G, Weitzel H, Vogt T *et al Phys. Rev. B* **48** 6087 (1993)

[13] Chaikin P M & Lubensky T C *Principles of condensed matter physics*, Cambridge University Press (1995)

[14] Weitzel H, *Solid State Commun*, **8**, 2071 (1970)

[15] Ehrenberg H, Weitzel H, Heid C *et al J. Phys.: Condens. Matter* **9** 3189 (1997)

[16] Ehrenberg H, Weitzel H, Fuess H, Hennion B *J. Phys.: Condens. Matter* **1**1 3189 (1999)

[17] Ehrenberg H, Weitzel H, Theissmann R, *et al. Physica B* **276** 644 (2000)

[18] Tian C, Lee C, Xiang H, *et. al.*, *Phys. Rev. B* **80** 104426 (2009)

[19] Tolédano P, Mettout B, Schranz W and Krexner G, *J. Phys.: Condens. Matter*, **22** , 065901, (2010)

[20] Harris A B *Phys. Rev. B* **76**, 054447 2007

[21] Mostovoy M *Phys. Rev. Lett.* **96** 067601 (2006)

[22] Schweizer J, Villain J and Harris A B, *Eur J Phys*, **38**, 41 (2007)

[23] Radaelli P G and Chapon L C *Phys Rev B* **76**, 054428, (2007)

[24] Chaudhury R P, Yen F, de la Cruz C R, Lorenz B, Wang Y Q, Suna Y Y, Chu C W *Physica B* **403** 1428 (2008)

[25] Taniguchi K, Abe N, Sagayama H, Ohtani S, Takenobu T, Iwasa Y, and Arima T, *Phys. Rev. B* **77**, 064408 (2008)

[26] Chapon L C, Radaelli P G, Blake G R, Park S and Cheong S-W *Phys Rev Lett* **96**, 097601 (2006)

[27] Blundell S, *Magnetism in Condensed Matter*, Oxford University Press, Oxford, (2001)

[28] Kundys B, Simon C and Martin C *Phys. Rev. B* **77** 172402 (2008)

[29] Taniguchi K, Abe N, Sagayama H, Ohtani S, Takenobu T, Iwasa Y and Arima T *Phys. Rev. B* **77**, 064408 (2008)

[30] Meier D, Leo N, Maringer M, Lottermoser Th, Fiebig M, Becker P and Bohatý L *Phys. Rev. B*, **80**, 224420 (2009)

[31] Finger T, Senff D, Schmalzl K, Schmidt W, Regnault L P, Becker P, Bohatý L, Braden M, *J. Phys.: Conf. Ser.*, **211** 012001(2010)

[32] Finger T, Senff D, Schmalzl K, Schmidt W, Regnault L P, Becker P, Bohatý L, Braden M, *Phys. Rev. B*, **81** 054430 (2010)

[33] Gukasov A, *Physica B*, **267**, 97 (1999)

[34] Lelièvre-Berna E, Bourgeat-Lami E, Fouilloux P, *et al* 2005 *Physica B* 131

[35] Poole A, Wills A S and Lelièvre-Berna E *J. Phys.: Condens. Matter* **19** 452201(2007)

[36] Blume M *Phys. Rev.* 1670 (1963)

[37] Brown P J, Forsyth J B and Tasset F *Proc. R. Soc. Lond. A* 147 (1993)

[38] Nunez V, Brown P J, Chattopadhyay T, Forsyth J B and Tasset F *Physica B* **180** 903 (1992)

[39] Paschen F 1889 *Wied. Ann.*, **37**, 69.

[40] Abdel-Salam M, Stanek E *IEEE Trans. Ind. App.* **24** 1025 (1988)

[41] The Mufit is program written by Bertrand Roessli in Octave to fit neutron polarimetry data.

[42] Brown J, *private communication*

[43] Brown J *Neutron Polarimetry: Theory of Polarised Neutron Scattering* , url:http://webusers.fis.uniroma3.it/sns_fpr/lecture/lecture06.htm

CHAPTER 6

Conclusion

This chapter seeks to summarize the work in this thesis and discuss further work that could be undertaken. The work presented in this thesis confirms the magnetic structures of $Er_2Ti_2O_7$ and $MnWO_4$ and shows that the magnetic structure of $MnWO_4$ can be controlled with the application of an electric field. The materials studied both had domains that lead to cancellation of elements within the polarization matrix, which in the case of $MnWO_4$ was overcome by the application of an electric field.

6.1. $Er_2Ti_2O_7$

6.1.1. Summary. The polarimetry measurements made on $Er_2Ti_2O_7$ indicate that the static magnetic structure is described by the basis vectors of the Γ_5 IR and lie in the XY plane, in agreement with the results of Champion *et. al.*, [**1**]. The data also indicate there are rotationally related S-domains present in the sample and these are equally populated, such that the basis vector that the order is described by cannot be found from these measurements. Routines were written in Mathematica to analyze and plot the data, and also to correct for the depolarization of the ^{3}He cells. These routines were intended to be a more general analysis approach than that previously available and to simplify the interpretation of neutron polarimetry data.

6.1.2. Conclusions. Despite fitting the domain populations it is not possible to determine specific orientation of the moments when equally populated S-domains are present in a sample. The ambiguity arises due to the depolarization of the neutron beam when there are equal an opposite interference effects. The finding underlines

the fact that neutron scattering is a probe of the bulk material and if the global symmetry is not broken those terms in the intensity that are not squared, will cancel, i.e. the scattering from all parts must be in phase for the off-diagonal and interference terms of the polarization matrix not to sum to zero. From this observation it can understood that it is not possible to determine the unique direction of a moment described by a degenerate set of basis vectors in a highly symmetric system, unless an external force, such as a magnetic or electric field, is applied to make one direction energetically favourable.

The static magnetic structure of $Er_2Ti_2O_7$ determined by Champion *et. al.*, [**1**], and this thesis, implies that the system undergoes an order-by-disorder transition. The original theoretical work by Villain describing order-by-disorder describes a system that consists of ferromagnetically ordered chains, labelled A, that alternate with antiferromagnetically ordered chains, labelled B. The ferromagnetic A chains become colinearly aligned in the entire system, despite there being no exchange interaction between the A chains, due to spin flip excitiations that occur in the B chains. It can visualized such the A chain may have a total spin of +1 or -1 and the B chains are all zero (if the number of atoms in the chain is even), any excitation in the B chain will make the B chain non-zero and thus links, weakly, the A chains. The disorder in the B chains may or may not be dynamic, e.g. spin flip excitations would be dynamic but the same effect occurs (i.e. the value for the B chain is non-zero) when there are an odd number of atoms in the chain. The disorder in the B chain serves to make the system 2D rather than one 1D and this allows the system to order. The way in which it orders (+1 or -1 throughout), is a matter of chance.

The reason for the theoretical diversion is to illustrate that only the long range ordered part of the $Er_2Ti_2O_7$ structure has been determined, and if the order is genuinely described by an order-by-disorder transition there must also be a part that is either fluctuating or static but disordered. Experiments by Ruff *et al* measured the

inelastic scattering in $Er_2Ti_2O_7$ in different applied fields and show that there is no gap, or energetic barrier, to the fluctuations in the system [**3**]. Lago *et al* show with their muon measurements that the system continues to fluctuate, even at dilution temperatures [**4**]. Static disorder is much harder to detect, especially when it is not entirely clear what the disordered component may be. Measurements of the diffuse scattering in $Er_2Ti_2O_7$ show that there the (0, 0, 2) peaks are broad, but this is not conclusive evidence either for or against the order-by-disorder model, [**3**]. The susceptibility measurements made by Cao *et al*, [**5**] indicate that the moment is not stringently restricted to the XY plane, as does the measurement of the crystal field by Shirai, [**6**].

So overall the experimental results imply that there is also a fluctuating component that exists simultaneously with the static order described in this thesis, which lends some support to the idea that the transition is order-by-disorder. This fluctuation may well be out of the local XY plane, as the restriction of the moment to remain in the plane is not that strong. The out of plane fluctuations would not occur at zero temperatures, as the moments would have to be in the ground state, which would be the XY plane. This again agrees with the ideas within the order-by-disorder model, that suggest that order is only stabilised at non-zero temperatures.

6.1.3. Future Work. A model of these fluctuations may allow a better understanding of the magnetic structure, the fluctuations, and the order-by-disorder model. This understanding may also be improved by fitting the inelastic measurements made by Ruff *et al*, [**3**].

6.2. $MnWO_4$

6.2.1. Summary. The magnetic structure of the three antiferromagnetic phases of $MnWO_4$ has been found to agree very well with that described in the literature,

[**7**]. The low temperature magnetic structure, CC (AF1) $< 7.5K$ is a commensurate collinear antiferromagnet, with propagation vector **k**= ($\frac{1}{4}$, $\frac{1}{2}$, $\frac{1}{2}$). The moment was found to lie in the *ac* plane and makes an angle of 35° to the *a* axis, there is no evidence that the electric field has any effect on the structure in this phase.

The intermediate incommensurate, non-colinear antiferromagnetic phase, ICNC (AF2), is found between 7.5 K and 12.5 K and has propagation vector **k**= (-0.214, $\frac{1}{2}$, 0.457). The magnetic structure is cycliodal, and is constructed from two, out of phase components: one that lies in the *ac* plane, that makes an angle of 35° to the direction of *a* and one in the *b* direction, out of phase with that in the *ac* plane. The cycloid was shown to be elliptical with a ratio of 0.85:1 of the *b*:*ac* 8.6 K, and less than 0.85:1 at higher temperatures. The phase is multiferroic as the antiferromagnetic order is accompanied by a spontaneous electric polarization in the direction of *b*. The magnetic order and the electric polarization are strongly coupled and this was demonstrated by measuring the change in the magnetic structure on the application of an electric field. The electric field selected one handedness of domain, which could be interconverted by switching the polarity of the field. The electric field required to interconvert the domains showed hysteresis effects and these effects increased as the temperature increased. The increase in the field required to convert between the different chiral domains mirrors the decrease in the ellipticity of the magnetic structure, and the increase in the magnitude of the electric polarization.

The high temperature magnetic structure, ICC (AF3) is incommensurate but collinear and exists between the transition temperature, 13.5 K and 12.5 K. The propagation vector is the same as that found in the ICNC (AF2) phase **k**= (-0.214, $\frac{1}{2}$, 0.457). The magnetic structure is an amplitude modulated sine wave that lies in the *ac* plane at 35° from the *a* direction. There is no perpendicular *b* component and no response to an applied electric field.

6.2.2. Conclusions. Conclusions regarding the work in this thesis are presented at the end of the chapter and here conclusions will be drawn in a broader context. The multiferroic phase exists between 12.5 K and approximately 7.5 K, where the lower temperature transition is sample dependent demonstrated by a comparison of the work of Lautenschläger and that in this thesis, [**7**]. The usual difference between samples is their quality and the number of imperfections that they contain. The sample dependence of the transition temperature indicates that these imperfections are important for the magnetic structure in the ICNC (AF2) phase. Furthermore, the electric field required to interconvert between different chiral domains varies greatly from sample to sample. A comparison may be made between the the coercive fields required by Finger *et al*, [**8**], to change the handedness of the magnetic structure in their sample, table 6.1. It can be seen that in our experiment the required electric fields are consistently larger. Also, the hysteresis loops that are measured by Finger *et al* on their sample of $MnWO_4$ show an asymmetry that is not present in the work presented in this thesis.

All of these differences serve to underline the importance of the sample in these experiments and indicate that the defects in these materials play an important role in the ordering process. If one considers that the magnetic order simultaneously gives rise to a distortion in the crystallographic structure it could be the case that a local defect would lower the energy for that distortion to occur. If there are a few defects and the majority lower the energy for one direction of the electric polarization rather than the other the situation a magnetic domain imbalance would be expected. The scenario would explain the chiral terms that were observed in this work when no electric field was applied. These features could also give rise to the history effects that are observed in $MnWO_4$, [**8**], such that any distortion to the structure remain in the area of these defects, even when the temperature is reduced, such that when the temperature is increased once more these regions act as a seed to determine the direction in which the magnetic domains will grow.

Temperature [K]	Coercive Field [Vmm^{-1}]	
	This Thesis	Finger *et al*
10	≈ 500	200
11	300	50
12	100	10

TABLE 6.1. The coercive field required to switch the magnetic structure in $MnWO_4$ found in this thesis compared to half the total width of the hysteresis measured by Finger *et al*, [**8**].

6.2.3. Further Work. A comparison between different samples and the rate of domain switching may be an interesting way to investigate the importance of the pinning to defects in these samples. The SHG experiments of Fiebig *et al*, [**9**], directly visualise of the antiferromagnetic and electric domains in multiferroic samples and this may be the ideal tool with which to make this comparison.

6.3. Polarimetry

6.3.1. Summary. The magnetic structures of both of the materials was found to agree with those published, thus it could be concluded that the polarimetry technique gave no further insight to the magnetic structures of these materials than the published fits to single crystal diffraction data.

The measurements of the magnetic structure of $MnWO_4$ in applied electric field showed beautifully what can be measured when the symmetry is broken. However, Sagayama *et al*, [**10**], measured the change in intensity on scattering of neutron beam polarized with $\mathbf{Q}$ before an electrically poled $MnWO_4$ sample i.e. a more simple, uniaxial polarization technique allowed the measurement of the change in the intensity on scattering due to the chirality of a magnetic structure.

6.3.2. Conclusions. The ambiguity in these magnetic structures arises because of the domains that are present in these systems. The technique allows the measurements of the interference of the components of the magnetic structure, both with themselves and with the nuclear scattering. These interference effects will sum to zero in cases where domains are present. In the case of $MnWO_4$ the crystal is monoclinic and only 180° and chiral domains are possible. The de-polarization observed in the ICNC (AF2) phase had to be due to chiral domains as 180° domains make no difference to the diffracted intensity. This allowed the matrices to be fitted unambiguously. $Er_2Ti_2O_7$, however, is cubic and ambiguity due to the equivalence of the crystallographic directions. The equivalence of a, b and c meant that the direction of the basis vectors could not be determined. To take full advantage of the polarimetry technique the cubic symmetry would need to be broken, which could have been achieved by cooling the sample in a magnetic field, before insertion into the CRYOPAD. The problem with this approach, is that you are no longer sampling the genuine ground state, as the electric or magnetic field has perturbed the sample.

The advantage of polarimetry, is that a large amount of information can be inferred from the neutron polarimetry data, when plotted in a way that allows the data to read easily. The disadvantage is that is a complex technique that is not well understood, and as such is regarded by as being able to produce results that it cannot.

The plotting of data is an essential part of understanding what one has measured and the inability to plot the data in a format that is easily read and understood has impeded the development of polarimetry as a tool for the determination of magnetic structures. The understanding of the data was enhanced by the plotting the experimental matrices in reciprocal space, and indeed it was the point at which the $Er_2Ti_2O_7$ data was plotted that the mistakes made in the analysis were identified.

The plots allow the visualization of the polarimetry data and the understanding of the evolution of the magnetic structure with respect to $\mathbf{Q}$.

6.3.3. Future Work. It is intended that the plotting routines will be made available to the neutron scattering community to improve the polarimetry toolset and aid the understanding of polarimetry data. Furthermore, many of the routines that were written in Mathematica may be useful in the future, as there was not any neutron scattering analysis tools written using this software at the beginning of this work.

The polarimetry technique itself is extremely useful for complex magnetic structures, but only in those instances that the global symmetry of these structures has been broken. It is intended to measure more materials with an applied electric field and to develop techniques to apply poling magnetic fields to select the S-domain formation of samples.

References

[1] Champion J D M, Harris M J, Holdsworth P C W, et al. 2003 *Phys. Rev. B*, **68**, 020401(R)

[2] Villain J, Bideaux R, Carton J.-P, Conie R, *J. Phys*, **41**, 1263, (1980)

[3] Ruff J P C, Clancy J P, Bourque A, White M A, Ramazanoglu M, Gardner J S, Qiu Y, Copley J R D, Johnson M B, Dabkowska H A and Gaulin B D *Phys. Rev. Lett.*, **101**, 147205 (2008)

[4] Lago J, Lancaster T, Blundell S J, Bramwell S T, Pratt F L, Shirai M and Baines C, *J. Phys.: Condens. Mat.*, **17**, 979, (2005)

[5] Cao H, Gukasov A, Mirebeau I, Bonville P, Decorse C, Dhalenne G, *Phys. Rev. Lett.*, **103**, 056402 (2009)

[6] Shirai M, *Experimental Investigations of Frustrated Antiferromagnets* , UCL

[7] Lautenschläger G, Weitzel H, Vogt T *et al Phys. Rev. B* **48** 6087 (1993)

[8] Finger T, Senff D, Schmalzl K, Schmidt W, Regnault L P, Becker P, Bohatý L, Braden M, *Phys. Rev. B*, **81** 054430 (2010)

[9] Meier D, Leo N, Maringer M, Lottermoser Th, Fiebig M, Becker P and Bohatý L *Phys. Rev. B*, **80**, 224420 (2009)

[10] Sagayama H, Taniguchi K, Abe N, Arima T, Soda M, Matsuura M and Hirota K *Phys. Rev. B*, **77**, 220407 (2008)

APPENDIX A

Magnetic Representations

In order to follow the development and terminology used by Izyumov, Naish and Ozerov in 'Neutron Diffraction of Materials' let us begin at the point that a magnetic representation is first stated (page 63).

A magnetic representation is developed when an axial vector is assigned to an atomic site in a crystal. A magnetic moment is described by an axial vector as the magnetic moment can be considered as a current loop that generates a magnetic moment. The function that describes this for each of the j atomic sites is φ,

$$\varphi_{\mathbf{k}}^{j,\beta} = \sum_{n}^{\oplus} \sigma_0^{j\beta} e^{i\mathbf{k}\mathbf{t}_n}, \tag{A.1}$$

where the sum is over all n cells of the crystal. The three orthogonal directions are indicated by β, which can take the value x, y or z, $\mathbf{k}$ is the wave vector describing the direction and period of the magnetic structure modulation, if one is present, and $\mathbf{t}_n$ is an integer describing the translation through the crystal to the n^{th} cell. Finally, $\sigma_0^{j\beta}$ denotes a $3\sigma N$-dimensional column in which the β projection of the $\mathrm{j}^t h$ atom in the zeroth unit cell is the only non-zero component. The functions $\varphi_{\mathbf{k}}^{j,\beta}$ are eigenfunctions of the translation operator $T(\mathbf{t}_n)$ and as such $\varphi_{\mathbf{k}}^{j,\beta}$ and $\mathbf{k}$ are Bloch functions.

The transformation of the function $\varphi_{\mathbf{k}}^{j,\beta}$ with the symmetry element $g\,\{h|\tau_h\}$ of group $G_{\mathbf{k}}$ describes: a) the permutation, which can generate a symmetrically equivalent atom i, with the position $\mathbf{r}_i$ from atom j,

$$g\mathbf{r}_j = h\mathbf{r}_j + \tau_h = \mathbf{r}_i + \mathbf{a}_p(g,j), \tag{A.2}$$

where the vector $\mathbf{a}_p$ returns the atom i to the original cell; b) the rotation of the axial vectors that denote the magnetic moment. The description of the rotation of symmetry element h that acts upon a vector in the β direction, to generate a vector in the α direction is constructed of two parts $R^h_{\alpha\beta}$ and δ^h. Where $R^h_{\alpha\beta}$ is a matrix that describes the rotational transformation of a set of polar vectors from orientation β to orientation α, if we were describing an atomic displacement, only this component would be required. The second component is required due to the axial vector description of a magnetic moment: axial vectors do not change sign under inversion and hence in order to invert the sign of the vector we need the component $\delta^h = -1$, when no inversion takes place $\delta^h = 1$. Overall the effect of the operator $T(g)$ upon the function $\varphi^{j,\beta}_{\mathbf{k}}$ gives:

$$T(g)\varphi^{j\beta}_{\mathbf{k}} = \sum_{i\alpha} \left\{d^{\mathbf{k}}_m(g)\right\}_{i\alpha,\ j\beta} \varphi^{i\alpha}_{\mathbf{k}} \tag{A.3}$$

where the magnetic representation,

$$\left\{d^{\mathbf{k}}_m(g)\right\}_{i\alpha,\ j\beta} = \exp\left[-i\mathbf{k}\mathbf{a}_p(g,j)\right] \delta^h R^h_{\alpha\beta}\delta_{i,gj} \tag{A.4}$$

and,

$$d^{\mathbf{k}}_m = \sum_{\nu} n_\nu d^{\mathbf{k}\nu}, \tag{A.5}$$

where the $d^{\mathbf{k}\nu}$ is the are the irreducible representations of the group $G_{\mathbf{k}}$ and n_ν is the multiplicity of the ν^{th} representation. The quantity n_ν is given by the relation,

$$n_\nu = \frac{1}{n\left(G^0_{\mathbf{k}}\right)} \sum_{h \in G^0_{\mathbf{k}}} \chi^{\mathbf{k}}_m(g) \chi^{\star \mathbf{k}\nu}(g), \tag{A.6}$$

$$\chi^{\mathbf{k}}_m(g) = \delta_h \mathrm{Sp} R^h \sum_j \exp\left[-i\mathbf{k}\mathbf{a}_p(g,\ j)\right] \delta_{j,\ gj}, \tag{A.7}$$

where $\chi^{\mathbf{k}}_m(g)$ is the character of the magnetic representation of the group $G_{\mathbf{k}}$, $\chi^{\star \mathbf{k}\nu}(g)$ is the character of the of the irreducible representation $d^{\mathbf{k}\nu}$ and Sp R^h is the spur of the matrix $R^h_{\alpha\beta}$ that describes the rotation for the element $g = \{h|\tau_h\}$. The expressions above combine to give the the vector $\mathbf{S}\left(\begin{smallmatrix}\mathbf{k}\nu \\ \lambda\end{smallmatrix}|i\right)$, which can be considered to be the vectors of the magnetic moments on the crystal sites.

$$\mathbf{S}\left(\begin{array}{c|c} \mathbf{k}\nu & i \\ \lambda & \end{array}\right) = \sum_{h \in G^0_{\mathbf{k}}} d^{\star \mathbf{k}\nu}_{\lambda[\mu]}(g) \exp\left[-i\mathbf{k}\mathbf{a}_p(g,\ j)\right] \delta_{i,\ g[j]} \delta^h \begin{pmatrix} R^h_{x[\beta]} \\ R^h_{y[\beta]} \\ R^h_{z[\beta]} \end{pmatrix} \tag{A.8}$$

This vector is complex and knowledge of these vectors along with the values of the propogation vector $\mathbf{k}$ will allow the determination of the magnetic structure. The vector $\mathbf{S}\left(\begin{smallmatrix}\mathbf{k}\nu \\ \lambda\end{smallmatrix}|i\right)$ corresponds to the basis vector output from Sara$h$ and it is the sum over these vectors, combined with the complex coefficient C^ν_λ that gives the magnetic moment on atom site i in the zeroth unit cell, denoted by the $0i$ subscript.

$$\mathbf{S}_{0i}^{\mathbf{k}_L\nu} = \sum_{\lambda} C_{\lambda}^{\nu} \mathbf{S} \left(\begin{array}{c|c} \mathbf{k}_L\nu & i \\ \lambda & \end{array} \right) \tag{A.9}$$

The sum is over all ν irreducible representations and all λ basis vectors, for the L^{th} $\mathbf{k}$ vector.

$$\mathbf{S}_{ni} = \sum_{L} \mathbf{S}_{0i}^{\mathbf{k}_L\nu} \exp\left(i\mathbf{k}_L\mathbf{t}_n\right) \tag{A.10}$$

Where each of the L values of $\mathbf{S}_{0i}^{\mathbf{k}_L}$ are related by symmetry,

$$\mathbf{S} \left(\begin{array}{c|c} \mathbf{k}_L\nu & i' \\ \lambda & \end{array} \right) = \exp\left[-i\mathbf{k}_L\mathbf{a}_p(g_L,\ i)\right] \delta^{h_L} R^{h_L} \mathbf{S} \left(\begin{array}{c|c} \mathbf{k}\nu & i \\ \lambda & \end{array} \right). \tag{A.11}$$

The sum over all L $\mathbf{k}$ vectors gives the magnetic structure of the crystal. This quantity must be real.

It is the value $\mathbf{S}_{0i}^{\mathbf{k}_L}$ that is used in the magnetic form factor, this quantity can be imaginary.

APPENDIX B

Axes transformations

The conversion of the the crystallographic lattice axis system to that of the polarisation orientation is essential to understand the SNP data. The magnetic structure is a vector that is described with respect to the crystallographic basis (**a**, **b**, **c**), whereas the information returned in a cryopad experiment is with respect to the instrumental axes (**x**, **y**, **z**) where **x** is in the direction of the scattering vector, **z** is in the direction of the zone axis and **y** makes up the right hand set and therefore defines the plane of scattering when considered with the **z** axis. In order to map the magnetic vector onto the instrumental axis system the first step is to find the matrix that will convert the crystallographic structure into an orthogonal setting so the magnetic may be converted to a vector that is described in a cartesian axes system. The cartesian axis system is then rotated so that it fits on to the instruemtntal axes for each reflection.

The description of how one converts from one set of crystallographic basis vectors to another is described in the International Tables Volume A, Chapter 5.1, pp 78-85, [**1**]. A summary of this section will be given below, along with some examples and a description of how it is applied in the routines that have been written to calculate the polarisation matrices.

When we are considering the rotation of a coordinate system we consider the objects that are described by the coordinate system to be at rest. In this example we consider the crystal and magnetic structure to remain at rest whilst the axis system is changed around it. Let us first consider the transformation of the length of the axes and then the effect that this would have on the position vector.

The transformation $\mathbf{c} \rightarrow \frac{1}{2}\mathbf{c}$ would be described by,

(B.1)
$$\mathbf{P} = \begin{pmatrix} 1 & 0 & 0 \\ 0 & 1 & 0 \\ 0 & 0 & \frac{1}{2} \end{pmatrix}$$

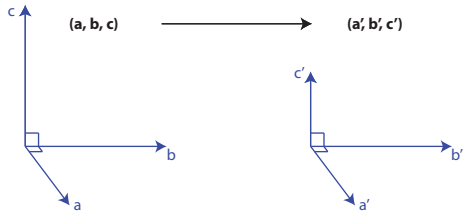

FIGURE B.1. Conversion of unit axes with transformation matrix, B.1

if we then consider a vector $\mathbf{r}$, that describes a position X, with coordinates (x, y, z) in the original setting, ($\mathbf{a}$,$\mathbf{b}$, $\mathbf{c}$), would be transformed by the inverse matrix $\mathbf{Q}$= $\mathbf{P}^{-1}$,

(B.2)
$$\mathbf{Q} = \begin{pmatrix} 1 & 0 & 0 \\ 0 & 1 & 0 \\ 0 & 0 & 2 \end{pmatrix}$$

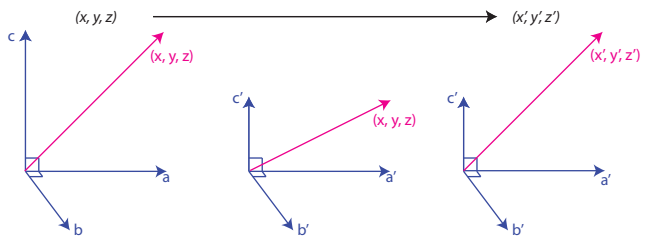

FIGURE B.2. Conversion of vector with rotation matrix, B.2

In the above example it can be seem that the inverse of the matrix that describes the transformation of the crystallographic basis is used to transform the coordinates that describe the vector. The same relationship is true when we transform the internal angles of a crystallographic basis,

$$\mathbf{P} = \begin{pmatrix} 1 & 1 & 0 \\ 0 & 2 & 0 \\ 0 & 0 & 1 \end{pmatrix} \tag{B.3}$$

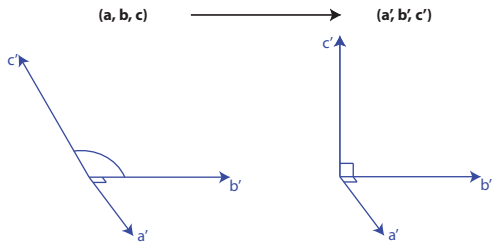

FIGURE B.3. Conversion of axes with transformation matrix, B.3

$$\mathbf{Q} = \begin{pmatrix} 1 & \frac{1}{2} & 0 \\ 0 & \frac{1}{2} & 0 \\ 0 & 0 & 1 \end{pmatrix} \tag{B.4}$$

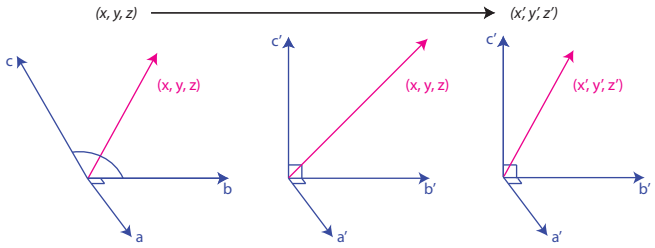

FIGURE B.4. Conversion of vector with rotation matrix, B.4

This can be summarised,

$$
\begin{aligned}
(\mathbf{a}', \mathbf{b}', \mathbf{c}') &= (\mathbf{a}, \mathbf{b}, \mathbf{c})\mathbf{P} \\
&= (\mathbf{a}, \mathbf{b}, \mathbf{c}) \begin{pmatrix} P_{11} & P_{12} & P_{13} \\ P_{21} & P_{22} & P_{23} \\ P_{31} & P_{32} & P_{33} \end{pmatrix}
\end{aligned}
$$

$$
\begin{aligned}
\begin{pmatrix} x' \\ y' \\ z' \end{pmatrix} &= \mathbf{Q} \begin{pmatrix} x \\ y \\ z \end{pmatrix} \\
&= \begin{pmatrix} Q_{11} & Q_{12} & Q_{13} \\ Q_{21} & Q_{22} & Q_{23} \\ Q_{31} & Q_{32} & Q_{33} \end{pmatrix} \begin{pmatrix} x \\ y \\ z \end{pmatrix}
\end{aligned}
$$

The crystallographic properties that are manipulated in the same way as the basis vectors, and as such are described with a row vector are termed *covarient*. These properties are:

- The basis vectors of in direct space (**a**, **b**, **c**)
- The Miller indices of a plane in direct space (h k l)
- The coordinates of a point in reciprocal space h, k, l

The properties that are manipulated in the same way as the coordinates of a point, and as such are described by a column vector, are termed *contravarient*. These properties are:

- The basis vectors of in reciprocal space (**a***, **b***, **c***)
- The indices of a direction in direct space [u v w]
- The coordinates of a point in direct space x, y, z

References

Editor Hahn T *International Tables of Crystallography Volume A: Space-Group Symmetry* Kluwer Academic Publishers, London, (2002)

APPENDIX C

Routines used for calculating and plotting data

Input

- **Constants**

- **Lattice Paramters**

```
αLatPar = 90;
βLatPar = 90;
γLatPar = 90;
aLatPar = 10.04;
bLatPar = 10.04;
cLatPar = 10.04;
```

- **Nuclear Scattering Lengths**

Values for scattering lengths are from the ILL website page:
www.ill.fr/yellowbook- select D3
select b and choose atom from periodic table

```
NSbAtom1=0.77900;
NSbAtom2=-0.34380;
NSbAtom3=0.58050;
NSbAtom4=0.58050;

ScatteringLength={NSbAtom1,NSbAtom2,NSbAtom3,NSbAtom4};
```

- **Thermal Factors**

```
TFBEr = 0.10825;
TFBTi = 0.19556;
TFBO1 = 0.11092;
TFBO2 = 0.14929;

TFBAllAtoms={TFBEr,TFBTi,TFBO1,TFBO2};
```

- **Magnetic Form Factors**

From the ILL website

```
Atom1FF =
  {0.0586, 17.980, 0.3540, 7.096, 0.6126, 2.748, -0.0251, 0.0171};

AtomFF = {Atom1FF, Atom1FF};
```

Moment

```
Moment1 = 3;

Moment={Moment1};
```

- **Magnetic Propagation Vector**

```
k := {0, 0, 0};
```

- **Neutron Wavelength**

From the History file generated by Igor Pro - value in Angstroms

```
Lamda = 0.825;
```

- **Location Input and Translation**

Where atom 1 is magnetic

```
Atom1 = {{0, 0, 0}, {1 / 2, 3 / 4, 1 / 4},
   {1 / 4, 1 / 2, 3 / 4}, {3 / 4, 1 / 4, 1 / 2}};
Atom2 = {{1 / 2, 1 / 2, 1, 2}, {1 / 4, 3 / 4, 0},
   {3 / 4, 0, 1 / 4}, {0, 1 / 4, 3 / 4}};
Atom3 = {{1 / 8, 1 / 8, 1 / 8}, {7 / 8, 3 / 8, 3 / 8}};
Atom4 = {{x, 1 / 8, 1 / 8}, {-x + 3 / 4, 1 / 8, 5 / 8},
   {1 / 8, x, 1 / 8}, {5 / 8, -x + 3 / 4, 1 / 8}, {1 / 8, 1 / 8, x},
   {1 / 8, 5 / 8, -x + 3 / 4}, {7 / 8, x + 1 / 4, 3 / 8},
   {7 / 8, -x, 7 / 8}, {x + 3 / 4, 3 / 8, 3 / 8}, {-x + 1 / 2, 7 / 8, 3 / 8},
   {7 / 8, 3 / 8, -x + 1 / 2}, {3 / 8, 3 / 8, x + 3 / 4}};

x = 0.4194;


Trans = {{0, 0, 0}, {0, 1 / 2, 1 / 2}, {1 / 2, 0, 1 / 2}, {1 / 2, 1 / 2, 0}} ;

numMagSites = 1;

AtomTypes = {Atom1, Atom2, Atom3, Atom4};
```

```
numTrans = Length[Trans];
numATypes = Length[AtomTypes];
numASites =
  Table[Table[Dimensions[AtomTypes[[a]]], {a, numATypes}][[a, 1]],
   {a, numATypes}];


Coordinates = Table[0, {n, numATypes}];

(*The Do Loop below generates the coordinates
  of all the sites that the different atoms inhabit -
 this is done by adding the translations (Trans) to the
  locations (AtomTypes).  The table is then flattened to
  produce a list of coordinates for each type of Atom.  Note
  that if the value that is generated by adding the translation
  to the location is greater than or equal to one the value
  is reduced by one and if the value that is generated is
  less than zero the value is increased by one.  This is to
  ensure that all points lie within the first unit cell*)

Do[Coordinates[[n]] =
   Table[If[AtomTypes[[n, a, c]] + Trans[[b, c]] ≥ 1,
     AtomTypes[[n, a, c]] + Trans[[b, c]] - 1,
     If[AtomTypes[[n, a, c]] + Trans[[b, c]] < 0,
      AtomTypes[[n, a, c]] + Trans[[b, c]] + 1,
      AtomTypes[[n, a, c]] + Trans[[b, c]]]],
    {a, numASites[[n]]}, {b, numTrans}, {c, 3}], {n, numATypes}];

TraditionalForm[Coordinates]
```

$$\left\{\begin{pmatrix} \{0,\,0,\,0\} & \left\{0,\,\frac{1}{2},\,\frac{1}{2}\right\} & \left\{\frac{1}{2},\,0,\,\frac{1}{2}\right\} & \left\{\frac{1}{2},\,\frac{1}{2},\,0\right\} \\ \left\{\frac{1}{2},\,\frac{3}{4},\,\frac{1}{4}\right\} & \left\{\frac{1}{2},\,\frac{1}{4},\,\frac{3}{4}\right\} & \left\{0,\,\frac{3}{4},\,\frac{3}{4}\right\} & \left\{0,\,\frac{1}{4},\,\frac{1}{4}\right\} \\ \left\{\frac{1}{4},\,\frac{1}{2},\,\frac{3}{4}\right\} & \left\{\frac{1}{4},\,0,\,\frac{1}{4}\right\} & \left\{\frac{3}{4},\,\frac{1}{2},\,\frac{1}{4}\right\} & \left\{\frac{3}{4},\,0,\,\frac{3}{4}\right\} \\ \left\{\frac{3}{4},\,\frac{1}{4},\,\frac{1}{2}\right\} & \left\{\frac{3}{4},\,\frac{3}{4},\,0\right\} & \left\{\frac{1}{4},\,\frac{1}{4},\,0\right\} & \left\{\frac{1}{4},\,\frac{3}{4},\,\frac{1}{2}\right\} \end{pmatrix},\right.$$

$$\begin{pmatrix} \left\{\frac{1}{2},\,\frac{1}{2},\,0\right\} & \left\{\frac{1}{2},\,0,\,\frac{1}{2}\right\} & \left\{0,\,\frac{1}{2},\,\frac{1}{2}\right\} & \{0,\,0,\,0\} \\ \left\{\frac{1}{4},\,\frac{3}{4},\,0\right\} & \left\{\frac{1}{4},\,\frac{1}{4},\,\frac{1}{2}\right\} & \left\{\frac{3}{4},\,\frac{3}{4},\,\frac{1}{2}\right\} & \left\{\frac{3}{4},\,\frac{1}{4},\,0\right\} \\ \left\{\frac{3}{4},\,0,\,\frac{1}{4}\right\} & \left\{\frac{3}{4},\,\frac{1}{2},\,\frac{3}{4}\right\} & \left\{\frac{1}{4},\,0,\,\frac{3}{4}\right\} & \left\{\frac{1}{4},\,\frac{1}{2},\,\frac{1}{4}\right\} \\ \left\{0,\,\frac{1}{4},\,\frac{3}{4}\right\} & \left\{0,\,\frac{3}{4},\,\frac{1}{4}\right\} & \left\{\frac{1}{2},\,\frac{1}{4},\,\frac{1}{4}\right\} & \left\{\frac{1}{2},\,\frac{3}{4},\,\frac{3}{4}\right\} \end{pmatrix},$$

$$\begin{pmatrix} \left\{\frac{1}{8},\,\frac{1}{8},\,\frac{1}{8}\right\} & \left\{\frac{1}{8},\,\frac{5}{8},\,\frac{5}{8}\right\} & \left\{\frac{5}{8},\,\frac{1}{8},\,\frac{5}{8}\right\} & \left\{\frac{5}{8},\,\frac{5}{8},\,\frac{1}{8}\right\} \\ \left\{\frac{7}{8},\,\frac{3}{8},\,\frac{3}{8}\right\} & \left\{\frac{7}{8},\,\frac{7}{8},\,\frac{7}{8}\right\} & \left\{\frac{3}{8},\,\frac{3}{8},\,\frac{7}{8}\right\} & \left\{\frac{3}{8},\,\frac{7}{8},\,\frac{3}{8}\right\} \end{pmatrix},$$

$$\left.\begin{pmatrix} \left\{0.4194,\,\frac{1}{8},\,\frac{1}{8}\right\} & \left\{0.4194,\,\frac{5}{8},\,\frac{5}{8}\right\} & \left\{0.9194,\,\frac{1}{8},\,\frac{5}{8}\right\} & \left\{0.9194,\,\frac{5}{8},\,\frac{1}{8}\right\} \\ \left\{0.3306,\,\frac{1}{8},\,\frac{5}{8}\right\} & \left\{0.3306,\,\frac{5}{8},\,\frac{1}{8}\right\} & \left\{0.8306,\,\frac{1}{8},\,\frac{1}{8}\right\} & \left\{0.8306,\,\frac{5}{8},\,\frac{5}{8}\right\} \\ \left\{\frac{1}{8},\,0.4194,\,\frac{1}{8}\right\} & \left\{\frac{1}{8},\,0.9194,\,\frac{5}{8}\right\} & \left\{\frac{5}{8},\,0.4194,\,\frac{5}{8}\right\} & \left\{\frac{5}{8},\,0.9194,\,\frac{1}{8}\right\} \\ \left\{\frac{5}{8},\,0.3306,\,\frac{1}{8}\right\} & \left\{\frac{5}{8},\,0.8306,\,\frac{5}{8}\right\} & \left\{\frac{1}{8},\,0.3306,\,\frac{5}{8}\right\} & \left\{\frac{1}{8},\,0.8306,\,\frac{1}{8}\right\} \\ \left\{\frac{1}{8},\,\frac{1}{8},\,0.4194\right\} & \left\{\frac{1}{8},\,\frac{5}{8},\,0.9194\right\} & \left\{\frac{5}{8},\,\frac{1}{8},\,0.9194\right\} & \left\{\frac{5}{8},\,\frac{5}{8},\,0.4194\right\} \\ \left\{\frac{1}{8},\,\frac{5}{8},\,0.3306\right\} & \left\{\frac{1}{8},\,\frac{1}{8},\,0.8306\right\} & \left\{\frac{5}{8},\,\frac{5}{8},\,0.8306\right\} & \left\{\frac{5}{8},\,\frac{1}{8},\,0.3306\right\} \\ \left\{\frac{7}{8},\,0.6694,\,\frac{3}{8}\right\} & \left\{\frac{7}{8},\,0.1694,\,\frac{7}{8}\right\} & \left\{\frac{3}{8},\,0.6694,\,\frac{7}{8}\right\} & \left\{\frac{3}{8},\,0.1694,\,\frac{3}{8}\right\} \\ \left\{\frac{7}{8},\,0.5806,\,\frac{7}{8}\right\} & \left\{\frac{7}{8},\,0.0806,\,\frac{3}{8}\right\} & \left\{\frac{3}{8},\,0.5806,\,\frac{3}{8}\right\} & \left\{\frac{3}{8},\,0.0806,\,\frac{7}{8}\right\} \\ \left\{0.1694,\,\frac{3}{8},\,\frac{3}{8}\right\} & \left\{0.1694,\,\frac{7}{8},\,\frac{7}{8}\right\} & \left\{0.6694,\,\frac{3}{8},\,\frac{7}{8}\right\} & \left\{0.6694,\,\frac{7}{8},\,\frac{3}{8}\right\} \\ \left\{0.0806,\,\frac{7}{8},\,\frac{3}{8}\right\} & \left\{0.0806,\,\frac{3}{8},\,\frac{7}{8}\right\} & \left\{0.5806,\,\frac{7}{8},\,\frac{7}{8}\right\} & \left\{0.5806,\,\frac{3}{8},\,\frac{3}{8}\right\} \\ \left\{\frac{7}{8},\,\frac{3}{8},\,0.0806\right\} & \left\{\frac{7}{8},\,\frac{7}{8},\,0.5806\right\} & \left\{\frac{3}{8},\,\frac{3}{8},\,0.5806\right\} & \left\{\frac{3}{8},\,\frac{7}{8},\,0.0806\right\} \\ \left\{\frac{3}{8},\,\frac{3}{8},\,0.1694\right\} & \left\{\frac{3}{8},\,\frac{7}{8},\,0.6694\right\} & \left\{\frac{7}{8},\,\frac{3}{8},\,0.6694\right\} & \left\{\frac{7}{8},\,\frac{7}{8},\,0.1694\right\} \end{pmatrix}\right\}$$

- **Basis Vector Input and Combination**

```
psiArray = {{{{{4, -2, -2}, {4, 2, 2}, {-4, -2, 2}, {-4, 2, -2}},
      {{0, 2 Sqrt[3], -2 Sqrt[3]}, {0, -2 Sqrt[3], 2 Sqrt[3]},
       {0, 2 Sqrt[3], 2 Sqrt[3]}, {0, -2 Sqrt[3], -2 Sqrt[3]}}},
     {{{0, 2, -2}, {0, -2, 2}, {0, -2, -2}, {0, 2, 2}},
      {{-2, 0, 2}, {2, 0, 2}, {2, 0, -2}, {-2, 0, -2}},
      {{2, -2, 0}, {-2, -2, 0}, {2, 2, 0}, {-2, 2, 0}}}}},

   {{{{{-4, 2, 2}, {-4, -2, -2}, {4, 2, -2}, {4, -2, 2}},
      {{0, -2 Sqrt[3], 2 Sqrt[3]}, {0, 2 Sqrt[3], -2 Sqrt[3]},
       {0, -2 Sqrt[3], -2 Sqrt[3]}, {0, 2 Sqrt[3], 2 Sqrt[3]}}},
     {{{0, -2, 2}, {0, 2, -2}, {0, 2, 2}, {0, -2, -2}},
      {{2, 0, -2}, {-2, 0, -2}, {-2, 0, 2}, {2, 0, 2}},
      {{-2, 2, 0}, {2, 2, 0}, {-2, -2, 0}, {2, -2, 0}}}}},

   {{{{{-2, 4, -2}, {-2, -4, 2}, {2, 4, 2}, {2, -4, -2}},
      {{-2 Sqrt[3], 0, 2 Sqrt[3]}, {-2 Sqrt[3], 0, -2 Sqrt[3]},
       {2 Sqrt[3], 0, -2 Sqrt[3]}, {2 Sqrt[3], 0, 2 Sqrt[3]}}},
     {{{-2, 0, 2}, {2, 0, 2}, {2, 0, -2}, {-2, 0, -2}},
      {{0, 2, -2}, {0, -2, 2}, {0, -2, -2}, {0, 2, 2}},
      {{2, -2, 0}, {-2, -2, 0}, {2, 2, 0}, {-2, 2, 0}}}}},

   {{{{{2, -4, 2}, {2, 4, -2}, {-2, -4, -2}, {-2, 4, 2}},
      {{2 Sqrt[3], 0, -2 Sqrt[3]}, {2 Sqrt[3], 0, 2 Sqrt[3]},
       {-2 Sqrt[3], 0, 2 Sqrt[3]}, {-2 Sqrt[3], 0, -2 Sqrt[3]}}},
     {{{2, 0, -2}, {-2, 0, -2}, {-2, 0, 2}, {2, 0, 2}},
      {{0, -2, 2}, {0, 2, -2}, {0, 2, 2}, {0, -2, -2}},
      {{-2, 2, 0}, {2, 2, 0}, {-2, -2, 0}, {2, -2, 0}}}}},

   {{{{{-2, -2, 4}, {-2, 2, -4}, {2, -2, -4}, {2, 2, 4}},
      {{2 Sqrt[3], -2 Sqrt[3], 0}, {2 Sqrt[3], 2 Sqrt[3], 0},
       {-2 Sqrt[3], -2 Sqrt[3], 0}, {-2 Sqrt[3], 2 Sqrt[3], 0}}},
     {{{2, -2, 0}, {-2, -2, 0}, {2, 2, 0}, {-2, 2, 0}},
      {{0, 2, -2}, {0, -2, 2}, {0, -2, -2}, {0, 2, 2}},
      {{-2, 0, 2}, {2, 0, 2}, {2, 0, -2}, {-2, 0, -2}}}}},

   {{{{{2, 2, -4}, {2, -2, 4}, {-2, 2, 4}, {-2, -2, -4}},
      {{-2 Sqrt[3], 2 Sqrt[3], 0}, {-2 Sqrt[3], -2 Sqrt[3], 0},
       {2 Sqrt[3], 2 Sqrt[3], 0}, {2 Sqrt[3], -2 Sqrt[3], 0}}},
     {{{-2, 2, 0}, {2, 2, 0}, {-2, -2, 0}, {2, -2, 0}},
      {{0, -2, 2}, {0, 2, -2}, {0, 2, 2}, {0, -2, -2}},
      {{2, 0, -2}, {-2, 0, -2}, {-2, 0, 2}, {2, 0, 2}}}}};




numSDom = Dimensions[psiArray][[1]];
numMagSites = Dimensions[psiArray][[2]];
numIR = Table[
```

```
    Table[Dimensions[psiArray[[1, a]]], {a, numMagSites}][[a, 1]],
    {a, numMagSites}];
numpsi = Table [Table[Dimensions[psiArray[[1, a, b]]],
      {a, numMagSites}, {b, numIR[[a]]}][[a, b, 1]],
    {a, numMagSites}, {b, numIR[[a]]}];
```

Experimental Data Input and De - Polarisation correction

Read-in of experimental data

Read in of experimental input

This box describes where the experimental data is within your computer reads it in, and is the window for you to describe your preferences with regard to the subsequent data manipulation.

1. The first line is the read in of the data.

2. The Control Reflections are used to correct for the decrease of the polarisation of the He cell

3. MinNCount is the minimum nuetron count for the reflections that are included in Experimental list - the lower the numer of neutrons recorded the worse the statistics

4. Sortby is the criteria that will be used to sort the data the criteria that are availble are:

1 => Reflection - this sorts by hkl and then zone axis
2 => Orientation- this sorts by the zone axis and then hkl
3 => Family - this sorts by the value of the Magnetic Interaction Vector using the equation: $\sum_{c=1}^{numASites[[b]]} Exp[2 * I * Pi * (hklUnsort[[a]].Coordinates[[b, c, 1]])]$
4 => QFactor - this sorts by QFactor where Q is the inverse of the D spacing

```
Data = Import["Desktop/Data_ErTi2O5.csv", "CSV"];

D9Data = Import["Desktop/Data_ErTi2O5_D9.csv", "CSV"];

ControlReflection1 = {4, 0, 0};

ControlReflection2 = {0, 0, 4};

ControlReflection3 = {4, 0, 0};

MinNCount = 100;

Sortby = 2;
```

- **De-Polarisation Correction**

- **Determination of polarisation correction parameters.**

```
numDataUnsort = Dimensions[Data][[1]];

Epoints = {};


(*Select the control reflections from the data,
with the time that they were
 measured and the measured polarization*)

Do[
 If[Or[Data[[a * 6 - 5, {5, 6, 7}]] == ControlReflection1,
   Data[[a * 6 - 5, {5, 6, 7}]] == ControlReflection2,
   Data[[a * 6 - 5, {5, 6, 7}]] == ControlReflection3], AppendTo[
   Epoints, {{(Abs[Data[[a * 6 - 1, 8]]] + Abs[Data[[a * 6 - 1, 9]]]),
     Abs[Data[[a * 6 - 1, 16]]]}}]], {a, numDataUnsort / 6}]


Epoints = Flatten[Epoints, 1];
a = 0;


(*Make a list of control reflections,
where the polarization for the subsequent
 reflection is less than the one that proceeds it*)

Epolabs = {{}, {}, {}, {}, {}, {}, {}, {}, {}, {}};

Do[{a = a + 1,

  While[
   (Epoints[[a, 2]] + 0.05 * Epoints[[a, 2]]) > Epoints[[a + 1, 2]],
   AppendTo[
    Epolabs[[n]], Epoints[[a]]];
   a++ 1]},
 {n, 10}]

Clear[a]

polLine = Table[{}, {n, Length[Epolabs]}];


(*Make a linear fit,
where the line is describe by y = m*pol + c*1,
where pol is the time and y is the polarization*)

Do[polLine[[n]] = Fit[Epolabs[[n]], {1, pol}, pol],
  {n, Length[Epolabs]}];
```

- **Extraction of data from file and application of polarisation correction**

```
(* Extract from the data the time at which
 measurement is made and assign this value to pol *)

pol = Table[(Data[[a * 2 - 1, 9]] + Data[[a * 2 - 1, 8]]),
   {a, numDataUnsort / 2}];



(* Take all the data and ... *)
DataUnsort = {};

a = 1;

Do[{a = a,


   While[

    (*whilst the polarization is continuing to decrease ...
       (to compensate for instances where a nuclear
         peak was not measured either just before
      or just after the new cell was delivered)*)

    Abs[
      Data[[a * 6 - 5, 12]] / polLine[[n, a * 3 - 2]]] < 1.15,

    (*if the intensity is large
      enough to give a meaningful plot... *)

    If[Data[[a * 6 - 4, 18]] > MinNCount,

     (*extract from the data the useful parts...*)

     AppendTo[

      DataUnsort, {

       (*hkl...*)
       Data[[a * 6 - 5, {1, 2, 3}]],

       (*orientation...*)
       Data[[a * 6 - 5, {5, 6, 7}]],

       (*polarization direction*)
       Data[[a * 6 - 5, 11]],

       (*intensity...*)
       Data[[a * 6 - 4, 18]],

       (*calculate Q...*)
```

```
        Q[Data[[a * 6 - 5, {5, 6, 7}]]],


        (*calculate the magnetic interaction vector...*)
        Chop[ Sum_{c=1}^{numASites[[1]]}  Exp[2 * I * Pi *
            (Data[[a * 6 - 5, {5, 6, 7}]].Coordinates[[1, c, 1]])]],


        (*the symbolic magnetic interaction vector - which
          describes which family the reflection belongs to *)
        Chop[ Sum_{c=1}^{numASites[[1]]}  Exp[2 * I * Pi * (Data[[a * 6 - 5, {5, 6, 7}]].
              Coordinates[[1, c, 1]])] * m[c]],


        (*The corrected polarization matrix...*)
        {Data[[a * 6 - 5, {12, 14, 16}]] / polLine[[n, a * 3 - 2]],
         Data[[a * 6 - 3, {12, 14, 16}]] / polLine[[n, a * 3 - 1]],
         Data[[a * 6 - 1, {12, 14, 16}]] / polLine[[n, a * 3]]}

        ,
        (*The corrected errors for the polarization matrix...*)
        {Data[[a * 6 - 5, {13, 15, 17}]] / polLine[[n, a * 3 - 2]],
         Data[[a * 6 - 3, {13, 15, 17}]] / polLine[[n, a * 3 - 1]],
         Data[[a * 6 - 1, {13, 15, 17}]] / polLine[[n, a * 3]]}}

      ]

     ];

     a++ 1]},
   {n, 10}];


Clear[numData]
Clear[a]
Clear[pol]
```

■ Sorting and Extraction of experimental data

■ Sorting of polarisation corrected data

1 = > Reflection - this sorts by hkl and then zone axis
2 = > Orientation - this sorts by the zone axis and then hkl

3 = > Family – this sorts by the value of the Magnetic Interaction Vector using the equation : $\sum_{c=1}^{\text{numASites}[[b]]} \text{Exp}[2 * I * \text{Pi} * (\text{hklUnsort}[[a]].\text{Coordinates}[[b, c, 1]])]$

4 = > QFactor – this sorts by QFactor where Q is the inverse of the D spacing

```
If[Sortby == 1, DataSort = Sort[DataUnsort,
    OrderedQ[{Take[#1][[{2, 1, 5}]], Take[#2][[{2, 1, 5}]]}] &],
  If[Sortby == 2, DataSort = Sort[DataUnsort,
     OrderedQ[{Take[#1][[{1, 2, 5}]], Take[#2][[{1, 2, 5}]]}] &],
   If[Sortby == 3, DataSort = Sort[DataUnsort,
      OrderedQ[{Take[#1][[{6, 2, 3}]], Take[#2][[{6, 2, 3}]]}] &],
    If[Sortby == 4, DataSort = Sort[DataUnsort,
       OrderedQ[{Take[#1][[{5, 2, 4, 3}]],
          Take[#2][[{5, 2, 4, 3}]]}] &]]], Print["Error"]];
```

- **Extraction of Nuclear Data**

```
numData = Length[DataSort];



hkl = Table[DataSort[[a, 2]], {a, numData}];

numD9Data = Dimensions[D9Data];

Clear[NucData]

a = 1;
n = 1;

NucData = Table[{}, {a, numData}];
Nuchkl = Table[{}, {a, numData}];

(* Extract the nuclear reflections measured on D9
  that are the same as those measured on D3 ... *)

Do[
  Do [
   If [
    hkl[[a]] == D9Data[[n, {1, 2, 3}]],

    And[
     AppendTo[NucData[[a]], D9Data[[n, {4, 5}]]],
     AppendTo[Nuchkl[[a]], D9Data[[n, {1, 2, 3}]]
     ]
    ]
   ],
   {n, numD9Data[[1]]}],
  {a, numData}];


(* If the nuclear reflections were not measured -
  try and extract the Friedel pairs ... *)

a = 1;
n = 1;

Do[
  If[
   Dimensions[
      NucData[[a]]][[1]] == 0,
   Do[If [(-1 * hkl[[a]]) == D9Data[[n, {1, 2, 3}]],
     And[AppendTo[NucData[[a]], D9Data[[n, {4, 5}]]],
      AppendTo[Nuchkl[[a]], D9Data[[n, {1, 2, 3}]]]]],
    {n, numD9Data[[1]]}]], {a, numData}];


(* If neither of these were measured take
```

```
  the intensity for any other reflection that has
  the same absolute values of h k and l  ... *)

a = 1;
n = 1;

Do[
  If[
   Dimensions[
      NucData[[a]]][[1]] == 0,
   Do[If [Abs[ hkl[[a]]] == Abs[D9Data[[n, {1, 2, 3}]]],
     And[AppendTo[NucData[[a]], D9Data[[n, {4, 5}]]],
      AppendTo[Nuchkl[[a]], D9Data[[n, {1, 2, 3}]]]]],
    {n, numD9Data[[1]]}]], {a, numData}];


(*take an avearage of the nuclear data points*)
MeanNucData = Table[If[ Dimensions[NucData[[a]]][[1]] != 0,
    Mean[NucData[[a]]], {a, numData}];

(*identify the position of those
 refelctions that were not measured*)

posNucNull = Position[MeanNucData, Null];
```

- **Extraction of Sorted Data**

```
(*Delete those points that have no nuclear data*)
DataSort = Delete[DataSort, posNucNull];


(*Label all data *)

hkl = DataSort[[All, 2]];

ZoneAxis = DataSort[[All, 1]];

PolSign = DataSort[[All, 3]];

Counts =  DataSort[[All, 4]];

QTable = DataSort[[All, 5]];

MIV = DataSort[[All, 7]];

PfExptList = DataSort[[All, 8]];

 PfExptListErr = DataSort[[All, 9]];

fam = DataSort[[All, 6]];

MeanNucData = Delete[MeanNucData, posNucNull];


(*undo the corrections of the nuclear data applied in racer *)
NExpt = Table[Sqrt[MeanNucData[[a, 1]] / MeanNucData[[a, 2]] / 73.9] *
    Sign[Chop[FN[hkl[[a]]]]], {a, Length[MeanNucData]}];
```

★ **Functions**

- **Blumes Equations**

The functions below determine the interaction between the nuclear structure factor (N) and the magnetic scattering vector (M).
The third input into these equations is the value of the polarisation in (P) this describes what the orientation of the spin is on the incident neutron using the crystallographic rather than cartesian axes.

Sigma represents the cross section and can be described:

$$\sigma = \sigma n + \sigma m + \sigma i$$

PfSigma represents the final polarization and can be described:

$$Pf\sigma = (P\sigma)n + (P\sigma)m + (P\sigma)i$$

The subscripts represent the different parts of the equations:

n - the nuclear part
m - the magnetic part
i - the part that describes the interference between the nuclear and magnetic parts

- **Input for Sigma the denominator of the Blumes equations - the out put generated is a scalar.**

```
Sigma[N_,P_,M_]:= N*Conjugate[N]+
                  P.M*Conjugate[N] +
                  P.Conjugate[M]*N +
                  M.Conjugate[M] -
                  I*P.(Conjugate[M]×M)
```

- **Input for PfSigma the numerator in the Blumes equations - the out put generated is a vector.**

```
PfSigma[N_,P_,M_]:= P*N*Conjugate[N] +
                    M*Conjugate[N] +
                    Conjugate[M]*N -
                    I*(P×M*Conjugate[N]) +
                    I*(P×Conjugate[M]*N) +
                    M*(P.Conjugate[M]) +
                    Conjugate[M]*(P.M) -
                    P*(M.Conjugate[M]) +
                    I*(Conjugate[M]×M)
```

- **Determination of the Outgoming (final) Polarisation Pf - by combining the above two equations.**

```
Pf[N_, P_, M_] := Chop[PfSigma[N, P, M] / Sigma[N, P, M]]
```

- **Polarisation In and Out**

Pf in is described initially by vectors in the Cartesian axes where:
x = {1, 0, 0}
y = {0, 1, 0}
z = {0, 0, 1}

This is then converted, by RotL2C, to the Crystallographic axes where:
x = Q - parallel to the scattering vector
z = up - the axis along which the crystal is oriented
y = (x x z) - the cross product of x and z to make up the right-handed set

After Blumes equations have been called and the calculations are complete the axes of the polarisation are converted back, by calling RotC2L.

In order to generate an outgoing polarisation that is comprable to the polarisation generated by experiment the domains need to be accounted for this is done by the final function, Pf Out Dom. This function calls Pf Out and hence Blumes equations seperately for each of the domains and sums over them all, allowing for different amounts of each domain with the variable DomCoeff.

- **Generation of the Incoming polarisation converting from the Cartesian to Crystallographic Axes by calling RotL2C**

```
PfIn[PolSign_, PfInVar_] := (PolSign * PfInVar)
```

- **Generation of the Outgoing polarisation calling Blumes equations and converting the output from the Crystallographic to Cartesian Axes by**

```
PfOut[nucData_, PolSign_, ZoneAxis_, hkl_, KDomain_, SDomain_, PfInVar_, Coeff_, Moment_] :=
 Pf[nucData, PfIn[PolSign, PfInVar], MkPerp[ZoneAxis, hkl, KDomain, SDomain, Coeff, Moment]]
```

- **Generation of the Outgoing polarisation calling Blumes equations and converting the output from the Crystallographic to Cartesian Axes by calling RotC2L**

```
SigmaSum[nucData_, PolSign_, ZoneAxis_, hkl_, KDomain_, SDomain_, PfInVar_, Coeff_, Moment_] :=
 Sum[Sigma[nucData, PfIn[PolSign, PfInVar],
   MkPerp[ZoneAxis, hkl, KDomain, SDomain[[i]], Coeff, Moment]], {i, numSDom}]
```

- **Generation of the Outgoing polarisation including the summing over different domains**

```
PfOutDom[nucData_, PolSign_, ZoneAxis_, hkl_, KDomain_, SDomain_, PfInVar_,
  Coeff_, DomCoeff_, Moment_] := Chop[(Sum[DomCoeff[[i]]*Sigma[nucData,
      PfIn[PolSign, PfInVar], MkPerp[ZoneAxis, hkl, KDomain, SDomain[[i]], Coeff, Moment]]*
     PfOut[nucData, PolSign, ZoneAxis, hkl, KDomain, SDomain[[i]], PfInVar, Coeff, Moment]/
      SigmaSum[nucData, PolSign, ZoneAxis, hkl, KDomain, SDomain, PfInVar, Coeff, Moment]),
   {i, 1, numSDom}])]
```

- **Magnetic Interaction Vector**

The magnetic interaction vector is called by Blumes equations. In these equations it is represented by M.
The equations below call on input from:

Thermal Factor Calculations
Form Factor Calculations
Moment Input - the magnetic moment for the crystal
k Input - the **k** vector describing the propagation of the spin orientations
Trans Input - the translations that are allowed by symmetry for each of the atom sites - the interaction between the k vector and the translations mean that each site related by translational symmetry needs to be considered in turn.
Coordinates Input - coordinates of the magnetic sites within the conventional unit cell
hkl Variable - the reflection that is being considered by the calculation
Coeff Variable - the Coefficients for the basis vectors that determine the amount of mixing.
psiArray Variable - the array of the basis vectors belonging to the symmetry allowed irreducible representation

The sum Mk sums over all the basis vectors of each atom at each magnetic atom site. This is normalised with respect to the first atom, with translation of (0 0 0)

This sum is then converted to the perpendicular magnetic interaction vector MkPerp

- **Generation of the magnetic interaction vector - Mk**

```
Mk[hkl_, KDomain_, SDomain_, Coeff_, Moment_] :=
 0.2695*Sum[Moment[[h]]*FormFactor[hkl, AtomFF[[h]]]*
    ThermalFactor[hkl, TFBAllAtoms[[h]]]*Sum[Sum[Exp[-2*Pi*I*KDomain.Trans[[i]]]
        Exp[2*Pi*I*(hkl.Coordinates[[h, j, i]])]
        Normalize[Sum[Sum[Coeff[[h, l, m]] SDomain[[h, l, m, j]],
            {m, 1, numpsi[[h, l]]}], {l, numIRStart[[h]], numIREnd[[h]]}]],
      {j, 1, numASites[[h]]}], {i, 1, numTrans}], {h, 1, numMagSites}]
```

- **Generation of the perpendicular magnetic interaction vector - MkPerp**
  Step one - convert from crystallographic axes to orthogonal axes - MkOrth - nb this is a change in the axes system about a vector in real space - hence the P matrix is used
  Step two - rotate vector to allign with cryopad polarisation - MkXYZ - nb the axes system remains the same with a change in the orientation of the vector in real space - hence the Q matrix is used
  Step three - With polarisation axes alligned with x parrallel to the scattering vector

```
MkOrth[hkl_, KDomain_, SDomain_, Coeff_, Moment_] :=
 Mk[hkl, KDomain, SDomain, Coeff, Moment].PabcTOorthNorm
```

```
MkXYZ[ZoneAxis_, hkl_, KDomain_, SDomain_, Coeff_, Moment_] :=
 QorthTOxyz[hkl, ZoneAxis].MkOrth[hkl, KDomain, SDomain, Coeff, Moment]
```

```
MkPerp[ZoneAxis_, hkl_, KDomain_, SDomain_, Coeff_, Moment_] :=
 Chop[Cross[{1, 0, 0}, Cross[MkXYZ[ZoneAxis, hkl, KDomain, SDomain, Coeff, Moment], {1, 0, 0}]]]
(* same as MkPerp2[hkl_]:= Mk[hkl]- Hat[hkl](Mk[hkl].Hat[hkl]) *)
```

- **Generation of the complex conjuate of the magnetic structure factor**

```
M2[hkl_, psiArray_, Coeff_, Moment_] := Chop[Simplify[ComplexExpand[
    Mk[hkl, psiArray, Coeff, Moment]*Conjugate[Mk[hkl, psiArray, Coeff, Moment]], hkl∈ Reals]]]
```

- **Nuclear Structure Factor**

The nuclear structure factor is called by Blumes equations. In these equations it is represented by N.
The equations below call on input from:

Thermal Factor Calculations
Scattering Length Calculations
Coordinates Input - coordinates of the magnetic sites within the conventional unit cell
hkl Variable - the reflection that is being considered by the calculation

The sum FN sums over all atoms of each type for each of the reflections hkl.

Note that as all of the atomic sites that are related by translations are equivalent with respect to the nuclear structure factor the sum is multiplied by the number of translations rather than summed over each of them.

- **Generation of the nuclear structure factor - N**

```
(*FN[hkl_]:=∑_{h=1}^{numATypes} ∑_{i=1}^{numASites[[h]]} ∑_{j=1}^{numTrans} ThermalFactor[hkl][[h]]*
     ScatteringLength[[h]]*Exp[2*I*Pi*(hkl.Coordinates[[h,i,j]])]*)

FN[hkl_] := numTrans * ( Sum_{h=1}^{numATypes} ThermalFactor[hkl, TFBAllAtoms[[h]]] *
     ScatteringLength[[h]] * ( Sum_{i=1}^{numASites[[h]]} Exp[2 * I * Pi * (hkl.Coordinates[[h, i, 1]])] ) )
```

- **Generation of the complex conjuate of the nuclear structure factor**

```
N2[hkl_] := Chop[Simplify[ComplexExpand[FN[hkl]*Conjugate[FN[hkl]], hkl∈ Reals]]]
```

- **Rotation Matrices**

This set of calculations translates the axes of the incoming polarised neutrons - described as x y z - to the crystallographic system and back again. The third function (RotC2L - cryopad to lattice) is a rotation matrix that converts the polarisation from the description given by the instrumentation to the description required by Blumes equations. The second function (RotL2C - lattice to cryopad) is a rotation matrix that converts it back to the x y z coordinate system.

The polarisation is always described in real space as it is described by uvw (the vector normal to the plane) NOT hkl (the plane).

NB - is the normal to a miller plane always described by the same values

- **Conversion of any value to the 'hatted' version - used to convert the hkl plane to the normal vector**

```
Hat[QVector_] := QVector / Sqrt[QVector.QVector]
```

- **Generation of the rotational matrix that converts from crystallographic to orthogonal axes**

```
PabcTOorth := {{(aLatPar Sin[βLatPar Degree] + aLatPar Sin[γLatPar Degree]) - aLatPar, 0, 0},
    {aLatPar Cos[γLatPar Degree], bLatPar, 0}, {aLatPar Cos[βLatPar Degree], 0, cLatPar}};

NormP :=
   (((aLatPar Sin[βLatPar Degree] + aLatPar Sin[γLatPar Degree]) - aLatPar) * bLatPar * cLatPar) ^
    (1 / 3);

PabcTOorthNorm := PabcTOorth / NormP
```

- **Generation of the rotational matrix that converts from the cartesion to the crystallographic axis - this is the inverse of the above matrix**

```
QabcTOorthNorm[ZoneAxis_, hkl_] := Inverse[PabcTOorthNorm[ZoneAxis, hkl]]
```

- **Conversion from Orthogonal, crystallographic to Polarisation axes (xyz)**

```
QorthTOxyz[hkl_, ZoneAxis_] :=
 {Hat[hkl.PabcTOorthNorm ], Cross[Hat[ZoneAxis.PabcTOorthNorm ], Hat[ hkl.PabcTOorthNorm ]],
  Hat[ZoneAxis.PabcTOorthNorm ]}
```

- **Reciprocal Lattice Formulae**

- **Generalised definition for dspace calculated in degrees**

$$\text{DSpace}[hkl\_] := \sqrt{\left(1 - (\text{Cos}[(\alpha\text{LatPar})\,°])^2 - (\text{Cos}[(\beta\text{LatPar})\,°])^2 - (\text{Cos}[(\gamma\text{LatPar})\,°])^2 + 2\,\text{Cos}[(\alpha\text{LatPar})\,°]\,\text{Cos}[(\beta\text{LatPar})\,°]\,\text{Cos}[(\gamma\text{LatPar})\,°]\right) * \left(\frac{\text{hkl}[[1]]^2}{\text{aLatPar}^2}(\text{Sin}[(\alpha\text{LatPar})\,°])^2 + \frac{\text{hkl}[[2]]^2}{\text{bLatPar}^2}(\text{Sin}[(\beta\text{LatPar})\,°])^2 + \frac{\text{hkl}[[3]]^2}{\text{cLatPar}^2}(\text{Sin}[(\gamma\text{LatPar})\,°])^2 + \frac{2\,\text{hkl}[[2]]\,\text{hkl}[[3]]}{\text{bLatPar}\,\text{cLatPar}}(\text{Cos}[(\beta\text{LatPar})\,°]\,\text{Cos}[(\gamma\text{LatPar})\,°] - \text{Cos}[(\alpha\text{LatPar})\,°]) + \frac{2\,\text{hkl}[[1]]\,\text{hkl}[[3]]}{\text{aLatPar}\,\text{cLatPar}}(\text{Cos}[(\alpha\text{LatPar})\,°]\,\text{Cos}[(\gamma\text{LatPar})\,°] - \text{Cos}[(\beta\text{LatPar})\,°]) + \frac{2\,\text{hkl}[[1]]\,\text{hkl}[[2]]}{\text{aLatPar}\,\text{bLatPar}}(\text{Cos}[(\alpha\text{LatPar})\,°]\,\text{Cos}[(\beta\text{LatPar})\,°] - \text{Cos}[(\gamma\text{LatPar})\,°])\right)^{-1}\right)}$$

- **Calculation for Q the inverse of d-space**

```
Q[hkl_] := (2 π) / DSpace[hkl]
```

- **Calculation for Sin θ on λ**

```
SinThetaLamda[hkl_] := 1 / (2 * DSpace[hkl])
```

- **Calculation for θ**

```
Theta[hkl_] := (ArcSin[SinThetaLamda[hkl] / Lamda]) / Degree
```

- **Calulation for Lorentz Factor**

```
LorentzFactor[hkl_] := 1 / (2 * (Sin[(Theta[hkl]) °]) ^ 2 * Cos[(Theta[hkl]) °])
```

- **Conversion from direct to reciprocal space**

```
QRecipToDirect :=
 {{aLatPar^2, aLatPar bLatPar Cos[(γLatPar) °], aLatPar cLatPar Cos[(βLatPar) °]},
  {aLatPar bLatPar Cos[(γLatPar) °], bLatPar^2, bLatPar cLatPar Cos[(αLatPar) °]},
  {aLatPar cLatPar Cos[(βLatPar) °], bLatPar cLatPar Cos[(αLatPar) °], cLatPar^2}}

PRecipToDirect := Inverse[QRecipToDirect]
```

- **Thermal and Form Factor Equations**

- **Thermal Factor equation**

```
ThermalFactor[hkl_, TFBAllAtoms_] := Exp[-(TFBAllAtoms * (SinThetaLamda[hkl])^2)]
```

- **Form Factor equation**

```
FormFactor[hkl_, AtomFF_] := AtomFF[[1]] * Exp[-AtomFF[[2]] * (SinThetaLamda[hkl])^2] +
   AtomFF[[3]] * Exp[-AtomFF[[4]] * (SinThetaLamda[hkl])^2] +
   AtomFF[[5]] * Exp[-AtomFF[[6]] * (SinThetaLamda[hkl])^2] +
   AtomFF[[7]] * Exp[-AtomFF[[8]] * (SinThetaLamda[hkl])^2];
```

- **Chi Equation**

```
leastsquares[numData_, PfExptList_, Domain_, Coeff_, DomCoeff_, Moment_] :=
 1/(3 * (numData)) (Sum_{i=1}^{numData} Sum_{j=1}^{3} (* 2/((({{0,1,1},{1,0,1},{1,1,0}}[[j]].Abs[PfExptList[[i,j]]]+0.01)) *)
     ((PfExptList[[i, j]] - PfOutDom[PolSign[[i]], ZoneAxis[[i]], hkl[[i]],
           Domain, IdentityMatrix[3][[j]], Coeff, DomCoeff, Moment])^2.{1, 1, 1}))
```

Matrix Plots

```
plotMat[xAxis_, yAxis_, hklList_, polList_, recipUnit_] := Module[
  {xPos, yPos, diff, xUnit, yUnit, xyPoint, lineTable},

  (*Find position in x direction*)
  xPos = hklList[[All, 3]] / xAxis[[3]];

  (*Find position in y direction*)
  yPos = Table[-(hklList [[n]] - xAxis * xPos[[n]])[[2]], {n, Length[xPos]}];

  (*Add out of plane bit*)
  diff = Table[(hklList [[n]] - yAxis * yPos[[n]] - xAxis * xPos[[n]]), {n, Length[yPos]}];

  xPos = xPos + diff[[All, 1]] * xAxis[[1]] / Total[Abs[xAxis]];

  yPos = yPos + diff[[All, 1]] * yAxis[[1]] / Total[Abs[yAxis]];

   (*Make all lengths equivalent*)
  xUnit = Norm[xAxis * recipUnit];

  yUnit = Norm[yAxis * recipUnit];

  (*Break into quadrants with respect to the yAxis*)
  xyPoint = {yPos * yUnit, -xPos * xUnit} / -(yUnit * 0.1);

  xyPoint = Transpose[IntegerPart[xyPoint] -
      {Min[IntegerPart[xyPoint][[1, All]]], Min[IntegerPart[xyPoint][[2, All]]]} + 3];

  xyPoint = Flatten[
    Table[xyPoint[[l]] + {m, 0} + {0, n}, {l, Length[xyPoint]}, {m, -1, 1}, {n, -1, 1}], 2];

  lineTable = Transpose[
    {Transpose[xyPoint][[2]], Max[xyPoint[[All, 1]]] - Transpose[xyPoint][[1]]}];


  lineTable = Take[lineTable, {1, Length[lineTable], 9}];
  lineTable =
   Table[{lineTable[[n]] + {-1, 1}, lineTable[[n]] + {2, 1}, lineTable[[n]] + {2, -2},
     lineTable[[n]] + {-1, -2}, lineTable[[n]] + {-1, 1}}, {n, Length[lineTable]}];



  (*Generate Sparse Array and plot *)
  ArrayPlot[SparseArray[xyPoint → polList], ColorFunction → "TemperatureMap",
   PlotRange → {-1.2, 1.2}, Epilog -> {Black, Line[lineTable]}]


 ]
```

```
plotCirc[xAxis_, yAxis_, hklList_, polInList_, polFinList_, recipUnit_] := Module[
  {xPos, yPos, diff, xUnit, yUnit, xyPoint, localXAxes, localYAxes,
   polInYZ, polInXYZ, polFinYZ, polFinXYZ, momentYZ, momentXYZ, circlePlot},


  (*Find position in x direction*)
  xPos = hklList[[All, 3]] / xAxis[[3]];

  (*Find position in y direction*)
  yPos = Table[-(hklList [[n]] - xAxis * xPos[[n]])[[2]], {n, Length[xPos]}];

  (*Add out of plane bit*)
  diff = Table[(hklList [[n]] - yAxis * yPos[[n]] - xAxis * xPos[[n]]), {n, Length[yPos]}];

  xPos = xPos + diff[[All, 1]] * xAxis[[1]] / Total[Abs[xAxis]];

  yPos = yPos + diff[[All, 1]] * yAxis[[1]] / Total[Abs[yAxis]];

   (*Make all lengths equivalent*)
  xUnit = Norm[xAxis * recipUnit];

  yUnit = Norm[yAxis * recipUnit];

  (*Describe as an xy point*)

  xyPoint = Transpose[{xPos * xUnit, yPos * yUnit}];

  (*Generate axes*)

  localXAxes = Flatten[Table[{xyPoint[[n]] + {x, 0}, xyPoint[[n]] - {x, 0}},
     {x, -0.05, 0.05}, {n, Length[xyPoint]}], 1];

  localYAxes = Flatten[Table[{xyPoint[[n]] + {0, y}, xyPoint[[n]] - {0, y}},
     {y, -0.05, 0.05}, {n, Length[xyPoint]}], 1];




  (*Describe incident polarisation*)

  polInYZ = Transpose[{xyPoint + polInList[[All, 2 ;; 3]] / 20, xyPoint}];

  polInYZ = Table[Arrow[polInYZ[[n]]], {n, Length[xyPoint]}];

  polInXYZ =
   Table[Arrow[{xyPoint[[n]] + {polInList[[n, 1]], Norm[polInList[[n, 2 ;; 3]]]} / 20,
      xyPoint[[n]]}], {n, Length[xyPoint]}];



  (*Describe final polarisation*)

  polFinYZ =
```

```
 Table[Arrow[{xyPoint[[n]] + Normalize[polFinList[[n, 2 ;; 3]]] / 20, xyPoint[[n]]}],
  {n, Length[xyPoint]}];


polFinXYZ =
 Table[Arrow[{xyPoint[[n]] + {polFinList[[n, 1]], Norm[polFinList[[n, 2 ;; 3]]]} / 20,
    xyPoint[[n]]}], {n, Length[xyPoint]}];


momentYZ = Table[Arrow[{xyPoint[[n]] +
      (Normalize[polInList[[n, 2 ;; 3]] + Normalize[polFinList[[n, 2 ;; 3]]]]) / 20,
    xyPoint[[n]] - (Normalize[polInList[[n, 2 ;; 3]] +
         Normalize[polFinList[[n, 2 ;; 3]]]]) / 20}], {n, Length[polInList]}];



momentXYZ = Table[
  Arrow[{xyPoint[[n]] + (Normalize[{polInList[[n, 1]], Norm[polInList[[n, 2 ;; 3]]]} +
         {polFinList[[n, 1]], Norm[polFinList[[n, 2 ;; 3]]]}]) / 20, xyPoint[[n]] -
     (Normalize[{polInList[[n, 1]], Norm[polInList[[n, 2 ;; 3]]]} + {polFinList[[n, 1]],
        Norm[polFinList[[n, 2 ;; 3]]]}]) / 20}], {n, Length[polInList]}];



circlePlot = Table[Circle[xyPoint[[n]], 0.05], {n, Length[xyPoint]}];

(*Generate a line from point*)

{Show[Graphics[{Line[localXAxes], Line[localYAxes], Point[xyPoint], Thin,
    Black, circlePlot, Arrowheads[0.02], Purple, Thick, polInYZ, Cyan, Thick,
    Arrowheads[{-0.02, 0}], polFinYZ, Blue, Arrowheads[{-0.02, 0.02}], momentYZ}]],

 Show[Graphics[{Line[localXAxes], Line[localYAxes], Point[xyPoint], Thin,
    Black, circlePlot, Purple, Thick, Arrowheads[0.02], polInXYZ, Cyan, Thick,
    Arrowheads[{-0.02, 0}], polFinXYZ, Blue, Arrowheads[{-0.02, 0.02}], momentXYZ}]]}



]
```

The routines from the previous notebooks have been separated and written as independent modules. These are described below:

sara*h*Mathematica

Introduction

This notebook is designed to so that there is a guide to all the routines that can be used to analyse neutron data in *Mathematica.*

Each set of routines is grouped by the file in which they can be found.

To use the routines independent of the input files:

1. Set the directory to where the neutronFormulae folder has been placed, where the default is the home directory:

```
$HomeDirectory
```

```
/Users/amy
```

2. Copy and paste the opening input in from the relevant subsection below into your notebook, to set the directory and declare the packages and follow the instructions for the routines you wish to use.

Routines

Crystallographic Calculations

```
SetDirectory[ToFileName[{$HomeDirectory, "neutronFormulae", "crystalMaths"}]];
```

- Lattice Parameters

```
SetDirectory[ToFileName[{$HomeDirectory, "neutronFormulae", "crystalMaths"}]];

DeclarePackage["recipLattice`", {"dSpace", "unitCellVolume", "aStarLatPar", "bStarLatPar",
   "cStarLatPar", "abcStarLatPar", "angleStarLatPar", "unitCellVolumeStar",
   "scatteringQ", "sinThetaLambda", "theta", "twoTheta", "reciprocalLatticeTable"}];

Names["recipLattice`*"]
```

Instructions

```
?dSpace
```

Determines lattice spacing from reflection indices.

Arguments are [{h,k,l} , a, b, c, $\alpha°$, $\beta°$, $\gamma°$].

Returns a scalar value with units equivalent to the the units of a, b, c, usually Å

```
?unitCellVolume
```

Calculates unit cell volume for any crystal system.

Arguments are [a, b, c, $\alpha°$, $\beta°$, $\gamma°$].

Returns a scalar value with units of a, b or c cubed, usually Å^3.

?aStarLatPar

Returns the reciprocal lattice vector a∗.

Arguments are [a, b, c, α°, β°, γ°].

Returns a scalar value with units of a, usually Å^(−1).

?bStarLatPar

Returns the reciprocal lattice vector b∗.

Arguments are [a, b, c, α°, β°, γ°].

Returns a scalar value with units of b, usually Å^(−1).

?cStarLatPar

Returns the reciprocal lattice vector c∗.

Arguments are [a, b, c, α°, β°, γ°].

Returns a scalar value with units of c, usually Å^(−1).

?abcStarLatPar

Returns the reciprocal lattice vectors a∗, b∗, c∗.

Arguments are [a, b, c, α°, β°, γ°].

Returns a list of scalar values with units of a, b, c; usually Å^(−1).

?angleStarLatPar

Returns the reciprocal lattice angles ∠∗.

Arguments are [$\angle^\circ$, $\angle^\circ$, $\angle^\circ$, ...].

Where the number of angles entered can be any number greater than 0.

Returns an angles described by degrees.

?unitCellVolumeStar

Returns the reciprocal cell volume for any crystal system.

Arguments are [a, b, c, α°, β°, γ°].

Returns a scalar value with units of a, b or c, usually Å^(−3).

```
?scatteringQ
```

Returns 2π over the dSpace.

Arguments are [{h,k,l}, a, b, c, $\alpha°$, $\beta°$, $\gamma°$].

Returns a scalar value with units equivalent to the the units of a, b or c, usually Å^(−1).

```
?sinThetaLambda
```

Returns the reciprocal of the D−spacing∗2 for a given reflection.

Arguments are [{h,k,l}, a, b, c, $\alpha°$, $\beta°$, $\gamma°$].

Returns a scalar value with units equivalent to the the units of a, b or c, usually Å^(−1).

```
?theta
```

Returns the two theta for a given reflection with at a given wavelength.

Arguments are [λ,{h,k,l}, a, b, c, $\alpha°$, $\beta°$, $\gamma°$].

Returns an angle in degrees.

```
?twoTheta
```

Returns the two theta for a given reflection with at a given wavelength.

Arguments are [λ,{h,k,l}, a, b, c, $\alpha°$, $\beta°$, $\gamma°$].

Returns an angle in degrees.

```
?reciprocalLatticeTable
```

Returns all reciprocal crystallographic quantities associated with the lattice information that is input.

Arguments are [a, b, c, $\alpha°$, $\beta°$, $\gamma°$].

Returns a list of two lists:

{{a, b, c, α, β, γ, Volume}, {a∗, b∗, c∗, α∗, β∗, γ∗, Volume}}

Where the units are degrees and the unit of length of a, b and c, usually Å.

- Lattice Rotations

```
SetDirectory[ToFileName[{$HomeDirectory, "neutronFormulae", "crystalMaths"}]];
DeclarePackage["rotation`", {"abc2orth", "hkl2xyz", "mag2xyz"}];
Names["rotation`*"]
```

```
{abc2orth, hkl2xyz, mag2xyz}
```

Instructions

?abc2orth

A rotational matrix that can be used to convert
from the crystallographic axis system to an orthogonal axis system.

The arguments are the lattice parameters and are given in degrees:

[aLatPar, bLatPar, cLatPar, alphaLatPar, betaLatPar, gammaLatPar]

The routine returns a normalised rotation matrix.

In order to use this routine with the axis system
defined by cryopad the reciprocal lattice vectors must be used:

[aStarLatPar, bStarLatPar, cStarLatPar, alphaStarLatPar, betaStarLatPar, gammaStarLatPar]

?hkl2xyz

A rotational matrix that transforms from the reciprocal lattice vectors hkl and the zone axis
to the direct space vectors that define the x, y, z directions in cryopad.

The arguments are:

[{h,k,l}, {zoneAxis}, abc2orthIn]

hkl – The {vector} for the current reflection

zoneAxis – The {vector} that describes the orientation of the crystal

abc2orthIn – The rotational {{matrix}} generated from abc2orth using reciprocal lattice parameters as input

?mag2xyz

Takes the magnetic structure vector and converts it from the
direct crystallogrphic axis system to the direct cryopad, x, y, z axis system.

The arguments are:

[{magVecIn}, {{hkl2xyzIn}}, {{abc2orthIn}}]

magVecIn – The magnetic structure {vector}.
This can be generated using:
1. magStrucVec, which includes the moment and form factor
2. hklMagVec,
which will give the resultant magnetic direction with unit magnitude

hkl2xyzIn – The rotation {{matrix}} that describes the orientation of the incoming beam

abc2orthIn – The rotational {{matrix}} generated from abc2orth using reciprocal lattice parameters as input

Import Files

```
SetDirectory[ToFileName[{$HomeDirectory, "neutronFormulae", "dataImport"}]];
```

- Sarah Import

```
SetDirectory[ToFileName[{$HomeDirectory, "neutronFormulae", "dataImport"}]];

DeclarePackage["importSarah`", {"importSym", "importKVector", "importRot",
   "importSites", "importTrans", "importBasisVectors", "readAllSarah"}];

Names["importSarah`*"]
```

```
{importBasisVectors, importKVector, importRot,
 importSites, importSym, importTrans, readAllSarah}
```

Instructions

```
?importSym
```

Imports the Jones faithful description of the symmetry operations
for the space group G entered into Sarah from the latex file generated by Sarah.

The argument is:
["fileName"]

Where file name is a string, that includes the path to that file.

The output is the lists G and Gk, where G and Gk are a list of operations in symbolic form:

{G,Gk},

```
?importKVector
```

Imports the kVector from a Sarah file

The argument is:
["fileName"]

Where file name is a string, that includes the path to that file.

The output is the propogation vector used for the calculations done by Sarah

```
?importRot
```

Imports the rotational matrices in the appendix of the Sarah Files.

The argument is:
["fileName"]

Where file name is a string, that includes the path to that file.

The output is two lists the rotational matrices of {G, Gk}.

?importSites

Imports the atomic sites in the order they are listed in the Sarah file.

The argument is:
["fileName"]

Where file name is a string, that includes the path to that file.

The output is the list of atomic sites organised by corep in the order of the basis vectors in the pdf.

?importTrans

Imports the translational information to determine the sites as described in the international tables

The argument is:
["fileName"]

Where file name is a string, that includes the path to that file.

The output is the list of translations associated with each rotation for the groups {G, Gk}

?importBasisVectors

Reads in the latex file written by Sarah and outputs
a list of basis vectors that is broken down into a list of atom sites,
if there is more than one orbit for each site the atom sites are grouped by orbit,

The argument is:
["fileName"]

Where file name is a string, that includes the path to that file.

If there is only one orbit the output is a list of basis vectors =>
{{{bv1atom1},{bv1atom2}...},{{bv2atom1},{bv2atom2}...}...} which has length equal to the number of basis vectors and width of numAtoms.

If there is more than one orbit the ouput is a list of basis vectors for each atom grouped by orbit =>
{{{{orb1bv1atom1},{orb1bv1atom2}...},{{orb1bv2atom1},{orb1bv2atom2}...}...},{{{orb2bv1atom1},{orb2bv1atom2}...},{{orb2bv2atom1},{orb2bv2atom2}...}...}}

The order agrees with the latex document
produced by Sarah and is best used in conjunction with the pdf.

```
?readAllSarah
```

Opens and reads the sarah file and outputs a text file that can be easily read in by mathematica.

The argument is:
["fileName"]

The order of the output is:

{kVector, magSites, symTrans, symRot, basisVectors}

The output can be read and interpreted by all programs that require basis vector information. The name of the out file is the same as the in file with the suffix .txt
More than one Sarah file can be read in at a time, this will return as many files as are input – remember to give them different names!

Data Manipulation

```
SetDirectory[ToFileName[{$HomeDirectory, "neutronFormulae", "dataManip"}]];
```

- Generating and manipulating reflections

```
SetDirectory[ToFileName[{$HomeDirectory, "neutronFormulae", "dataManip"}]];
DeclarePackage["hklOrg`", {"hklMake", "hklSort", "hklGroup", "hklFamily"}]
Names["hklOrg`*"]
hklOrg`
{hklFamily, hklGroup, hklMake, hklSort}
```

Instructions

```
?hklFamily
```

Identifies the contribution of each atom to each reflection.

The arguments are hklFamily[hkl, sites, centreTrans]

Where:

hkl can be either a list of reflections or a single reflection,

sites is the list of atomic sites in the unit cell,

centreTrans are the centering translations. The input of the centring translations is optional.

?hklMake

Makes a sorted list of combinations of h, k and l
that can be used for calculations, the {0,0,0} reflection is removed.

To generate reflections with integer values the arguments are:
hklMake[H, K, L] – list of all combinations from, but not including, {0, 0, 0} to {H, K, L}
hklMake[{Hmin, Hmax}, {Kmin, Kmax}, {Lmin, Lmax}]
– list of all combinations from {Hmin, Kmin, Lmin} to {Hmax, Kmax, Lmax}.
hklMake[{Hmin, Hmax, Hinc}, {Kmin, Kmax, Kinc}, {Lmin, Lmax, Linc}] – list of all combinations
from {Hmin, Kmin, Lmin} to {Hmax, Kmax, Lmax} in the increments Hinc, Kinc, Linc.

To generate reflections with non–integer values the argument includes a propogation vector:
hklMake[H, K, L, kVector] – list of all combinations from, but
not including, {0, 0, 0} to {H, K, L}, with the kVector added and subtracted.
hklMake[{Hmin, Hmax}, {Kmin, Kmax}, {Lmin, Lmax}, kVector] – list of all combinations from
{Hmin, Kmin, Lmin} to {Hmax, Kmax, Lmax}, with the kVector added and subtracted.
hklMake[{Hmin, Hmax, Hinc}, {Kmin, Kmax, Kinc}, {Lmin, Lmax, Linc}, kVector]
– list of all combinations from {Hmin, Kmin, Lmin} to {Hmax, Kmax, Lmax}
in the increments Hinc, Kinc, Linc; with the kVector added and subtracted.

The k vector may either be a single vector or a list of vectors:
{k1, k2, k3}
{{k11, k12, k13}, {k21, k22, k23}, ...}

If the k vector introduces repeats these will be removed and the returned list is sorted.

?hklSort

Calculates the d spacing and sinθ/λ for a list of reflections.

Arguments are [{{h,k,l}...{h,k,l}}, a, b, c, α, β, γ,sortType].
Where the value sortType can be:
0 => no sorting
1 => sort by hkl
2 => sort by d space
3 => sort by sinθ/λ

?hklGroup

Calculates the d spacing and sinθ/λ for a list
of reflections and groups the reflections with the same d–spacing.

Arguments are [{{h,k,l}...{h,k,l}}, a, b, c, α, β, γ].

This can be used to predict which reflections contribute to a peak in a powder pattern.

- Sorting and grouping experimental data

```
SetDirectory[ToFileName[{$HomeDirectory, "neutronFormulae", "dataManip"}]];

DeclarePackage["dataOrg`", {"dataColumn", "dataGroup", "dataSort"}]

Names["dataOrg`*"]
dataOrg`

{dataColumn, dataGroup, dataSort}
```

Instructions

```
?dataColumn
```

Imports data and changes the order of the columns of data so that it may be used by subsequent routines.
The arguments are:

dataColumn["fileName", columnNumList,"fileFormat"]

"fileName" needs to be a string the gives the name of the file to be sorted and the path to that file.

columnNumList is an integer, n, or a list of
integers, {m, n, ..}, which describe the final order of the columns.
The output is only those columns entered, as such this
routine can be used to remove unwanted columns of data.

"fileFormat" is optional and only required if the data to be imported is not in a "Table" format.
To find out more about import formats please enter ?Import.

?dataGroup

mports data and groups the rows of data so that they may be used by subsequent routines.
The arguments are:

dataGroup["fileName", groupCriteria, columnNumber, "fileFormat"]

The routine exports text files as a file that can be read in as a list by Mathematica with only
the information that agrees with the boundary conditions described by groupCriteria.

Where the groupCriteria is a list which is a long as the criteria you wish to group by.

There are 3 options:

1. K Vector
   Groups when the reflection has been generated by the kVector in the groupCriteria list
   – groupCriteria is a list of kvectors – {{k1_a,k1_b,k1_c}, ..., {kn_a,kn_b,kn_c}}
   – columnNumber set to 0

2. Equivalent
   Groups when data in the file is the same as the element in the groupCriteria list
   – groupCriteria is a list of numbers – {gC1, gC2, ... , gCn}
   – columnNumber has non−zero integer value

3. Between
   Groups when data in the file is between the values in the groupCriteria list
   – groupCriteria is a list of 2D lists – {{gC1_min, gC1_max}, ... , {gCn_min, gCn_max}}
   – columnNumber has non−zero integer value

The output is:

A set of exported files of grouped data –
with the groupCriteria prepended to the name of the original file.

A list of the names of the exported files is returned to the screen.

To have more than one type of data included in the sort criteria, input the
column number as a list of column numbers and a corresponding list of groupCriteria:
– groupCriteria is a list of lists e.g. equivalent followed by between
(though any combination is acceptble and the list is as long as required)
– {{gC1_1, ... , gC1_n}, ... ,{{gCn_1_min, gCn_1_max}, ... , {gCn_n_min, gCn_n_max}}}

– columnNumber is a list of integers which is as long as the the list of groupCriteria.
– {cN1, cN2, ... cNn}

"fileFormat" is optional and only required if the data to be imported is not in a "Table" format.
To find out more about import formats please enter ?Import.

```
?dataSort
```

Imports the data and sorts it by the values in the
column specified, and removes any lines of data that begin with a string.
The default file format is "Table".

The arguments are:

dataOrder["fileName", columnNumList,"fileFormat"]

"fileName" needs to be a string the gives the name of the file to be sorted and the path to that file.

columnNumList is an integer, n, or a list of integers,
{m, n, ..}, which describe the columns to sort, in the order to be sorted.
the value of columnNumList may be negative this will sort
the data in the corresponding column in descending order.

"fileFormat" is optional and only required if the data to be imported is not in a "Table" format.
To find out more about import formats please enter ?Import.

- Using Sarah input

```
SetDirectory[ToFileName[{$HomeDirectory, "neutronFormulae", "dataManip"}]];

DeclarePackage["symOperations`", {"makeAllSites", "makeKDoms", "makeSDoms"}]

Names["symOperations`*"]
```

```
symOperations`

{makeAllSites, makeKDoms, makeSDoms}
```

Instructions

?makeAllSites

Calculates the sites of the atoms in the unit cell and
returns them as lists grouped by the different type of atom entered.

The arguments are:

[atoms, G0, trans, centreTrans]

atoms is a list of the unique atom sites in the
unit cell, e.g. {{atom1a,atom1b,atom1c}, {atom2a,atom2b,atom2c}...}.
Note that this has to be a list of vectors –> so a cell that contains
one type of atom site is described {{atom1a,atom1b,atom1c}}

G0 is a list of the rotational operations described by 3x3 matrices
and may be read in from the Sarah file with importRot["fileName"]. Where G0 is
the first part of the output and is selected by entering importRot["fileName"][[1]].

trans is a list of the translational operations described by a vector and may be read in from
the Sarah file with importTrans["fileName"]. Where the list of translations associated with
G0 is the first part of the output and is selected by entering importTrans["fileName"][[1]].

centreTrans is an optional list of centring translations.
These can be found at the top of the page in the International Tables.

?makeKDoms

Calculates the arms of the star of the k Vector using the rotational matrices in the group G0, returning
a list of the kVectors that are left unchanged by the symmetry operations in the group G0.

The arguments are:

[kVector, G0]

kVector is the propagation vector of the modulation or magnetic
structure and may be read in from the Sarah file with importKVector["fileName"].

G0 is a list of the rotational operations described by 3x3 matrices
and may be read in from the Sarah file with importRot["fileName"]. Where G0is
the first part of the output and is selected by entering importRot["fileName"][[1]].

```
?makeSDoms
```

Calculates the S–Domains that are associated with
a set of basis vectors and returns the expanded set of basis vectors.

The arguments are:

[bv, atomSites, G0]

bv is a list of vectors that is the same length as the list of
atom sites, describing the direction of the magnetic moment on those sites.

atomSites is a list of the atomic sites that are associated with each bv, in the same order as the bvs.

G0 is a list of the rotational operations described by 3x3 matrices
and may be read in from the Sarah file with importRot["fileName"]. Where G0 is
the first part of the output and is selected by entering importRot["fileName"][[1]].

Potential Calculations

```
SetDirectory[ToFileName[{$HomeDirectory, "neutronFormulae", "potential"}]];
```

- Generating the Magnetic Vector from Basis Vectors

```
SetDirectory[ToFileName[{$HomeDirectory, "neutronFormulae", "potential"}]];

DeclarePackage["magVector`",
  {"hklMagVec", "hklSites", "kVectorTrans", "magIntVec", "magVectorSum"}];

Names["magVector`*"]
```

```
{hklMagVec, hklSites, kVectorTrans, magIntVec, magVectorSum}
```

Instructions

```
?hklSites
```

Combines each plane with the atom coordinates
and calculates how each atom contributes to each reflection.
The function is described by the equation Exp(2 π i hkl. atomSites). The output is a scalar value.

Arguments are:

hklSites[hkl, atomSites, centringTrans]

hkl is an individual reflection {h,k,l}.

atomSites is a list of the equivalent sites to be included in
the sum. These can be read in from Sarah using importSites["fileName"].

centreTrans is an optional list of centring translations.
These can be found at the top of the page in the International Tables.

```
?kVectorTrans
```

Combines the propagation vector (k vector) and the centring translations of the atoms
within the unit cell to give the phase of the magnetic structure within the zeroth unit cell.

The function can be described by the equation Exp(2 π i kVector.trans). The output is a scalar value.

Arguments are:

kVectorTrans[kVector,centringTrans],

kVector is the propagation vector of the modulation or magnetic
structure and may be read in from the Sarah file with importKVector["fileName"].

centreTrans is an optional list of centring translations.
These can be found at the top of the page in the International Tables.

?magVectorSum

Calculates the sum over the basis vectors for n number of atomic sites in the unit cell,
Arguments are [{bvs}, {bvCoeffs}, bvList],

The input:

{bvs}:
The set of basis vectors – imported from Sarah:

{{{psi1_atom1_a, psi1_atom1_b, psi1_atom1_c },{psi1_atom2_a, psi1_atom2_b, psi1_atom2_c } ,...} ,...}

{bvCoeffs}:
The coefficients of the basis vectors:

{number1, number2, ...}

where the number of basis vector coeficients should be
the same as the number of basis vectors, these can be complex numbers.

bvList:
The list of basis vectors to be included in the
sum, this has the same syntax as Part, without the square brackets,

if all of basis vectors are to be included:
bvlist = All

if some of the basis vectors are to be included:
bvList=2;;4
or
bvList={2,3,4}

For more info enter $Part.

The output:
basisVectorCoeffNorm::The normalised set of the basis vectors for each atomic site.

?magIntVec

Calculates the magnetic interaction vector for a given reflection and magnetic structure factor, returning the component of the magnetic structure in the plane. The equation the describes this routine is M(Q)perp=Qx(M(Q)xQ) and can be found in Squires on page 143. The output is a vector.

Arguments are:

magIntVec[magStrucVec, hkl]

magStrucVec is the magnetic structure factor for the given reflection.

hkl is the reflection for which the magnetic structure factor has been calculated.

```
?hklMagVec
```

Gives the total sum of the magnetic interaction vector for one type of element across
all the sites that element is located with no form factor or thermal corrections applied

Arguments are:

hklMagVec[magVectorSum, kVectorTrans, hklSites].

magVec is a list of vectors with length = numAtoms.

kVecTrans is a list of vectors with length = numTrans.

hklCoor is a 3D Array with dimensions hkl by numAtoms by numTrans

- Factors for Nuclear and Magnetic Scattering

```
SetDirectory[ToFileName[{$HomeDirectory, "neutronFormulae", "potential"}]];

DeclarePackage["factors`", {"sphericalFormFac", "thermalFactor"}];

Names["factors`*"]
{sphericalFormFac, thermalFactor}
```

Instructions

```
?sphericalFormFac
```

As defined by Jane Brown in the international tables, volume C, page 457, and available on the ILL website:
http://www.ill.eu/sites/ccsl/ffacts/ffachtml.html
Uses a bessel function to model a spherical approximation to the distribution of the electron density.
Takes the arguments [atomFormFac, sinThetaLambda],

atomFormFac is a list of the 8 form factor parameters

sinThetaLambda is the value of sin θ / λ for an individual reflection

```
?thermalFactor
```

Debye Waller factors to describe the isotropic displacement of the atoms due to thermal excitation.

The arguments are:

thermalFactor[thermalFactor, sinThetaLambda]

thermalFactor is a list of the thermal factors of a single atom.

sinThetaLambda is the value of sin θ / $\lambda$for an individual reflection

- Structure Factor Calculations

```
SetDirectory[ToFileName[{$HomeDirectory, "neutronFormulae", "potential"}]];

DeclarePackage["structureFactor`", {"magStruc", "nucStruc"}];

Names["structureFactor`*"]
{magStruc, nucStruc}
```

Instructions

```
?magStruc
```

Calculates the overall sum over one type of
element in the unit cell that contribute to the magnetic structure.
Takes the arguments magStruc[formFactor_,thermalFactor_,moment_,magVector_]
Uses the dipole approximation

```
?nucStruc
```

Calculates the overall sum over one type of element in the unit cell that contribute to the nuclear structure.
Takes the arguments nucStruc[scatteringLength_,thermalFactor_,hklSitesIn_].

Experimental Calculations

```
SetDirectory[ToFileName[{$HomeDirectory, "neutronFormulae", "exptCalc"}]];
```

- Polarised Neutron Calculations

```
SetDirectory[ToFileName[{$HomeDirectory, "neutronFormulae", "exptCalc"}]];

DeclarePackage["polarInt`", {"polarIntSNP", "polarIntSNPError"}];

Names["polarInt`*"]
{polarIntSNP, polarIntSNPError}
```

Instructions

```
?polarIntSNP
```

calculates the intensity of the polarisation for an ideal expt

Takes the arguments [initialPol_String, finalPol_String, NuclearPotential, Magnetic Interaction Vector]

and returns {polarisation, positive Intensity, negative Intensity}

```
?polarIntSNPError
```

polarInt`polarIntSNPError

APPENDIX D

Input for Mufit program

```
!lattice
4.8229     5.7533       4.9923       90      91.075      90
!# atoms
2
!AT   x         y        z        B         occ
Mn1   0.5  0.68530   0.2500   0.370 1
Mn2   0.5  0.31470   0.7500   0.370 1
! input switch 0: components along axis RMx,RMy,RMz,Imx,Imy,Imz,phase;
! 1: polar coordinates Rm,Rphi,Rtheta,Im,Iphi,Itheta,phase
0
!             RMx    RMy   RMz     Imx     Imy      Imz             phase (units of 2*pi)
2
Mn1  MF_Mn2    1        0   0.65       0   0.00    0.000     0.0
      C1     0      C3       0   0.00     0.00          0
Mn2  MF_Mn2    1       0   0.65       0   0.00    0.000    0.0
              C1     0      C3      0   0.00      0.00       0
!# symmetry operations in space group and symmetry elements
1
        X             Y           Z     RMx     RMy     RMz     IMx     IMy     IMz     0.0
        X             Y           Z     RMx     RMy     RMz     IMx     IMy     IMz     0.0
!# of translations and translations
0
! propagation vectors
1
k01    0.214 -0.5       -0.457
!#spin domains, populations and parameters
1
!population and rotation matrices for domains
1.0    1 0 0    0  1 0    0  0  1  T
!c1     c2     c3     c4     c5     c6     c7     c8     c9     c10
1 0 0.65 0 0 0 0 0 0 0
!steps dC1 to DC30
1  1  1  1   0 0 0 0 0 0
```

```
!c11    c12    c13    c14    c15    c16    c17    c18    c19    c20
0 0 0 0 0 0 0 0 0 0
!steps dC11 to DC20
0 0 0 0 0 0 0 0 0 0
!c21    c22    c23    c24    c25    c26    c27    c28     c29    c30
0 0 0 0 0 0 0 0 0 0
!steps dC1 to DC30
 +0.00  +0.00  +0.00  +0.00  +0.00  +0.00  +0.00  +0.00  +0.00  +0.00
!D1     D2     D3     D4     D5     D6     D7     D8      D9     D10
1.00 0.00  +0.00  +0.00  +0.00  +0.00  +0.00  +0.00  +0.00  +0.00
!steps dD1 to DD30
0.00 0.00   +0.00  +0.00  +0.00  +0.00  +0.00  +0.00  +0.00  +0.00
! fit algorithm: levenberg-marquard (0), simplex (1), simulated annealing (2)
2
!levenberg-marquard options: stol niter verbose (0/1)
0.1 10 1
!simplex options: stol niter chisq_min simplex verbose (0/1)
0.001 3000 5  0 1
!simulated anneling options
* nt - integer: # of iterations between temperature reductions
* ns - integer: # of iterations between bounds adjustments
* rt - (0 < rt <1): temperature reduction factor
* maxevals - integer: limit on function evaluations
* neps - integer:  number of values final result is compared to
* functol -   (> 0): the required tolerance level for function value comparisons
* paramtol -  (> 0): the required tolerance level for parameters
* verbosity - scalar: 0, 1, or 2.
20  5  0.95  100000  5  0.1  0.1 2
! flag for calculation k0 + -k0 (1); flag for pure magnetic reflection (0)
0     0
! polarizer/analyzer efficiencies 0.5 <= P_1, P_2 <= 1
1 1
! hkl, prop. vector, vector in scattering plane, incident pol., scattered pol., error on scatt. pol.
-1.214  -0.5  1.457    -1.957  2.6713  -0.713    -1  0  0    0.972  0.017  -0.024      0.026  0.029  0.029
-1.214  -0.5  1.457    -1.957  2.6713  -0.713    0  -1  0    -0.083 0.179  -0.9384    0.028  0.029  0.026
-1.214  -0.5  1.457    -1.957  2.6713  -0.713    0  0  -1    -0.076  -0.929  -0.124    0.029  0.029  0.029
-1.214  -0.5  1.457    -1.957  2.6713  -0.713    1  0  0    -0.991 -0.008  0.023    0.027  0.029  0.029
-1.214  -0.5  1.457    -1.957  2.6713  -0.713    0  1  0    0.003  -0.142  0.923    0.029  0.029  0.028
-1.214  -0.5  1.457    -1.957  2.6713  -0.713    0  0  1    -0.000  0.924  0.224    0.029  0.027  0.029
-0.21402  0.5  -0.543    1.0431  -0.329  -0.714    -1  0  0    0.922  -0.077  0.051    0.026  0.028  0.028
```

```
-0.21402  0.5  -0.543    1.0431  -0.329  -0.714    0  -1  0    -0.016  0.425  0.835    0.027  0.027  0.025
-0.21402  0.5  -0.543    1.0431  -0.329  -0.714    0  0  -1    0.0184 0.810  -0.443    0.028  0.027  0.028
-0.21402  0.5  -0.543    1.0431  -0.329  -0.714    1  0  0    -0.977  -0.063  -0.062    0.025  0.027  0.027
-0.21402  0.5  -0.543    1.0431  -0.329  -0.714    0  1  0    0.009   -0.523  -0.809    0.028  0.027  0.026
-0.21402  0.5  -0.543    1.0431  -0.329  -0.714    0  0  1    0.041  -0.785  0.444   0.028  0.027  0.028
```

APPENDIX E

Data tables of the collinear commensurate (AF1) polarimetry data collected on $MnWO_4$

	Reflection			Incident Polarization			Final Polarization				Calculated Polarization			Difference			RMS
	h	k	l	x	y	z	x	y	z		x	y	z	x	y	z	Average
1	-0.75	0.5	0.5	-1.	0.	0.	1.08 (0.01)	-0.11 (0.01)	-0.06 (0.01)		1.	0.	0.	0.08	-0.11	-0.06	0.09
	-0.75	0.5	0.5	0.	-1.	0.	-0.1 (0.01)	0.39 (0.01)	-1. (0.01)		0.	0.46	-0.89	-0.1	-0.07	-0.11	0.09
	-0.75	0.5	0.5	0.	0.	-1.	-0.1 (0.01)	-1.03 (0.01)	-0.26 (0.01)		0.	-0.89	-0.46	-0.1	-0.14	0.2	0.15
	-0.75	0.5	0.5	1.	0.	0.	-1.01 (0.01)	0.03 (0.01)	0.04 (0.01)		-1.	0.	0.	-0.01	0.03	0.04	0.03
	-0.75	0.5	0.5	0.	1.	0.	0.07 (0.01)	-0.28 (0.01)	1.03 (0.01)		0.	-0.46	0.89	0.07	0.18	0.14	0.14
	-0.75	0.5	0.5	0.	0.	1.	0.05 (0.01)	1.02 (0.01)	0.38 (0.01)		0.	0.89	0.46	0.05	0.13	-0.08	0.09
2	-0.25	-0.5	0.5	-1.	0.	0.	0.99 (0)	-0.01 (0.01)	-0.01 (0.01)		1.	0.	0.	-0.01	-0.01	-0.01	0.01
	-0.25	-0.5	0.5	0.	-1.	0.	-0.06 (0.01)	0.28 (0.01)	-0.95 (0.01)		0.	0.36	-0.93	-0.06	-0.08	-0.02	0.06
	-0.25	-0.5	0.5	0.	0.	-1.	-0.04 (0.01)	-0.95 (0.01)	-0.23 (0.01)		0.	-0.93	-0.36	-0.04	-0.02	0.13	0.08
	-0.25	-0.5	0.5	1.	0.	0.	-0.99 (0.01)	0. (0.01)	0.02 (0.01)		-1.	0.	0.	0.01	0.	0.02	0.01
	-0.25	-0.5	0.5	0.	1.	0.	0.02 (0.01)	-0.24 (0.01)	0.95 (0.01)		0.	-0.36	0.93	0.02	0.12	0.02	0.07
	-0.25	-0.5	0.5	0.	0.	1.	0.02 (0.01)	0.95 (0.01)	0.27 (0.01)		0.	0.93	0.36	0.02	0.02	-0.09	0.05
3	-0.25	0.5	-0.5	-1.	0.	0.	0.94 (0.01)	0.01 (0.01)	0.04 (0.01)		1.	0.	0.	-0.06	0.01	0.04	0.04
	-0.25	0.5	-0.5	0.	-1.	0.	-0.04 (0.01)	0.58 (0.01)	0.74 (0.01)		0.	0.66	0.75	-0.04	-0.08	-0.01	0.05
	-0.25	0.5	-0.5	0.	0.	-1.	-0.03 (0.01)	0.7 (0.01)	-0.62 (0.01)		0.	0.75	-0.66	-0.03	-0.05	0.04	0.04
	-0.25	0.5	-0.5	1.	0.	0.	-0.95 (0.01)	-0.01 (0.01)	-0.09 (0.01)		-1.	0.	0.	0.05	-0.01	-0.09	0.06
	-0.25	0.5	-0.5	0.	1.	0.	0.01 (0.01)	-0.61 (0.01)	-0.74 (0.01)		0.	-0.66	-0.75	0.01	0.05	0.01	0.03
	-0.25	0.5	-0.5	0.	0.	1.	0. (0.01)	-0.72 (0.01)	0.59 (0.01)		0.	-0.75	0.66	0.	0.03	-0.07	0.04
4	-0.25	1.5	-1.5	-1.	0.	0.	0.9 (0.03)	-0.03 (0.04)	-0.01 (0.04)		1.	0.	0.	-0.1	-0.03	-0.01	0.06
	-0.25	1.5	-1.5	0.	-1.	0.	-0.05 (0.03)	0.42 (0.03)	0.8 (0.03)		0.	0.53	0.85	-0.05	-0.11	-0.05	0.08
	-0.25	1.5	-1.5	0.	0.	-1.	-0.02 (0.04)	0.75 (0.04)	-0.49 (0.04)		0.	0.85	-0.53	-0.02	-0.1	0.04	0.06
	-0.25	1.5	-1.5	1.	0.	0.	-0.86 (0.03)	-0.03 (0.04)	-0.05 (0.04)		-1.	0.	0.	0.14	-0.03	-0.05	0.09
	-0.25	1.5	-1.5	0.	1.	0.	0.03 (0.03)	-0.53 (0.03)	-0.7 (0.03)		0.	-0.53	-0.85	0.03	0.	0.15	0.09
	-0.25	1.5	-1.5	0.	0.	1.	0.02 (0.04)	-0.68 (0.03)	0.47 (0.04)		0.	-0.85	0.53	0.02	0.17	-0.06	0.1

	Reflection			Incident Polarization			Final Polarization				Calculated Polarization			Difference			RMS
	h	k	l	x	y	z	x	y	z		x	y	z	x	y	z	Average
5	0.25	-0.5	0.5	-1.	0.	0.	1.06	(0.01)	-0.17	(0.02)	-0.15	(0.02)	1.	0.	0.	0.06	-0.17	-0.15	0.14
	0.25	-0.5	0.5	0.	-1.	0.	-0.11	(0.02)	0.53	(0.02)	-0.94	(0.02)	0.	0.66	-0.75	-0.11	-0.13	-0.19	0.15
	0.25	-0.5	0.5	0.	0.	-1.	-0.17	(0.02)	-0.93	(0.02)	-0.43	(0.02)	0.	-0.75	-0.66	-0.17	-0.18	0.23	0.2
	0.25	-0.5	0.5	1.	0.	0.	-0.95	(0.01)	0.07	(0.02)	0.04	(0.02)	-1.	0.	0.	0.05	0.07	0.04	0.05
	0.25	-0.5	0.5	0.	1.	0.	0.11	(0.02)	-0.44	(0.02)	0.96	(0.01)	0.	-0.66	0.75	0.11	0.22	0.21	0.19
	0.25	-0.5	0.5	0.	0.	1.	0.11	(0.02)	0.91	(0.02)	0.58	(0.02)	0.	0.75	0.66	0.11	0.16	-0.08	0.12
6	0.25	0.5	-0.5	-1.	0.	0.	1.07	(0.01)	-0.05	(0.01)	0.	(0.01)	1.	0.	0.	0.07	-0.05	0.	0.05
	0.25	0.5	-0.5	0.	-1.	0.	0.03	(0.01)	0.42	(0.01)	1.02	(0.01)	0.	0.36	0.93	0.03	0.06	0.09	0.06
	0.25	0.5	-0.5	0.	0.	-1.	0.02	(0.01)	0.88	(0.01)	-0.55	(0.01)	0.	0.93	-0.36	0.02	-0.05	-0.19	0.11
	0.25	0.5	-0.5	1.	0.	0.	-1.04	(0.01)	0.06	(0.01)	-0.05	(0.01)	-1.	0.	0.	-0.04	0.06	-0.05	0.05
	0.25	0.5	-0.5	0.	1.	0.	-0.1	(0.01)	-0.55	(0.01)	-0.91	(0.01)	0.	-0.36	-0.93	-0.1	-0.19	0.02	0.12
	0.25	0.5	-0.5	0.	0.	1.	-0.06	(0.01)	-0.92	(0.01)	0.44	(0.01)	0.	-0.93	0.36	-0.06	0.01	0.08	0.06
7	1.25	-0.5	-0.5	-1.	0.	0.	1.05	(0.02)	-0.07	(0.02)	-0.08	(0.02)	1.	0.	0.	0.05	-0.07	-0.08	0.07
	1.25	-0.5	-0.5	0.	-1.	0.	0.03	(0.02)	0.59	(0.02)	0.91	(0.02)	0.	0.35	0.94	0.03	0.24	-0.03	0.14
	1.25	-0.5	-0.5	0.	0.	-1.	-0.02	(0.02)	0.79	(0.02)	-0.68	(0.02)	0.	0.94	-0.35	-0.02	-0.15	-0.33	0.21
	1.25	-0.5	-0.5	1.	0.	0.	-1.05	(0.02)	0.06	(0.02)	0.02	(0.02)	-1.	0.	0.	-0.05	0.06	0.02	0.05
	1.25	-0.5	-0.5	0.	1.	0.	-0.15	(0.02)	-0.67	(0.02)	-0.82	(0.02)	0.	-0.35	-0.94	-0.15	-0.32	0.12	0.22
	1.25	-0.5	-0.5	0.	0.	1.	-0.02	(0.02)	-0.83	(0.02)	0.58	(0.02)	0.	-0.94	0.35	-0.02	0.11	0.23	0.15
8	1.75	-0.5	-1.5	-1.	0.	0.	0.92	(0.03)	0.02	(0.03)	0.05	(0.03)	1.	0.	0.	-0.08	0.02	0.05	0.06
	1.75	-0.5	-1.5	0.	-1.	0.	-0.04	(0.03)	0.24	(0.03)	0.89	(0.03)	0.	0.26	0.97	-0.04	-0.02	-0.08	0.05
	1.75	-0.5	-1.5	0.	0.	-1.	0.05	(0.03)	0.91	(0.02)	-0.23	(0.02)	0.	0.97	-0.26	0.05	-0.06	0.03	0.05
	1.75	-0.5	-1.5	1.	0.	0.	-0.99	(0.02)	0.02	(0.03)	-0.06	(0.03)	-1.	0.	0.	0.01	0.02	-0.06	0.04
	1.75	-0.5	-1.5	0.	1.	0.	-0.03	(0.03)	-0.18	(0.03)	-0.95	(0.03)	0.	-0.26	-0.97	-0.03	0.08	0.02	0.05
	1.75	-0.5	-1.5	0.	0.	1.	0.02	(0.03)	-0.93	(0.03)	0.14	(0.03)	0.	-0.97	0.26	0.02	0.04	-0.12	0.07

	Reflection			Incident Polarization			Final Polarization			Calculated Polarization			Difference			RMS
	h	k	l	x	y	z	x	y	z	x	y	z	x	y	z	Average
9	2.25	-1.5	-0.5	-1.	0.	0.	1.08 (0.05)	-0.04 (0.05)	0.01 (0.05)	1.	0.	0.	0.08	-0.04	0.01	0.05
	2.25	-1.5	-0.5	0.	-1.	0.	-0.04 (0.05)	0.68 (0.05)	0.91 (0.05)	0.	0.58	0.82	-0.04	0.1	0.09	0.08
	2.25	-1.5	-0.5	0.	0.	-1.	-0.05 (0.05)	0.81 (0.05)	-0.73 (0.05)	0.	0.82	-0.58	-0.05	-0.01	-0.15	0.09
	2.25	-1.5	-0.5	1.	0.	0.	-1.11 (0.05)	0.04 (0.05)	-0.05 (0.05)	-1.	0.	0.	-0.11	0.04	-0.05	0.07
	2.25	-1.5	-0.5	0.	1.	0.	0.03 (0.05)	-0.65 (0.05)	-0.83 (0.05)	0.	-0.58	-0.82	0.03	-0.07	-0.01	0.04
	2.25	-1.5	-0.5	0.	0.	1.	-0.01 (0.05)	-0.78 (0.05)	0.55 (0.05)	0.	-0.82	0.58	-0.01	0.04	-0.03	0.03
10	2.25	-0.5	-1.5	-1.	0.	0.	1. (0.03)	0. (0.03)	0.02 (0.03)	1.	0.	0.	0.	0.	0.02	0.01
	2.25	-0.5	-1.5	0.	-1.	0.	-0.04 (0.03)	0.26 (0.03)	0.99 (0.03)	0.	0.24	0.97	-0.04	0.02	0.02	0.03
	2.25	-0.5	-1.5	0.	0.	-1.	-0.04 (0.03)	0.97 (0.03)	-0.31 (0.03)	0.	0.97	-0.24	-0.04	0.	-0.07	0.05
	2.25	-0.5	-1.5	1.	0.	0.	-1.05 (0.03)	-0.01 (0.03)	-0.01 (0.03)	-1.	0.	0.	-0.05	-0.01	-0.01	0.03
	2.25	-0.5	-1.5	0.	1.	0.	-0.03 (0.03)	-0.31 (0.03)	-1.03 (0.03)	0.	-0.24	-0.97	-0.03	-0.07	-0.06	0.06
	2.25	-0.5	-1.5	0.	0.	1.	0.05 (0.03)	-0.99 (0.03)	0.22 (0.03)	0.	-0.97	0.24	0.05	-0.02	-0.02	0.03

APPENDIX F

Data tables of the non-collinear incommensurate (AF2) polarimetry data collected on $MnWO_4$

	Reflection			Incident Polarization			Final Polarization				Calculated Polarization			Difference			RMS
	h	k	l	x	y	z	x	y	z		x	y	z	x	y	z	Average
1	-2.214	0.5	1.457	-1.	0.	0.	1.05 (0.01)	0.01 (0.02)	0. (0.02)		1.	0.	0.	0.05	0.01	0.	0.03
	-2.214	0.5	1.457	0.	-1.	0.	0.54 (0.02)	0.11 (0.02)	-0.08 (0.02)		0.54	0.1	-0.12	0.	0.01	0.04	0.02
	-2.214	0.5	1.457	0.	0.	-1.	0.49 (0.02)	-0.09 (0.02)	-0.09 (0.02)		0.54	-0.12	-0.1	-0.05	0.03	0.01	0.03
	-2.214	0.5	1.457	1.	0.	0.	-0.68 (0.03)	-0.02 (0.04)	0.06 (0.04)		-1.	0.	0.	0.32	-0.02	0.06	0.19
	-2.214	0.5	1.457	0.	1.	0.	0.54 (0.02)	-0.09 (0.02)	0.14 (0.02)		0.54	-0.1	0.12	0.	0.01	0.02	0.01
	-2.214	0.5	1.457	0.	0.	1.	0.51 (0.02)	0.14 (0.02)	0.09 (0.02)		0.54	0.12	0.1	-0.03	0.02	-0.01	0.02
2	-2.214	1.5	0.457	-1.	0.	0.	1.05 (0.02)	-0.02 (0.02)	0.04 (0.02)		1.	0.	0.	0.05	-0.02	0.04	0.04
	-2.214	1.5	0.457	0.	-1.	0.	0.42 (0.03)	0.43 (0.03)	0.08 (0.03)		0.49	0.46	0.05	-0.07	-0.03	0.03	0.05
	-2.214	1.5	0.457	0.	0.	-1.	0.47 (0.03)	-0.01 (0.03)	-0.38 (0.03)		0.49	0.05	-0.46	-0.02	-0.06	0.08	0.06
	-2.214	1.5	0.457	1.	0.	0.	-0.67 (0.04)	-0.01 (0.04)	0.03 (0.04)		-1.	0.	0.	0.33	-0.01	0.03	0.19
	-2.214	1.5	0.457	0.	1.	0.	0.5 (0.03)	-0.42 (0.03)	-0.05 (0.03)		0.49	-0.46	-0.05	0.01	0.04	0.	0.02
	-2.214	1.5	0.457	0.	0.	1.	0.53 (0.03)	-0.03 (0.03)	0.4 (0.03)		0.49	-0.05	0.46	0.04	0.02	-0.06	0.04
3	-1.786	0.5	1.543	1.	0.	0.	-1.13 (0.08)	0.09 (0.08)	-0.07 (0.09)		-1.	0.	0.	-0.13	0.09	-0.07	0.1
	-1.786	0.5	1.543	0.	1.	0.	-0.47 (0.05)	-0.2 (0.05)	0.13 (0.05)		-0.54	-0.1	0.17	0.07	-0.1	-0.04	0.07
	-1.786	0.5	1.543	0.	0.	1.	-0.67 (0.04)	0.19 (0.03)	-0.02 (0.03)		-0.54	0.17	0.1	-0.13	0.02	-0.12	0.1
4	-1.214	-0.5	1.457	-1.	0.	0.	1.09 (0.05)	0.01 (0.05)	0. (0.06)		1.	0.	0.	0.09	0.01	0.	0.05
	-1.214	-0.5	1.457	0.	-1.	0.	0.51 (0.08)	0. (0.08)	-0.23 (0.08)		0.53	0.	-0.23	-0.02	0.	0.	0.01
	-1.214	-0.5	1.457	0.	0.	-1.	0.45 (0.08)	-0.22 (0.1)	0. (0.09)		0.53	-0.23	0.	-0.08	0.01	0.	0.05
	-1.214	-0.5	1.457	1.	0.	0.	-0.79 (0)	-0.01 (0)	-0.01 (0)		-1.	0.	0.	0.21	-0.01	-0.01	0.12
	-1.214	-0.5	1.457	0.	1.	0.	0.54 (0.01)	-0.01 (0.01)	0.23 (0.01)		0.53	0.	0.23	0.01	-0.01	0.	0.01
	-1.214	-0.5	1.457	0.	0.	1.	0.52 (0.01)	0.23 (0.01)	0. (0.01)		0.53	0.23	0.	-0.01	0.	0.	0.01

	Reflection			Incident Polarization			Final Polarization			Calculated Polarization			Difference			RMS
	h	k	l	x	y	z	x	y	z	x	y	z	x	y	z	Average
5	-1.214	0.5	0.457	-1.	0.	0.	1.07 (0.01)	0.03 (0.01)	0.01 (0.01)	1.	0.	0.	0.07	0.03	0.01	0.04
	-1.214	0.5	0.457	0.	-1.	0.	0.49 (0.01)	0.17 (0.01)	0.02 (0.01)	0.53	0.24	-0.01	-0.04	-0.07	0.03	0.05
	-1.214	0.5	0.457	0.	0.	-1.	0.41 (0.01)	0. (0.01)	-0.14 (0.01)	0.53	-0.01	-0.24	-0.12	0.01	0.1	0.09
	-1.214	0.5	0.457	1.	0.	0.	-0.69 (0.01)	-0.06 (0.01)	0. (0.01)	-1.	0.	0.	0.31	-0.06	0.	0.18
	-1.214	0.5	0.457	0.	1.	0.	0.54 (0.01)	-0.16 (0.01)	0. (0.01)	0.53	-0.24	0.01	0.01	0.08	-0.01	0.05
	-1.214	0.5	0.457	0.	0.	1.	0.51 (0.01)	-0.02 (0.01)	0.18 (0.01)	0.53	0.01	0.24	-0.02	-0.03	-0.06	0.04
6	-0.786	-0.5	1.543	-1.	0.	0.	1.05 (0.01)	-0.05 (0.02)	-0.05 (0.02)	1.	0.	0.	0.05	-0.05	-0.05	0.05
	-0.786	-0.5	1.543	0.	-1.	0.	-0.64 (0.01)	0.09 (0.01)	-0.2 (0.01)	-0.53	0.04	-0.24	-0.11	0.05	0.04	0.07
	-0.786	-0.5	1.543	0.	0.	-1.	-0.64 (0.01)	-0.19 (0.01)	-0.08 (0.01)	-0.53	-0.24	-0.04	-0.11	0.05	-0.04	0.07
	-0.786	-0.5	1.543	1.	0.	0.	-1.1 (0.08)	-0.02 (0.08)	0.01 (0.07)	-1.	0.	0.	-0.1	-0.02	0.01	0.06
	-0.786	-0.5	1.543	0.	1.	0.	-0.56 (0.04)	0.05 (0.04)	0.28 (0.04)	-0.53	-0.04	0.24	-0.03	0.09	0.04	0.06
	-0.786	-0.5	1.543	0.	0.	1.	-0.63 (0.04)	0.28 (0.04)	0.03 (0.04)	-0.53	0.24	0.04	-0.1	0.04	-0.01	0.06
7	-0.786	0.5	0.543	-1.	0.	0.	1.12 (0.03)	0. (0.03)	-0.01 (0.03)	1.	0.	0.	0.12	0.	-0.01	0.07
	-0.786	0.5	0.543	0.	-1.	0.	-0.56 (0.04)	0.21 (0.04)	-0.14 (0.04)	-0.53	0.25	-0.15	-0.03	-0.04	0.01	0.03
	-0.786	0.5	0.543	0.	0.	-1.	-0.58 (0.04)	-0.13 (0.04)	-0.21 (0.04)	-0.53	-0.15	-0.25	-0.05	0.02	0.04	0.04
	-0.786	0.5	0.543	1.	0.	0.	-1.03 (0.01)	0. (0.01)	-0.02 (0.01)	-1.	0.	0.	-0.03	0.	-0.02	0.02
	-0.786	0.5	0.543	0.	1.	0.	-0.55 (0.01)	-0.21 (0.01)	0.14 (0.01)	-0.53	-0.25	0.15	-0.02	0.04	-0.01	0.03
	-0.786	0.5	0.543	0.	0.	1.	-0.67 (0.01)	0.16 (0.01)	0.22 (0.01)	-0.53	0.15	0.25	-0.14	0.01	-0.03	0.08
8	-0.786	1.5	-0.457	-1.	0.	0.	1.06 (0)	0.03 (0.01)	0.04 (0.01)	1.	0.	0.	0.06	0.03	0.04	0.05
	-0.786	1.5	-0.457	0.	-1.	0.	-0.1 (0.01)	0.99 (0.01)	0.34 (0.01)	-0.03	0.94	0.34	-0.07	0.05	0.	0.05
	-0.786	1.5	-0.457	0.	0.	-1.	-0.05 (0.01)	0.19 (0.01)	-1.01 (0.01)	-0.03	0.34	-0.94	-0.02	-0.15	-0.07	0.1
	-0.786	1.5	-0.457	1.	0.	0.	-1.05 (0.01)	-0.03 (0.01)	-0.08 (0.01)	-1.	0.	0.	-0.05	-0.03	-0.08	0.06
	-0.786	1.5	-0.457	0.	1.	0.	-0.04 (0.01)	-1.01 (0.01)	-0.28 (0.01)	-0.03	-0.94	-0.34	-0.01	-0.07	0.06	0.05
	-0.786	1.5	-0.457	0.	0.	1.	-0.09 (0.01)	-0.3 (0.01)	1.01 (0.01)	-0.03	-0.34	0.94	-0.06	0.04	0.07	0.06

	Reflection			Incident Polarization			Final Polarization				Calculated Polarization			Difference			RMS
	h	k	l	x	y	z	x	y	z		x	y	z	x	y	z	Average
9	-0.214	-1.5	1.457	-1.	0.	0.	1.01 (0.01)	-0.06 (0.01)	0.04	(0.01)	1.	0.	0.	0.01	-0.06	0.04	0.04
	-0.214	-1.5	1.457	0.	-1.	0.	0.43 (0.01)	0.28 (0.01)	-0.11	(0.01)	0.47	0.31	-0.4	-0.04	-0.03	0.29	0.17
	-0.214	-1.5	1.457	0.	0.	-1.	0.43 (0.01)	-0.15 (0.01)	-0.17	(0.01)	0.47	-0.4	-0.31	-0.04	0.25	0.14	0.17
	-0.214	-1.5	1.457	1.	0.	0.	-0.96 (0.04)	0.04 (0.04)	-0.01	(0.04)	-1.	0.	0.	0.04	0.04	-0.01	0.03
	-0.214	-1.5	1.457	0.	1.	0.	0.54 (0.06)	-0.13 (0.07)	0.08	(0.07)	0.47	-0.31	0.4	0.07	0.18	-0.32	0.22
	-0.214	-1.5	1.457	0.	0.	1.	0.46 (0.06)	0.03 (0.06)	0.11	(0.06)	0.47	0.4	0.31	-0.01	-0.37	-0.2	0.24
10	-0.214	-0.5	0.457	-1.	0.	0.	1.14 (0.1)	0. (0.1)	0.	(0.1)	1.	0.	0.	0.14	0.	0.	0.08
	-0.214	-0.5	0.457	0.	-1.	0.	0.48 (0.06)	0.17 (0.06)	-0.32	(0.06)	0.49	0.18	-0.43	-0.01	-0.01	0.11	0.06
	-0.214	-0.5	0.457	0.	0.	-1.	0.31 (0.06)	-0.3 (0.07)	-0.14	(0.06)	0.49	-0.43	-0.18	-0.18	0.13	0.04	0.13
	-0.214	-0.5	0.457	1.	0.	0.	-0.63 (0)	-0.02 (0)	0.02	(0)	-1.	0.	0.	0.37	-0.02	0.02	0.21
	-0.214	-0.5	0.457	0.	1.	0.	0.53 (0)	-0.16 (0)	0.34	(0)	0.49	-0.18	0.43	0.04	0.02	-0.09	0.06
	-0.214	-0.5	0.457	0.	0.	1.	0.45 (0)	0.38 (0)	0.18	(0)	0.49	0.43	0.18	-0.04	-0.05	0.	0.04
11	-0.214	1.5	-1.543	-1.	0.	0.	0.34 (0.01)	0.02 (0.01)	0.	(0.01)	1.	0.	0.	-0.66	0.02	0.	0.38
	-0.214	1.5	-1.543	0.	-1.	0.	-0.44 (0)	0.22 (0)	0.22	(0)	-0.45	0.45	0.35	0.01	-0.23	-0.13	0.15
	-0.214	1.5	-1.543	0.	0.	-1.	-0.35 (0)	0.19 (0)	-0.5	(0)	-0.45	0.35	-0.45	0.1	-0.16	-0.05	0.11
	-0.214	1.5	-1.543	1.	0.	0.	-0.81 (0.02)	-0.04 (0.02)	-0.03	(0.02)	-1.	0.	0.	0.19	-0.04	-0.03	0.11
	-0.214	1.5	-1.543	0.	1.	0.	-0.37 (0.02)	-0.27 (0.02)	-0.24	(0.02)	-0.45	-0.45	-0.35	0.08	0.18	0.11	0.13
	-0.214	1.5	-1.543	0.	0.	1.	-0.36 (0.02)	-0.22 (0.02)	0.49	(0.02)	-0.45	-0.35	0.45	0.09	0.13	0.04	0.09
12	0.214	-1.5	1.543	-1.	0.	0.	-0.35 (0.01)	-0.04 (0.02)	-0.03	(0.02)	1.	0.	0.	-1.35	-0.04	-0.03	0.78
	0.214	-1.5	1.543	0.	-1.	0.	-0.25 (0.02)	-0.3 (0.02)	-0.19	(0.02)	-0.45	0.45	-0.35	0.2	-0.75	0.16	0.46
	0.214	-1.5	1.543	0.	0.	-1.	-0.2 (0.02)	-0.13 (0.02)	-0.83	(0.02)	-0.45	-0.35	-0.45	0.25	0.22	-0.38	0.29
	0.214	-1.5	1.543	1.	0.	0.	-0.15 (0.06)	0.01 (0.06)	-0.04	(0.06)	-1.	0.	0.	0.85	0.01	-0.04	0.49
	0.214	-1.5	1.543	0.	1.	0.	-0.23 (0.05)	0.29 (0.05)	0.2	(0.05)	-0.45	-0.45	0.35	0.22	0.74	-0.15	0.45
	0.214	-1.5	1.543	0.	0.	1.	-0.2 (0.05)	0.23 (0.06)	0.84	(0.05)	-0.45	0.35	0.45	0.25	-0.12	0.39	0.28

	Reflection			Incident Polarization			Final Polarization				Calculated Polarization			Difference			RMS
	h	k	l	x	y	z	x	y	z		x	y	z	x	y	z	Average
13	0.214	0.5	-0.457	-1.	0.	0.	1.02	(0.04)	0.	(0.04)	0.03	(0.04)	1.	0.	0.	0.02	0.	0.03	0.02
	0.214	0.5	-0.457	0.	-1.	0.	0.49	(0.05)	0.19	(0.05)	0.39	(0.05)	0.49	0.18	0.43	0.	0.01	-0.04	0.02
	0.214	0.5	-0.457	0.	0.	-1.	0.66	(0.05)	0.37	(0.05)	-0.21	(0.06)	0.49	0.43	-0.18	0.17	-0.06	-0.03	0.11
	0.214	0.5	-0.457	1.	0.	0.	-1.16	(0)	-0.01	(0.01)	-0.06	(0.01)	-1.	0.	0.	-0.16	-0.01	-0.06	0.1
	0.214	0.5	-0.457	0.	1.	0.	0.52	(0.01)	-0.19	(0.01)	-0.33	(0.01)	0.49	-0.18	-0.43	0.03	-0.01	0.1	0.06
	0.214	0.5	-0.457	0.	0.	1.	0.56	(0.01)	-0.33	(0.01)	0.17	(0.01)	0.49	-0.43	0.18	0.07	0.1	-0.01	0.07
14	0.786	-0.5	-0.543	-1.	0.	0.	0.65	(0.01)	0.	(0.01)	0.	(0.01)	1.	0.	0.	-0.35	0.	0.	0.2
	0.786	-0.5	-0.543	0.	-1.	0.	-0.55	(0.01)	0.2	(0.01)	0.11	(0.01)	-0.53	0.25	0.15	-0.02	-0.05	-0.04	0.04
	0.786	-0.5	-0.543	0.	0.	-1.	-0.5	(0.01)	0.12	(0.01)	-0.22	(0.01)	-0.53	0.15	-0.25	0.03	-0.03	0.03	0.03
	0.786	-0.5	-0.543	1.	0.	0.	-1.11	(0)	0.	(0)	-0.03	(0)	-1.	0.	0.	-0.11	0.	-0.03	0.07
	0.786	-0.5	-0.543	0.	1.	0.	-0.53	(0)	-0.2	(0)	-0.14	(0)	-0.53	-0.25	-0.15	0.	0.05	0.01	0.03
	0.786	-0.5	-0.543	0.	0.	1.	-0.43	(0)	-0.12	(0)	0.18	(0)	-0.53	-0.15	0.25	0.1	0.03	-0.07	0.07
15	1.214	-0.5	-0.457	-1.	0.	0.	1.07	(0)	-0.02	(0)	0.03	(0)	1.	0.	0.	0.07	-0.02	0.03	0.05
	1.214	-0.5	-0.457	0.	-1.	0.	0.54	(0)	0.13	(0)	-0.01	(0)	0.53	0.24	0.01	0.01	-0.11	-0.02	0.06
	1.214	-0.5	-0.457	0.	0.	-1.	0.67	(0)	-0.01	(0)	-0.15	(0)	0.53	0.01	-0.24	0.14	-0.02	0.09	0.1
	1.214	-0.5	-0.457	1.	0.	0.	-1.13	(0.01)	-0.01	(0.01)	-0.04	(0.01)	-1.	0.	0.	-0.13	-0.01	-0.04	0.08
	1.214	-0.5	-0.457	0.	1.	0.	0.57	(0.02)	-0.17	(0.02)	0.04	(0.02)	0.53	-0.24	-0.01	0.04	0.07	0.05	0.05
	1.214	-0.5	-0.457	0.	0.	1.	0.6	(0.02)	0.03	(0.02)	0.18	(0.02)	0.53	-0.01	0.24	0.07	0.04	-0.06	0.06
16	1.214	0.5	-1.457	-1.	0.	0.	1.05	(0.02)	0.01	(0.03)	0.03	(0.03)	1.	0.	0.	0.05	0.01	0.03	0.03
	1.214	0.5	-1.457	0.	-1.	0.	0.52	(0.02)	0.	(0.02)	0.24	(0.02)	0.53	0.	0.23	-0.01	0.	0.01	0.01
	1.214	0.5	-1.457	0.	0.	-1.	0.61	(0.02)	0.24	(0.02)	-0.01	(0.02)	0.53	0.23	0.	0.08	0.01	-0.01	0.05
	1.214	0.5	-1.457	1.	0.	0.	-1.07	(0)	-0.01	(0.01)	-0.04	(0.01)	-1.	0.	0.	-0.07	-0.01	-0.04	0.05
	1.214	0.5	-1.457	0.	1.	0.	0.55	(0.01)	-0.01	(0.01)	-0.22	(0.01)	0.53	0.	-0.23	0.02	-0.01	0.01	0.01
	1.214	0.5	-1.457	0.	0.	1.	0.54	(0.01)	-0.25	(0.01)	0.01	(0.01)	0.53	-0.23	0.	0.01	-0.02	0.01	0.01

	Reflection			Incident Polarization			Final Polarization			Calculated Polarization			Difference			RMS
	h	k	l	x	y	z	x	y	z	x	y	z	x	y	z	Average
17	1.214	0.5	-1.457	-1.	0.	0.	1.06 (0.01)	0.02 (0.01)	0.04 (0.01)	1.	0.	0.	0.06	0.02	0.04	0.04
	1.214	0.5	-1.457	0.	-1.	0.	0.55 (0.01)	0. (0.01)	0.25 (0.01)	0.53	0.	0.23	0.02	0.	0.02	0.02
	1.214	0.5	-1.457	0.	0.	-1.	0.6 (0.01)	0.27 (0.01)	0.01 (0.01)	0.53	0.23	0.	0.07	0.04	0.01	0.05
	1.214	0.5	-1.457	1.	0.	0.	-1.08 (0.01)	-0.01 (0.01)	-0.05 (0.01)	-1.	0.	0.	-0.08	-0.01	-0.05	0.05
	1.214	0.5	-1.457	0.	1.	0.	0.58 (0.01)	-0.01 (0.01)	-0.26 (0.01)	0.53	0.	-0.23	0.05	-0.01	-0.03	0.03
	1.214	0.5	-1.457	0.	0.	1.	0.56 (0.01)	-0.23 (0.01)	0.02 (0.01)	0.53	-0.23	0.	0.03	0.	0.02	0.02
18	1.786	-0.5	-1.543	-1.	0.	0.	0.77 (0.02)	-0.07 (0.02)	-0.02 (0.02)	1.	0.	0.	-0.23	-0.07	-0.02	0.14
	1.786	-0.5	-1.543	0.	-1.	0.	-0.53 (0.01)	0.11 (0.01)	0.16 (0.01)	-0.54	0.1	0.17	0.01	0.01	-0.01	0.01
	1.786	-0.5	-1.543	0.	0.	-1.	-0.49 (0.01)	0.11 (0.01)	-0.04 (0.01)	-0.54	0.17	-0.1	0.05	-0.06	0.06	0.06
	1.786	-0.5	-1.543	1.	0.	0.	-1.02 (0.06)	-0.01 (0.05)	-0.04 (0.05)	-1.	0.	0.	-0.02	-0.01	-0.04	0.03
	1.786	-0.5	-1.543	0.	1.	0.	-0.45 (0.03)	-0.16 (0.03)	-0.17 (0.03)	-0.54	-0.1	-0.17	0.09	-0.06	0.	0.06
	1.786	-0.5	-1.543	0.	0.	1.	-0.55 (0.04)	-0.21 (0.04)	0.09 (0.04)	-0.54	-0.17	0.1	-0.01	-0.04	-0.01	0.02
19	2.214	-1.5	-0.457	-1.	0.	0.	1.1 (0.02)	-0.07 (0.02)	0. (0.03)	1.	0.	0.	0.1	-0.07	0.	0.07
	2.214	-1.5	-0.457	0.	-1.	0.	0.39 (0.03)	0.34 (0.03)	-0.07 (0.03)	0.49	0.46	-0.05	-0.1	-0.12	-0.02	0.09
	2.214	-1.5	-0.457	0.	0.	-1.	0.61 (0.03)	-0.08 (0.03)	-0.52 (0.04)	0.49	-0.05	-0.46	0.12	-0.03	-0.06	0.08
	2.214	-1.5	-0.457	1.	0.	0.	-0.97 (0.06)	-0.05 (0.06)	0.25 (0.06)	-1.	0.	0.	0.03	-0.05	0.25	0.15
	2.214	-1.5	-0.457	0.	1.	0.	0.46 (0.09)	-0.56 (0.09)	0.15 (0.1)	0.49	-0.46	0.05	-0.03	-0.1	0.1	0.08
	2.214	-1.5	-0.457	0.	0.	1.	0.58 (0.08)	-0.01 (0.09)	0.41 (0.09)	0.49	0.05	0.46	0.09	-0.06	-0.05	0.07
20	2.214	-0.5	-1.457	-1.	0.	0.	1.03 (0.14)	0.06 (0.13)	0. (0.14)	1.	0.	0.	0.03	0.06	0.	0.04
	2.214	-0.5	-1.457	0.	-1.	0.	0.44 (0.08)	0.13 (0.08)	0.12 (0.08)	0.54	0.1	0.12	-0.1	0.03	0.	0.06
	2.214	-0.5	-1.457	0.	0.	-1.	0.55 (0.08)	0.1 (0.08)	-0.11 (0.08)	0.54	0.12	-0.1	0.01	-0.02	-0.01	0.01
	2.214	-0.5	-1.457	1.	0.	0.	-0.77 (0.03)	0.24 (0.03)	-0.08 (0.04)	-1.	0.	0.	0.23	0.24	-0.08	0.2
	2.214	-0.5	-1.457	0.	1.	0.	0.56 (0.04)	-0.07 (0.04)	-0.11 (0.04)	0.54	-0.1	-0.12	0.02	0.03	0.01	0.02
	2.214	-0.5	-1.457	0.	0.	1.	0.41 (0.03)	-0.07 (0.03)	0.18 (0.04)	0.54	-0.12	0.1	-0.13	0.05	0.08	0.09

APPENDIX G

Data tables of the collinear incommensurate (AF3) polarimetry data collected on $MnWO_4$

	Reflection			Incident Polarization			Final Polarization			Calculated Polarization			Difference			RMS
	h	k	l	x	y	z	x	y	z	x	y	z	x	y	z	Average
1	-1.214	-0.5	1.457	-1	0	0	0.97 (0.03)	0.02 (0.03)	-0.02 (0.03)	1	0	0	-0.03	0.02	-0.02	0.02
	-1.214	-0.5	1.457	0	-1	0	-0.08 (0.03)	0.18 (0.03)	-0.94 (0.03)	0	0.14	-0.99	-0.08	0.04	0.05	0.06
	-1.214	-0.5	1.457	0	0	-1	-0.08 (0.03)	-0.93 (0.03)	-0.12 (0.03)	0	-0.99	-0.14	-0.08	0.06	0.02	0.06
	-1.214	-0.5	1.457	1	0	0	-0.99 (0.03)	-0.01 (0.03)	0.02 (0.03)	-1	0	0	0.01	-0.01	0.02	0.01
	-1.214	-0.5	1.457	0	1	0	0 (0.03)	-0.14 (0.03)	0.92 (0.03)	0	-0.14	0.99	0	0	-0.07	0.04
	-1.214	-0.5	1.457	0	0	1	0 (0.03)	0.92 (0.03)	0.22 (0.03)	0	0.99	0.14	0	-0.07	0.08	0.06
2	-0.214	0.5	-0.543	-1	0	0	0.92 (0.03)	-0.08 (0.03)	0.05 (0.03)	1	0	0	-0.08	-0.08	0.05	0.07
	-0.214	0.5	-0.543	0	-1	0	-0.02 (0.03)	0.43 (0.03)	0.84 (0.03)	0	0.47	0.88	-0.02	-0.04	-0.04	0.03
	-0.214	0.5	-0.543	0	0	-1	0.02 (0.03)	0.81 (0.03)	-0.44 (0.03)	0	0.88	-0.47	0.02	-0.07	0.03	0.05
	-0.214	0.5	-0.543	1	0	0	-0.98 (0.03)	-0.06 (0.03)	-0.06 (0.03)	-1	0	0	0.02	-0.06	-0.06	0.05
	-0.214	0.5	-0.543	0	1	0	0.01 (0.03)	-0.52 (0.03)	-0.81 (0.03)	0	-0.47	-0.88	0.01	-0.05	0.07	0.05
	-0.214	0.5	-0.543	0	0	1	0.04 (0.03)	-0.78 (0.03)	0.44 (0.03)	0	-0.88	0.47	0.04	0.1	-0.03	0.06
3	-0.214	1.5	-1.543	-1	0	0	-0.15 (0.07)	-0.07 (0.08)	-0.02 (0.08)	1	0	0	-1.15	-0.07	-0.02	0.67
	-0.214	1.5	-1.543	0	-1	0	-0.12 (0.07)	-0.35 (0.07)	0.42 (0.07)	0	0.42	0.91	-0.12	-0.77	-0.49	0.53
	-0.214	1.5	-1.543	0	0	-1	-0.02 (0.06)	0.32 (0.07)	-0.72 (0.07)	0	0.91	-0.42	-0.02	-0.59	-0.3	0.38
	-0.214	1.5	-1.543	1	0	0	0.19 (0.07)	-0.02 (0.07)	0.07 (0.07)	-1	0	0	1.19	-0.02	0.07	0.69
	-0.214	1.5	-1.543	0	1	0	0.12 (0.09)	0.27 (0.07)	-0.4 (0.07)	0	-0.42	-0.91	0.12	0.69	0.51	0.5
	-0.214	1.5	-1.543	0	0	1	-0.04 (0.06)	-0.31 (0.07)	0.71 (0.07)	0	-0.91	0.42	-0.04	0.6	0.29	0.39
4	0.214	-1.5	1.543	-1	0	0	-0.69 (0.07)	-0.01 (0.07)	-0.1 (0.07)	1	0	0	-1.69	-0.01	-0.1	0.98
	0.214	-1.5	1.543	0	-1	0	0 (0.07)	-0.73 (0.07)	-0.14 (0.07)	0	0.42	-0.91	0	-1.15	0.77	0.8
	0.214	-1.5	1.543	0	0	-1	0.02 (0.07)	0.03 (0.07)	-0.88 (0.08)	0	-0.91	-0.42	0.02	0.94	-0.46	0.6
	0.214	-1.5	1.543	1	0	0	0.75 (0.06)	0.03 (0.06)	-0.1 (0.07)	-1	0	0	1.75	0.03	-0.1	1.01
	0.214	-1.5	1.543	0	1	0	-0.01 (0.07)	0.91 (0.07)	0.14 (0.07)	0	-0.42	0.91	-0.01	1.33	-0.77	0.89
	0.214	-1.5	1.543	0	0	1	0.07 (0.07)	0.15 (0.07)	1 (0.07)	0	0.91	0.42	0.07	-0.76	0.58	0.55

	Reflection			Incident Polarization			Final Polarization			Calculated Polarization			Difference			RMS
	h	k	l	x	y	z	x	y	z	x	y	z	x	y	z	Average
5	0.214	0.5	-0.457	-1	0	0	1.07 (0.03)	0.03 (0.04)	0.03 (0.04)	1	0	0	0.07	0.03	0.03	0.05
	0.214	0.5	-0.457	0	-1	0	-0.02 (0.04)	0.35 (0.04)	1.03 (0.03)	0	0.33	0.94	-0.02	0.02	0.09	0.05
	0.214	0.5	-0.457	0	0	-1	-0.08 (0.04)	0.97 (0.03)	-0.32 (0.04)	0	0.94	-0.33	-0.08	0.03	0.01	0.05
	0.214	0.5	-0.457	1	0	0	-1.03 (0.03)	0.06 (0.04)	-0.09 (0.04)	-1	0	0	-0.03	0.06	-0.09	0.06
	0.214	0.5	-0.457	0	1	0	0.03 (0.04)	-0.33 (0.04)	-1 (0.04)	0	-0.33	-0.94	0.03	0	-0.06	0.04
	0.214	0.5	-0.457	0	0	1	0.02 (0.04)	-0.96 (0.033)	0.3 (0.04)	0	-0.94	0.33	0.02	-0.02	-0.03	0.02
6	0.786	-1.5	0.457	-1	0	0	1.01 (0.02)	0.01 (0.02)	-0.02 (0.02)	1	0	0	0.01	0.01	-0.02	0.01
	0.786	-1.5	0.457	0	-1	0	-0.06 (0.02)	0.98 (0.02)	-0.21 (0.02)	0	0.97	-0.23	-0.06	0.01	0.02	0.04
	0.786	-1.5	0.457	0	0	-1	-0.04 (0.02)	-0.23 (0.03)	-0.97 (0.02)	0	-0.23	-0.97	-0.04	0	0	0.02
	0.786	-1.5	0.457	1	0	0	-0.99 (0.02)	0.01 (0.02)	0.02 (0.02)	-1	0	0	0.01	0.01	0.02	0.01
	0.786	-1.5	0.457	0	1	0	-0.02 (0.02)	-1 (0.02)	0.26 (0.02)	0	-0.97	0.23	-0.02	-0.03	0.03	0.03
	0.786	-1.5	0.457	0	0	1	0.04 (0.02)	0.19 (0.02)	0.97 (0.02)	0	0.23	0.97	0.04	-0.04	0	0.03
7	0.786	-0.5	-0.543	-1	0	0	0.99 (0.01)	0.02 (0.02)	0 (0.02)	1	0	0	-0.01	0.02	0	0.01
	0.786	-0.5	-0.543	0	-1	0	-0.03 (0.02)	0.5 (0.02)	0.85 (0.01)	0	0.48	0.88	-0.03	0.02	-0.03	0.03
	0.786	-0.5	-0.543	0	0	-1	-0.03 (0.02)	0.81 (0.02)	-0.5 (0.02)	0	0.88	-0.48	-0.03	-0.07	-0.02	0.05
	0.786	-0.5	-0.543	1	0	0	-1.01 (0.01)	0 (0.02)	-0.06 (0.02)	-1	0	0	-0.01	0	-0.06	0.04
	0.786	-0.5	-0.543	0	1	0	-0.02 (0.02)	-0.49 (0.02)	-0.79 (0.02)	0	-0.48	-0.88	-0.02	-0.01	0.09	0.05
	0.786	-0.5	-0.543	0	0	1	0.02 (0.02)	-0.83 (0.01)	0.5 (0.02)	0	-0.88	0.48	0.02	0.05	0.02	0.03
8	1.214	0.5	-1.457	-1	0	0	1.08 (0.04)	-0.06 (0.04)	0.01 (0.04)	1	0	0	0.08	-0.06	0.01	0.06
	1.214	0.5	-1.457	0	-1	0	-0.01 (0.05)	0.18 (0.04)	0.94 (0.04)	0	0.14	0.99	-0.01	0.04	-0.05	0.04
	1.214	0.5	-1.457	0	0	-1	0.07 (0.04)	0.9 (0.04)	-0.31 (0.04)	0	0.99	-0.14	0.07	-0.09	-0.17	0.12
	1.214	0.5	-1.457	1	0	0	-1.04 (0.04)	0.01 (0.04)	-0.05 (0.04)	-1	0	0	-0.04	0.01	-0.05	0.04
	1.214	0.5	-1.457	0	1	0	0.04 (0.04)	-0.22 (0.04)	-0.97 (0.04)	0	-0.14	-0.99	0.04	-0.08	0.02	0.05
	1.214	0.5	-1.457	0	0	1	-0.06 (0.04)	-0.97 (0.04)	0.15 (0.05)	0	-0.99	0.14	-0.06	0.02	0.01	0.04

APPENDIX H

Orientation information for the AF1 phase

UB matrix	h	k	l	*gamma*	*omega*	*nu*
1	0.	1.	1.	−12.558	−82.762	0.
2	0.	1.	−1.	−12.558	−82.504	0.
$diff$				0.	0.258	0.
1	0.25	−0.5	−0.5	−6.573	118.514	−1.303
2	0.25	−0.5	0.5	−6.636	118.475	1.318
$diff$				0.063	0.039	0.015
1	−0.75	0.5	−0.5	−9.651	14.486	−1.303
2	−0.75	0.5	0.5	−9.513	13.641	1.318
$diff$				0.138	0.845	0.015
1	−0.75	0.5	0.5	−8.777	−36.461	3.913
2	−0.75	0.5	−0.5	−8.905	−37.348	−3.956
$diff$				0.128	0.887	0.043
1	−0.75	−0.5	−1.5	−16.636	59.808	−1.303
2	−0.75	−0.5	1.5	−16.396	60.105	1.318
$diff$				0.24	0.297	0.015
1	1.25	−1.5	−0.5	−17.976	144.606	−1.303
2	1.25	−1.5	0.5	−18.097	143.68	1.318
$diff$				0.121	0.926	0.015
1	1.25	0.5	1.5	−19.419	−131.543	−1.303
2	1.25	0.5	−1.5	−19.074	−131.564	1.318
$diff$				0.345	0.021	0.015
1	0.21	−1.5	−1.46	−18.646	100.111	−0.891
2	0.21	−1.5	1.54	−19.3	98.939	1.355
$diff$				0.654	1.172	0.464
1	0.21	−0.5	−0.46	−6.236	118.282	−0.891
2	0.21	−0.5	0.54	−6.806	114.081	1.355
$diff$				0.57	4.201	0.464
1	1.21	−1.5	−0.46	−17.659	145.223	−0.891
2	1.21	−1.5	0.54	−17.971	142.088	1.355
$diff$				0.312	3.135	0.464

TABLE H.1. The angles that describe the detector and sample positions where **UB** matrix 1 was the original, incorrect matrix calculated for a sample oriented with the [1 1 $\bar{1}$] direction upward the **UB** matrix 2 had the [1 1 1] direction upward. The value $diff$ is the difference of the absolute values of the angles. All the instrument angles change for out of plane reflections.

UB matrix 1 [1 1 $\bar{1}$]

$$\begin{pmatrix} 0.170065 & -0.0958421 & 0.0338484 \\ 0.043891 & 0.0941092 & 0.163777 \\ -0.110312 & -0.110312 & 0.110312 \end{pmatrix}$$

UB matrix 2 [1 1 1]

$$\begin{pmatrix} 0.170504 & -0.094383 & -0.0312254 \\ 0.0387912 & 0.0941375 & -0.163466 \\ 0.111539 & 0.11154 & 0.11154 \end{pmatrix}$$

TABLE H.2. The **UB** matrices taken from the log files used to calculate the instrument angles during the $MnWO_4$ experiment on D3.